Design of monoaxial and coaxial electrospun membranes for biomedical applications

Raffaele Longo

UNIVERSITY OF SALERNO

DEPARTMENT OF INDUSTRIAL ENGINEERING

Ph.D. Course in Industrial Engineering
Curriculum in Chemical Engineering - XXXV Cycle

DESIGN OF MONOAXIAL AND COAXIAL ELECTROSPUN MEMBRANES FOR BIOMEDICAL APPLICATIONS

Supervisor
Prof. Liberata Guadagno

Ph.D. student
Raffaele Longo

Scientific Referees
Prof. Patrizia Lamberti
Prof. Giovanna Della Porta
Prof. Luigi Vertuccio

Ph.D. Course Coordinator
Prof. Francesco Donsì

\

Published Paper List

1. Guadagno L., Raimondo M., **Longo R.**, Sarno M., Iuliano M., Mariconda A., Saturnino C., Ceramella J., Iacopetta D., Sinicropi M. S. (2020). Development and characterization of antitumoral electrospun polycaprolactone/functionalized Fe3O4 hybrid membranes. MATERIALS TODAY CHEMISTRY, vol. 17, Article number 100309, p. 1-11, ISSN: 2468-5194, doi: 10.1016/j.mtchem.2020.100309

2. Gorrasi G., **Longo R.**, Viscusi G. (2020). Fabrication and characterization of electrospun membranes based on "poly(ε-caprolactone)", "poly(3-hydroxybutyrate)" and their blend for tunable drug delivery of curcumin. POLYMERS, vol. 12, p. 1-16, ISSN: 2073-4360, doi: 10.3390/polym12102239

3. **Longo R.**, Gorrasi G., Guadagno L. (2021). Electromagnetically stimuli-responsive nanoparticles-based systems for biomedical applications: Recent advances and future perspectives. NANOMATERIALS, vol. 11 (848), p. 1-28, ISSN: 2079-4991, doi: 10.3390/nano11040848

4. **Longo R.**, Catauro M., Sorrentino A., Guadagno L., Thermal and Mechanical Characterization of complex electrospun systems based on Polycaprolactone and Gelatin, Journal of Thermal Analysis and Calorimetry, 2022, vol. 147 (9), 5391-5399

5. Guadagno L., Raimondo M., Vertuccio L., Lamparelli E. P., Ciardulli M. C., Longo P., Mariconda A., Della Porta G., **Longo R.**, Electrospun Membranes Designed for Burst Release of New Gold-Complexes Inducing Apoptosis of Melanoma Cells, International Journal of Molecular Sciences, vol. 23 (13), 7147

6. **Longo R.**, Guadagno L., Lamberti P. (2020). Electromagnetic Characterization of Polycaprolactone electrospun nanofibers filled with Fe_3O_4 Nanoparticles. In: 4th International Symposium on Multidisciplinary Studies and Innovative Technologies, ISMSIT 2020 - Proceedings. p. 1-5, Institute of Electrical and Electronics Engineers Inc., ISBN: 978-1-7281-9090-7, Istanbul (TURKEY), 22 October 2020 through 24 October 2020, doi: 10.1109/ISMSIT50672.2020.9254745

7. Raimondo M., **Longo R.**, Guadagno L. (2021). Electrical behavior at nanometer scale of functionalized graphene-based structural resins. In: AIP Conference Proceedings. vol. 2327 (020035), p. 1-9,

American Institute of Physics Inc., ISBN: 978-073544071-5, Surya Engineering College [SEC], ind, 2020, doi: 10.1063/5.0039477

8. Raimondo M., **Longo R.**, Lotti N., Soccio M., Catauro M., Guadagno L., Electrospun membranes of poly(butylene succinate) and poly(butylene/2-butyl,2-ethyl-propylene succinate), Macromolecular Symposia, 2022, 405, 2100210, doi: 10.1002/masy.202100210

9. Guadagno L., Aliberti F., **Longo R.**, Raimondo M., Pantani R., Sorrentino A., Catauro M., Vertuccio L., 3D printed materials with electrical properties tailored for thermal management, Materials & Design, 2023, 225, 111507

10. **Longo R.,** Raimondo M., Vertuccio L., Ciardulli M. C., Sirignano M., Mariconda A., Della Porta G., Guadagno L., Bottom-up strategy to forecast the drug location and release kinetics in antitumoral electrospun drug delivery systems, International Journal of Molecular Sciences, 2023, 24, 1507, https://doi.org/10.3390/ijms24021507

11. Guadagno L., **Longo R.**, Aliberti F., Lamberti P., Tucci V., Pantani R., Spinelli G., Catauro M., Vertuccio L., Role of MWCNTs loading in designing self-sensing and self-heating structural elements, Nanomaterials, 2023, 13, 495, https://doi.org/10.3390/nano13030495

12. Guadagno L., Raimondo M, **Longo R.**, Aliberti F., Passaro J., Catauro M., Calabrese E., Spectroscopic investigation of supramolecular self-healing resins based on covalently modified carbon nanotubes, Macromolecular Symposia *(accepted)*

13. Vertuccio L., Calabrese E., D'Angelo A., Piccirillo A. M., **Longo R.**, FTIR analysis of the curing behaviors of bi-functional epoxy resin with anhydride based hardener, Macromolecular Symposia *(accepted)*

14. **Longo R.**, Catauro M., Vertuccio L., Guadagno L., Comparison between morphological and mechanical properties of membranes produced via Coaxial and Monoaxial Electrospinning, Macromolecular Symposia *(under review)*

15. Scala P., Manzo P., **Longo R.**, Giudice V., Ciardulli M. C., Serio B., Selleri C., Guadagno L., Rehak L., Maffulli N., Della Porta G., Contribution of Peripheral Blood Mononuclear Cells isolated by advanced filtration system to myogenesis of Human Bone Marrow Mesenchymal Stem Cells co-cultured with Myoblasts, Heliyon *(submitted)*

\

16. **PATENT**: Guadagno L., Vertuccio L., **Longo R.**, Pantani R., Gallo G. S., Iannuzzo G., Russo S., Albolino A., De Luca D., Manufatto con film riscaldante, Domanda Numero 102022000017019, Data di presentazione: 09/08/2022 [Applied by LEONARDO S.P.A.]

Index

Index of Figures

Index of Tables

Abstract

According to the Institute for Health Metrics and Evaluation, cancer is a disease that each year causes above 17% of all global deaths (2017). Currently, the most used therapies are generally administrated orally or via injection. However, topical systems, differently from the traditional ones, can guarantee a way slower release of drugs in the biological environment that can be delivered directly to the zone of interest, providing less invasive treatment with fewer side effects.

In this scenario, the present Ph.D. thesis aims to develop cutting-edge nanofibrous materials obtained through the electrospinning process designed for application in the biomedical field, in particular for cancer treatment.

This process allows producing innovative drug delivery systems with peculiar morphology that can well mimic the structures of the human tissue (scaffolds). For this reason, they are particularly interesting for post-surgical cancer treatments.

The present research is focused mainly on biocompatible and biodegradable polymers, to have no negative immune response by the system. Natural and synthetic biopolymer present significantly different properties, such as mechanical ones, biocompatibility, etc. Thus, the research has explored how the use of different process configurations (uniaxial electrospinning and coaxial electrospinning) affects the thermal, structural, and mechanical properties of the natural-synthetic biopolymer electrospun systems.

Two types of fillers have been loaded in the electrospun systems: nanoparticles and active molecules.

The first part of the performed research deals with the use of functionalized magnetic nanoparticles included in nanofibrous systems and the strategy of obtaining efficient dispersion of nanoparticles in polymeric nanofibers by enhancing the compatibility between the filler and the matrix. Relevant results have been obtained controlling the morphology and the thermal and mechanical properties.

Antitumoral tests have shown highly promising results against several types of skin cancers.

The second part of the activity involved two different approaches: on the one hand, the use of commercial chemotherapeutics (Dacarbazine), the drug used in the treatment of melanoma; on the other hand, the use of non-commercial complexes, ad hoc synthesized.

The nanofibrous systems loaded with synthetic antitumoral metal complexes have shown outstanding activity against some very aggressive skin cancer. The systems have been investigated to understand how the affinity between the filler and the matrix affects the location of the active substance in

nanofibrous systems, determining noticeable effects on the morphology and the drug release mechanism.
Further investigations have been performed through a coaxial electrospinning process, which allows for obtaining bilayer nanofibers. The performed research highlighted that, by using a coaxial process, it is possible to control the release kinetics of the active substance. Furthermore, by selecting the chemical nature of the external and internal nature of the polymers of the coaxial nanofiber and the processing parameters appropriately, it is possible also to enhance the material's performance in terms of biocompatibility and mechanical performance. The coaxial configuration also allows for designing multistep release processes through a single biomedical device.

Chapter One

Introduction

Chapter I
Introduction

I.1 Cancer: The Global Challenge

Cancer is a disease that, according to the Institute for Health Metrics and Evaluation (IHME), each year causes above 17% of all global deaths (2017). (Institute for Health Metrics and Evaluation, 2018)

Nowadays it affects more than 2.6 million people per year only in European Union (EU), (Directorate-General for Research and Innovation, 2020) with about 1.2 million deaths (2016). In Europe, given also the high average age expectancy, a quarter of all the deaths are due to cancer, and these values are given to even raise. (Eurostat, 2017; Directorate-General for Research and Innovation, 2020) In this scenario, EU has established which are the most relevant topics to research for in these years (2021-2027). The EU has faced the climate change challenge and has consistently promoted the development of technologies for advancements of climate change and for the reconstruction of healthy oceans. Among the five pillars of the EU for these years, the main one regarding the public health is the fight against cancer. The EU line for the next 10 years for the cancer fight is summarized in **Figure I.1**.

Figure I.1 *EU Program for Mission Cancer in program H2020 (Directorate-General for Research and Innovation, 2020)*

The pillars represent the EU approach to fighting cancer. Firstly, it is necessary to perform an important screening activity, to detect and identify in time potentially dangerous cancers. Regarding this aspect, by December 2003 the EU Council presented an official recommendation to the member states to intensify and better organize the screening activities, promoting these activities and looking for high participation. (‘COUNCIL

RECOMMENDATION of 2 December 2003 on cancer screening', 2003) However, it is still necessary to improve this point, and mostly adapt the national strategies with the technology's advancements. These are the main focus of the research: on the one hand, the researchers explore the causes and the effects of the tumors. On the other hand, they improve the technologies for the diagnosis and the therapies, widening the understanding and increasing the number of effective therapies. Obviously, to promote these types of initiatives it is necessary to financially support the scientific community with social and political actions. The Surveillance, Epidemiology, and End Results program (SEER) reports data about the incidence and survival rate of the various tumor disease that can affect people depending on the year of the diagnosis, reported in **Table I.1.**

Table I.1 *- Cancer Survival Rate in 1950 and 2010*

Type of Cancer	**5-Year Relative Survival Rates** (National Cancer Institute, 2018)	
	Diagnosis in 1950-1954	**Diagnosis in 2007-2013**
Breast Cancer (females)	60%	92.2%
Prostate	43%	99.6%
Leukemia	10%	64.8%
Melanoma of the skin	49%	93.6%
Colon and Rectum	37%	67.1%
Lung Cancer	6%	19.6%
All Sites	**35%**	**70%**

These types of cancers are among the most common in the world. Thus, the corresponding research receives the highest amount of funding, and it is well evident how it has led to an enhancement of human life expectance. Breast cancer is the most diffuse type of tumor, with a mortality of 40% in 1950.

Thanks to the prevention and screening campaigns, the improved understanding of the problem, and the new diagnosis and therapies methods, nowadays the survival rate of cancer is doubled.

Crossing the **Table I.1** data with the research funding and grants given by most of the organizations, it is evident how, investing in cancer research, it is possible to sensitively increase the survival rate. In **Table I.2** the funding and grants given by some of the most important organizations for cancer research are reported.

Table I.2*. Fundings for the type of cancer*

Type of Cancer	**National Cancer Institute Funding for Research Areas [M$] in 2017** (National Cancer Institute, 2018)	**American Cancer Society Funding for Research Areas [M$] in March 2020** (American Cancer Society, 2020)
Breast Cancer (females)	545.1	97.2
Prostate	233.0	34.6
Leukemia	250.5	36.4
Melanoma	153.2	46.1
Colon-Rectum	208.4	44.5
Lung Cancer	320.6	49.1
Total Funding for Type of cancer	**5636.4**	**678.3**

However, as underlined by Kamath et al.(Kamath, Kircher and Benson, 2019), the research on several types of cancer is still underfinanced, limiting the survival rate of the people affected by these types of disease. Moreover, COVID-19, has stressed even more the importance of research for cancer. In this period of severe pressure on hospitals and healthcare facilities, several national governments (e.g., Italy) decided to postpone non-urgent activities, such as screening for the earlier detection of cancer.

Recent scientific studies have shown how COVID-19 affected patients with comorbidities, mostly non-communicable diseases (such as hypertension, type 2-diabetes, cancer, ischaemic heart diseases, and chronic obstructive pulmonary diseases). Before the COVID-19 vaccination campaign, 16.8% of the deceased patients for SARS-CoV-2 in Italy presented active cancer in the previous 5 years (according to the report of Istituto Superiore di Sanità of 7th September 2020) (Istituto Superiore di Sanità, 2020), whereas Lee et al. (Lee *et al.*, 2020) focused their attention on the main types of tumors and how they affected the fatality rate, showing that, in case of lung tumors, for older male people with SARS-CoV-2 reach case-fatality rate above the 80%.

I.2 Innovative Materials

Nowadays, scientific interest is focused to produce increasingly high-performance materials using new technologies. One of the leading fields is research for biomedical applications, for which the aim is to use the most innovative technologies for obtaining new instruments as medical devices, such as wearable sensors, scaffolds, and cutting-edge drug delivery systems. For all these reasons, the scientific interest is now spreading to use

innovative types of materials, such as polymeric nanofibrous ones. According to Buzea et al., a nanomaterial is a physical component smaller than 1 µm in at least one dimension(Buzea, Pacheco and Robbie, 2007), and they show high specific area, (Hong, 2019) permeability, (Patel *et al.*, 2012) interesting optical (Zhong, 2009) and electronic properties (Pitkethly, 2004).

Among the numerous techniques used to produce polymeric nanofibers, the electrospinning process is one of the most versatile, since it allows the manufacture of small-sized polymer fibers (50 ÷ 5000 nm) by exploiting the action of an electric field. As displayed in **Figure I.2**, the process is usually structured in this way: a polymeric solution is fed to the climate chamber, where it passes through a needle by which it is injected. The polymeric jet is thus exposed to the electric field during the path between the needle (injector) and where the polymer is collected (collector); the whole solution is stretched by the strong electric field, which depends on the potential difference between injector and collector and the injector-collector distance. Simultaneously, the solvent starts to evaporate, allowing to obtained stretched fibers on the collector. By a certain distance between Injector-Collector, the charge density is so high that the jet starts to whip, with a movement known as whipping, that contributes to the fiber diameter decrease. As it is well evident, there are three main types of parameters: solution parameters, process parameters, and environmental conditions, as reported in **Figure I.2**.

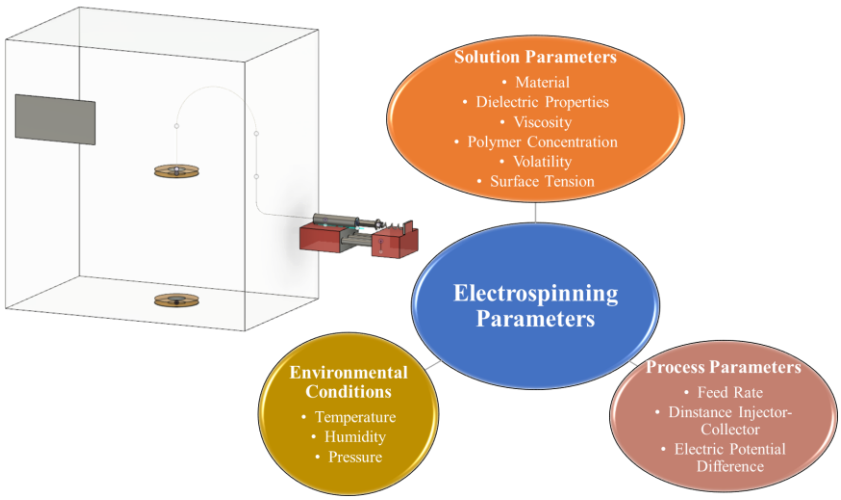

***Figure I.2**. Electrospinning Process Scheme (left) and process parameters (right)*

Since the morphology of the final product affects its properties, it is necessary to optimize the process parameters to obtain a homogenous distribution of fiber diameters. The electrospinning process in the biomedical

field contains several advantages: it is suitable for biodegradable and biocompatible materials, and thus ideal for biomedical engineering. Widely studied materials are polyphosphenes, poly (lactic-co-glycolic acid) (PLGA), polylactic acid (PLA), and polycaprolactone (PCL). PCL is one of the materials most studied for its production via electrospinning; it allows to obtaining fibers with reduced average dimensions, it is biocompatible, biodegradable, and it shows good mechanical properties. (Mochane *et al.*, 2019) However, there are other families of polymers that at the date are not so much studied for the electrospinning process: polyhydroxyalkanoates (PHAs) are a class of polymers synthesized biologically by microorganisms as carbon and energy storage compounds. (S Y Lee, 1996) They are polyesters that show complete biodegradability. In particular, the polyhydroxybutirate (PHB) is one of the most important polymers of the PHAs class: it shows good biocompatibility (Hoi-Kuan Lao *et al.*, 2006)is hydrophobic and a slow rate of biodegradation. (Chan *et al.*, 2017)

However, the interest in the electrospun polymeric nanofibers is due to several reasons: firstly, the nanofibers are used to mimic the extracellular matrix, so they can be used as scaffolds. (Lim, Sardinha and Myers, 2014)

Secondly, they can be used to carry active substances to be delivered into the surrounding system. (Son, Kim and Yoo, 2014) The possibilities of drug administration are (U. S. Food and Drug Administration, 1992):

- Enteral (e. g. Ingestion);
- Parenteral (e. g. Injection);
- Topical (e. g. Transdermal delivery).

The differences among all of them are various, but the most important is probably the release rate, and consequent absorption, of the drug. For each active substance in the human system, three fundamental values (reported in **Figure I.3**) can be detected: the effective dose, for which the drug concentration is sufficient to fulfill its property (e.g. Anti-inflammatory, antibiotic, etc.), the toxic dose, for which the drug concentration is too high in the system causing a toxic effect, and the lethal dose, for which the drug concentration is so high that causes the death in the patient. **Figure I.3** well shows as in an injection the drug is at the highest concentration by the very first moment, guaranteeing an immediate response by the system. However, with time the concentration rapidly goes down, and for this reason in several chronic therapies, such as insulin for diabetics, it is necessary to repeat numerous injections to always stay up to the effective dose. The transdermal systems, on the other hand, are not able to guarantee an immediate release of active substance but can guarantee a slower release of drug in the system, so that the drug can be effective for way longer time. Thus, for therapies such as diabetes and cancers, thanks to these systems, it would be possible to ensure a wider period of action for one administration, to provide a less invasive treatment, and to reach lower concentration peaks with fewer side

effects. (Trevor, Katzung and kruidering-Hall, 2013; Martínez and Quiñones, 2018)

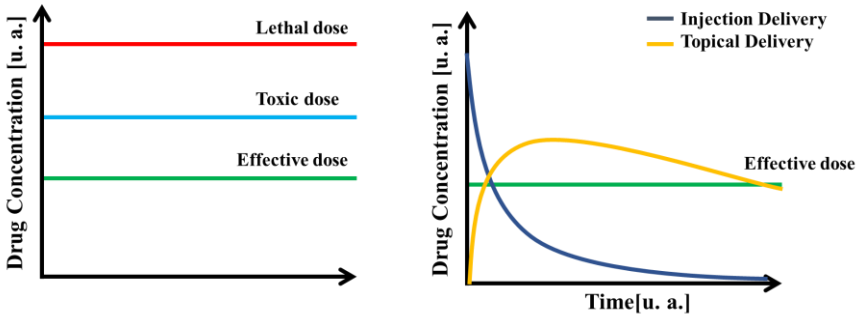

***Figure I.3**. Relevant Values of Drug Concentration in Human Beings (left); Drug Release of different administration routes (right)*

Drug delivery for electrospinning membranes is probably the most studied application. This is a promising technology since there are active substances that need recurring dosing for some treatments and some patients. (Church and Haines, 2016) Using electrospun membranes as transdermal drug delivery systems it is possible to reduce, for example, multiple doses per day thanks to the release kinetic lower than the injection delivery system. For this reason, methods to enhance the control of drug release in these systems have been studied. On the one hand, it has been explored the potentiality to foresee the release kinetics in a monoaxial electrospun membrane. On the other hand, coaxial electrospinning has been explored. It is a cutting-edge process that allows the production of nanofibers bilayer using two coaxial injectors. (Jalaja *et al.*, 2016; Han and Steckl, 2019a) In this way, loading the active substance in only one layer (usually in the core) it is possible to slow down the drug release and design a tailor-made system depending on the application. This is a very interesting process, and it is confirmed by the scientific interest shown in the last years, as reported in **Figure I.4**.

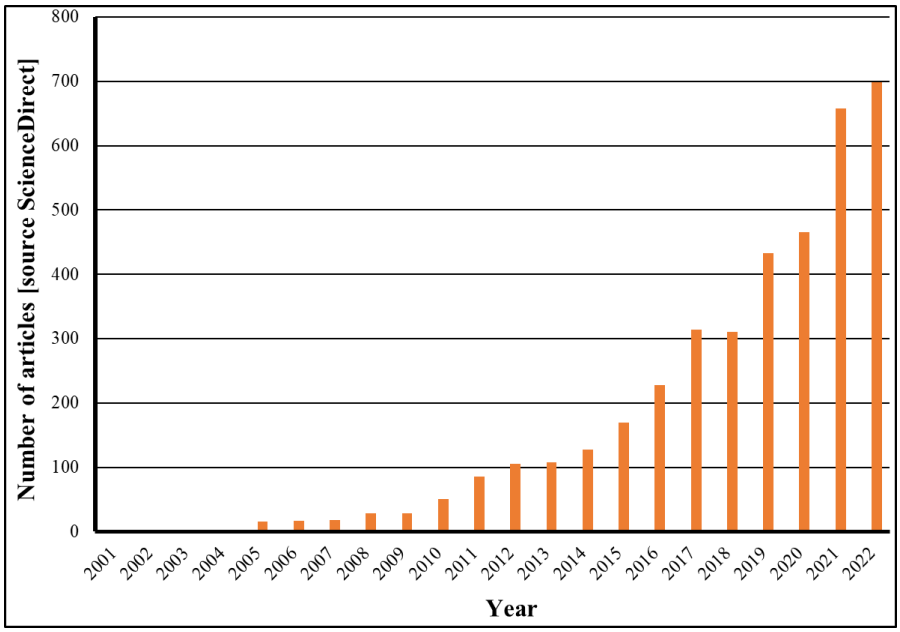

***Figure I.4**. Coaxial Electrospinning Scientific Papers*

However, coaxial electrospinning has not only function to slow down the drug release, avoiding the typical initial burst. It is even possible to mesh the excellent biocompatibility of natural polymers (such as gelatine, hyaluronic acid, etc.) and the good mechanical properties of synthetic biomaterials (such as PCL, PLA, and so on). (Jalaja *et al.*, 2016) However, it is not simple to electrospin two different polymers together, given the relevant number of parameters to handle, thus, it is still necessary to better study and understand this process.

I.3 Type of fillers

Understanding the main goal of the transdermal drug delivery systems, it is necessary to select which type of filler to load into the membrane. The fillers can be divided into two main groups: **active molecules** and **nanoparticles**, and they will be deeply discussed in the following paragraphs.

Nanoparticles

In the 1970s, Prof. Speiser's research team began to develop a new system that allows for better delivery of drugs within the human body. In that period of great effervescence and innovativeness in world research, the emerging

use of vaccines needed several injections to ascertain the correct absorption of the biological system. For this reason, the researchers started developing nanocapsules and nanoparticles (NPs) for drug delivery (Couvreur *et al.*, 1977, 1982; Brasseur *et al.*, 1980). A nanoparticle for pharmaceutical purposes is a solid colloidal particle characterized by a dimensional range between 10 and 1 μm. In the first period, it was not possible to obtain very small NPs: the dimensions of the NPs often were around 500–600 nm (Scheffel *et al.*, 1972). Several studies demonstrated that the properties and functionalities of the NPs are strictly dependent on their size, thus numerous processes were rapidly developed to obtain NPs of much lower dimensions and shape (e.g., co-precipitation, microemulsion, hydrothermia, sonochemistry, thermal decomposition, etc.) (Mahmoudi *et al.*, 2011). Several relevant aspects need to be considered for the design of the nanoparticles. In the case of magnetic nanoparticles, for example, higher magnetic properties were found for smaller sizes, but it is worth noting that an excessive dimensional reduction of the particle size may cause problems in the phase of its elimination from the human body. For example, Shapero et al. (Shapero *et al.*, 2011) proved that the silica NPs of different dimensions (from 50 nm up to 300 nm) are able to be uptaken by human cells, and the smaller the NPs are, the better the uptake efficiency is. Interestingly, studies proved that the cell uptake decreases for smaller dimensions than 50 nm (Osaki *et al.*, 2004; Chithrani, Ghazani and Chan, 2006), and they showed an optimum around 50 nm (this happened, for example, due to a more efficient receptor-mediated endocytosis) (Chithrani, Ghazani and Chan, 2006; Jiang *et al.*, 2008). **Figure I.5** reports a scheme of different types of endocytosis phenomena (Behzadi *et al.*, 2017).

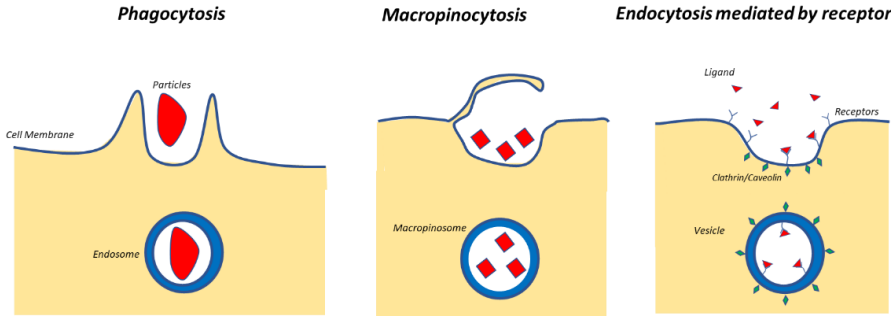

Figure I.5. *Main types of endocytosis of NPs*

Other studies demonstrated also that human cells can internalize several types of nanosystems (e.g., biopolymer nano-carriers, liposomal nanovesicles system), even if the mechanism is not still clear (Ciaglia *et al.*, 2019).

The scientific community has found a deep interest in studying NPs, for different reasons. Several drugs are not able to pass some biological barriers, or their permeability through these barriers (e.g., cell membrane, blood-brain barrier, etc.) is limited and not suitable for producing the desired effects. In this context, the NPs constitute a good "carrier" able to overcome these boundaries, and they provide two main advantages. Firstly, by using nanoparticles as carriers, it is possible to extend the range of drugs useful for planned purposes. Secondly, high efficiencies can be obtained with reduced amounts of drugs in the human body: This is a very relevant aspect, especially for drugs with high cytotoxicity (e.g., chemotherapy). For antitumor therapies, the research is mainly focused towards two directions: one is the development of new molecules (Saturnino *et al.*, 2018; Ceramella *et al.*, 2020; Iacopetta *et al.*, 2020; Sapio *et al.*, 2020), and the other is the development of completely different systems, such as nanoparticles, hybrid materials, and fibrous membranes, that can carry active molecules or fight against cancer (Ignatova *et al.*, 2010; Bae, Chung and Park, 2011; Vinardell and Mitjans, 2015; Catauro and Pacifico, 2017). This latter aspect has determined a spreading interest in nanoparticles for antitumor treatment and the biomedical field. In **Figure I.6**, the number of articles published per year on the application of nanoparticles in the biomedical field is reported according to ScienceDirect.

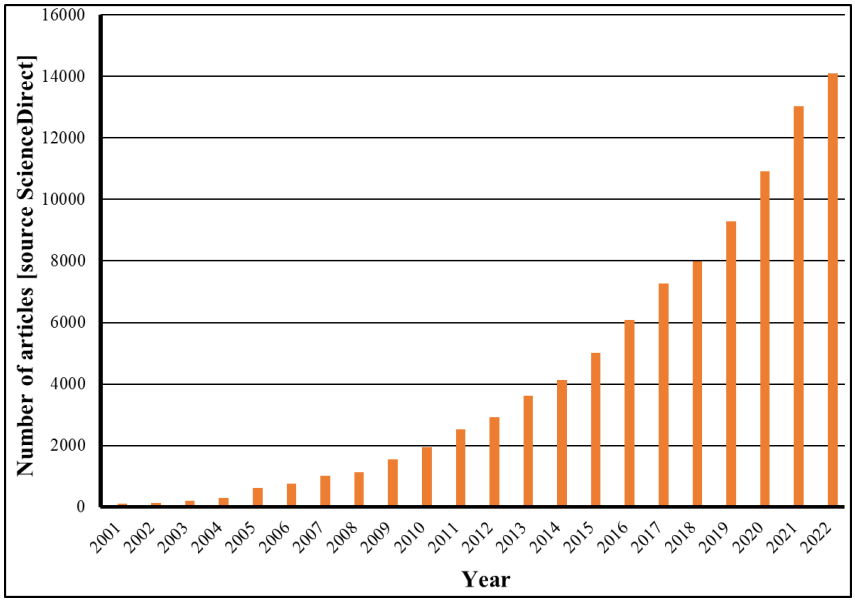

***Figure I.6**. Publications per year on ScienceDirect from 2001 to 2022 on NPs and biomedical*

However, there are several types of NPs. Depending on the chemical nature/composition, the nanoparticles can be classified into four groups (McNamara and Tofail, 2017), as shown in **Figure I.7**.

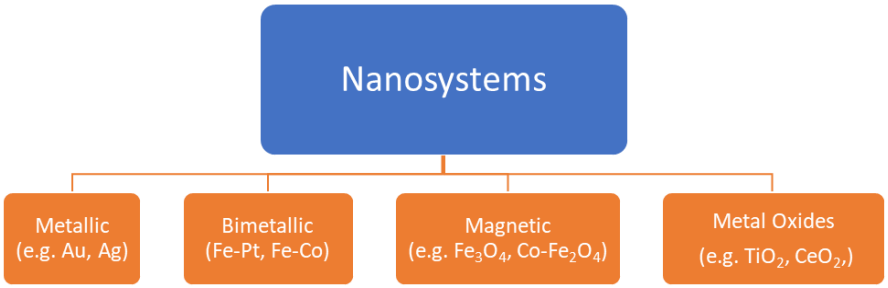

***Figure I.7**. Classification of NPs*

In this context, with a continuous need for innovative drug administration systems, another interesting topic is the design of smart materials (SMs). SMs are generally stimuli-responsive systems that change their behavior when triggered. The activating agents can be, for example, enzymes, pH, ultrasounds, electromagnetic radiations, etc. (Yoo *et al.*, 2011; Zelzer *et al.*, 2013; Joniec, Sek and Krysinski, 2016; Genchi *et al.*, 2017; Szlezak *et al.*, 2017; Tang *et al.*, 2018; Mackiewicz *et al.*, 2019).
In particular, electromagnetic radiations find a great variety of applications in the biomedical field, from diagnosis to therapy. **Figure I.8** illustrates some relevant applications of the wavelength ranges of electromagnetic radiations currently applied in the biomedical field (Schueler, 1998; Wang *et al.*, 2014; Funk, Stockham and Laack, 2016; Azman and Azman, 2017; Tsai and Hamblin, 2017; Esmaeili and Friebe, 2019).

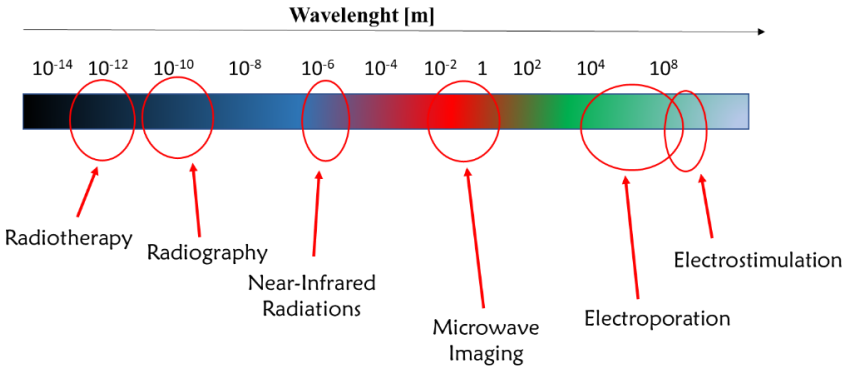

***Figure I.8**. Applications of electromagnetic radiations in medicine.*

The purpose of this paragraph is to present the main use of electromagnetically stimulable systems based on NP triggering. In particular, in the first section, NP functionalities and related results in the biological

environment are analyzed in depth, whereas in the second section, nanocomposite stimulable systems are presented and their features are explained based on NP performance. An overview of the content is reported in **Figure I.9** and **Table I.3**.

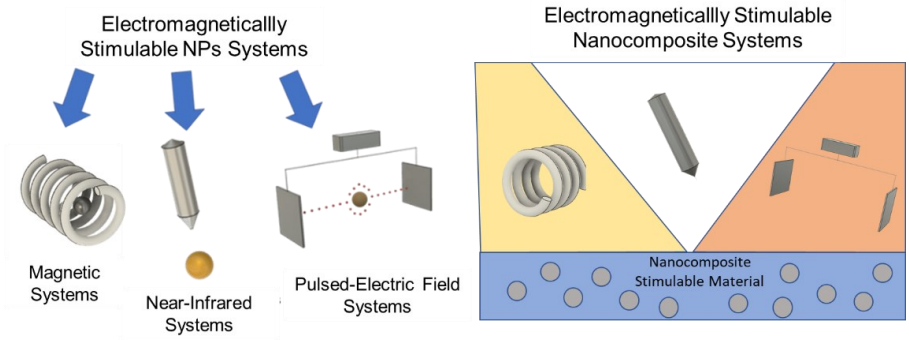

***Figure I.9**. Electromagnetically stimulable systems*

***Table I.3**. Table of contents*

Type of System	Type of Stimulus	Topics
Stimulable nanoparticles	Magnetically	Activation mechanism stimulus (NPs)
		Characteristics of NPs
		Preclinical and clinical studies
	NIR radiation	Activation mechanism stimulus (NPs)
		Characteristics of NPs
		Preclinical and clinical studies
	Pulsed electric field	Activation mechanism EP and interaction stimulus (NPs)
		Modulation of relevant parameters
		Preclinical tests and potentialities
Stimulable electrospun nanocomposite	Magnetic NIR radiation pulsed electric field	Characteristics of nanocomposite electrospun materials
		Stimulability of nanocomposite electrospun membranes
		Preclinical tests and potentialities of electrospun membranes

The first part of this paragraph is mainly focused on stimulable NPs, among which there are magnetic and metallic NPs. Magnetic NPs can be easily urged by a magnetic field and, moreover, can be also led to the interest area that exploits the magnetic force. For this purpose, mainly magnetite (Fe_3O_4) and maghemite (γ-Fe_2O_4) are used. By exploiting their interaction with an

alternate magnetic field (AMF), the stimulation leads to a temperature increase. This phenomenon is called hyperthermia, and in a certain range (around 41–47 °C) it is very effective for the treatment of many carcinomas. Similar effects are determined by metallic NPs, which can be urged by near-infrared (NIR) radiation, which stimulates the NP, leading to a temperature increase as well.
Concerning this last type of NPs, the potentiality of the pulsed electric field (PEF), which is clinically used for treatments of external solid tumors, was discussed in some studies. Hence, an interesting overview of the recent results with the combination of NPs and PEF is reported, which opens the way toward very interesting perspectives.
It is worth noting that the key for designing an effective smart nanomaterial for a defined system, is to choose appropriately the stimulus since it will be the way to interact with the NP.
The second part of the paragraph focuses on the biomedical applications of electrospun membranes composed of micro/nanofibers that contain integrated promising functionalities resulting from the abovementioned NPs embedded in the hosting fibers. This final analysis is carried out in terms of performance in the stimuli-responsive efficiency.

Magnetic Nanoparticles

Activation of an External Magnetic field

A magnetic NP is a type of particle that manifests magnetic properties. In order to understand how to optimize the results, it is crucial to study the most important characteristics of this kind of particles. The magnetic nanoparticles that are mainly analyzed are iron oxides (usually magnetite). Magnetite has ferromagnetic properties: for this reason, once it has been magnetized through an external magnetic field, even if the external field stops, the magnetite works like a magnet. If the dimensions of the NP are small enough, the NP is not ferromagnetic but superparamagnetic. This happens when the dimensions of the particle are comparable to the ones of a single magnetic domain (Held *et al.*, 2001). This dimension for the magnetite should be below 76 nm (Q. Li *et al.*, 2017). This phenomenon may happen for each NP that shows reticular energy similar to that necessary to invert the direction of the magnetic moment. The time requested for the inversion of the magnetic moment direction is known as the Néel relaxation time. If this time is lower than the time necessary to test the measure of the magnetic moment, the measure will report a value of 0. For this reason, the material may seem paramagnetic, but it will show a magnetic susceptibility as a ferromagnetic material does. However, there are differences between a ferromagnetic nanoparticle and a superparamagnetic one, especially regarding the potential applications. If an external magnetic field would urge a ferromagnetic NP, it would reach the condition of magnetization saturation

(B_{SAT}) quickly, independent of whether the NP is superparamagnetic or ferromagnetic. Once the magnetic field is stopped, the nanoparticle loses magnetization. However, it is not able to return to the value of 0 (the start point) of the magnetic field. The ferromagnetic materials store their history. The magnetic field that stores it without an external field is called magnetization residual (B_{RES}). To force the magnetization to come back to 0, it is necessary to use another external field in a different direction. The point for which the magnetic field of the ferromagnetic NP is 0 is called coercivity (H_{COE}). Obviously, it is possible to obtain another magnetization of the material with this external field, whereby it can reach another B_{SAT} condition. To reach the first magnetic saturation, it is necessary to reach another point of coercivity: the route of the diagram shows a hysteresis. The route for the superparamagnetic materials is different: in fact, they do not show any magnetic residual field and therefore no hysteresis (Farzin *et al.*, 2020). **Figure I.10** reports the route of magnetization for a ferromagnetic and a superparamagnetic material.

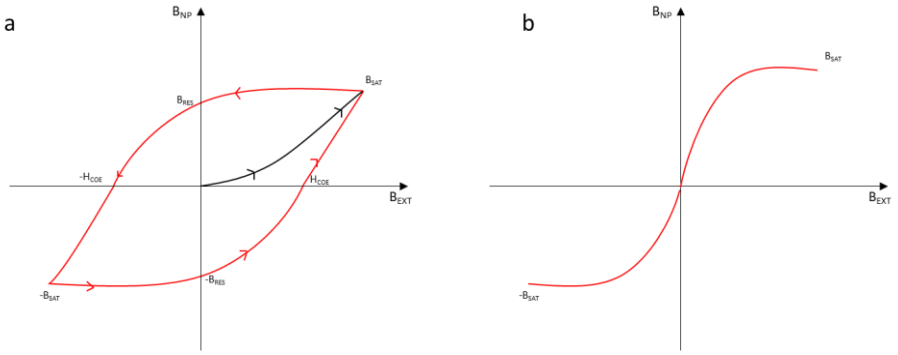

***Figure I.10**. Route of the magnetic field provided by a NP (BNP) depending on the external magnetic field (Bext) applied for a ferromagnetic material (a) and a superparamagnetic material (b).*

The energy lost by the ferromagnetic materials because of the hysteresis is released in the surrounding environment as heat. For this reason, the magnetic NPs often are triggered by AMF to increase the average temperature of the interested area (located hyperthermia) (Cherukuri, Glazer and Curley, 2010). The main parameters of the material for these NPs are saturation magnetization, coercivity, and residual magnetization (Dutz and Hergt, 2013).

Although there is no hysteresis for superparamagnetic materials, it is possible to notice that in applying an external magnetic field, there is an increase in the temperature of the NP due to the Néel relaxation time (NRT) and the Brownian relaxation time (BRT). Néel relaxation, as cited previously, is the phenomenon of the NPs able to invert their magnetic moments overcoming an energy barrier. When this happens, there is heat

formation by the NP, which will affect the surrounding environment. The equation that describes the NRT is reported in eq. (1):

$$\tau_N = t_0 * \exp\left(\frac{K * V}{k_b * T}\right) \quad (1)$$

where t_0 is generally 10^{-9} s, K is the anisotropy constant, V is the NP volume, k_b is the Boltzmann constant, and T is the temperature. It is evident that the smaller the particle is, the shorter the Néel relaxation time. As regards the BRT, it is related to the interaction of the nanoparticle with the medium. eq. (2) presents the model of the BRT.

$$\tau_B = \frac{3 * \mu * t_0 * V}{k_b * T} \quad (2)$$

There is only one new term, μ, the viscosity of the system. Both BRT and NRT are strictly related to the dimensions of the particle, but Néel relaxation is related by an exponential form. This is the reason for which usually the assessments on the nanoparticles are done only referring to the NRT. To obtain a quantitative measure of heat dissipation, it is possible to use eq. (3):

$$P = \mu_0 * \nu * f * H^2 \quad (3)$$

where P is the heat dissipation, f is the frequency of the external magnetic field, H is the strength of the external magnetic field, μ_0 is the magnetic field constant, and ν is the imaginary part of the magnetic susceptibility (Laurent *et al.*, 2011). For this reason, it is necessary to carefully choose the material and the size: Several studies showed the dependence of the heating rate on the size of NPs (Rosensweig, 2002). Rosensweig demonstrated that there was a maximum rate that was independent of the external magnetic field. Moreover, it was shown that the magnetite, which did not show a monotone behavior, showed a maximum heating rate around 7 nm. However, studies confirm (in an intuitive way) that it is possible to enhance the hyperthermia effect by increasing the amplitude of the external magnetic field and the frequency.

Physicochemical Properties and Choice of Coating for Biomedical Application

Several studies reported that the NP design needs to be accurately chosen in a way that also depends on the physicochemical properties (e.g., size, surface charges) (Shin, Song and Um, 2015). The size of the NPs strongly affects their distribution in the biological environment: In the case of injection, to make sure that the NPs would not be removed by the kidneys, their dimensions need to be more than 50 nm. Moreover, for dimensions higher than 200 nm, the NPs are removed by the spleen and the liver. For this reason, the medicine establishes a range that is 50–200 nm for the systematic

delivery NPs (Krishnan, 2010; Shin, Song and Um, 2015). A similar behavior is obtained in the case of inhalation: Braakhuis et al (Braakhuis *et al.*, 2016) demonstrated that NPs above 60 nm accumulate in the lungs, whereas below 34 nm they accumulate in the alveoli. In addition, the uptake efficiency can be sensitively affected by the dimensions. For example, receptor-mediated internalization shows a higher uptake efficiency for 50 nm NPs, which seems to be the compromise between the curvature of NPs and the binding rigidity. Moreover, by appropriately designing the NPs' physicochemical characteristics, it is often possible to affect the cytotoxic effects: For this reason, some of these are considered essential information for toxicity studies (e.g., size, surface area, agglomeration state, composition, concentration) (Oberdörster *et al.*, 2005).
On the other hand, other parameters such as the surface charge (controllable, for example, by changing the NP coating (Jurašin *et al.*, 2016)) usually are accurately chosen for controlling the uptake efficiency (Jo *et al.*, 2015). Several studies reported for example that positively charged NPs are more easily uptaken than neutral and negatively charged NPs (Yue *et al.*, 2011; Fröhlich, 2012; Lunnoo, Assawakhajornsak and Puangmali, 2019), and this behavior strongly depends on the interaction between the membrane and the NPs. **Table I.4** reports the main effects of the physicochemical properties on biological variables.

***Table I.4**. Effect of the physicochemical properties of NPs on biological performance.*

Physicochemical Parameter of NPs	**Effect**
Shape	Cytotoxicity (Sukhanova *et al.*, 2018)
	Uptake (Zhao *et al.*, 2017)
	Distribution(Huang *et al.*, 2011)
Size	Uptake (Shin, Song and Um, 2015)
	Distribution(De Jong *et al.*, 2008)
	Cytotoxicity(Shin, Song and Um, 2015)
Surface charge	Uptake (Fröhlich, 2012)
	Cytotoxicity(Fröhlich, 2012)
	Distribution(Xiao *et al.*, 2011)

However, to modify the physicochemical properties of NPs and their effect (e.g., biodistribution), it is possible to vary the architecture of NPs, creating heterogeneous NPs (e.g., Janus type) (Pradhan, Ghosh and Chen, 2009; Rabanel *et al.*, 2019). Due to the heterogeneity of NPs, for example, it is possible to obtain NPs with two faces that present different characteristics (e.g., metal and polymer). These NPs manifest interesting properties for NP

solubility in complex systems and allow for dual-phase release kinetics, theranostics, and drug targeting (Tran, Lesieur and Faivre, 2014; Ju *et al.*, 2017; Zhang *et al.*, 2018; Safaie and Ferrier, 2020).

The magnetic NPs generally are delivered in biological systems via two ways: direct injection, in which the magnetic NPs are directly injected in the tumor, or via systematic delivery, in which the NPs are injected intravenously in order to be delivered in the interested area (Farzin *et al.*, 2020).

Direct delivery is generally preferable; it is possible to be quite sure of the concentration of NPs delivered in the tumor. However, the problem is that the tumor may not be accessible for direct injection in situ. In these cases, it is preferable to use systematic delivery: this works mainly due to the enhanced permeability and retention effect (EPR), which enhances the absorption of nanoparticles in the tumor tissue rather than the healthy one. This effect is widely studied and, even if not all the reasons are clear, the main reason is probably due to the leaky vascular system in the tumor tissue that promotes the permanence of the NPs in that zone (Kobayashi, Watanabe and Choyke, 2014). In the case where NPs are accumulated in a certain zone only because of the physiology and anatomy of the system, passive targeting occurs (Hilger, 2013).

However, to enhance the selectivity of the delivery (especially for the systematic ones), the NPs can be functionalized to perform active targeting (Hilger, 2013). By coating the nanoparticles with agents (such as antibodies) that have a chemical affinity to the target cells, it is possible to selectively bind the NPs to the cells (Ivkov *et al.*, 2006). Thus, in coating the magnetic NPs, it is possible to obtain core-shell NPs usable to protect the NP from oxidation and to avoid the agglomeration phenomenon (Tran and Webster, 2010), thus preserving the magnetic properties (Mahmoudi *et al.*, 2011). For example, Sarno et al. (Sarno *et al.*, 2017) in 2017 analyzed how different types of coating affect NP properties. For three different types of coating (oleic acid, citric acid, and lipase-citric acid), the magnetic tests showed that the main parameters, such as the saturation magnetization and the coercivity, were found very similar, proving that the coating molecules slightly affect the magnetic properties. However, this strategy is able to enhance the EPR effect and the uptake by the cells as well. The efficiency of the NPs was demonstrated to change depending on the coating, which modifies magnetic properties (such as the coercivity), but some NPs, such as oleic acid-coated NPs (OANPs), were evaluated to have a higher heating rate than the uncoated ones, where the effect may be due to the relaxations losses (Tomitaka *et al.*, 2011). **Figure I.11** presents a magnetite NP functionalized with oleic acid.

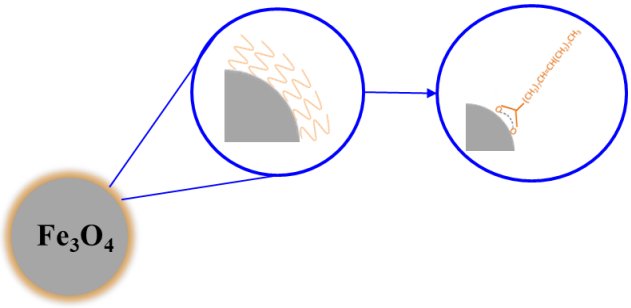

***Figure I.11**. Magnetite NP functionalized with oleic acid.*

The coating agents usually used are polymers and polysaccharides (such as polyvinyl-alcohol (Chastellain, Petri and Hofmann, 2004), polyacrylic acid (Lojk *et al.*, 2015), dextran (Moore *et al.*, 2000), chitosan (Dung *et al.*, 2009)), or agents such as oleic acid (Zhang, He and Gu, 2006) and citric acid (L. Li *et al.*, 2013). It is necessary to choose the coating accurately because it can directly or indirectly affect cell uptake. The balance between hydrophilicity and hydrophobicity for the NPs is particularly challenging. In fact, on the one hand, the hydrophilicity allows for a good dispersion in serum or in water, thereby avoiding aggregation. For water dispersibility, generally, it is possible to attach hydrophilic functional groups to the ligands (e.g., carboxylic acids, sulfonic acids, PEG, etc.) (Kobayashi *et al.*, 2014). On the other hand, hydrophobicity enhances the interactions between the NPs and the cell membrane and therefore their uptake (Honary and Zahir, 2013; Fratoddi, 2018). Given the fact that surface charge affects cell uptake (generally positive surface charge increases the uptake), the use of cationic ligands was one of the main ways used to overcome the cell membrane. However, now the research is also going toward the development of cutting-edge NPs with hydrophobic/hydrophilic faces (Janus type) or hydrophilic/hydrophobic triggerable properties (Kobayashi *et al.*, 2014).
As explained before, it is possible to use agents able to target a certain type of cells: For example, Pala's group (Pala *et al.*, 2013) produced a dextran-coated superparamagnetic nanoparticle with HER2 aptamer (HNP) and tested these NPs to cell lines that express the HER2 receptor and those that do not express the HER2 receptor. It was possible to notice that the HNPs were much more specific than the NPs without the HER2 aptamer. The second reason is related to the changes in the electromagnetic and physicochemical properties: As anticipated before, the coating of the NPs would affect their surface charge, and the uptake of NPs by cells is strictly dependent on this (Osaka *et al.*, 2009; Ayala *et al.*, 2013). Ayala et al. (Ayala *et al.*, 2013) synthesized iron oxide NPs with different values of substitution of carboxymethyl-substituted dextran, and they monitored the variations of the surface charge. Through the evaluation of different uptakes of these NPs by the colon cancer cells, they found that the best uptake was

manifested by the most charged nanoparticles. A different approach to improve the bioavailability of magnetic nanoparticles (mean size of 6.5 ± 3.0 nm) was the fabrication of nano-capsules with a shell of poly-lactic-co-glycolic acid (PLGA) or polylactic acid (PLA), further covered by carboxybetaine-functionalized chitosan by using dense gas technology. These systems were responsive to an external magnetic field that released an in vitro loaded fluorescent payload with a remote on/off control, achieved with alternating magnetic field (Cricchio *et al.*, 2017).
In synthesis, on the one hand, the coating affects the uptake and cytotoxicity due to changes in relevant parameters (e.g., surface charge) (Fröhlich, 2012); on the other hand, it can be exploited to improve the selectivity of the NPs and promote active targeting.

Effectiveness of Magnetic Hyperthermia

Since the first studies, nanoparticles seemed to be promising for application in drug delivery. Magnetic hyperthermia can cause protein denaturation and DNA damage to the cells. It can enhance the immune response and drug perfusion within the tumor (Cellai *et al.*, 2017; Chang *et al.*, 2018). Cell death via magnetic hyperthermia can be due to apoptosis or necrosis. However triggering cell death via apoptosis is preferred over necrosis since necrosis can provoke inflammation or metastasis (Moise *et al.*, 2018).
In 1983, Widder et al. (Widder *et al.*, 1983) produced magnetically responsive microspheres containing doxorubicin (DOX) hydrochloride as a treatment for Yoshida sarcoma tumors in rats. Over 77% of the rats showed total remission of the tumor, and the others showed a significant decrease in the tumor mass. For the animals non-treated in the same way (using free DOX and placebo microspheres), there was a relevant increase of the tumor mass with successive death. In this experiment, the magnetic field was generated by a permanent bipolar magnet, as chemotherapy was not combined with hyperthermia yet. The following studies with DOX bounded on magnetite NPs showed how the results improved if the NPs were exploited to generate heat. Ha et al. (Ha *et al.*, 2019) synthesized superparamagnetic NPs with an alginate shell and DOX. Moreover, a folate factor was added to the surface of the cell to enhance the entrance and the permanence of the NPs in the system. Due to the external alternate magnetic field, the NPs generated heat, and by in vivo tests, a promising decrease in the tumor size in the system was proven. In addition, studies on other chemotherapy agents were proven to be more effective: Petryk et al. (Petryk *et al.*, 2009) proved that it was possible to reduce the amount of cisplatinum (CP) necessary than the free CP or the CP with traditional heating techniques. In this case, the NPs were inserted after the chemotherapy treatment in mice for MTG-B flank tumors, and a significant loss of tumor size compared to the initial one was found.

This enhancement of the effectiveness of hyperthermia in combination with chemotherapy is due to several factors. First of all, it has a beneficial effect on enhancing the immune response of the biological system. Secondly, when combined with chemotherapy, it shows an enhancement of the transport phenomena (that of the drug uptake and of the flux of anticancer drug concentration), which leads to major DNA damage of the cancer cells and a reduction of the radical oxygen detoxification (Yagawa *et al.*, 2017).
Recently, doping magnetic NPs with small percentages of lanthanides has become an interesting pathway in cancer treatment (Teo, Termini and Gray, 2016). Firstly, it is possible to produce NPs with higher magnetization properties. For example, in 2020 Kowalik et al. (Kowalik *et al.*, 2020) produced iron oxide NPs with different percentages of yttrium (from 0.1 to 10%), and they reported differences in terms of the magnetic properties (hence heating capability) and cytotoxicity of the systems. Interestingly, an increase of over 60% in the heating capability was recorded with a 0.1% inclusion of yttrium in the system, which probably affected the crystalline structure and in turn, indirectly, the magnetic characteristics. Moreover, lanthanides can be exploited for their characteristics as radionuclides, leading to interesting horizons also in the diagnosis (Ognjanović *et al.*, 2019) or for antitumor treatment where the lanthanides are used as the internal radio emitter.
Even if recent magnetic studies are now well investigating the treatment of several types of cancers (Chang *et al.*, 2018) (e.g., epidermoid (Mai *et al.*, 2019), prostate (Albarqi *et al.*, 2020), breast (Denardo *et al.*, 2007)), the use of magnetic nanoparticles find great application for the treatment of brain cancer; this happens mainly because most of the active substances are not able to overcome the blood-brain barrier (BBB), which safeguards the brain from the substances that may circulate in the blood. For this reason, it is very challenging to find delivery systems able to overcome the BBB (Agarwal *et al.*, 2009). In 2015, Dan et al. (Dan *et al.*, 2015) studied the effect on the permeability of iron oxide NPs stimulated by AMF-induced hyperthermia through the BBB. In this study, citrate-coated iron oxide NPs were synthesized, and crosslinked nanoassemblies loaded with iron oxide NPs were successfully obtained. The in vitro tests were done at 37 and 43 °C, comparing the results with the local hyperthermia caused by AMF. This work showed that induced hyperthermia with magnetic NPs can be effective to overcome the BBB by accurately choosing the functionalization of the NPs and that the results can be very different for different cell lines. In vivo studies for the treatment of glioma were performed by Yanase et al. (Yanase *et al.*, 1998), who showed how with three applications of AMF (one each 24 h), 87.5% of the tumor had a reduction. Moreover, the distribution of NPs stimulated through AMF in the tumor tissue was homogeneous, whereas in the test without AMF the distribution of NPs was more heterogeneous. Encouraging in vivo results were also obtained by Jordan et al. (Jordan *et al.*,

2006). They proved that a superparamagnetic iron oxide NP with aminosilane coating, after the exposure to AMF, guaranteed a decrease in cell proliferation and an enhancement of the survival rate for animals affected by malignant glioma.
Given these performances, clinical trials were performed for magnetic hyperthermia treatment of glioblastoma. The NPs used are aminosilane-coated superparamagnetic iron oxide NPs dispersed in water (NanoTherm), with a magnetic field frequency of 100 kHz, an intensity of 0–15 kA/m (NanoActivator) (Etemadi and Plieger, 2020). Comparing the results obtained for conventional treatments, the median survival rate was increased from 12.1 months for patients treated only with radiotherapy (median age 57 years old) and 14.6 months for patients treated with radiotherapy and chemotherapy (median age 56 years old) (Stupp *et al.*, 2005) to 23.2 months for the 59 patients tested (median age 56 years old) with magnetic hyperthermia and radiotherapy (Maier-Hauff *et al.*, 2011; Mahmoudi *et al.*, 2018).

Metallic Nanoparticles

Activation via Near-Infrared Radiation (NIR)

Metallic NPs are made, for example, of gold, copper, or silver, and are characterized by free-moving electrons. The quasi-particle formed by interactions of these moving electrons is called a plasmon. The plasmons on the surface of the materials are known as surface plasmons, and they are exposed to the surrounding environment and therefore to external radiation. If the metallic NPs are smaller than the wavelength of the incident radiation, a phenomenon known as localized surface plasmon (LSP) can occur, which is responsible for the oscillation of the plasmon with a defined frequency (Willets and Van Duyne, 2007). The oscillation that the NP gives back depends on the incident radiation. It has been noted that the highest oscillation amplitude given for a specific frequency is known as the local surface plasmon resonance (Huang and El-Sayed, 2010). As reported in eq. 4, the whole extinction cross section (C_{ext}) is generally due to two contributions: the scattering (C_{sca}) and the absorption (C_{abs}) (Hlaing *et al.*, 2016).

$$C_{ext} = C_{abs}(\lambda) + C_{sca}(\lambda) \tag{4}$$

Considering spherical NPs with dimensions lower than 20 nm, it is possible to theoretically obtain the extinction cross-section value by Mie's solution of Maxwell's relations (Petryayeva and Krull, 2011) in eqs. 5 and 6.

$$C_{ext} = \frac{24 * \pi^2 * R^3 * \varepsilon_m^{\frac{3}{2}} * N}{\lambda * \ln(10)} * \frac{\varepsilon_i}{(\varepsilon_r + \chi * \varepsilon_m)^2 + \varepsilon_i^2} \quad (5)$$

$$\varepsilon = \varepsilon_r + i * \varepsilon_i \quad (6)$$

where R is the radius of the NP, ε_m is the dielectric constant of the medium, λ is the wavelength of the incident radiation, N is the electron density, ε is the complex dielectric constant of the NP, and χ is a factor describing the shape of the NP. In **Figure I.12**, a metallic NP surface plasmon resonance induced by external radiation is represented.

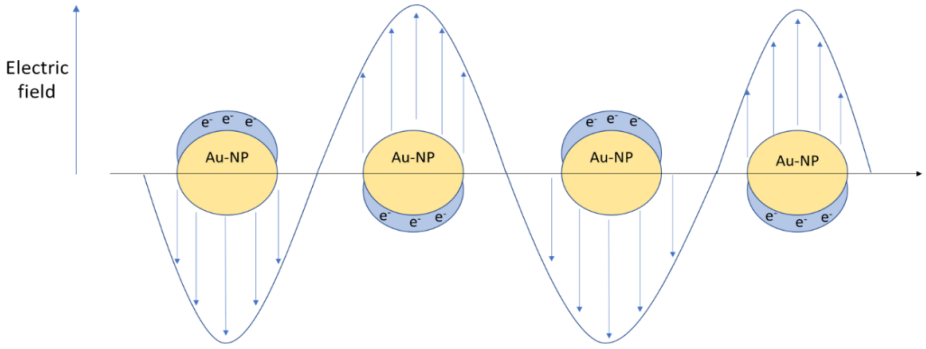

***Figure I.12**. Localized surface plasmon resonance (LSPR) induced by external radiation.*

Eq. (5) highlights the point that the material's response strongly depends on the size of the NP, the shape, and the dielectric environment (Carrillo-Cazares *et al.*, 2017). It is proven that at low dimensions (≈20 nm), the extinction cross section is almost completely due to the absorption. By increasing the dimensions, the magnitude of the scattering phenomena starts to be relevant, and by nanospheres of 80 nm, the phenomenon starts to be comparable (Jain *et al.*, 2006). However, the NP shape is a significant parameter as well: increasing the aspect ratio, the magnitude of the scattering and the absorption are equal at a much lower volume of the NP. Moreover, for these NPs, it is easier to modify the extinction cross section since there are two parameters by which it is possible to act, i.e., the diameter and the aspect ratio (Jain *et al.*, 2006). For metal NPs such as Au and Ag, the resonance frequency is in the near-infrared range (Huang and El-Sayed, 2010), but it is interesting to notice a particular effect of the radiation: the radiation absorbed is dissipated by the material via heat release. NIR radiation in a range of 650– 1350 nm can penetrate safely in depth in human tissue (Smith, Mancini and Nie, 2009). This is interesting because it means that by properly choosing the NP size and type of surface functionalization, it is possible to enhance and control the heat generated in the tissue that

causes hyperthermia (Zahid *et al.*, 2019). To obtain the LSPR in the NIR region, nanoshells are often produced with a core of SiO_2 and the outer layer of Au. Modifying the thickness of the outer layer, it is possible to vary the resonance frequency (Y. C. Wang *et al.*, 2018). In **Figure 13**, a difference of the heat generated for various sizes of Ag-NPs under a 532 nm wavelength radiation through photothermal lens spectroscopy is shown (Hlaing *et al.*, 2016).

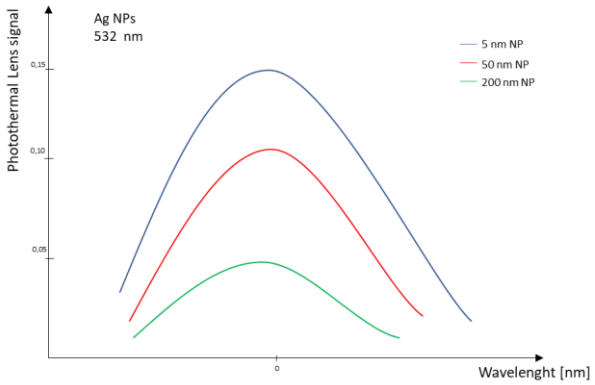

***Figure 13**. Photothermal lens signal vs. wavelength for various sizes of NPs*

The behavior of the graph in **Figure 13** clearly evidences how the size of the NPs for a defined wavelength also affects the photothermal effect.
In synthesis, a suitable NIR-responsive NP should show a relevant absorption in the NIR region, which can be converted in heat. The most used materials in this sense are noble metal nanomaterials because of the strong plasmon resonance, even if other types of materials are now also gaining interest in being studied (e.g., graphene-based materials) (Chen *et al.*, 2016; Lv *et al.*, 2021).

Use of Gold Nanoparticles with NIR radiation for biomedical application

Au-NPs are widely studied and are one of the most interesting metallic NPs. This is due to their low toxicity (Zhang *et al.*, 2011) and cytotoxicity (Connor *et al.*, 2005); these characteristics highlight a promising potentiality for their use for biomedical purposes. However, to enhance their compatibility with biological molecules and to use the NPs as drug carriers, they often need to be functionalized. Sulfur has a strong affinity to gold, and for this reason, thiols are often used to functionalize the Au-NP surface, which organizes themselves regularly on the NP surface, forming a self-assembled monolayer (SAM) (Skrabalak *et al.*, 2007; Zahid *et al.*, 2019). The choice of the thiol is very important. The sulfur forms a bind with Au, but the rest of the organic molecule is free to react, as shown in **Figure I.14**. For example, if the organic molecule has a carboxyl group (Chen and

Kimura, 1999), it would be reactive toward amine and therefore proteins (Medintz *et al.*, 2005). In addition, the polyethylene-glycol (PEG) is often used to functionalize the Au-NPs surface, given its capacity to be bounded with molecules such as biotin, lactose, etc. (Otsuka *et al.*, 2001; Takae *et al.*, 2005). Depending on the type of ligand, the NPs manifest different properties and possible applications. In 2008, Lee et al. (Lee *et al.*, 2008) used Au-NPs functionalized by amine as carriers for intracellular delivery of small interfering RNA (siRNA) conjugated with PEG for the treatment of prostate cancer. In this case, the gold has the function of enhancing the internalization of siRNA in the cell lines. By choosing the ligand accurately, it is even possible to do nuclear targeting (Sun, Liu and Wang, 2008). In 2003, Tkachenko et al. (Tkachenko *et al.*, 2003) produced Au-NPs able to enhance a selective nuclear uptake of peptide-Au-NPs for liver carcinoma cells.

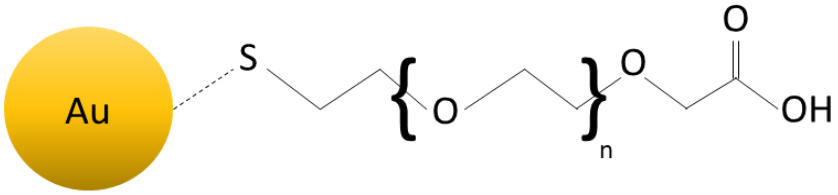

***Figure I.14**. Example of Au-NP functionalized with the thiol-carboxyl group.*

The dimensions obtained for these functionalized NPs can be very different depending on the ligands and the original dimensions of the NPs. For example, for the nanoshells used under NIR radiation, the dimensions are often around 150 nm (Riley and Day, 2017). For this reason, they are suitable to be administrated not only via direct injection but also via systematic delivery, which permits them to reach the tumor site due to the EPR effect. Hyperthermia caused by NIR radiation has several physiological effects on the cells. Firstly, cancer's vessels and cell membrane permeability increase due to the rise in temperature, which causes a more efficient drug uptake. However, there are also other effects directly inside the cells: The temperature increase also causes protein denaturation and DNA damage, as detected in the case of magnetic hyperthermia (Riley and Day, 2017). This may lead to cell death, which can be of two types: necrosis or apoptosis. Even if the necrosis causes tumor cell death, this may cause the release of damaged biological material in the surrounding environment that may degenerate, in turn causing inflammatory and immunogenic responses, whereas apoptosis leads to tumor cell death that discourages inflammation (Melamed, Edelstein and Day, 2015). For this reason, it is crucial to choose the parameters and material characteristics correctly in order to obtain the desired heating, thus controlling the system response (Riley and Day, 2017). For this concern, research is developed toward the understanding and the

definition of the physical parameters of the NPs in order to control the effects as much as possible. Carrillo-Cazares et al. (Carrillo-Cazares *et al.*, 2017), for example, determined the optical properties of Au-NPs when they are inserted in the liver and colon tissue, and they focused on the differences in the temperature recorded between the two different environments. As with the case of magnetic hyperthermia, NIR radiation hyperthermia found scientific interest in the treatment of brain tumors. Bernardi et al. (Bernardi *et al.*, 2008) produced gold-silica nanoshells for in vitro treatment of medulloblastoma and glioma. The nanoshells were functionalized with antibodies to interact with characteristic receptors present on the cell membranes, in order to enhance cell targeting. Results showed that for cell lines with receptors overexpressed, the targeting was effective, and in this way, it was possible to continue the treatment of photothermal ablation. Similarly, Carpin et al. (Carpin *et al.*, 2011) studied NIR hyperthermia of Au-NPs causing photothermal ablation for trastuzumab-resistant breast cancer cells. The results showed that this treatment was effective even for cells characterized by resistance to drugs. Combining drugs with photothermal treatment, however, is now one of the fields that are more promising. You et al. (You *et al.*, 2012) produced Au-NPs coated with PEG and loaded with doxorubicin (DOX) for the treatment of breast and ovarian cancer in vivo. Under NIR radiation, the cell uptake of DOX increased for all the cell lines and showed a relevant decrease in the tumor size after more than 20 days of the treatment compared to the same treatment without NIR radiation. Even the chemotherapy treatment of DOX in vivo was much less effective compared to the combined treatments.

If the cell uptake is affected by the NIR-trigger, the drug release may be affected as well. Campardelli et al. (Campardelli *et al.*, 2014) produced gold-PLA nanocarriers (showing the possibility to submit other metals also to this coating (Campardelli *et al.*, 2013)), representing interesting possibilities to improve the bioavailability and compliance of these nanoparticles; furthermore, these nanocarriers provided an engineered system capable of transporting a specific payload and triggering it by remote control, obtaining tunable drug release (Campardelli *et al.*, 2014).

Concerning the treatments, they can be even more complex. Lee et al. (Lee, Park and Yoo, 2010) produced PLGA nanoparticles half-covered with an Au layer while the others were loaded with DOX for treatment of an epidermoid cancer line. The in vivo results were very interesting because for direct and systematic injection, they obtained a complete regression of the dimensions of the tumor in less than 10 days. For other treatments, such as the only chemotherapy one, the tumor size got doubled in less than one month, even for the same NPs without NIR hyperthermia. The synergic effect of hyperthermia and chemotherapy is accepted now as effective for tumor treatment.

The encouraging results obtained for the in vitro and in vivo trials led to the application of these technologies for clinical trials. In particular, AuroLase Therapy (promoted by Nanospectra Biosciences, Inc., Houston, TX, USA) is one of the first programs on this horizon. It uses gold nanoshells with silica core of ~150 nm, and the first results were published in 2019 for the treatment of prostate tumors on 16 patients (58–79 years old) with NIR photothermal ablation (~810 nm) (Rastinehad *et al.*, 2019), showing the safety and the feasibility of this technology for the treatment of prostate cancers. In the study, 1 patient did not complete the treatment; for 13 patients out of 15, no evident signs of cancer were detected after one year of treatment.

Nanoparticles activated via Pulsed Electric Field

Electroporation and Electrochemotherapy

At present, there is a spreading interest in cancer treatment via a pulsed electric field (PEF) for the promising effects evidenced through this kind of treatment. It can cause aqueous pores in the lipid bilayer due to very short high voltage pulses (generally around the μs and the ms), and it is called electroporation (EP). Even if the mechanism is not perfectly clear (Yadollahpour and Rezaee, 2014), the pore generation is probably due to increasing the transmembrane potential due to the electric field (Campelo *et al.*, 2017). When the transmembrane potential overcomes a determined threshold, the pores start to be generated on the cell membrane (Garcia *et al.*, 2016). Moreover, the interaction of the field with water molecules, which move because of the field gradient, penetrates the bilayer of the membrane and accelerates the pore formation process (Tieleman, 2004).
Depending on the force on the cell membrane, it is possible to study two types of EP: irreversible EP (IEP) or reversible EP (REP) (Kotnik *et al.*, 2012; Narayanan, 2015). In the case of IEP, the results can be compared to the photothermal ablation because the formation of pores induces cell death (Miller, Leor and Rubinsky, 2005). If the pores recover their initial structure so that the survival of the cell is guaranteed, the effects of the electroporation treatment are reversible (REP). The formation of the pores leads to an increase in the permeabilization of the cell membrane, which can be exploited for the diffusion of active substances in the cell. Given the fact that it is usually used as an antitumor treatment, it is interesting to study the phenomenon when it is used in combination with chemotherapy, i.e., electrochemotherapy (ECT), similarly to how it was previously done for hyperthermia treatment. Thus, while hyperthermia combined with chemotherapy is useful to enhance the transport phenomena and immune response, (Yagawa *et al.*, 2017) for the EP, what changes are the structure of the cell membrane, which leads to an enhancement of the transport

phenomena. For an electroporated membrane, the mass transport relation is reported in eq. (7) (Kotnik *et al.*, 2012).

$$\frac{V}{S} * \frac{dc}{dt} = -D * \frac{z * E * F}{\rho * T} c - D\nabla c \tag{7}$$

where V is the volume of the cell, S is the surface of the pores, c is the active substance concentration, t is the time, D is the diffusion coefficient, z is the electric charge of the molecules or ions, E is the local electric field acting on them, F is the Faraday constant, ρ is the gas constant, and T is the temperature. This relation shows that there are two contributions to the transport of molecules (Moore *et al.*, 2000). The first one is the diffusive term, $D\nabla c$, which is present until the concentration outside and inside the cell is in equilibrium. The second term $D*\frac{z*E*F}{\rho*T}$ is strictly related to the EP, and it remains until the cells recover from the EP. For this reason, it enhances the uptake by cells (Edhemovic *et al.*, 2011) of low-permeant drugs, such as bleomycin (Gothelf, Mir and Gehl, 2003). Heller et al. (Heller *et al.*, 1998) studied the combined effects of bleomycin and EP in 34 patients, for a total of 143 tumors, mostly skin tumors and melanomas. After 10 min by the injection of bleomycin, PEF was delivered to the interest zone by the electrode zone. After 12 weeks, the results showed that with only EP or chemotherapy, the results were not good. With ECT, 100% of the patients had a regression for basal carcinoma; 94% did not show a trace of tumor (CR), whereas the remaining 6% had a regression over 50% (PR). For melanoma, the regression was of 98.8% (with 89.3% CR and 9.5% PR), and the others had a 100% regression (80% CR, 20% PR). These results were interesting because they showed a synergistic effect of the combination of the two treatments. Moreover, this strategy showed the efficacy of bleomycin, which usually is not effective for the treatment of solid tumors (Heller *et al.*, 1998). It is a very cytotoxic agent, but it is limited by the fact that it is not able to overcome the plasma membrane (Mir, Tounekti and Orlowski, 1996). In this way, electroporation opened a new way for drugs potentially usable for cancer treatments. Gibot et al. (Gibot *et al.*, 2013) in 2013 proved the efficacy of ECT combined with bleomycin, cisplatin, and DOX administration for the treatment of colorectal carcinoma in a multicellular tumor spheroid. It was proven that the ECT-bleomycin treatment led to 10 times more apoptosis than the bleomycin alone. The same phenomenon happened for the cisplatin, whereas the ECT-DOX showed about 5 times more apoptosis than the DOX one. Moreover, it was observed that there was a maximum decrease in the apoptosis cells (which were in the external layers of the tumor) that went into the core. The electroporator is generally constituted by three main parts: the generator, the electrodes, and the AccuSync device. The generator and the electrodes

instruments are necessary for the electroporation, whereas the AccuSync device is used to deliver a PEF synchronized with the patient's electrocardiogram (Cannon *et al.*, 2013; Narayanan, 2015). The electrodes are crucial elements because their configuration substantially affects the electric field generated (Gehl *et al.*, 1999); for this reason, different types of electrodes were produced. For example, they can be regular plates placed on the side of the tumor in order to generate a homogenous electric field in the carcinoma. Moreover, if the interested region is subcutaneous, the parallel plates may not guarantee an adequate electric field. For example, they can be replaced by needle electrodes that show better performance and an easier application for some types of tumors (Gilbert, Jaroszeski and Heller, 1997). However, the most relevant problem of electroporation is that it is applicable for easily accessible tumors, mostly external, as well as the potential cell damage induced by using high voltage.

Electroporation and Nanoparticles

NPs combined with electroporation can considerably enhance EP performance, as they have beneficial effects on the classical drawbacks of the treatment. Zu et al. (Zu *et al.*, 2014) studied the differences in the classical EP inducted by electroporation for mammalian and leukemia cells in vitro by using gold NPs. To pore the cell, it is necessary to have a certain potential difference between two edges of the cell membrane, and it is found using eq. (8):

$$\Delta V_m = \frac{3}{2} * E_{ext} * r * \cos\theta \qquad (1)$$

where E is the electric field strength, r is the radius of the cell, and θ is the angle between the electric field and the membrane (Zu *et al.*, 2014). The necessary voltage delivered by the electroporator, however, is always more than the voltage required for the breakdown of the cell membrane. This happens because the cell surrounding environment works as a resistance for the two electrodes, as reported in ***Figure* I.*15***. This is one of the reasons that causes cell damage: It is necessary to work with a higher voltage than that valued necessary. Putting inside gold NPs, characterized by a high conductivity (~$4.5*10^6$ S/m), the resistance through the environment is considerably decreased. ***Figure* I.*15*** presents the scheme of this NP functionality.

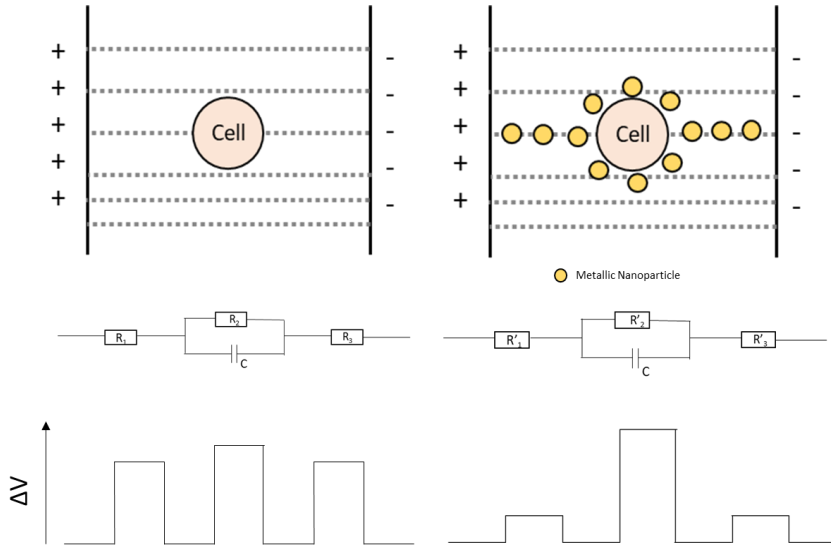

Figure* I.*15. *Differential of potential in a biological environment without metallic NPs (left) and with NPs (right).*

The results show that, as predicted, it is possible to work with a lower voltage, which increases the cell viability, in turn obtaining high transfection efficiency (analyzed by monitoring fluorescent molecules transfection in the cells). However, another important difference is reported regarding the genesis of pores. The NPs act as microelectrodes that polarize the cell by different sides. This is quite different from the standard electroporation, which causes mainly two large breakdowns. The same results were obtained also for the leukemia cells. In particular, the greatest results are obtained on cell viability, which seems to be higher than other innovative EP treatments in literature (Wang *et al.*, 2010). Continuing this path, Huang et al. (Huang *et al.*, 2014) produced Au-NPs coated with polyethyleneimine (PEI) and functionalized with siRNA or DNA plasmids (polyplex/Au-NPs). The PEI was fixed, exploiting electrostatic interactions; this was considered necessary in order to avoid degradation, during the EP, which leads to freeing cationic molecules. The results show a considerable improvement of the system Polyplex/Au-NPs compared to the free polyplex, both in terms of cell viability and in terms of transfection efficiency. This is probably due to the excellent biocompatibility of the Au-NPs, to the stability that the NPs give to the polyplex, and to the synergistic effect of EP with the NPs mentioned before. The scientific interest in this field is now spreading, and many researchers are working to investigate these phenomena in depth (Kim and Lee, 2017).

The first clinical trials for electrochemotherapy started in 1991 (Mir *et al.*, 1991), and over time it became clinically accepted for several types of tumors and treatments (Heller, Gilbert and Jaroszeski, 1999; Sersa, 2006).

However, the combination of these stimulations with NPs is still in development, and at the moment to the best of the author's knowledge, there is no information on clinical trials that are already reported in literature.

Transdermal Delivery Systems Stimuli-Responsive

Nanofibers and Nanoparticles system: Properties

In the last decade, the interest in the combination of nanoparticles with nanofibers has increased. Among all the existent processes for nanofibers production, electrospinning is probably the most interesting one for biomedical applications. In this process, the polymeric solution is fed to the injector, and in exploiting the electric field generated between the injector and the collector, the generated stresses go to thin the polymeric jet, reducing the dimension of the produced fibers (Ramakrishna *et al.*, 2005). Moreover, it is possible to produce Nanofibers of very different materials with very different properties. In **Figure I.16**, a schematic illustration of the electrospinning process and an SEM image of a polycaprolactone (PCL) membrane are shown.

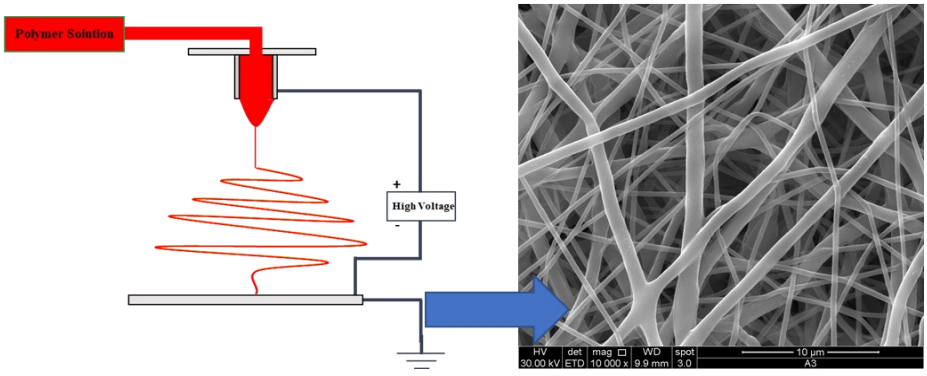

***Figure I.16**. Electrospinning process (left) and SEM image of a polycaprolactone (PCL) membrane (right).*

To produce composite materials, the NPs can be loaded both after the production of nanofibers (indirect method, for example, immersing the membrane in the colloidal solution) and during the electrospinning process (direct method, for example, dissolving the NPs in the polymeric solution), which is usually preferred since it allows for easy control of the amount loaded in the nanofibers (Zhang and Yu, 2014). Following this path, now the scientific community is showing interest in the encapsulation of the NPs in the nanofibers to make nanocomposite-materials stimuli-responsive. Before having nanofibers express the stimuli-responsive properties, it is relevant to underline those different types of NPs lead to different characteristics of the nanofibers in terms of morphology, mechanic properties, and general

performance. For example, Jin et al. (Jin *et al.*, 2010) produced polyvinyl-alcohol (PVA) nanofibers via electrospinning loaded with different sizes of silica (SiO_2) NPs. For a higher diameter (910 nm) of the NPs, the nanofibers presented a considerable change in morphology compared to the ones without NPs. The structure formed was similar to a necklace, where the polymer linked each particle. By decreasing the NPs size (143 nm), the morphology was found newly different compared to the previous nanofibers. In this last case, an aggregation of NPs, which created a visible crunch in the filament morphology, was observed. Finally, by reducing the NP diameter (<80 nm), it is possible to encapsulate NPs efficiently in the polymeric matrix without showing superficial modifications, making them bound in the filament (Cacciotti *et al.*, 2014; Zhang *et al.*, 2017). However, the NPs characteristics can be exploited also to modify the morphology of the Nanofibers. For example, Hu et al. (Hu *et al.*, 2013) produced poly(lactic-co-glycolide) (PLGA) loaded with magnetic NPs using an electrospinning system in the presence of a magnetic field (generated by a permanent magnet). The SEM analysis proved the alignment of the nanofibers caused by the interactions between the magnetic NPs and the magnet, demonstrating that the nanocomposite materials allow for changing the morphological properties. The mechanical properties are sensitive to the loading of NPs as well. Lee et al. (Lee *et al.*, 2009) produced PVA nanofibers loaded with different percentages of montmorillonite, proving that the filler affects the mechanical properties of the material, which in turn increased the tensile strength and modified many parameters (Kim *et al.*, 2014). Similarly, the research performed by McKeon-Fischer et al. (McKeon-Fischer and Freeman, 2011) and Wei et al. (Wei *et al.*, 2011), which concerns the changes in mechanical properties of an electrospun bio-matrix charged with Au-NPs and Fe_3O_4 NPs, showed very similar results. In this context, considerations of biomedical performance are even more interesting. In fact, McKeon-Fischer et al. (McKeon-Fischer and Freeman, 2011) also highlighted the lack of toxicity of the Au-NP/matrix system, which was used as a scaffold for the healing process of the skeletal muscle. The literature highlights how the biodegradation of the polymeric matrix generally occurs before for the nanocomposite material. In particular, the higher the number of NPs is, the faster the degradation of the biopolymer (Lee *et al.*, 2005; Ho *et al.*, 2014; Augustine, Kalarikkal and Thomas, 2016; Zhang *et al.*, 2017).

Stimuli-Responsive Nanocomposite Materials

Currently, even if several studies report the performance of the nanocomposite systems if stimulated by external sources, very few studies deal with the electromagnetic characteristics of the materials and the interaction between the radiation source and the nanocomposite materials. Electrospun systems are characterized by high porosity, and for this reason, electrospun membranes obviously show different electromagnetic

characteristics compared to bulk materials (Longo, Guadagno and Lamberti, 2020). Moreover, with the inclusion of nanoparticles, the characteristics can keep changing not only in terms of, for example, the electric conductivity and dielectric permittivity but also as regards the transmitted and reflected energy for waves interaction through the nanocomposite material containing the filler (Xu *et al.*, 2014; Silveira *et al.*, 2019). The EP is perfectly adaptable to applications conjugated with the drug delivery via electrospun membrane. Very recent studies started matching these two systems to investigate their potentialities if applied together. In 2018, Wang et al. (L. Wang *et al.*, 2018) loaded hydroxycamphothecin (HCPT) on an electrospun membrane to treat VX2 subcutaneous cancer of rabbits together after being ablated through IEP. The results were promising, since they showed a tumor inhibition rate of more than 80%, while the system with only electroporation or the one only with drug membrane manifested a tumor inhibition rate of 62 and 38%, respectively. Moreover, the tumor mass was almost around 30% compared to the control tumor mass, whereas for the other treatments the mass was about 40 and 62%, respectively. However, this highly cutting-edge system is now in development and promises to be highly interesting and with high potentiality, given its usability and the matching between two clinical-used systems (i.e., transdermal delivery and electroporation).

However, as regards the hyperthermic potentialities, certain NPs such as Au-NPs, for example, present an absorbance peak that is very similar even after being encapsulated in nanofibers during the electrospinning process (Wang *et al.*, 2007). This result suggests that the photothermal activity is conserved, as experimentally evidenced. In this last context, Cheng et al. (Cheng *et al.*, 2014) produced an electrospun membrane of poly(lactic-co-glycolic acid) (PLGA) and PLA-b-PEG loaded with gold nanorods. The nanorods were functionalized with PEG, with a dimension of 52 nm and a diameter of 10 nm. First of all, the Au-nanorods release was evaluated. In two hours, 30% of Au-Nanorods were released, while for the remaining 70%, it was necessary to wait three months, showing that the usage of a membrane is effective for the release control. Moreover, the cell uptake for a lung cancer cell line was almost 80%. The cell line was stimulated via NIR radiation, causing hyperthermia up to 42 °C, and not only was a high rate of cell death guaranteed for the lung carcinoma line, but by testing also a human bronchial Epithelial cell line, the selectivity of the treatment was proven, guaranteeing a high vitality for the healthy cells, a high cancerous cell death, and a selective inhibition of the cell proliferation (it decreases only for the cancerous cell line). Similar results were obtained with magnetic-induced hyperthermia treatment. As mentioned before, magnetite-based NPs can be loaded on or into electrospun fibers during the process (Zhong *et al.*, 2015) and at the end of the process (Amarjargal *et al.*, 2013). It was found that by increasing the number of NPs, the heating rate is generally higher, as well as the maximum reachable temperature; secondly, the increase in temperature

can lead to modifications in the polymer structure: For example, in the case of PCL, whose melting point is 61 °C, by exploiting adequately the hyperthermia, it is possible to induce the melting of the matrix. Eventually, by encapsulating the NPs in the matrix, it is possible to slow down the heating rate considerably, making the process more controllable (Lin, Lin and Lin, 2012). Lin et al. (Lin, Lin and Lin, 2012) in 2012 produced chitosan (CS) nanofibers that were then treated in two ways for the loading of NPs, i.e., immerged in a magnetic nanoparticle solution or immerged in a Fe^{2+}/Fe^{3+} solution followed by a coprecipitation of the NPs. The in vitro results were evaluated for the treatment of colon adenocarcinoma and on a lung fibroblast line, showing that the Fe_3O_4 NPs have no cytotoxic effect on that tumor line, but the hyperthermia treatment is very effective for the single NPs, and similar results were obtained for the systems Nanofibers-NPs with magnetic hyperthermia, inducing a cell death around the 70%. All these results, also obtained with the combination of other systems to generate hyperthermia (Zhang *et al.*, 2015) reasonably, led to a very new generated interest in these systems, especially if combined with chemotherapy. Niyama et al. (Niiyama *et al.*, 2019) in 2019 produced a PCL membrane loaded with magnetic nanoparticles and paclitaxel (PXL) to be implanted after surgical resection in the pleural cavity. In this case, the membrane was composed of a PCL matrix and two fillers: the magnetic NPs and PXL. The results show that the drug release was not improved by the hyperthermia, and the cell viability and the tumor size were considerably influenced. In particular, in vitro tests showed that in only one day of treatment, the PXL-NPs-hyperthermia membrane system was sensibly more effective with respect to the membrane without NPs and stimulus, inducing a cell death of 42% in 24 h, compared to the chemotherapeutic treatment on membrane having integrated only PXL, which determines cell death only of 8%. The promising results obtained in vitro were confirmed in vivo when treating the same tumor line in mice. In particular, with the stimulation of the alternate magnetic field of 15 min per week, for a total duration of 8 weeks, the evolution of the tumor mass in mice was studied. The study highlighted that the treatment was more effective via transdermal delivery than via injection (because of the short half-life of the chemotherapeutic agent alone), and the combined treatment brought a 87% reduction of the tumor mass, much higher than any other treatment. Similarly, Park et al. (Park *et al.*, 2019) produced a PCL membrane loaded with gold nanocages (receptive to NIR radiation), DOX (chemotherapy agent), and fatty acids for the treatment of a breast cancer cell line. The use of fatty acids has proven to be crucial for a sustainable release. As previously observed, PTX release was not influenced by the magnetic hyperthermia in the PCL membrane. The fatty acids are in fact a phase-changeable agent, which melts above 39 °C and goes out of the membrane. In this way, small pores are generated, and the superficial area is increased. In evaluating the release, it is possible to

observe that, without NIR radiation, the drug release is very slow. After 5 min of NIR radiation, the rate for the membrane without fatty acids was not sensibly changed, whereas increasing the amount of fatty acids, the kinetic of release changed sensibly. Cell viability confirms these results: Without NIR radiation, the cell viability is above 90%; because there are no effects of the hyperthermia and very low effects of the chemotherapy, after one treatment it decreases to 57% (without fatty acid is 77%) and after four cycles of treatment the viability decrease to 4%.

The abovementioned changes are irreversible: Once the fatty acids have left the membrane, the pores are generated, and the release rate results changed. Li et al. (Y. F. Li *et al.*, 2017) produced a poly(N-isopropylacrylamide) (PNIPAM) membrane loaded with DOX-silica-coated Au-nanorods with the polyhedral oligomeric silsesquioxane (POSS) as a crosslinking agent for a sustainable kinetic release that is very interesting. PNIPAM is a thermosensitive material that can reversibly change hydrophilic/swelling state to a hydrophobic/deswelling state when moving above a critical temperature, known as lower critical solution temperature (LCST). For the PNIPAM, it is usually around 30–34 °C, but it can be shifted through a copolymerization (which, in this case, is through the POSS) (Schmaljohann, 2006). In evaluating the photothermal effect on the volume phase transition of the material, it was possible to notice a great decrease in volume, about 83%, when irradiated by NIR radiation. Similar changes were reported from hydrophilic behavior to hydrophobic one. These structural changes determine a different release kinetic of DOX for the material, i.e., when not irradiated and when irradiated. In this way, it is possible to temporarily modify the material properties and then return to the non-irradiated ones. However, electrospinning is a process particularly versatile, which allows for the production of bilayer structure through the coaxial-electrospinning process. To optimize the release kinetics, the employment of sheath-core membranes is a very interesting strategy. Zheng et al. (Zheng *et al.*, 2020) produced a polymeric membrane in which the core is composed of polyethyleneimine (PEI) and a DNA plasmid that has to be transfected in the cells, whereas the sheath is composed of PLA/Gelatin with Au-nanorods (responsive filler). This study evaluated the gene transfection and the release through a coaxial system stimuli-responsive for the treatment of a fibroblast cell line. As regards the release, without NIR radiation after 90 s, less than 1.5 ng of the gene was detected, whereas with NIR radiation the same system released about 80 ng (about 50 times higher). Moreover, when stopping the irradiation, the release of the plasmid stopped, suggesting that it may be used for at least three cycles. Not only the rise of temperature may enhance the transport phenomena affecting the permeability, but also the disruption of the cell membrane near the mat (Zhang *et al.*, 2019). The transfection was evaluated through fluorescent protein, and the nanocomposite system under NIR shows a transfection efficiency at least 4

times higher than the system without radiation and without Au-NPs and guarantees cell viability higher than 90%.

Active Molecules

Electrospinning is a process that allows the loading of different types of molecules. Mainly, two approaches are currently possible to load active molecules in electrospun membranes: 1) coating the membrane with the substance of interest, for example impregnating the blank membrane in a solution in which the active substance is dissolved; 2) dissolving the active substance in the starting polymeric solution, in order to produce an active membrane directly during the process and having better control on the quantity of active substance in the membrane, having higher yields and having a better distribution of the filler in the matrix. (Wu *et al.*, 2020)
In literature, as reported before, several chemotherapy agents have been widely studied also for inclusion in electrospun nanofibers: DOX, for example, PXL, and many others, which are all characterized by being chemotherapy drugs already available and used for the therapies of the patients. In this horizon, it may be interesting to test active molecules already used for clinical treatments or new active molecules not already used for treatments, proposing in this way completely innovative systems. In the following chapters, different electrospun systems are described in which different active substances have been loaded.
Currently, different therapeutic options are related to the characteristic of the tumor (stage, location) and of the patient (age, health, and genetic profile), involving surgical resection, chemotherapy, radiotherapy, photodynamic, immuno, bio-chemo, and targeted therapies. (Dummer *et al.*, 2015) However, surely topical treatments using electrospun membranes allow reducing, for example, multiple doses per day thanks to the release kinetic lower than the injection delivery system. For this reason, methods to enhance the control of drug release in these systems have been intensely studied in the last chapters of the thesis.
Different types of active substances can be used for the treatment of cancer. Among them, there are surely drugs of choice commonly used for the treatment of most cancers. The above-cited Doxorubicin and Paclitaxel, for example, are wide-range drugs that are commonly used to treat different types of cancers, and, as displayed in the previous paragraph, now are intensely studied for their encapsulation in drug delivery systems, both in nanoparticle and nanofibrous forms. However, electrospun membranes are particularly suitable for topical treatments directly to the zone of interest, thanks to their peculiar morphology that ensure good breathing of the skin, enhances cell proliferation, and can be exploited for controlled drug delivery. On the behalf of these considerations, the membranes produced in the present Ph.D. thesis are mainly studied for topical treatments against

external tumors, in particular melanomas, considering this type of technology suitable to be applied to the zone of interest after oncological surgery or as containment treatment.
In the last decades, the Food and Drug Administration (FDA) approved several drugs useful in melanoma treatment. Particularly, in 1974 dacarbazine was introduced in the market and it is the first drug able to act against melanoma. Similarly, 5-Fluorouracil has been proved to be effective for the treatment of melanoma and, moreover, can be applied also in the form of topical cream, and is now widely employed for the treatment of skin cancer.(Ryan, Krementz and Litwin, 1988) Temozolomide has been proven to be effective in the treatment of metastatic melanoma. (Quirt *et al.*, 2007) The chemical structures of the common anti-melanoma chemotherapies cited above are reported in **Figure I.17**.

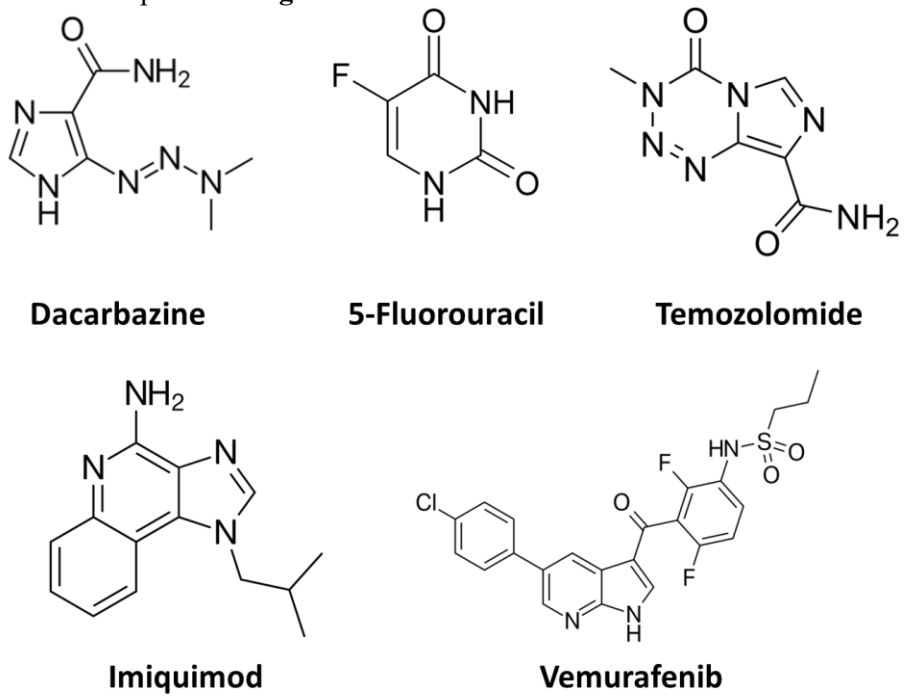

Figure I.17. *Chemical Structure of some of the main drugs used for melanoma treatment*

It is possible to notice that the various chemical structures of the drugs are very similar. In particular, they are N-heterocyclic compounds, and these characteristics are now followed also for new chemotherapy drugs tested in the fight against cancer. In fact, they are generally trying to use these NHC systems to develop innovative drugs. Since NHC can be applied as a center to link the metal to the ligand, now several studies are trying to develop NHC complexes, mainly with platinum, gold, or silver, to improve the

chemotherapic activity and improve some of the limits of the commercial systems (e. g. solubility).(Liu and Gust, 2012; Fung *et al.*, 2017; Harlepp *et al.*, 2019; Mora, Gimeno and Visbal, 2019; Mariconda *et al.*, 2020)
Together with synthesizing new active substances, the possibility to develop cutting-edge materials able to provide chemotherapic topical treatment against melanomas would allow for avoiding several side-effects, especially compared to the drugs delivered via injection. For this reason, the possibility to encapsulate specific chemotherapy for melanomas in electrospun membranes for topical treatments is surely interesting. It is worth noticing that very few studies at the moment look at encapsulating specific drugs for melanoma treatments in electrospun membranes. In 2020, (Steffens *et al.*, 2020) Steffens et al. produced electrospun membranes of polyvinylalcohol (PVA) loaded with dacarbazine, whereas Irani et al. (Irani, Mir Mohamad Sadeghi and Haririan, 2017) produced electrospun coaxial membranes loaded with Temozolomide; these systems were successfully tested for the treatment of glioblastoma. Li et al. (G. Li *et al.*, 2013) included 5-Fluorouracile in PLA electrospun matrix to test it against colorectal cancers. In light of these results, including chemotherapic drugs in electrospun membranes can be surely a promising pathway to develop cutting-edge materials for the topical treatment of melanoma.

Chapter Two

Electrospun membranes loaded with Fe_3O_4 Nanoparticles

Chapter II
Electrospun Membranes loaded with Fe_3O_4 Nanoparticles

II.1 Introduction

Since the 2000s, nanotechnologies are considered a powerful mean to open new frontiers in the field of biomedical applications. In the present chapter, the development and characterization of electrospun membranes loaded with different Fe_3O_4 percentages are presented.
In the last years, magnetic NPs, such as Fe_3O_4-NPs, have received more attention in the drug delivery system field. Thanks to their magnetic properties, these NPs permit to target the tumor cells without affecting non-tumoral cells (Salman and Ubed, 2018; Yew *et al.*, 2020). The human application of Fe_3O_4-NPs implies the need to use biocompatible and biodegradable nanoparticles to avoid toxic effects. After being modified surfaces, magnetic nanoparticles can possess excellent biocompatibility, suitable for medical applications (Guo *et al.*, 2018). In this chapter, functionalized Fe_3O_4 nanoparticles, characterized by functional groups able to increase the biocompatibility and the dispersion level in PCL matrices, have been dispersed in hybrid membranes using PCL matrix, chosen for its easy availability, low cost, and suitability for modification. Firstly, the electrospinning process parameters have been optimized both to obtain fibers in the dimensional range of a few micrometers and the uniform dispersion of nanoparticles along the fibers. The thermal analysis and mechanical map of the sample have been produced, analyzing how the inclusion of magnetic nanoparticles affects the thermal transitions, the crystallinity, and the mechanical properties of the sample, from a microscopic and a macroscopic point of view. Secondly, the membranes have been evaluated as an antitumoral device, investigating the antitumoral activity. The results of the tests *in vitro* against cervix uterine cancer and melanoma cell lines are reported. Lastly, an electromagnetic characterization of the membranes have been performed and is here presented.

II.2 Materials

PCL used for the membrane preparation was provided by Perstorp (Sweden), CAS N° 24980-41-4). It is a linear polyester characterized by a high molecular weight (about 80,000) and was provided in the form of pellets

(granules with an approximate diameter of 3 mm). The main physical parameters are shown in **Table II.5**.

Table II.5. *PCL characteristics*

Mean Molecular Weight	**Melting Point [°C]**	**Water Content [%]**	**Colour of 30% m/m solution, Hazen**	**Elongation at break [%]**	**Melt flow Index**	**Solubility parameters The solubility parameter [δ] [(cal/cm^3)$^{1/2}$]**
80000	58-60	<1.0	<75	800	3g/10 min with 2.16 kg, 1" PVC die at 160°C	9.34-9.43

Iron (III) acetylacetonate ($Fe(acac)_3$) (97%), 1,2-hexadecanediol (90%), oleic acid (OA), citric acid (CA), benzyl ether (90%), ethanol, hexane, and acetone were obtained from Aldrich Chemical Co. All chemical products employed in the tests were of analytical grade.

Biological Assay

The cell lines here tested were from the American Type Culture Collection (ATCC, Manassas, VA). A2058 and A375 human epithelial melanoma cells, highly and lowly metastatic respectively were maintained in Dulbecco's Modified Eagle Medium (DMEM) low glucose (1 g/mL), supplemented with 20% FBS and 100 U/ml penicillin/streptomycin. Cells were maintained at 37 °C in a humidified atmosphere of 95% air and 5% CO_2 and periodically screened for contamination using a previously described procedure. [148] HeLa human epithelial cervix carcinoma cells, estrogen receptor-negative (ER-), were maintained in minimum essential medium (MEM), supplemented with 10% FBS, 100 U/ml penicillin/ streptomycin and 1% non-essential amino acid. Cells were maintained at 37 °C in a humidified atmosphere of 95% air and 5% CO_2 and periodically screened for contamination as already performed in literature (Sinicropi *et al.*, 2018).

Synthesis and Functionalization of Functionalized Fe_3O_4 Nanoparticles

The synthesis of Fe_3O_4 magnetic nanoparticles (Fe_3O_4@OA) was performed under nitrogen using an experimental procedure already described in literature (Sarno *et al.*, 2017; Sarno and Iuliano, 2019). For the synthesis, benzyl ether (about 20 mL), iron (III) acetylacetonate (2 mmol), 1,2-hexadecanediol (10 mmol) and oleic acid (12 mmol) were magnetically stirred starting from 25 up to 200 °C (about 30 min) and then at 285 °C for other 30 min. Washing was carried out by centrifugation (7500 rpm, 30 min) in ethanol and then in an equal volume mixture of hexane and ethanol. This experimental procedure allowed obtaining 4 nm Fe_3O_4@OA Nanoparticle Seeds. The functionalization of Fe_3O_4@OA was performed by modifying the obtained nanoparticles through a ligand exchange with citric acid (CA) at room temperature 100 mg of Fe_3O_4@OA in 30 mL of hexane was added in a vessel previously loaded with a solution 3 M of citric acid in water. Ligand exchange was completed in 24 h. Fe_3O_4@CA nanoparticles were removed by a magnetic field and washed with water several times.

Preparation of solution for electrospinning membranes

A first solution was prepared by dissolving 17.5% w/w PCL in hot acetone and stirring for about 2 h. Nanoparticles were added to the system and then the solutions were ultrasonicated to prepare homogeneous and stable solutions. Other solutions were prepared considering a lower concentration of PCL until the best concentration was found to obtain optimized morphological parameters of the nanofibers in the membranes. The solution of PCL chosen to perform tests on antitumoral activity and other analysis was prepared by dissolving 14% w/w PCL in hot acetone and stirring for about 2 h. Then, appropriate amounts of functionalized Fe_3O_4 were dissolved in hot acetone. The solutions were ultrasonicated to prepare homogeneous and stable nanocomposite solutions, and then the system was stirred for about 2 h. The concentrations of Fe_3O_4 in PCL were determined at 2, 5.0 and 10 wt%, as for the membranes prepared using other concentrations of PCL.

Cell viability

Cell viability was evaluated using the 3-(4,5-dimethylthiazol-2- y1)-2,5-diphenyltetrazolium (MTT, Sigma Aldrich, Milan, Italy) assay as already reported [43] with some modifications. In detail, the cells were seeded for 24 h in 24 multiwell plate (at the density of 2 104 for HeLa cells and $3*10^4$ for A2058 and A375 cells) and after serum-starved to obtain cell cycle

synchronization for 24 h. PCL membranes (both free and conjugate with Fe_3O_4) were sterilized under UV light irradiation for 24 h before the treatment. Cells were after exposed to PCL membrane conjugate with Fe_3O_4 for 72 h in the treatment medium appropriate for each cell line. A parallel experiment using the same amount of PCL membrane without Fe_3O_4 was carried out, with the aim to verify the absence of cytotoxic effects by the PCL membrane by itself. At the end of the treatment, membranes or Fe_3O_4 were removed and fresh MTT resuspended in PBS was added to each well to a final concentration of 0.2 mg/mL. After 2 h incubation at 37 °C, cells were lysed with DMSO, and then optical density was measured at 570 nm using a microplate reader. MTT experiments were performed in triplicate and repeated three times. Absorbance values were used to determine the IC50 using GraphPad Prism 6 Software (GraphPad Inc., San Diego, CA). Data are representative of three independent experiments; standard deviations (SD) were shown.

Electrospinning Procedure

The solutions containing functionalized Fe_3O_4 nanoparticles were electrospun by climate-controlled electrospinning equipment (EC-CLI by IME Technologies, Spaarpot 147, 5667 KV, Geldrop, Netherlands). Each mixture was poured into a syringe (3 mL) with a 0.8 mm needle of stainless steel. The needle was connected to a power supply at high-voltage. A grounded aluminum foil, placed at a distance of 30 cm from the spinneret, was employed as the counter electrode. PCL fibers, in the form of continuous filaments, were collected in the form of a fibrous membrane on the aluminum foil. The parameters of the electrospinning process were optimized to avoid the formation of beads and hence to produce mats of fibrous PCL composed of individual fibrils characterized by continuity and homogeneity in the diameter dimension along the fiber. The optimization of the parameters, during the production of the membranes, was set by a trial-and-error procedure. In particular, the voltage for electrospinning was set at 25 kV (charge applied to collector -4 kV, charge applied to needle 21 kV), feeding rate 4.0 mL/h, temperature 25 °C, relative humidity (R.H.) 35%. The obtained membranes were put in a vacuum oven for 24 h at room temperature to eliminate any solvent residuals and moisture and then placed over silica gel in a dryer.

FESEM-EDX, TEM and Atomic Force Microscopy

The morphological characterization was performed by Transmission Electron Microscopy (TEM) and Field emission scanning electron microscopy (FESEM). TEM was performed using the FEI Tecnai electron microscope operating at 200 kV equipped with an EDX probe. The

dimension of the nanoparticles was investigated after their sonication in hexane for 5 min. FESEM investigation was carried out to analyze the geometrical parameters of the electrospun fibers and the size distribution.
The analysis to obtain the fiber size distribution has been done using ImageJ software, whereas the data to obtain the pore diameter distribution using MATLAB software following the procedure reported by Havlíček *et al*. (Havlíček *et al.*, 2020) The sections of the fiber mats were coated with a thin layer of gold prior to their morphological analysis. The distribution of the diameter of the fibers was obtained using Sigma ScanPro 5. For this last investigation, at least 300 fibers were considered. The values were measured considering the reference bar of the FESEM image. The images were collected with a FESEMLEO1550VP microscope. EDS investigation was performed by a FESEM LEO1525 microscope equipped with an EDX detector. EDX maps were obtained after covering the samples with chromium film.
Moreover, Atomic Force Microscopy (AFM) equipped with HarmoniX tool has been performed to characterize the morphology of the samples linking it with the local mechanical properties. AFM is a technique able to recreate a topographic map of the sample surface by exploiting the interactions between the tip and the sample surface. By acquiring information on the deflection of the cantilever through a laser, it is possible to obtain morphology accurate data on the surface of the sample. AFM measurements were taken using the HMX-10 probe, which has a nominal tip radius of 10 nm. This probe enables the mapping of nanometric mechanical properties in the range of 10 MPa to 10 GPa. Positions on the sample surface were measured with an accuracy of 10 nm, while the elastic modulus was measured with an accuracy of 10 MPa. The height and the local mechanical data, processed through Derjaguin-Muller-Toporov (DMT) model according to the procedure reported by Guadagno et al. (Guadagno *et al.*, 2019), have been processed along the fibers using NanoScope Analysis 1.40 Software (Bruker Corporation, Billerica, USA) and via OriginPro software (OriginLab Corporation, Northampton, USA)

Thermogravimetric investigation

Thermogravimetric investigation (TG-DTG) (SDTQ 600 Analyzer (TA Instruments) in flowing air at a 10 °C/min heating rate was performed to analyze the thermal stability of the synthesized nanoparticles.

Differential Scanning Calorimetry

Differential scanning calorimetry (DSC) has been performed using Mettler Toledo DSC 822e in N_2 atmosphere (50 ml/min) from -50 to 250 °C with 10 °C/min heating rate.

Structural Characterization

Structural characterization of the nanoparticles and the electrospun membranes was performed by X-Ray Diffraction (XRD) measurements were carried out using a Bruker D8 Advance diffractometer operating at 35 kV and 40 mA. The nickel filtered CuKa radiation (1.5418 Å) was used.
The thin film of PCL has been prepared by melting the PCL at 80 °C under 8 tons of pressure to avoid the inclusion of air inside the PCL film.

Electromagnetic Characterization

The electromagnetic characterization of the membranes has been performed by the impedance analyzer E4991A supported with the 16453A text fixture to study the impedance of dielectric materials. The impedance measurements have been performed in the frequency range between 1 MHz and 1 GHz. Through the impedance, it has been to evaluate the complex permittivity, defined in equation 9.

$$\varepsilon(\omega) = \varepsilon'(\omega) + j * \varepsilon''(\omega) \quad (9)$$

where ε' is the real part and ε'' is the imaginary part of the complex electrical permittivity. (De Vivo *et al.*, 2013) By equation (10) then it is possible to obtain the electric conductivity:

$$\sigma(\omega) = \varepsilon''(\omega) * \varepsilon_0 * 2\pi f \quad (10)$$

The text fixture also allows testing the samples at different electrodes pressure. All the electrospun samples have been tested at the minimum and maximum pressure.

II.3 Results and Discussion

Characterization of the functionalized Fe_3O_4@OA nanoparticles (NPs): TEM, XRD and TG-DTG analysis

In the first step, the nanoparticles have been functionalized with the oleic acid-based ligand, obtaining the functionalized nanoparticles Fe_3O_4@OA; in the second consecutive step, Fe_3O_4@OA nanoparticles have been transformed in Fe_3O_4@CA nanoparticles (coated with citric acid (CA)) through a ligand exchange-based reaction. The morphology and size of the oleic acid-coated nanoparticles Fe_3O_4@OA were determined by transmission electron microscopy (TEM) (see ***Figure II.18***a). TEM image shows uniform

size nanoparticles that tend to self-organize in a hexagonal layer. The dimensional distribution of the nanoparticle was detected for ~400 nanoparticles. The results highlight an average diameter of the inorganic domains of ~4.5 ± 1.5 nm, as clearly observable in ***Figure II.18***a. In ***Figure II.18***b XRD diffraction spectrum of the functionalized nanoparticles are reported. The XRD profile presents typical peaks of Fe_3O_4 NPs at 31.1 (220), 35.7 (311), 43.2 (400), 57.3 (511) and 62.7 (440). TG-DTG curves of Fe_3O_4@OA and OA are displayed in ***Figure II.19***a. The TG curve profile of Fe_3O_4@OA shows: (1) a very small weight loss (about 5-6 wt%) in the first part of the curve; (2) then a combined phenomenon oxidation/decomposition of the oleic chains bounded to the nanoparticles, involving about 20 wt % of the total loss, where 18.6% is due to the solid part, detectable at higher temperature with respect to free OA. TG-DTG curves of CA and Fe_3O_4@CA nanoparticles are reported in ***Figure II.19***b. The weight losses due to CA in Fe_3O_4@CA is shifted to higher temperatures. The shift, as in the previous case, is most likely due to the bond with the nanoparticles.

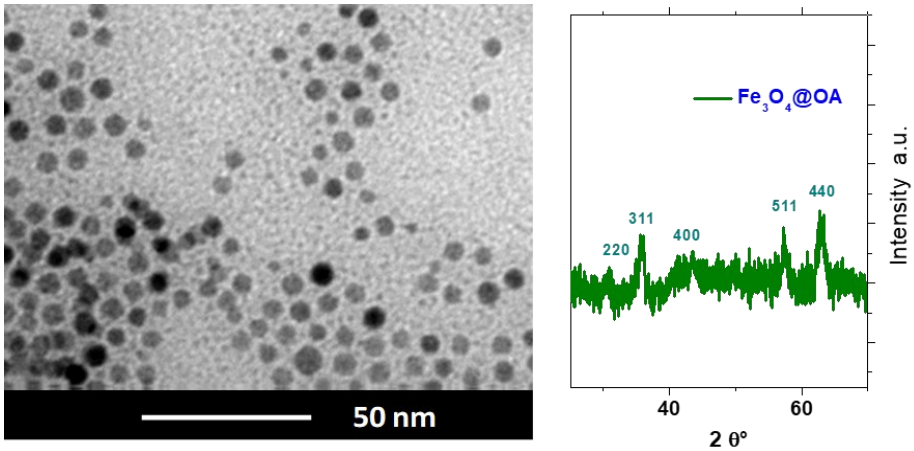

Figure II.18. *TEM images of Fe_3O_4@OA nanoparticles (a), XRD spectrum of Fe_3O_4@OA (b).*

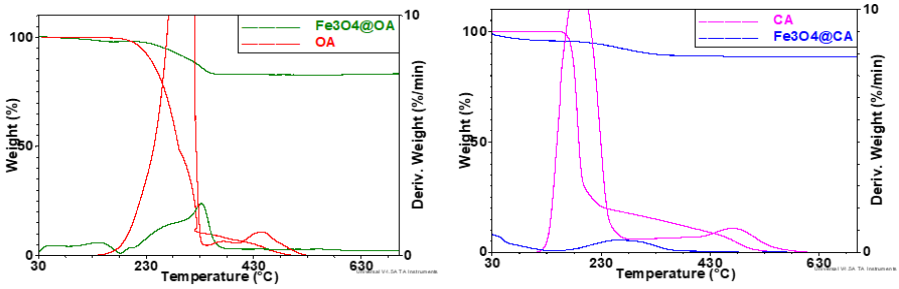

Figure II.19. *TG-DTG curves of (a) Fe_3O_4@OA and OA (on the left); (b) Fe_3O_4@CA and CA (on the right).*

However, as it is possible to observe by the thermal analysis performed on the membranes, PCL thermal degradation is anticipated by the inclusion of magnetite inside the matrix, as reported in **Figure II.20** and . According to literature, this phenomenon is probably due to the fact the Fe_3O_4 nanoparticles are responsible for the random pyrolysis of PCL chains and accelerates the thermal degradation. (Wang *et al.*, 2013)

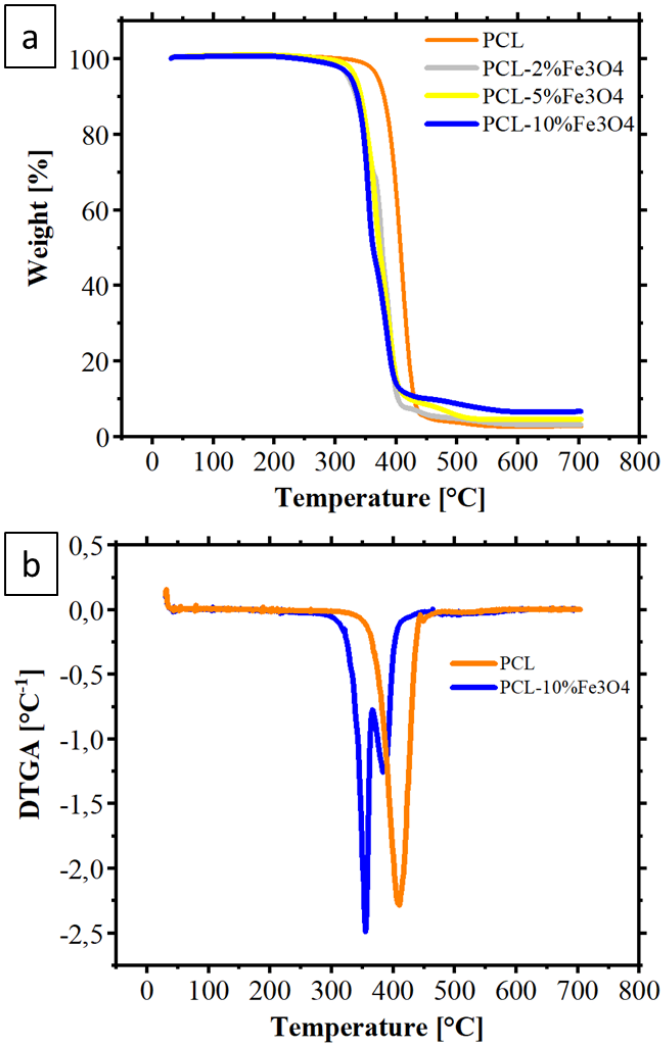

Figure* II.*20. *TGA (a) and DTGA (b) of PCL membranes loaded with magnetite nanoparticles*

In fact, as reported in **Table II.6**, the 5% weight loss is anticipated from 370 °C to around 330 °C by the inclusion of magnetite. However, this phenomenon is not a problem for the applicability of the system, given the study aims to verify its applicability in the biomedical field.

***Table* II.6.** *5% and 50% weight loss for PCL membranes loaded with Fe_3O_4 nanoparticles*

	Temperature at 5% mass loss / $T_{5\%}$ [°C]	Temperature at 50% mass loss / $T_{50\%}$ [°C]
PCL_0%Fe_3O_4	370	407
PCL_2%Fe_3O_4	322	377
PCL_5%Fe_3O_4	333	373
PCL_10%Fe_3O_4	325	362

DSC analyses have confirmed that these types of systems are thermally stable (no transitions) around human body temperature. In fact, PCL, which is characterized by a low melting point (around 60°C), tends to increase the melting temperature by increasing the Fe_3O_4 amount. The DSC graph is reported in **Figure II.21**.

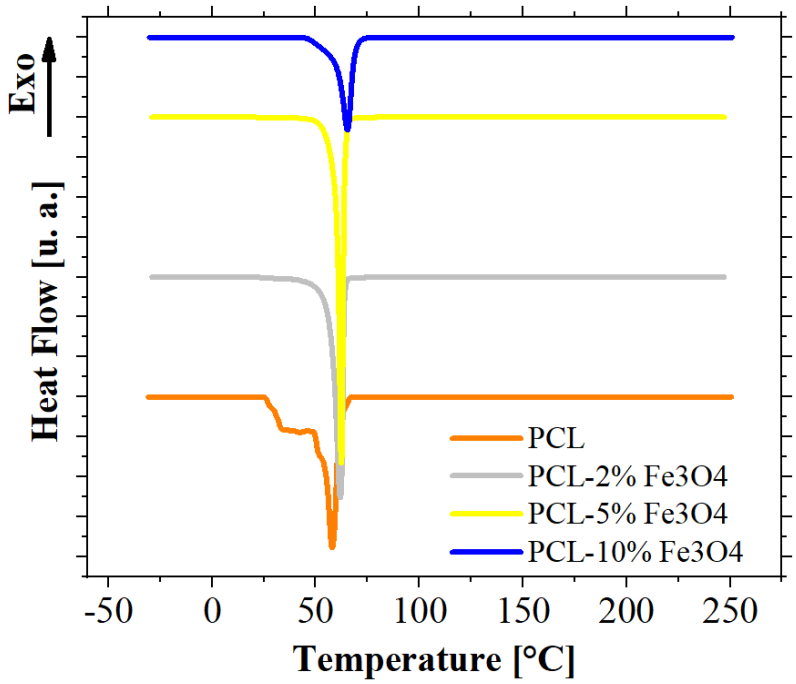

Figure II.21. *DSC on the PCL membranes loaded with Fe_3O_4@CA*

Evidently, the inclusion of the filler in the polymeric matrix has two roles: on the one hand, it causes the increase of the melting temperature given to an increase of the crystal size in the matrix. On the other hand, the crystallinity of the PCL, evaluated as the difference of melting enthalpy, is compared to the one of a theoretical 100% PCL (138.1 g/mol), By this analysis (reported in **Table II.7**) it is evaluated that the inclusion of magnetite enhances the crystallization of the PCL, that increase up to 5% of magnetite. In PCL membrane loaded with 10%Fe_3O_4, probably the magnetite is too much, and thus it obstacles the crystallization of the polymer.

Table* II.*7. *Melting Temperature and Crystallinity of PCL membranes loaded with magnetite nanoparticles*

	Melting Temperature [°C]	**Cristallinity [%]**
PCL_0%Fe_3O_4	58,3	39.1
PCL_2%Fe_3O_4	61,8	56.2
PCL_5%Fe_3O_4	62,2	64.5
PCL_10%Fe_3O_4	65,5	43.5

Characterization of electrospun polycaprolactone/functionalized Fe_3O_4 hybrid membranes

XRD Analysis

The XRD patterns of PCL with 2, 5 and 10% of Fe_3O_4@CA are shown in ***Figure II.22***. All diffraction patterns of the hybrid mats highlight the presence of a significant amount of PCL crystalline phase, as it can be deduced by the presence of the strong reflections at 2 q ¼ 21.5 and 23.8 corresponding to the (110) and (200) planes of the orthorhombic PCL crystalline structure. (Bittiger, Marchessault and Niegisch, 1970; Baji *et al.*, 2007) The presence of the reflections related to the Fe_3O_4 phase is almost imperceptible, due to small amount of Fe_3O_4; however, the increase in the concentration of Fe_3O_4@CA nanoparticles in the mat, from 2 to 10% by weight, makes the reflection 311 of Fe_3O_4, localized between 35° and 40° of 2 Theta, more visible.

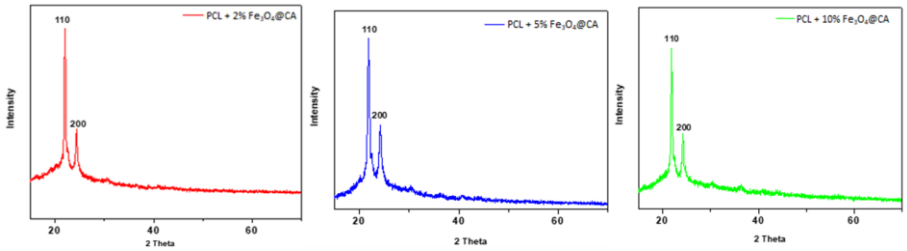

Figure II.22. *XRD profile of PCL add Fe_3O_4@CA: profile red is PCL 2 % Fe_3O_4@CA, profile blue is PCL 5 % Fe_3O_4@CA and profile green is PCL 10 % Fe_3O_4@CA.*

By the analysis of crystallinity done to the XRD, the crystallinity of the samples and the dimensions of the crystal have been defined using Scherrer and Brag's equations. The results are reported in **Table II.8**.

***Table* II.8.** *Crystallinity evaluated by the XRD analysis*

#	**Crystallinity**
PCL_0%Fe_3O_4	57,4%
PCL_2%Fe_3O_4	61,2%
PCL_5%Fe_3O_4	69,3%
PCL_10%Fe_3O_4	60,4%

By comparing the results obtained by DSC and XRD in terms of crystallinity, there are differences between the two results, but the trend of how the magnetite affects the crystallization remains constant.

FESEM Analysis

The morphology feature of the electrospun fibers using the first solution prepared by dissolving 17.5% w/w of PCL is shown in **Figure II.23**. Different small sections of the fiber mat corresponding to the developed membranes have been analyzed. The images of the reference membrane on the top side (unfilled sample) highlight that the concentration of PCL is not suitable to obtain membranes with applicative potentiality because together the nanometric fibers, spherical domains of polycaprolactone appear no electrospun. The incorporation of different concentrations of functionalized nanoparticles (from 2 to 10% by weight) does not improve the result of the electrospinning process (see image on the bottom) corresponding to a membrane with 5 wt% of Fe_3O_4@CA. To optimize the electrospun membranes in terms of uniformity in the diameter and morphological features of the fibers, solutions of PCL at lower concentrations of the polymer have been prepared. The best morphological feature of the membranes has been found for a concentration of PCL prepared by dissolving 14.0% w/w PCL in hot acetone. For this reason, the solution of 14.0% w/w of PCL has been chosen for the preparation of hybrid membranes intended for testing the antitumoral activity and other correlated analyses. The concentrations of Fe_3O_4@CA in PCL were fixed at 2, 5.0, and 10 wt%, as for the membranes prepared using other concentrations of PCL. ***Figure II.24*** shows the morphology of the membranes containing 2, 5, and 10 wt% of Fe_3O_4@CA together with the fibers' diameter distribution (on the right side). The reference sample has also been added for comparison. The membrane of unfilled PCL is composed of individual, uniform, and randomly oriented fibers with most of the diameters ranging around 0.4-1.5 mm. The incorporation of Fe_3O_4@CA determines a different fibers' diameter distribution. Statistically, the diameter increases with increasing the concentration of functionalized nanoparticles. This result is most likely due to an increase in the viscosity of the solution. It is well known that both a decrease in the concentration of the solution and in the molecular weight determine a reduction of the fiber diameter due to the lower viscosity (Tan *et al.*, 2005; Goki, 2006). An increase in the viscosity of the solution determines forces, which hinder the electrostatic repulsion responsible for stretching and thinning the solution jet. SEM images, as shown in ***Figure II.25***a, ***Figure II.26***a, and ***Figure II.27***a, display general morphology of the Fe_3O_4@CA loaded to PCL together the Energy-dispersive X-ray spectroscopy (EDX) maps, which were acquired to examine the distribution of the element Fe. The maps highlight that the Fe atoms (of Fe_3O_4) appear homogeneously distributed along the fibers of the membranes, as can be seen in ***Figure II.25***b, ***Figure II.26***b, and ***Figure II.27***b showing the Fe maps at increasing Fe_3O_4@CA loading.

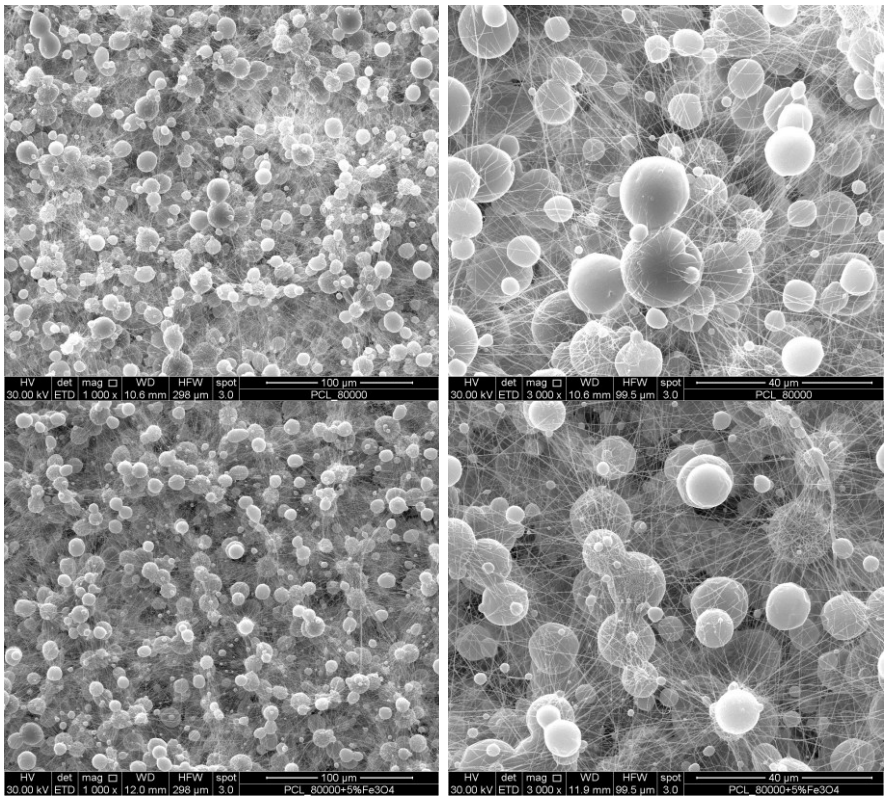

Figure* II.*23. *a) FESEM images of the reference membrane (on the top); and the membrane containing 5 wt% of Fe_3O_4@CA (on the bottom)*

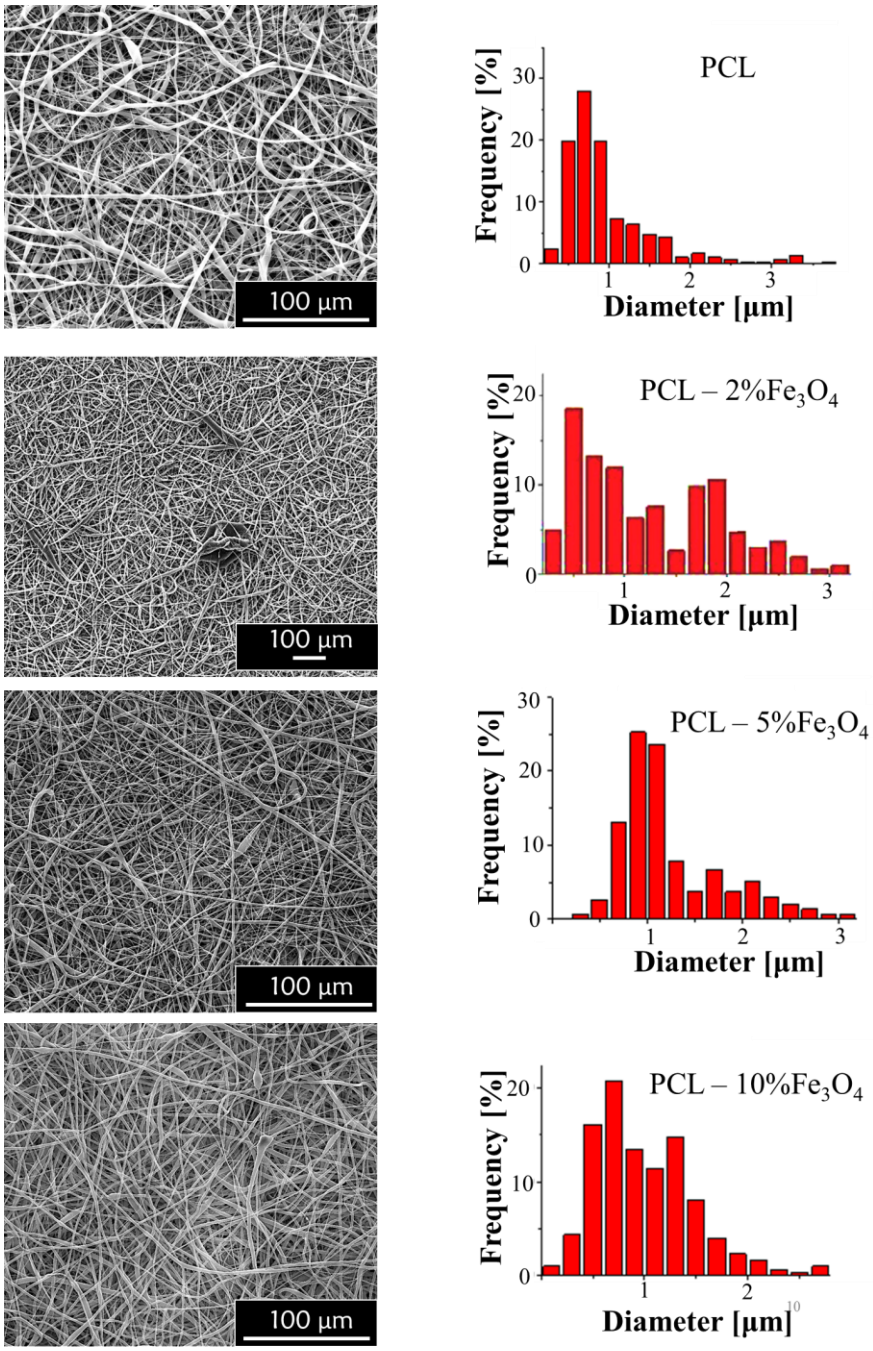

Figure II.24. *FESEM images of the a) reference membrane; and the membrane containing b) 2 wt%, c) 5 wt% and d) 10 wt% of Fe_3O_4@CA.*

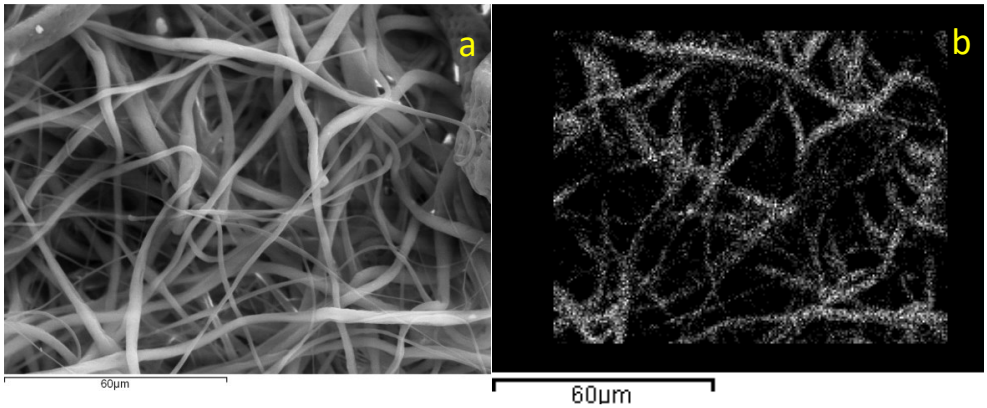

Figure II.25. *Electron micrograph showing the PCL with 2 wt% Fe_3O_4@CA (a); EDX maps and Fe (b).*

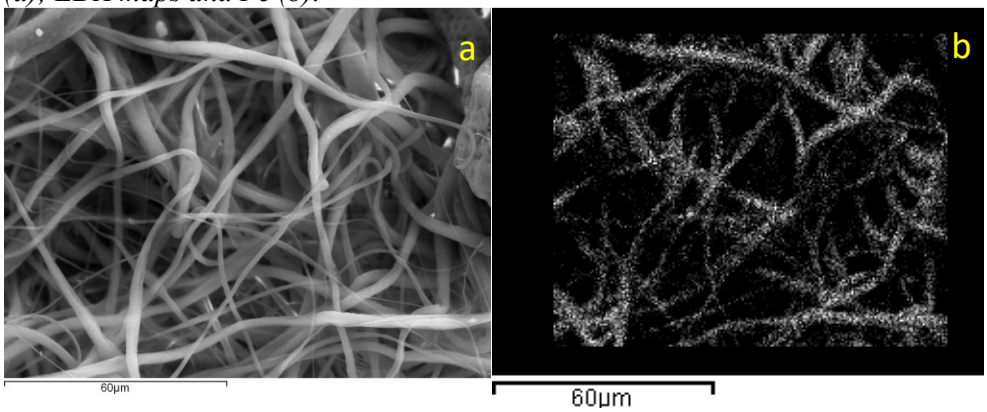

Figure II.26. *Electron micrograph showing the PCL with 5wt% Fe_3O_4@CA (a); EDX maps and Fe (b).*

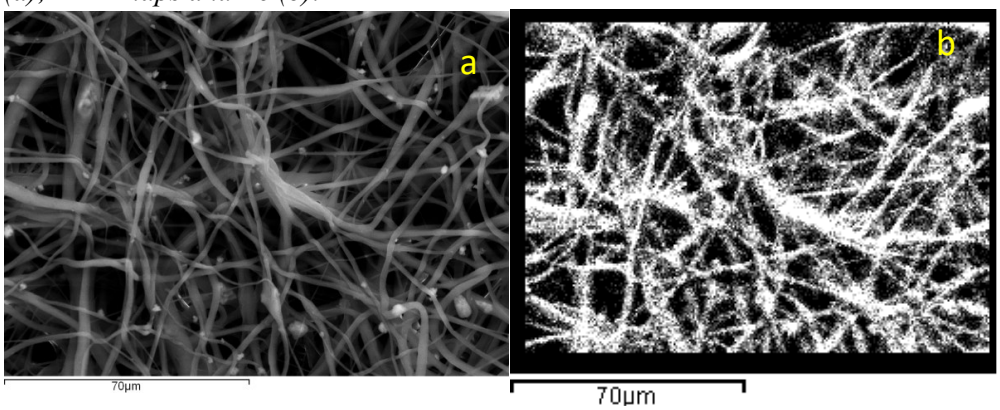

Figure II.27. *Electron micrograph showing the PCL with 10 wt% Fe_3O_4@CA (a); EDX maps and Fe (b).*

By the FESEM images elaboration, it is confirmed that the fiber dimension also affects the pore size, as already reported in literature. Generally, an increase in fiber dimensions determines an increase in the pore dimensions.(Boland *et al.*, 2005). However, the pores of the membranes are around 3-5 μm for all the obtained systems, as reported in **Table II.9**.

Table* II.*9. *Pore dimensions*

	PCL	**PCL-2%Fe_3O_4**	**PCL-5%Fe_3O_4**	**PCL-10%Fe_3O_4**
Mean [μm]	3,45	5,47	3,93	5,13
Standard Deviation [μm]	1,8	3,22	2,34	3,34

.

HarmoniX-AFM Analysis

The mechanical characteristics of the nanocomposites have been evaluated with an innovative approach, using the HarmoniX-AFM, through which it is possible to obtain an accurate mechanical mapping of the nanofiber surfaces. The height and DMT modulus images are reported in **Figure II.28**. As evident, the height morphology shows that the magnetite NPs are included in the nanofibers. Moreover, by the DMT modulus images, it is possible to see that the white dots (that correspond to higher mechanical modulus) are well distributed along the nanofibers. The formation of aggregations slightly increases by increasing the magnetite amount, but nevertheless, the functionalization is proved to be an effective way to distribute the NPs in the PCL matrix.

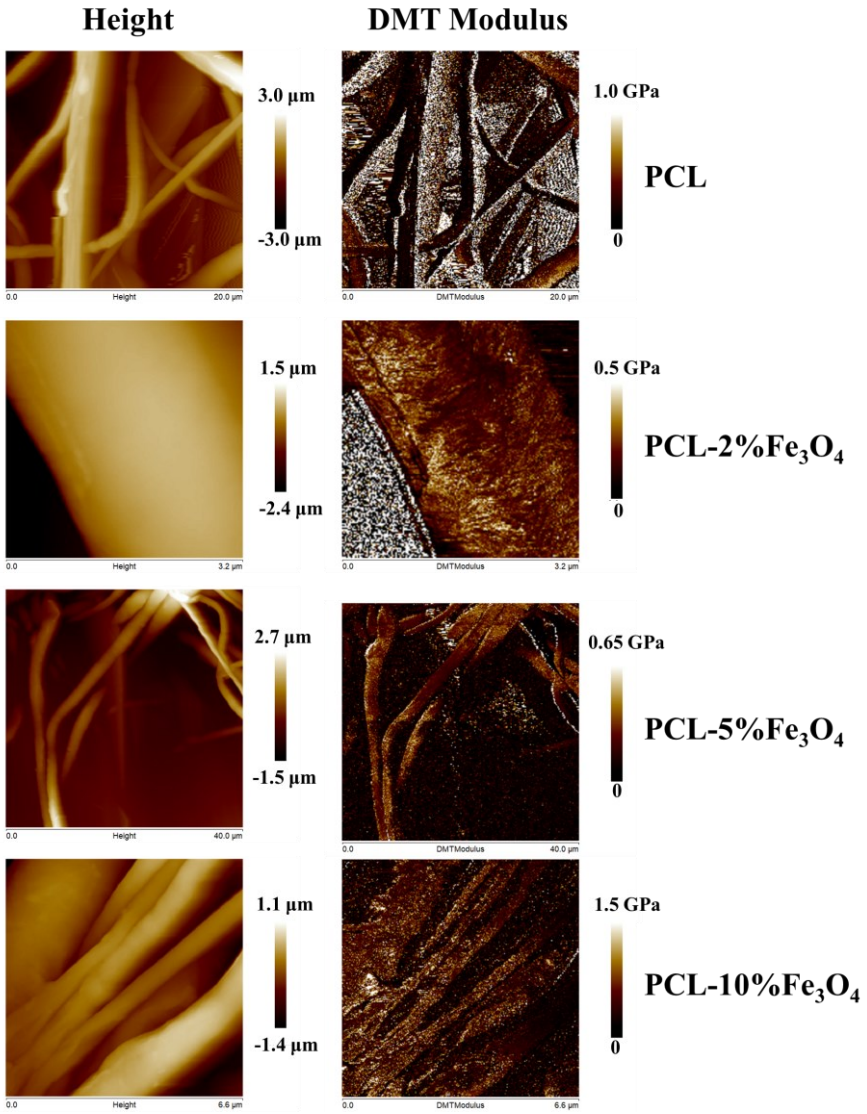

Figure* II.*28. *Height (left) and DMT Modulus (right) images for the samples from 0% to 10% Fe_3O_4 in electrospun PCL*

However, as anticipated before, the inclusion of magnetite in the matrix affects also the crystallinity. This phenomenon is evident also in HarmoniX analysis: in fact, as reported in **Figure II.30**, PCL at 0, 2 and 5% has DMT values that averagely increase by increasing the magnetite content (since the crystallinity is higher) and there is the presence of higher peaks (because of the presence of agglomerates in the matrix). In the case of 10%Fe_3O_4 PCL, the DMT peaks are even higher (higher content of magnetite), but the lower

values are even slightly lower than the sample loaded with 5% Fe_3O_4, given the fact that the crystallinity decreases.

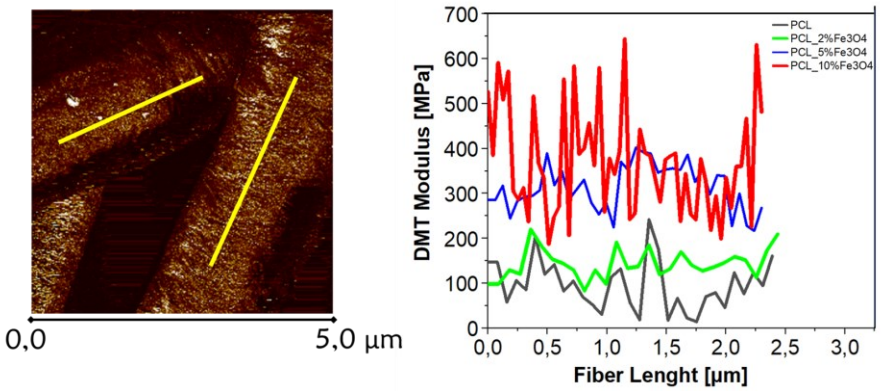

Figure* II.*29. *DMT Modulus profiles along the fiber lengths*

By graphing the distribution of values obtained for the various membranes, reported in **Figure II.30**, it is possible to observe that the average mechanical modulus increases by increasing the magnetite content. However, as noticed in **Figure II.29**, the crystallinity and the magnetite itself both contribute to the increase of the mechanical modulus. For this reason, the PCL-10%Fe_3O_4 system presents overall an average mechanical modulus higher than a PCL-10%Fe_3O_4, but a wider distribution, because of the presence of more magnetite aggregates but lower crystallinity.

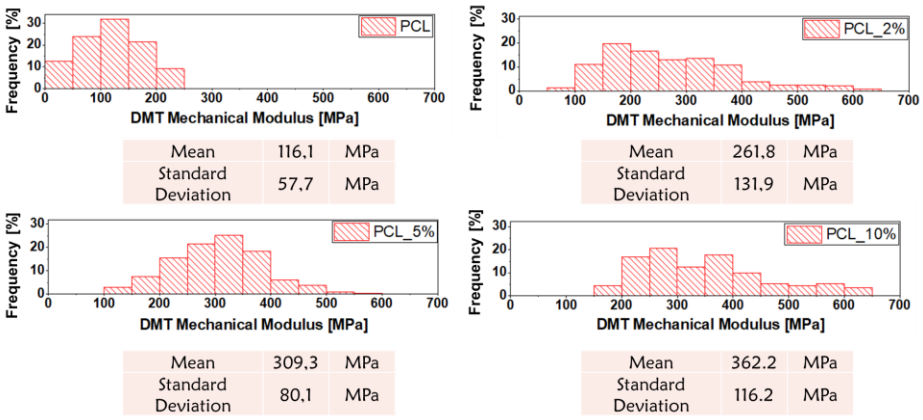

Figure* II.*30. *DMT frequency values of PCL (top-left), PCL-2%Fe_3O_4 (top-right), PCL-5%Fe_3O_4 (bottom-left), PCL-10%Fe_3O_4(bottom-right)*

The local mechanical properties of the material have been compared to the bulk mechanical properties in tensile, and the results are reported in **Table II.10**. As expected, the increase in Fe_3O_4 loading leads to an increase in the

rigidity of the material. However, the elastic values are different, since the HarmoniX evaluates the mechanical properties by propping the sample (similar to the indentation), whereas the bulk tests are in tensile.

Table* II.*10. *Young Modulus of Fe_3O_4 loaded membranes*

#	**Young Modulus [Mpa]**
PCL	4,06
2%Fe_3O_4	6,19
5%Fe_3O_4	6,40
10%Fe_3O_4	6,81

Electromagnetic Characterization

The dielectric permittivity has been evaluated for all the materials. Firstly, in **Figure II.31** it is reported ε' for PCL membrane and the film blank.

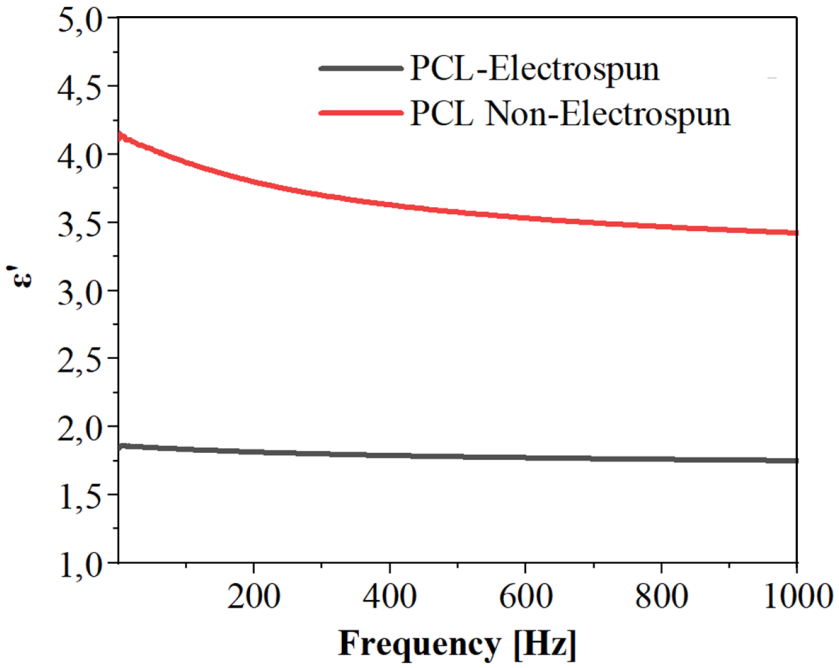

Figure* II.*31. *Dielectric Permittivity of blank PCLs*

As it is well evident, there is a relevant difference in terms of dielectric permittivity among the two samples: starting from an electrical permittivity of about 3.5 at the higher investigated frequency, the electrospinning process leads to a metamaterial of not higher than 1.7. In **Figure II.32** it is reported the analysis of the electrical conductivity for the same samples.

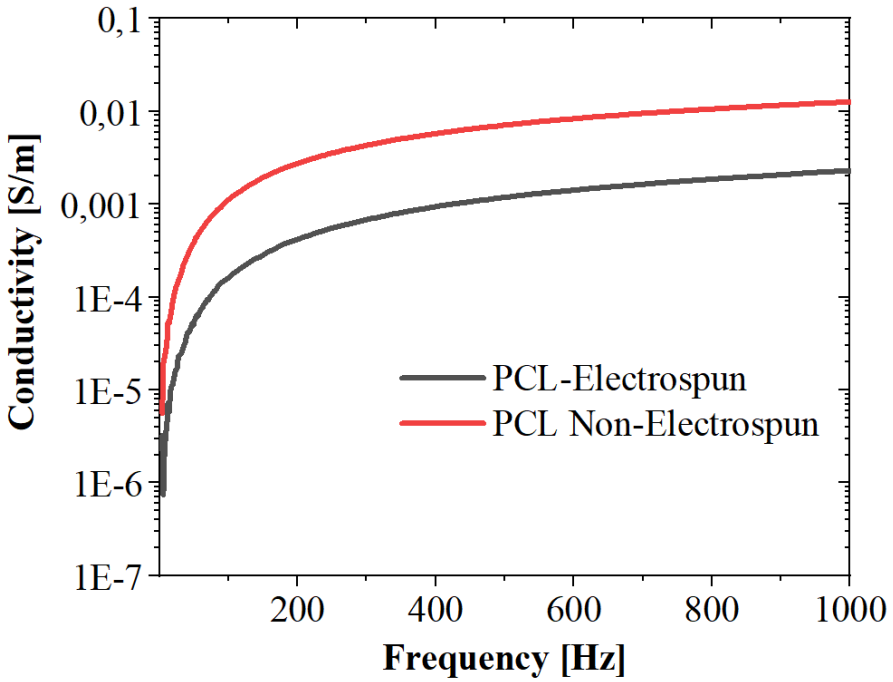

Figure* II.*32. *Electric conductivity of blank PCLs*

The high presence of air in the effective volume of the electrospun material leads to an electrical conductivity of only 2 µS/m at 1 GHz, much lower than the 13 µS/m measured for the bulk material. The decreasing of these two features has to be considered in order to optimize the material performances by operating, for example, on the production process parameters as for example production time. Moreover, it has been carried out also an evaluation of the dielectric permittivity for the minimum and maximum electrode pressure allowed by the instrument for electrospun PCL, PCL with 2 % Fe_3O_4NPs, PCL with 5 % $Fe_3O_4$and PCL with 10 % Fe_3O_4 NPs. ***Figure II.33*** and **Figure II.34** show the results.

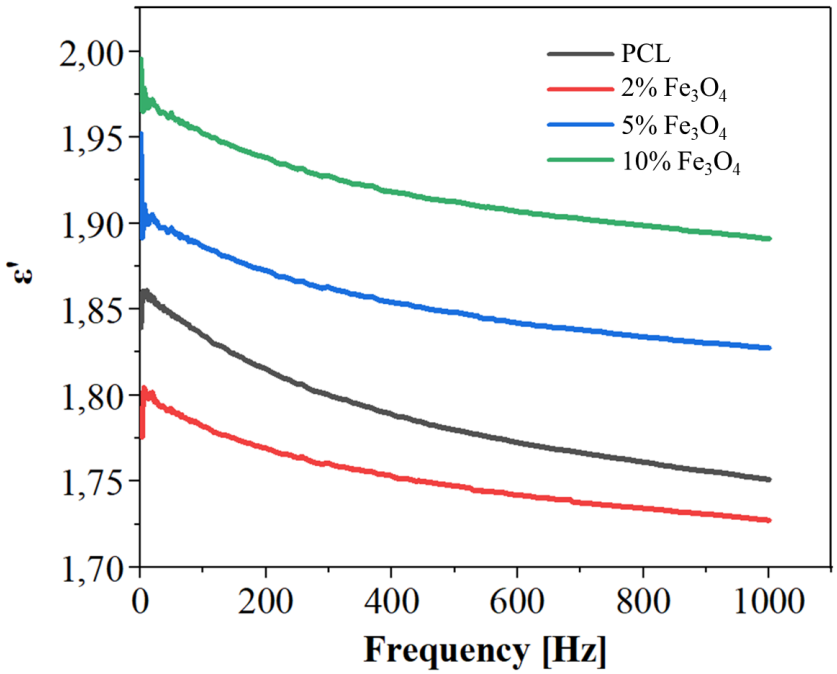

Figure II.33. *Dielectric Permittivity of electrospun membranes at low pressure*

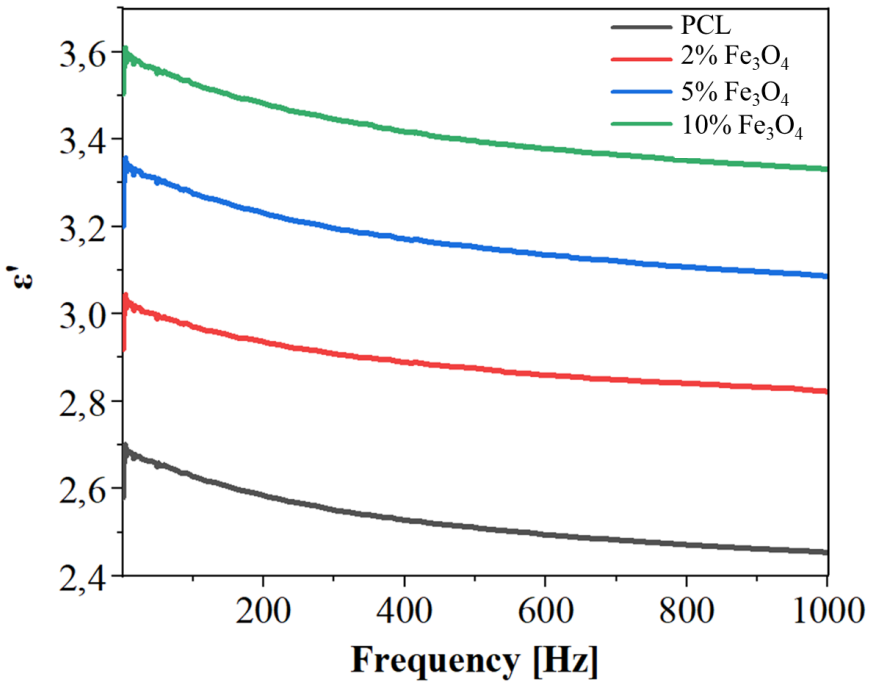

Figure* II.*34. *Dielectric Permittivity of electrospun membranes at high pressure*

As it is well evident, the effect of the pressure brings up the measures of ε' for all the samples. The same effect is reported for the electric conductivity in **Figure II.35** and **Figure II.36**.

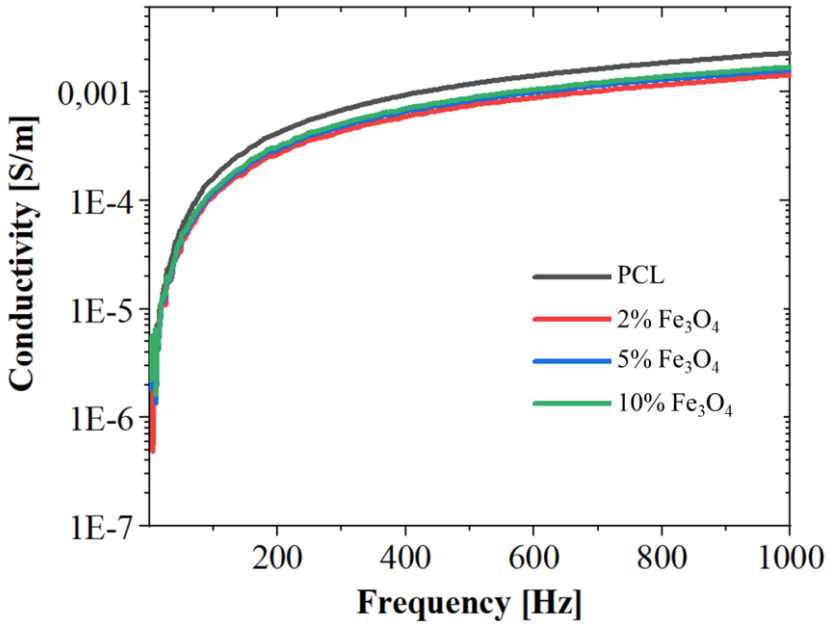

Figure* II.*35. *Electrical Conductivity of electrospun membranes at low pressure*

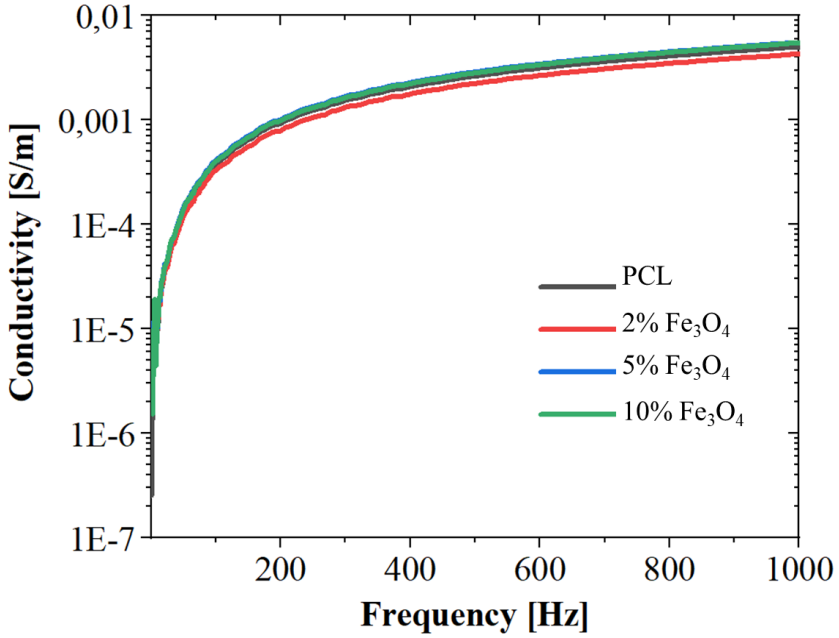

Figure* II.*36. *Electrical Conductivity of electrospun membranes at high pressure*

The electric properties of the PCL blank systems have been explored. By evaluating **Figure II.31** and **Figure II.32**, it is well evident how the electrospinning process has a great influence on the complex permittivity of the systems. The electrospun membrane shows half of the permittivity of the bulk material, whereas the conductivity is about 7-8 times lower at high frequency. The cause is probably the morphology of the membrane: during the electrospinning process, the nanofibers form a tridimensional structure with high porosity, causing a much lower density than the film system. For this reason, the air included among each fiber causes an important decrease of the dielectric permittivity. Because of the importance of the air in the system, it is extremely interesting to analyze the electric behavior of the membranes under different electrode pressures. Comparing the results in ***Figure II.33***-**Figure II.34** and **Figure II.35**-**Figure II.36**, the high-pressure measurements are for all the samples various times higher than the systems evaluated at low pressure. In fact, pressing the materials with a higher force causes compaction of the material: the void degree, reasonably, decreases because of the compaction (that leads to a density increase) and so the dielectric properties and the electric conductivities of the systems increase.

The analyzed systems are now deeply studied to be used in the biomedical field, and it is crucial to understand their behavior in the broad-band chosen, that is voluntarily in the radio-frequency and very close to the microwave analysis. These types of stimuli find now great interest in the scientific community since these electromagnetic radiations can affect the biological behaviour, leading, for example, to cell activations (Pakhomov *et al.*, 2019) or hyperthermia. (Chung *et al.*, 2018)

Focusing on the composite electrospun membranes, by **Figure II.35** and **Figure II.36** it seems that the trends depend on the pressure with which the electrodes have contact with the membranes. As regards the dielectric permittivity, the measurements at maximum pressures report the highest values for the 10% Fe_3O_4 membrane. It is reasonable, since the ε' is strictly related to the polarizability of the system, for this reason, a big amount of magnetite (highly polarizable and with ε' ≈ 20-30 at 1 MHz) can significatively increase the permittivity compared to the blank PCL membrane. (Radoń *et al.*, 2018) Decreasing the number of NPs, the values of dielectric permittivity decrease down to the PCL blank electrospun membranes. For the permittivity measurements at minimum pressure, the trend is quite similar, even if there is a switch in the 2% Fe_3O_4-PCL and the blank PCL membrane position. It suggests the theory for these electrospun systems cannot be considered as binary systems, but as ternary systems because of the big amount of air. At high electrode pressure, the trends are quite predictable, since the lowest amount of air; instead at low pressure, the ternary needs to be deeply characterized to predict the electric properties.

For the electric conductivity, at room temperature and above 0.5 MHz, for the Fe_3O_4 NPs also there would be two types of conduction mechanisms:

electron hopping and the non-overlapping small polaron tunneling. However, it seems that the NPs percentage it is not enough to have the percolation of the material: at maximum pressure, the membranes with 5% and 10% of Fe_3O_4 NPs show about the same values and trend between each other, but the values are quite similar to the blank PCL. The low pressures-analysis confirm the hypothesis of the air-role, for this reason, probably the PCL blank membrane shows the highest conductivity even if loaded with 10% of Fe_3O_4 NPs: the percolation has not been reached, so other phenomena affect the electric properties.

Anticancer Activity

The anticancer activity of the optimized hybrid membranes has been evaluated toward different cell lines: uterine HeLa cells, and A2058 and A375 melanoma cells.

Cell viability assay (Hela cells)

To study the antitumor activity of PCL Membrane containing embedded 5 wt% of functionalized Fe_3O_4 (Fe_3O_4@CA), HeLa cells, estrogen receptor-negative (ER-), were grown in a 24 multiwell plate and treated with increasing concentrations of Fe_3O_4 and PCL Membrane conjugate with 5 wt% of Fe_3O_4@CA, both used at the same concentrations (0.2-0.4-0.6-0.8-1.2 and 1.5 mg/mL). After 72 h, cell viability was investigated by MTT assay using a previously described procedure. (Iacopetta *et al.*, no date) Both the Fe_3O_4 and PCL Membrane conjugate with 5 wt% of Fe_3O_4@CA, manifested a dose-dependent reduction of HeLa cells viability as shown in **Figure II.37**. IC_{50} values, calculated for the HeLa cells (***Table II.11***), showed an increase of PCL Membrane conjugate with 5 wt% of functionalized Fe_3O_4 cytotoxic effect in tumoral cells, which is about 3.8-fold higher than that of Fe_3O_4 by itself (IC50 ¼ 0.4 and 1.86 mg/mL, respectively). Moreover, at the same concentrations and conditions used in this experiment, the PCL membrane alone did not exert any toxic effect on HeLa cells (Figure 35). Parallel experiments using PCL membrane with 2 wt % and 10 wt% of Fe_3O_4@CA were performed, and the calculated IC50 values were identical.

Table II.11. *IC50 values of PCL Membrane, Fe3O4, and PCL Membrane + 5% Fe3O4@CA.*

IC_{50} (mg/mL)	
Compound	HeLa
PCL Membrane	>3
Fe_3O_4	1.86±0.82
PCL Membrane + 5% Fe_3O_4@CA	0.49±0.64

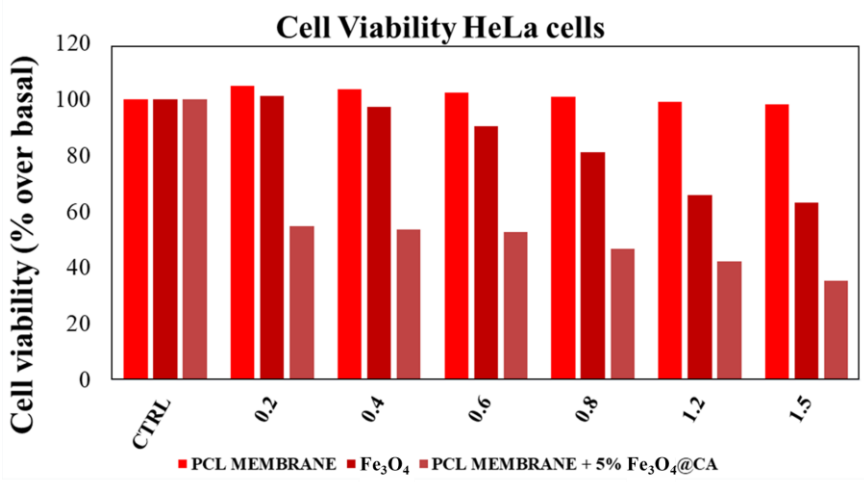

Figure* II.*37*.*** *HeLa cells viability for PCL membranes, Fe_3O_4 and PCL Membrane+5% Fe_3O_4@CA.*

Cell viability assay (A2058 and A375 melanoma cells)

To evaluate the antitumor activity of PCL membrane conjugate with Fe_3O_4, A2058 and A375 melanoma cells were grown in a 24 multiwell plate and treated for 72 h with PCL membrane conjugate with 2 wt%, 5 wt% and 10 wt% of functionalized Fe_3O_4, with Fe_3O_4 by itself used at the same % and with PCL membrane without Fe_3O_4. After 72 h, cell viability was determined by MTT assay. Both Fe_3O_4 and PCL membrane conjugate with Fe_3O_4@CA, exhibited a dose-dependent reduction of A2058 and A375 melanoma cells viability, as shown in **Figure II.38**. Experimental data demonstrated that PCL membranes conjugate with Fe_3O_4 @CA and Fe_3O_4 by itself possess a similar cytotoxic effect in both tumoral cells when they were used at the same percentage for 72 h (at 10% of Fe_3O_4: for A2058, % cell viability ¼ 50.59 and 55.44%, respectively; for A375, % cell viability ¼ 30.15 and 35.83%, respectively). Moreover, at the same concentrations and

conditions used in this experiment, PCL Membrane alone did not exert any cytotoxic effect toward low metastatic A375 melanoma cells (% cell viability ¼ 106.09%), while it exhibited cytotoxicity of approximately 50% against A2058 cell line (**Figure II.38**). The effect of the colloidal suspension of magnetite nanoparticles coated with oleic acid has also been studied on tumor cell lines (SKBR-3 and MCF-7 breast cancer cell lines) (Paunescu *et al.*, 2014). The authors of this last reference hypothesized for the first time a new mechanism inducing tumor cell death under in vitro conditions denucleation. They found that tumor cells develop a network of intracytoplasmic stress fibers, which induce the extrusion of nuclei, and enucleated cells die. Therefore, enucleation may be a potential mechanism of tumor cell death (Paunescu *et al.*, 2014). The anticancer activity of functionalized magnetite nanoparticles seems to be confirmed by many studies. Here, an effective method to vehicular the functionalized nanoparticles in specific areas, through the application of membranes, is highlighted.

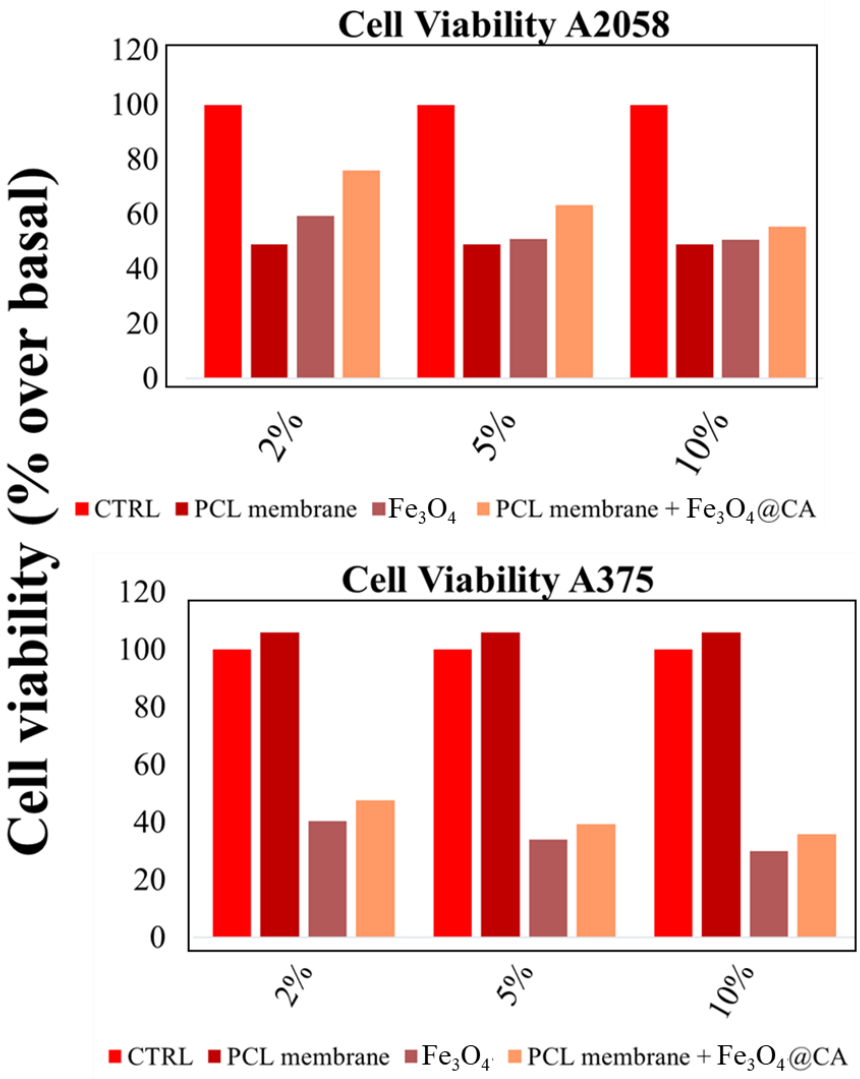

Figure II.38. *Graphs of A2058 (left) and A375 (right) cells viability exposed to vehicle (DMSO), PCL Membrane, Fe_3O_4 by itself and PCL Membrane conjugated with Fe_3O_4@CA*

Chapter Three

Development of complex PCL-Gelatin based electrospun systems

Chapter III
Development of complex PCL-Gelatin based electrospun systems

III.1 Introduction

The combination of synthetic and natural biopolymers can be particularly effective: on the one hand in fact natural polymers can guarantee relevant biocompatibility and, on the other hand, the synthetics can enhance the mechanical properties of the material. (Munj, Lannutti and Tomasko, 2017)
In this study, the electrospinning process is used to produce Gelatin (GN) and PCL membranes in blend and in coaxial systems, to understand how the configuration of the process acts on the thermal, mechanical properties and morphological features of the obtained membranes.
Even if several papers deal with the usability of electrospun membranes based on PCL and GN for biomedical applications (mainly as scaffolds), (Zhang *et al.*, 2005; Gautam, Dinda and Mishra, 2013; Yao *et al.*, 2016b; Coimbra *et al.*, 2017; Adeli-Sardou *et al.*, 2019) rarely thermal and mechanical characterization of these types of membranes have been simultaneously analyzed using different process configuration with the same chemical composition of the blend. Zhang et al. (Zhang *et al.*, 2005) already noticed that GN and PCL electrospun blend (50:50 mass/mass) can have a higher strain at break, up to 138%. On the other hand, Yao et al. (Yao *et al.*, 2016b) proved that PCL/GN blend electrospun membranes in different mass ratio (1:4 to 4:1) have strongly different mechanical properties, with the higher elongation at break reported at 4:1 mass ratio (PCL/GN), that is around 90%, significantly lower than the results reported in our work (349%). This result is most likely due to the fact that SEM images of membranes presented by Yao et al. show fibers with a very wide diameter distribution, which could strongly affect the mechanical properties.(Rashid, Gorga and Krause, 2021)
In particular, in the present chapter PCL-GN based electrospun membranes are produced in blend and in coaxial systems. Firstly, the morphology of the membranes is presented, then the mechanical properties are discussed in light of the thermal investigation of the different membranes, in order to show the mechanical potentialities of blend and coaxial systems explaining the differences mainly through thermal and structural characterization.

III.2 Materials and Methods

Materials

Poly(ε-caprolactone) used for the membrane preparation was provided by Perstorp (Sweden), CAS N° 24980-41-4. It is a linear polyester characterized by a high molecular weight (about 80000 Da) and was provided in the form of pellets (granules with an approximate diameter of 3 mm). GN from Porcine skin type A used for the membrane preparation was provided by Sigma Aldrich (CAS N°9000-70-8). Hexafluoro-isopropanol (HFIP) used for the polymeric solution has been purchased by Apollo Scientific Limited.

Preparation of polymeric solutions for electrospinning

The solutions were prepared by dissolving the polymers in HFIP. The mass percentage of 5% of the polymers in HFIP has been chosen for the formulations containing both components (PCL and GN). A percentage by mass of 6% of PCL has been chosen for the membranes composed of PCL alone. These percentages allow good spinnability and processability of the solutions, that have been kept under stirring at 40 °C for 24 hours just after the preparation to obtain a complete dissolution of the components. In blend systems, PCL-GN (Blend 80:20), and PCL-GN (Blend 60:40) samples, the ratios 80/20 and 60/40 refer to the mass ratio percentage of the two components.
The polymeric solutions have been fed at a flow rate of 1 ml/h to the injector of the electrospinning equipment (EC-CLI by IME Technologies, Spaarpot 147, 5667 KV, Geldrop, Netherlands, injector diameter of 0.8 mm) and have been spun thanks to the electric field in a controlled climate room at 25°C and 35% relative humidity.
In coaxial electrospinning, GN and PCL are spun in parallel using a coaxial injector, that allows for obtaining bilayer nanofibers. For the blend membrane, GN and PCL are solved in the same solution and spun using monoaxial electrospinning. The process parameters have been optimized for obtaining membranes with no-evident defects. The optimized parameters are shown in **Table III.12**.

Table III.12*. Electrospinning Process Parameters*

	Materials	***Concentration/g g^{-1}***	***Injector-Collector Distance/cm***	***Positive and Negative Electrods Voltages/kV***
PCL	PCL	6	25	17/-2
PCL-GN (Blend 80:20)	Blend 80% PCL and 20% GN (in mass)	5	22.5	13/0
PCL-GN (Blend 60:40)	Blend 60% PCL and 40% GN (in mass)	5	22.5	18/0
PCL-GN (Coaxial Core-Shell)	**Core:** PCL	5	24	22/0
	Shell: GN	5		
GN-PCL (Coaxial Core-Shell)	**Core:** GN	5	24.5	20/0
	Shell: PCL	5		
GN	GN	5	24.5	14/0

All the membranes have been kept in vacuum for 24 h after the production to remove any solvent residuals.

Morphological Analysis

The morphological analysis has been performed using scanning electron microscopy (SEM) by which information about the size and the distribution of fibers have been obtained. The electrospun membranes have been metalized using an Agar Automatic Sputter Coater before SEM analysis. A thin layer of Au is deposed on the membrane surface to improve the quality of the morphological acquisitions. The analysis to obtain the fiber size distribution has been done using ImageJ software, whereas the data to obtain the pore diameter distribution using MATLAB software following the procedure reported by Havlíček *et al*. (Havlíček *et al.*, 2020) Distribution curves are normalized so that the area under the histograms is equal to 1.

Thermal Analysis

Thermogravimetric analysis (TGA) has been performed using Mettler Toledo TC-10 thermobalance in air atmosphere (50 ml/min) with 10 °C /min heating rate from 30 to 700 °C.
Differential scanning calorimetry (DSC) has been performed using Mettler Toledo DSC 822e in N_2 atmosphere (50 ml/min) from -50 to 250 °C with 10°C/min heating rate.

Structural Analysis
X-Ray Diffraction (XRD) measurements have been performed using a Bruker D8 Advance diffractometer at 35 kV and 40 mA.

Mechanical Characterization
Mechanical characterization has been performed using Dual ColumnTabletop Testing Systems (INSTRON, series 5967-INSTRON, Norwood, MA, USA) in tensile tests. For each membrane, five samples have been prepared of 1 cm (width) per 5 cm (length) per 0.1 mm (thickness) in ambient conditions. The tensile tests have been performed by lifting at 10 mm/min the beam and acquiring data about force and distance covered. Thus, the data are converted into stress-strain curves.

III.3 Results and Discussion

Morphological Analysis

Since PCL is a hydrophobic polymer and Gelatin is hydrophilic, it is necessary to find solvents that can be suitable to dissolve both the polymers (especially for the blend uniaxial process). Based on literature studies, PCL and Gelatin can be successfully dissolved in fluoroalcohols, (Coimbra *et al.*, 2017; Adeli-Sardou *et al.*, 2019) in particular in Hexafluoro-2-propanol (HFIP). (Yao *et al.*, 2016a) However, to successfully produce coaxial electrospun membranes with a homogeneous morphology, it has been necessary to optimize the process parameters.
In particular, setting the core flow rate (Gelatin solution) at 1 cm^3/h, the shell flow rate (PCL solution) has been varied from 0.5 cm^3/h to 2 cm^3/h under the same environmental conditions, without changing the polymeric solution and applying similar voltages and injection-collector distances.
As reported in
Figure III.39a-b, for low shell flow rate (0.5 cm^3/h) the SEM images show several defects, especially beads, that are uniformly distributed in all the membranes. By increasing the PCL solution flow rate (shell), at 1.0 cm^3/h

the membrane morphology is uniform, and the nanofibers do not present evident defects (
Figure III.39c-d). Interestingly, by further increasing the shell flow rate, the membrane seems homogeneous, but at higher image magnifications it is evident that, along a single fiber, the fiber diameter is not homogeneous. The swelling of the fibers in certain zones is probably due to the high shell flow rate so the core flow rate is not sufficient to be electrospun continuously with the shell. However, as evident in the first case, a low shell flow rate leads to the formation of beads, probably because the Gelatin (core) in that condition needs sufficient external stress to be spun, which can be reached by increasing the shell flow rate. For this reason, the best process condition among the ones considered is the second, in which the core (Gelatin) and the shell (PCL) has equal flow rate.

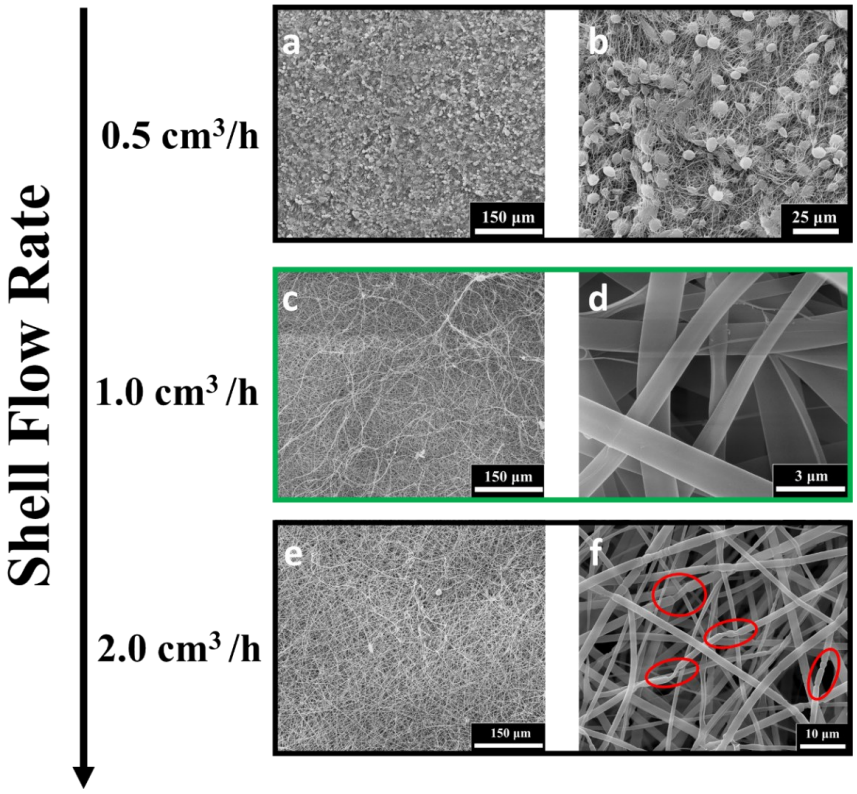

Figure III.39. Optimization of the membrane morphology by varying the shell flow rate

In the present chapter, several blend and coaxial membranes have been produced, comparing their properties to those of PCL and Gelatin. All the obtained membranes have been processed at 25 °C, 35% relative humidity,

at a flow rate of 1 cm^3/h and 5% wt/wt of polymeric solution (except for PCL membrane, in which it has been necessary to use 6% wt/wt of concentration).
SEM images have been acquired for all the membranes to obtain a wide range of information about the morphology. They are reported in **Figure III.40**.

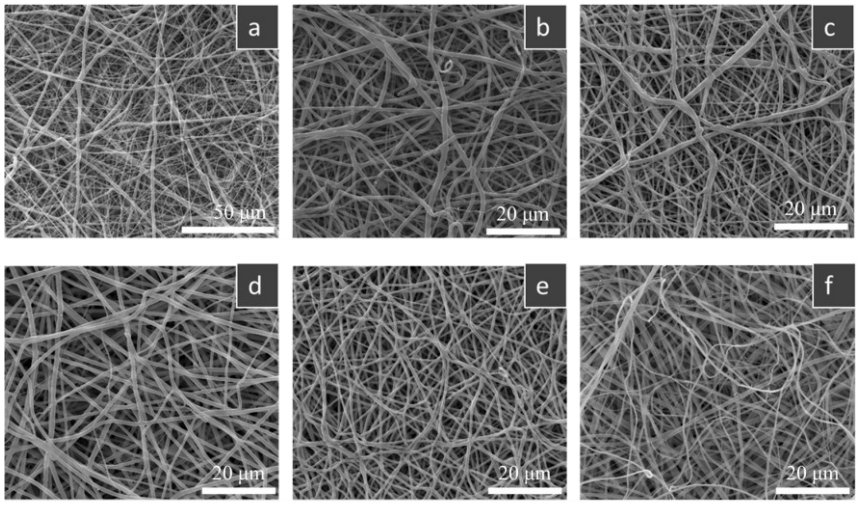

Figure III.40. *SEM images of membranes: a) PCL; b) GN; c) PCL-GN (Blend 80:20); d) PCL-GN (Blend 60:40); e) PCL-GN (Coaxial Core-Shell); f) GN-PCL (Coaxial Core-Shell)*

The morphological parameters of the membranes are reported in **Table III.*13***.

Table I*II.*13. *Fiber and Pore Diameter*

		PCL	***GN***	***PCL-GN Blend (80:20)***	***PCL-GN Blend (60:40)***	***PCL-GN (Coaxial Core:Shell)***	***GN-PCL (Coaxial Core:Shell)***
Fiber Diameter	Mean/µm	0.49	0.79	0.52	0.89	0.65	0.78
Pore Diameter	Mean/µm	1.25	2.47	1.52	2.67	1.62	2.31

Figure III.40. SEM images of membranes: a) PCL; b) GN; c) PCL-GN (Blend 80:20); d) PCL-GN (Blend 60:40); e) PCL-GN (Coaxial Core-Shell); f) GN-PCL (Coaxial Core-Shell) shows a monomodal narrow fiber distribution, as evidenced in **Figure III.41**, for all the membranes with no evident defects, with the formation of a non-oriented mat. The thinnest nanofibers are produced for the PCL (≈490 nm), but however, nano-sizes are

obtained also for the other systems (up to 890 nm). Moreover, the fiber dimension also affects the pore size, as already reported in literature. Generally, an increase in fiber dimensions determines an increase in pore dimensions. (Boland *et al.*, 2005)

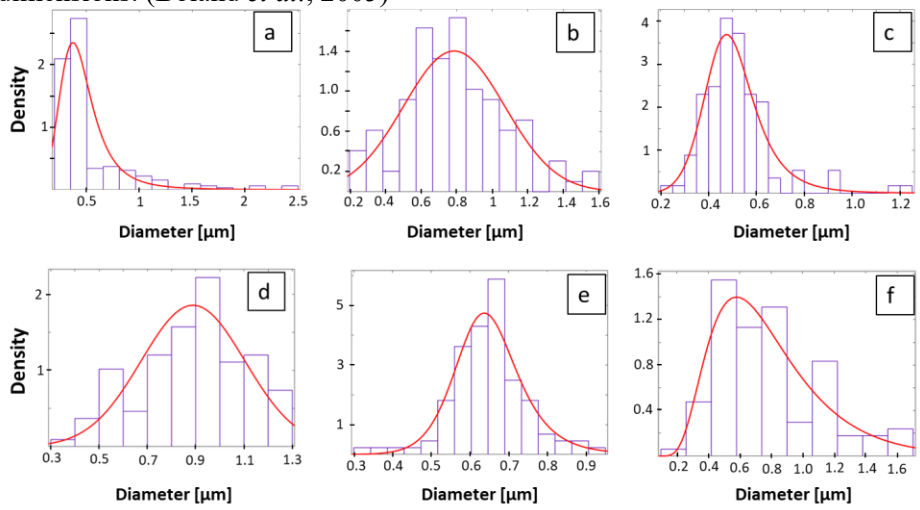

Figure III.41. *Fiber Diameter Distribution of: a) PCL; b) GN; c) PCL-GN (Blend 80:20); d) PCL-GN (Blend 60:40); e) PCL-GN (Coaxial Core-Shell); f) GN-PCL (Coaxial Core-Shell)*

Thermogravimetric Analysis

TGA analysis is reported in **Figure II.42**.

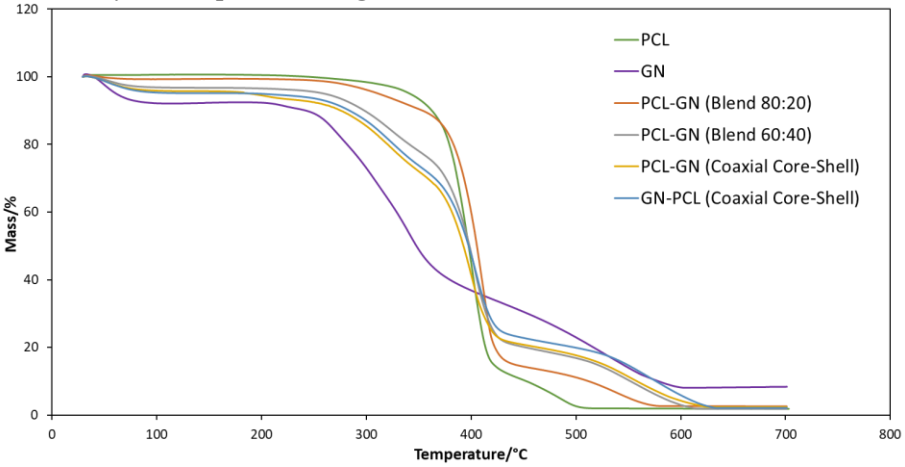

Figure II.42. *Thermogravimetric Analysis*

The derivative TGA of electrospun GN and PCL are reported in **Figure III.43**.

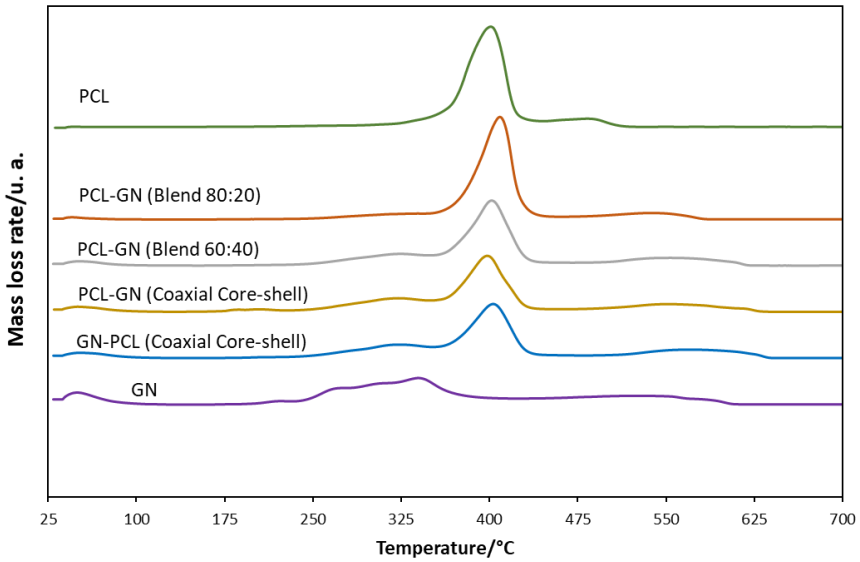

Figure III.43. *Derivative TGA of PCL and GN*

PCL and GN are characterized by different thermal curves. On the one hand, PCL shows two steps of degradation. The first begins around 320 °C and has its maximum rate of mass loss in DTG graph around 400 °C, and is due to the rupture of the ester chains, leading to the formation of H_2O, CO_2, and 5-hexenoic acid. Then, around 450 °C, the second degradation peak leads to depolymerization, producing ε-caprolactone. (Persenaire *et al.*, 2001)
On the other hand, GN mass loss can be divided into three different steps: the first one (up to 100 °C) corresponds to the loss of water; probably due to the water absorption because of the high hydrophilicity of GN. The second one (from 200 °C to 400 °C) is caused by protein degradation, whereas the third one is by the rupture and decomposition of the GN network. (Correia *et al.*, 2013)
As reported in **Figure III.43**, the steps of degradation of GN and PCL are still well visible also for the blend and the coaxial systems. In particular, for the coaxial systems, a visible acceleration especially in the first degradation step is observed. This behavior is most likely due to the occurrence that in the coaxial configuration the GN component is characterized by weaker interactions with PCL component; hence its behavior tends to be more similar to GN alone.

Differential scanning calorimetry

DSC curves are reported in **Figure III.44**.

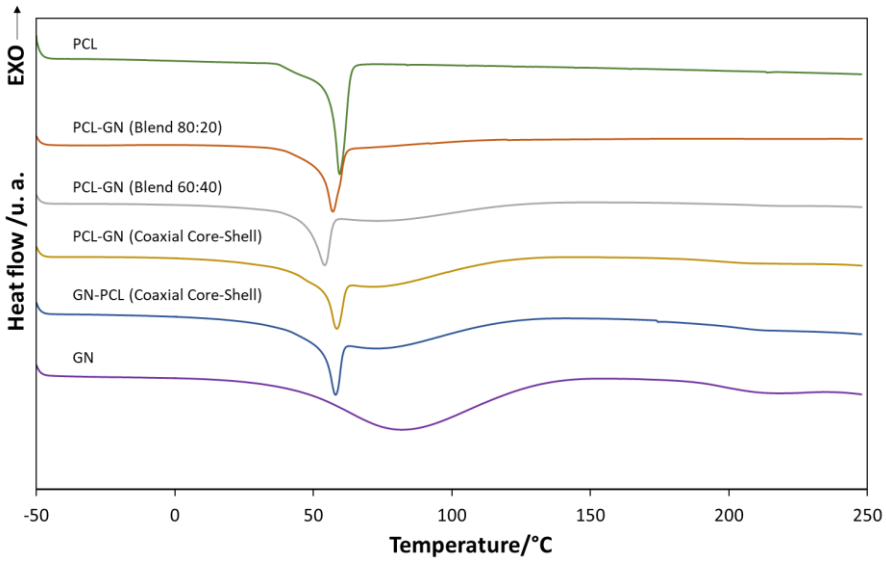

Figure III.44. *DSC of the membranes*

DSC graph of the PCL alone shows the melting point at 59.3 °C, whereas the graph of GN manifests a very wide endothermic peak most likely due to water evaporation during the thermal scanning. This hypothesis is confirmed by the profile of the TGA and DTG curves shown in Figures 3-4. The peak related to water evaporation is present also for the coaxial and blend systems, whereas it is absent for the PCL alone, confirming that water absorption is due to the high GN hydrophilicity, suggesting, as expected, that the more the GN quantity, wider and more relevant is the peak (between 50 °C and 100 °C) after the main melting point of PCL.

The melting peak of the PCL is affected by the presence of GN; it results strongly depending on the configuration process of electrospinning. In fact, different results are observed for coaxial and blend systems. On the one hand, the PCL melting peak is slightly anticipated from 59.3 °C for the pure PCL to 58 °C for both the coaxial systems, whereas the blend systems show higher anticipation of the melting point according to the GN amount. For the system PCL-Blend (80:20), the melting point is detected at 57.0 °C, whereas for PCL-Blend (60:40) at 54.0 °C. The anticipation of the melting point suggests the formation of smaller crystallites that requires lower temperature energy to melt. (Feng and Kamal, 2004)

DSC results are confirmed by XRD analysis, displayed in ***Figure* III.*45***. PCL typical peaks at 21.5° and 23.8° (slightly shifted) are evident in the three diffractometric profiles. They are generated by the 110 and 200 reflections of the orthorhombic PCL crystalline structure. (Baji *et al.*, 2007)
As expected, by increasing GN percentage an increase in the amorphous phase is observed. Furthermore, smaller crystallites size are well-evident by the profile of the diffractometric peaks corresponding to the samples obtained by the blends.
The half-height widening of the 110 and 200 reflections, which is diagnostic of smaller and defective crystals in the membranes from the blends with respect to that from pure PCL is perfectly in line with the calorimetric results which highlight a decrease in the melting temperature of the membranes from blends compared to that obtained from the pure polycaprolactone.

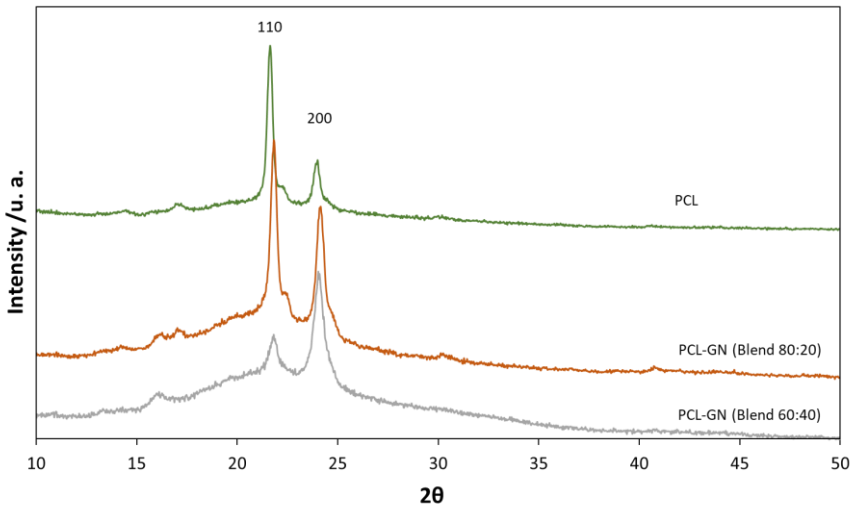

Figure* III.*45. *XRD Spectra of PCL, PCL-(Blend 80:20) and PCL (Blend 60:40) samples*

Mechanical Characterization

The mechanical properties of the membranes have been studied in tensile mode to understand how the composition of the polymeric system and the process configuration affect the tensile properties of the membranes. The stress-strain curves are shown in **Figure III.46**.

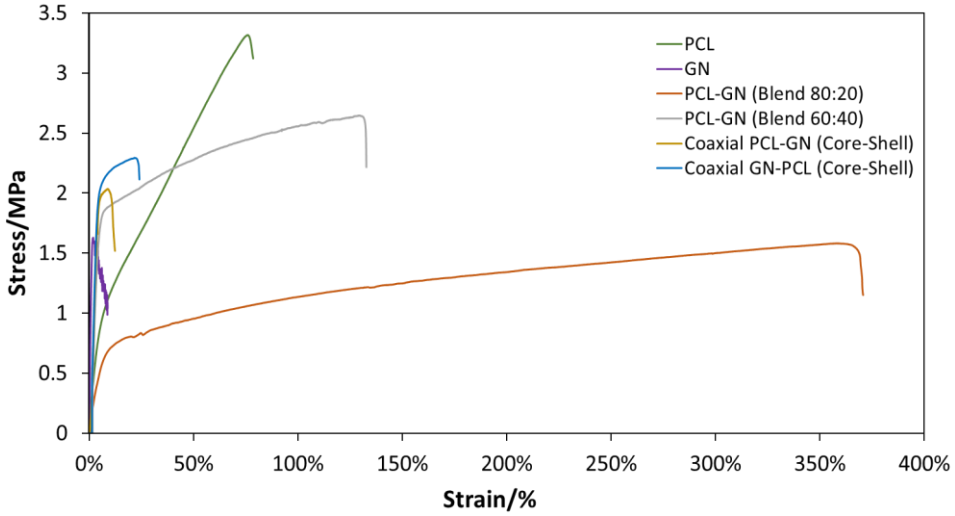

Figure III.46. *Stress-Strain Curves*

The main parameters obtained for the different obtained membranes are displayed in **Table III.14**.

Table III.14*. Mechanical Properties Membranes*

		PCL	***GN***	***PCL-GN Blend (80:20)***	***PCL-GN Blend (60:40)***	***PCL-GN (Coaxial Core:Shell)***	***GN-PCL (Coaxial Core:Shell)***
Young Modulus /MPa	Mean	17.7	111.3	21.3	54.5	47.35	63.3
	Standard Deviation	2.00	22.7	6.59	8.92	5.08	15.4
Strain at yield/ mm mm^{-1}	Mean	3.88	2.34	4.27	2.72	3.71	3.78
	Standard Deviation	0.577	0.733	0.262	0.151	0.353	0.843
Stress at break /MPa	Mean	3.16	1.97	1.99	2.14	1.84	2.3
	Standard Deviation	0.71	0.368	0.272	0.41	0.508	0.32
Strain at break	Mean	78.8	3.15	349.3	112.8	10.95	22.2
	Standard	15.7	0.980	22.8	15.1	1.76	3.78

/mm mm^{-1}	Deviation						

The mechanical behavior of the PCL and GN are strongly different. GN is more elastic and, as expected, shows a lower elongation at break than all other compositions. The coaxial systems, that are formed by bilayer nanofibers, show elastic modulus values between the GN and PCL (111.3 MPa and 17.7 MPa), and therefore higher than the pure PCL.
Concerning the strain at break, with this type of morphological configuration, a very strong reduction is detected with respect to the membranes of PCL alone. For the membrane PCL-GN blends, very good results in the tensile properties are detected, the presence of GN is able to enhance the elastic modulus together with the elongation at break with respect to the pure PCL. This behavior is most likely due to an intimate interaction between GN and PCL. This favorable occurrence seems confirmed in Figure 46 by the anticipation of the melting point of PCL in the blend.
GN determines the formation of smaller crystallites allowing better compatibility between GN and PCL in the amorphous phase. This good compatibility confers to PCL chains better mobility which allows high values of strain. PCL-GN (Blend 80:20) system shows strain at break around 350% with an increase of about 270% with respect to the strain at break of the pure PCL. PCL-GN (Blend 60:40) shows a strain at break around 110% (still higher than pure PCL) because even if the crystallites of PCL are even smaller, the GN amount starts to be very high and causes a diminution of the strain at break of the material.

Chapter Four

Active membranes loaded with synthetic Gold-Complexes for Melanoma Treatment

Chapter IV
Active membranes loaded with synthetic Gold-Complexes for Melanoma Treatment

IV.1 Introduction

Cancer is one of the main diseases of this century (Kaidar-Person, Bar-Sela and Person, 2011). Given the existence of numerous types of tumors, different possible therapies are envisaged, depending on the stage of progress of the pathology (Epstein *et al.*, 2012; De Luna-Bertos *et al.*, 2013; Cricchio *et al.*, 2017).
In the drug delivery field, the need for new more effective therapies has led to scientific progress mainly in two directions: the development of new active molecules and the development of innovative systems for drug administration (Moses, Brem and Langer, 2003; Paunescu *et al.*, 2014; Naves *et al.*, 2017; Faramarzi *et al.*, 2018; Elkhoury *et al.*, 2019; Feng *et al.*, 2019; Zhong *et al.*, 2021).
Combining these two approaches, the present study proposes a highly innovative material with synthetic antitumoral gold-based complexes, developing a cutting-edge wearable patch-like device that shows excellent performance against melanoma.
The use of metal-based molecules for cancer treatment is widely accepted, from cisplatin to titanocene dichloride, and they are generally based to Pt, Au, Ag, Rh, etc. (Desoize, 2004). The complexes selected for this study are based on gold. Gold has been used since ancient times to treat various diseases. The first scientific evidence on the therapeutic efficacy of gold dates back to the 1920s and relates to the compound $K[Au(CN)_2]$, whose antituberculous activity has been clinically tested (Orvig and Abrams, 1999). Currently, Auranofin (1-thio-β-D-glucopyranosatotriethylphosphine gold-2,3,4,6-tetraacetate) is used in the treatment of rheumatoid arthritis and has also been tested in experiments carried out to evaluate its antitumor activity giving important results (Mora, Gimeno and Visbal, 2019). Its target is mainly represented by the mitochondrial enzyme thioredoxin reductase (TrxR) (Gottlieb, 1982). Gold complexes with N-heterocyclic carbene (NHC) ligands can potently inhibit TrxR and decrease tumor cell proliferation (Hindi *et al.*, 2009; Liu and Gust, 2012). Furthermore, they interfere with the metabolism of tubulin and/or actin and therefore play an important role in regulating the dynamics of the cytoskeleton (Muenzner *et*

al., 2016; Fung *et al.*, 2017; Iacopetta *et al.*, 2017, 2020; Magherini *et al.*, 2018). Previously, two NHC-ligated gold-based molecules, namely AuL20 and AuM1 (Figure 1)(Iacopetta *et al.*, 2017, 2020), were identified which showed remarkable antitumor activity. The chemical structure is reported in **Figure IV.47**.

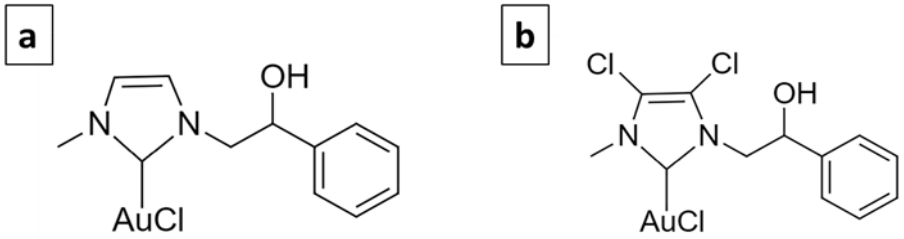

Figure IV.47. *AuL20 (a) and AuM1 (b).*

In the present chapter, the applicability of Au-complexes to promote topical drug delivery has been investigated. Different percentages of the two complexes have been loaded in electrospun polymeric matrices. Membrane's design and production are tailored to make them easily applied for topical treatments, providing an efficient release directly in the zone needing for the treatment.

In particular, electrospun membranes produced have been tested against human malignant melanoma, MeWo cell line, evaluating their cytotoxicity. MeWo represents one of the most aggressive forms of Melanoma tumor; these cells are harvested from a metastatic site in the lymph node tissue. No effective treatment for metastatic melanoma exists, hence currently, an intense effort for new drug evaluation is strongly desirable (Welch *et al.*, 1991).

In the current chapter, PCL electrospun membranes, loaded with different percentages of AuM1 and AuL20, have been produced, and the process conditions are described. The cytotoxicity of the complexes alone (free) and the functionalized membranes have been tested against MeWo cells. By Field Emission Scanning Electron Microscopy (FESEM) and Atomic Force Microscopy (AFM) analyses, the net morphology, the fiber dimensions, and the distribution of the complexes in the nanofibers have been studied. Eventually, the obtained release profiles have been modeled.

IV.2 Materials and Methods

Materials

Poly(ε-caprolactone) (PCL-CAS N° 24980-41-4; Molecular weight 80,000 Da) was purchased by Perstorp (Warrington, UK). Dimethylformamide

(DMF-CAS 68-12-2) was purchased from Sigma Aldrich (Burlington, US). Acetone was purchased from Aldrich Chemical Corporation (St. Louis, US). Chloroform was purchased from Carlo Erba (Cornaredo, Italy). Phosphate buffered saline (PBS) (pH 7.3) was purchased by Oxoid (Basingstoke, UK).
Au-complexes have been prepared according to the procedure reported by Mariconda et al. (Mariconda *et al.*, 2020). AuL20 was obtained using styrene-oxide, which by opening of epoxy-ring, reacts with imidazole giving the monoalkylated product N-methyl, N-[(2-hydoxy-2-phenyl)ethyl]-imidazolium iodide. The second nitrogen atom is methylated using CH_3I, producing the racemic mixture of the salt. It was reacted with silver oxide (Ag_2O) in inert nitrogen atmosphere. In these conditions, the silver oxide deprotonates the cationic carbon giving the corresponding Ag–NHC complex.
The silver complex is reacted with chloro-(dimethylsulfide)-gold(I) [$(CH_3)_2SAuCl$] in dichloromethane. The reaction was left for 1 h at room temperature, then the mixture was filtered, and the solvent was removed in vacuo. The obtained solid AuL20 was characterized by ^{1}H NMR and ^{13}C NMR, mass spectrometry, and elemental analysis. The same procedure was applied in the synthesis of AuM1 using 4,5-dichloroimidazole instead of imidazole. Both complexes were obtained in the form of solid powders. The complete analysis (^{1}H NMR, ^{13}C NMR, ESI-MS, CHN) of the synthesized complexes is provided in the section "Supplementary Materials (S.M.)".
The analysis of the hydrolytic stability of the complexes, carried out at 40 ° C in an aqueous solution of DMSO-d6 at 10% on these complexes, by means of ^{1}H NMR spectroscopy, demonstrated that these complexes are particularly stable. In fact, their spectra recorded after 24 h are practically identical to those recorded at zero time (an amount of more than 97% of complexes results not hydrolyzed). This ensures that the NHC ligands are ancillary ligands and therefore stably bound to the metal centers (Iacopetta *et al.*, 2020).

.*Preparation of solutions for electrospinning membrane*

PCL pellets have been added to Acetone/DMF mixture (3:1 in volume) at 11 wt%. Different amounts of complexes AuL20 and AuM1 have been added in the PCL solution: 0%, 1% and 3% by weight of active complex obtaining the samples named with the acronyms PCL, 1%AuL20, 3%AuL20, 1% AuM1 and 3%AuM1. The solutions were kept under magnetic stirring at 40 °C for 24 h to obtain homogeneous solutions.

Electrospinning procedure

The polymeric solutions have been electrospun by climate-controlled electrospinning equipment (EC-CLI by IME Technologies, Spaarpot 147,

5667 KV, Geldrop, Netherlands). Each solution has been loaded in a syringe of 5 ml and fed to a 0.8 mm diameter needle connected to a power supply. The flow was ejected by the needle in the climate room in presence of a strong electric field that allows the spinning of the polymer. It has been necessary to vary the process conditions among the various membranes depending on the spinnability of the solution, however, the room conditions have been set at a temperature of 25 °C and the relative humidity at 35%. The other process parameters are reported in **Table IV.15** for all the prepared and tested membranes. It is worth noting that samples loaded with a higher percentage of complexes required higher values of the Electrical Potential difference to obtain membranes with a good distribution of the morphological parameters, as discussed in the section "Morphological and structural characterization". **Table IV.15** shows only the electrospinning parameters employed for the membranes optimized from the point of view of the electrospinning process and subsequently tested for evaluating the anticancer effectiveness.

Table IV.15. *Process Parameters*

Sample (Acronym)	**Flow Rate [ml/h]**	**Distance Injector-Collector [cm]**	**Electric Potential Difference [kV]**	**Active Complex**
PCL	2.0	28.5	21.0	0%
1%AuL20	2.0	22.5	25.0	1% of AuL20
3%AuL20	0.8	22.5	22.6	3% of AuL20
1%AuM1	1.0	25.0	24.0	1% of AuM1
3%AuM1	1.0	25.0	25.0	3% of AuM1

Sample preparation and Sterilization protocol

Free metallic complexes were solubilized in dimethyl sulfoxide (DMSO) and diluted in Dulbecco′s Modified Eagle′s Medium (DMEM) high glucose (GIBCO, Invitrogen) at a final concentration of 1, 5, 10, 20 μM, for cell treatments.

For adhesion culture, not functionalized and functionalized PCL membranes were cut to obtain a cycle shape of 15 mm in diameter and then, dipped in 70% ethanol and washed twice in sterile PBS 1X. Samples were dried for 24h under a laminar flow cabinet.

Silicon rings were cut using a hollow cutter (outer diameter: 14mm; inner diameter: 11mm) and sterilized in 70% ethanol. After ethanol evaporation, silicon rings were stuck on PCL membranes using non-corrosive silicon rubber and living them dry overnight. Samples were dipped in 70% ethanol, exposed to UV rays for 5 minutes on both sides, and then used for cell seeding.

Cell culture in adhesion

To test the cytotoxicity of free metallic complexes, MeWo (ATCC®, HTB-65TM; P22) were seeded in 96-well plates at a density of 100.000 cells/mL. Cells were cultured in DMEM high glucose (GIBCO, Invitrogen) containing 10% Fetal Bovine Serum (Gibco™, Walthan, Massachusetts, United States), 1% Penicillin/Streptomycin (Corning, Manassas, VA, United States) and 1% Glutagro™ (Corning, Manassas, VA, United States) at 37 °C in a 5% CO_2 atmosphere. After 24h, different concentrations of each complex (1, 5, 10, 20 µM) were added to respective wells and incubated for 24h and 48h.
To test the cytotoxicity of functionalized PCL membranes, MeWo (ATCC®, HTB-65™; P27) were seeded within silicon rings on PCL membranes, to prevent cells flushing from the membrane area, at a density of 30.000 cells/cm^2. Samples were cultured in DMEM high glucose (GIBCO, Invitrogen) supplemented with 10% Fetal Bovine Serum (Gibco™, Walthan, Massachusetts, United States), 1% Penicillin/Streptomycin (Corning, Manassas, VA, United States) and 1% Glutagro™ (Corning, Manassas, VA, United States) at 37 °C in a 5% CO_2 atmosphere (Ciardulli *et al.*, 2021; Lamparelli *et al.*, 2021; Palazzo *et al.*, 2021).

Cell Viability assay

For suspension culture, after 24h and 48h, 0.5 mg/ml of 3-(4,5-Dimethylthiazol-2-yl)-2,5-diphenyl-tetrazolium bromide (MTT) was directly added in the culture medium and incubated for 4h, protecting the plate from the light. Then the supernatant was removed and 100 µL of 100% DMSO was added to solubilize formazan crystals.
The absorbance was measured at 490 nm using a microplate reader (Infinite F200 PRO, Tecan Group Ltd., SW). Cell viability was calculated as the percentage of the control group, considered as 100%. The percentage viability of cells was calculated according to equation (11):

$$\%Cell\ viability = \frac{Abs\ of\ sample - Abs\ blank}{Abs\ of\ control - Abs\ blank} * 100 \qquad (11)$$

Time-lapse Live-Cell Imaging System assay

Specific MeWo culture was performed using a Time-lapse Live-Cell Imaging System formed by a Bold Line Top Stage Incubator for 35 mm Petri dishes (H301-T UNIT BL; Okolab S.r.l., Italy), which allows the acquisition of the same images along the culture time in fixed culture point mapped by the fully-automated stage. The incubator has independent control of gas (CO_2/O_2), humidity, and temperature and assures an environment with 37°C of temperature and 5% of CO_2 atmosphere. The system allows acquisition in brightfield and fluorescence. All images of different points within the culture

chamber were reached automatically, using Olympus IX83 time-lapse microscope by motorized stage and CCD monochrome camera (mod. XM10, Olympus), and with all operations under the control of the X-Excellence advanced live-cell imaging software (rel. 2.0, Olympus Inc., DE). Cells' images were captured in brightfield using a 10X objective every 4-hour intervals along the 48 h of culture, further details on cells characterization were reported elsewhere (Scala *et al.*, 2022). The related videos reported in additional data were generated with windows movie maker software (version 2.0, Microsoft) starting from the acquired frames.

Statistical analysis

Results from multiple experiments are presented as mean ± standard deviation (SD). Statistical analysis was performed using the two-tailed independent Student's T-test for comparisons of two independent groups. P values less than 0.05 were accepted as significant (Winter, 2019). All statistical analysis was conducted using GraphPad Prism software (6.0 for Windows).

Morphology Analysis

Morphological analysis has been performed by using Field emission scanning electron microscopy (FESEM). The samples have been coated with a thin gold layer before the FESEM analysis. By the acquired images, geometrical information and the size distribution of the nanofibers have been obtained. The analysis of the fiber distribution has been performed by using ImageJ, considering at least 150 fibers. The analysis of the pore size has been performed by using the software MATLAB (Natick, USA) following the procedure reported in literature (Gorrasi, Longo and Viscusi, 2020; Havlíček *et al.*, 2020). The images were collected with a FESEMLEO1550VP microscope (Oberkochen, Germany).

For Energy Dispersive X-ray Analysis (EDX) investigation, a FESEM LEO1525 microscope (Oberkochen, Germany) equipped with an EDX detector has been used. EDX maps were obtained after sputtering the samples with a thin coating of chromium. This investigation has been performed for AuM1-loaded membranes.

Moreover, Atomic Force Microscopy (AFM) has been performed to better characterize the morphology of the samples. AFM is a technique able to recreate a topographic map of the sample surface by exploiting the interactions between the tip and the sample surface. By acquiring information on the deflection of the cantilever through a laser, it is possible to obtain morphology accurate data on the surface of the sample. In this case, Bruker NanoScope V multimode AFM (Digital Instruments, Santa Barbara, CA, USA) has been used, in tapping mode and ambient atmosphere. The tip used has a nominal spring constant of 20-100 N/m, resonance frequencies of

200-400 kHz, and a tip radius of 5-10 nm. This investigation has been performed both for blank PCL and AuM1-loaded membranes. The height profiles along the fibers have been acquired using NanoScope Analysis 1.40 Software (Bruker Corporation, Billerica, USA), and have been elaborated via OriginPro software (OriginLab Corporation, Northampton, USA) to consider the height profile without being affected by the fiber slope in the chosen region. The data elaboration is displayed in **Figure IV.48**.

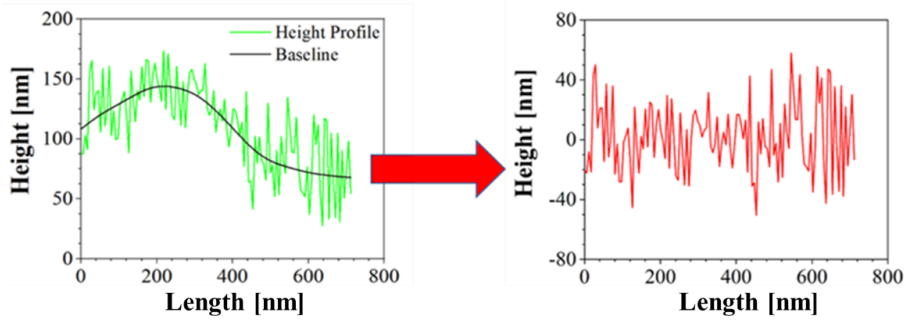

Figure IV.48. *Correction of Height profile for roughness evaluation*

In this way, the average surface roughness (R_a) and the root mean square roughness parameter (R_q) have been evaluated for the various membranes, according to (12) and (13):

$$R_a = \frac{1}{l_r}\int_0^{l_r} |z(x)| * dx \qquad (12)$$

$$R_q = \sqrt{\frac{1}{l_r}\int_0^{l_r} z(x)^2 dx} \qquad (13)$$

where l_r is the length of the line, z is the height and x is the position.

2.10. Structural Characterization

Structural characterization of electrospun membranes has been performed by X-Ray Diffraction (XRD) measurements using the diffractometer Bruker D8 Advance diffractometer (Bruker Corporation, Billerica, US) operating at 35 kV and 40 mA. The analysis has been performed in an angle range (2θ) of 10-80°. The spectra presented in the section of the "Results" are shown between 15-35° because the curves are flat out of this range. This investigation has been performed both for blank PCL and AuM1-loaded membranes.

Crystallite sizes have been determined using Scherrer equation (14):

$$\tau = K * \frac{\lambda}{\beta * \cos(\theta)} \qquad (14)$$

Where τ is the mean size of the crystallite, λ is the wavelength of the x-ray source (0.1542 nm), β is the width of the peak at half maximum intensity,

whereas θ is the diffraction angle. The data have been analysed with the same methodology reported by Naddeo et al. (Naddeo *et al.*, 2017).
The crystallinity of the sample has been obtained according to Sownthari et al. (Sownthari and Suthanthiraraj, 2013) by deconvoluting the spectra and considering the crystalline and the amorphous areas under the diffractometric curve profile, according to equation (15):

$$X_c = \frac{A_{crystalline}}{A_{crystalline} + A_{amorphous}} \qquad (15)$$

Release Profiles

Samples of membranes of 1 cm diameter have been placed in PBS and stirred at 300 rpm in an orbital shaker. The release medium was taken at a fixed time and then replaced with fresh PBS. Drug release kinetics have been monitored by using a Spectrometer UV-2401 PC (Shimadzu, Japan). The tests were performed using rectangular plates with an exposed area of about 3 cm^2 and 1 cm of the light path.
Considering the chemical structure of AuM1 and AuL20, the phenyl group has been tracked in the release medium to monitor drug release. However, it is known that benzene absorbs UV radiation causing a $\pi \rightarrow \pi^*$at 180 nm, 203.5 nm and 254 nm. (Romand and Vodar, 1951; Pavia *et al.*, 2015) In this case 254 nm peak has been monitored for 5 days. By tracking the absorbance of phenyl group of known quantities of AuM1 and AuL20, calibration curves have been that are well described by Lambert-Beer equation (16).

$$A=\varepsilon \cdot c \cdot l \qquad (16)$$

where A is the absorbance, ε is the absorptivity of the complex., c is the concentration of the solution and l is the light path length.
In **Table IV.16** are reported the ε values for the complexes.

Table IV.16. *Molar Absorptivity Coefficient of Complexes*

#	ε **[mL*mol^{-1}*cm^{-1}]**
AuL20	8.91
AuM1	4.98

The peak monitored for AuL20 is slightly shifted from 254 nm (typical peak of the phenyl group) to 260 nm; whereas the peak value of AuM1 complex is detected around the expected value (252 nm). The spectra are reported in **Figure IV.49**.

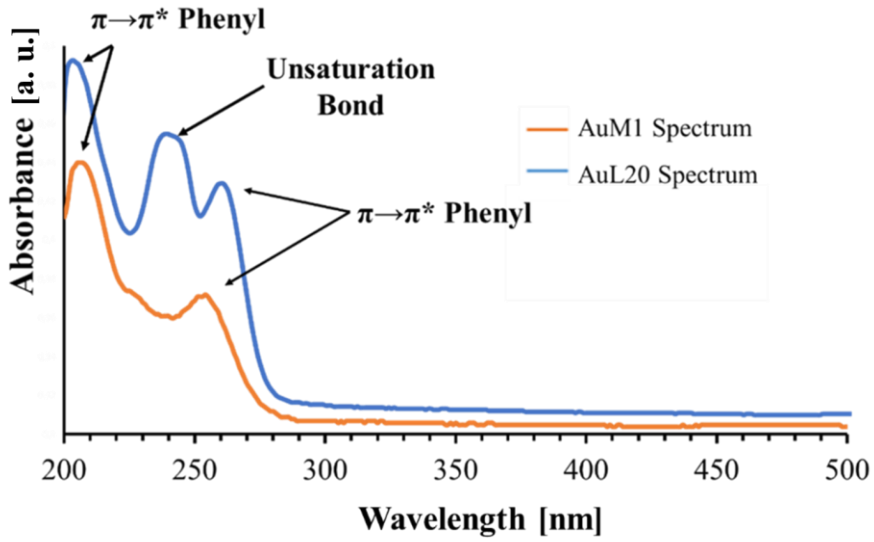

Figure IV.49. *Spectra of AuM1 and AuL20.*

Observing the spectra, π→π* transitions around 254 nm and around 200 nm caused by phenyl are evident for both complexes dissolved in the solution. However, for AuL20 a third peak is registered around 240 nm. Since AuM1 shows the presence of two chlorines on the backbone compared to AuL20 chemical structure, it is reasonable that Cl atoms attract electronic density given its high electronegativity, decreasing and shifting the intensity of the π→π* transition of the electrons involved in the double bond of the two carbonium (see the shoulder at 226 nm visible in AuM1 spectrum).
In AuL20, where there are two hydrogens instead of Cl, the transition is allowed and it is so evident in the spectrum. π→π* double bond transition in literature can be found in very different ranges of the UV-vis spectrum, from 184 nm for ethylene to over 400 nm for molecules such as β-carotene (Pavia *et al.*, 2015).
For release profiles fitting, a statistical approach has been followed by using a modified Weibull model (17) recently proposed in literature (Gorrasi, Longo and Viscusi, 2020):

$$\frac{m}{m_0} = \theta * [1 - \exp\left(-\frac{1}{A_1} * t^{b_1}\right)] + (1-\theta) * [1 - \exp\left(-\frac{1}{A_2} * t^{b_2}\right)] \qquad (17)$$

where m is the substance amount released at a certain time, m_0 is the total substance amount in the sample (evaluated by weighting the sample and knowing the complex percentage in the membrane), A_1, A_2, b_1, b_2 and θ are kinetic constant parameters, t is the time.
In general, the two parts of the model can describe two contributes, that are usually considered the Case II transport and the Fickian Diffusion, in

agreement with other variations of the Weibull Model (Papadopoulou *et al.*, 2006). In particular, θ defines which mechanism is more relevant, whereas A_1 , A_2, b_1 and b_2 define the kinetic of each mechanism.
Moreover, the first-order kinetic and Ritger-Peppas models have been used together to explain the mechanisms that control the release behaviour following the approach of Wu et al. (Wu *et al.*, 2020). The models used are reported below in Equation (18) and (19):

$$\frac{m}{m_0} = 1 - exp\ (-a * t) \quad (8)$$

$$\frac{m}{m_0} = k * t^n \quad (9)$$

Where a and k are kinetic constants and n is a descriptive parameter of the diffusive release.(Zhan *et al.*, 2019)

IV.3 Results and Discussion

Anticancer activity of complexes and functionalized membranes.

Viability data on free metallic complexes

Before testing the PCL membranes, the cell viability was assessed using the MeWo cell line cultured with different concentrations of the free metallic complexes. From the reported histograms (see **Figure IV.50**), it emerged that the two complexes are able to significantly reduce cell viability. Of note, the highest tested concentration of complexes (20 µM) was the most effective in inducing cell mortality. Moreover, AuM1 complex showed the best dose and time-dependent effect, suggesting it could be considered the most promising antiproliferative compound for these cells. Concerning the 10 µM concentration of AuL20, we found an apparent increase in cell viability at 24h that could be due to a possible interaction with some receptors involved in cell proliferation, even if the data showed an extremely large standard deviation and were not statistically significant. Furthermore, these results were not corroborated by a similar trend at 48h of 10µM treatment suggesting that it may be only a transient and not significant effect. On the other hand, the cell viability inhibition is particularly evident after 48h for the concentration of 20 µM for both complexes that significantly reduced cell viability. Particularly, the complex AuM1 resulted in the most effective with a specific dose-response trend and also seemed to be characterized by an excellent selectivity with respect to non-tumoral cell lines. Detailed data on this aspect will be published in a forthcoming paper currently in preparation.

These results suggest that metallic complexes, such as AuM1, could be particularly interesting for further investigation in the fight against these aggressive melanomas, especially considering the fact that they have

displayed a significantly higher cytotoxic activity than chemotherapic commonly used for melanoma treatments, such as Dacarbazine (not reported here).

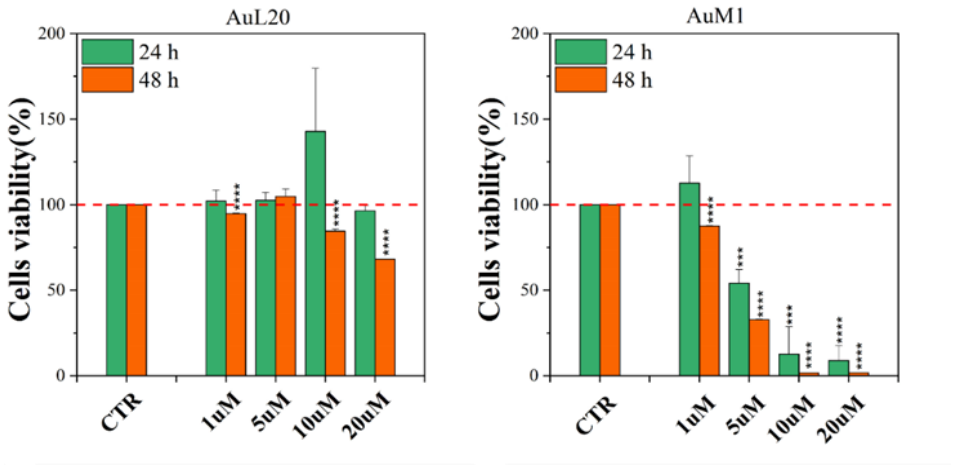

Figure IV.50. *Cell viability of MeWo cells treated with different concentrations of each metallic complex for 24 and 48h by the MTT assay. The experiments were analyzed by two-tailed Student's t-test, * $p \leq 0.05$, ** $p < 0.01$, *** $p < 0.001$ and **** $p \leq 0.0001$.*

To further investigate the effective activity of both complex and to understand if there was a time-dependence on their activity, it was performed a culture on an incubator under a camera acquiring time-lapse frames of the specific and previously fixed areas of culture and related videos were collected. Time-lapse cell imaging protocol was adopted to monitor the time necessary for cells to die when treated with 20μM of each metallic complex. The time-lapse images acquired are reported in **Figure IV.51**. The time-lapse videos are reported in the additional data section on the paper site.

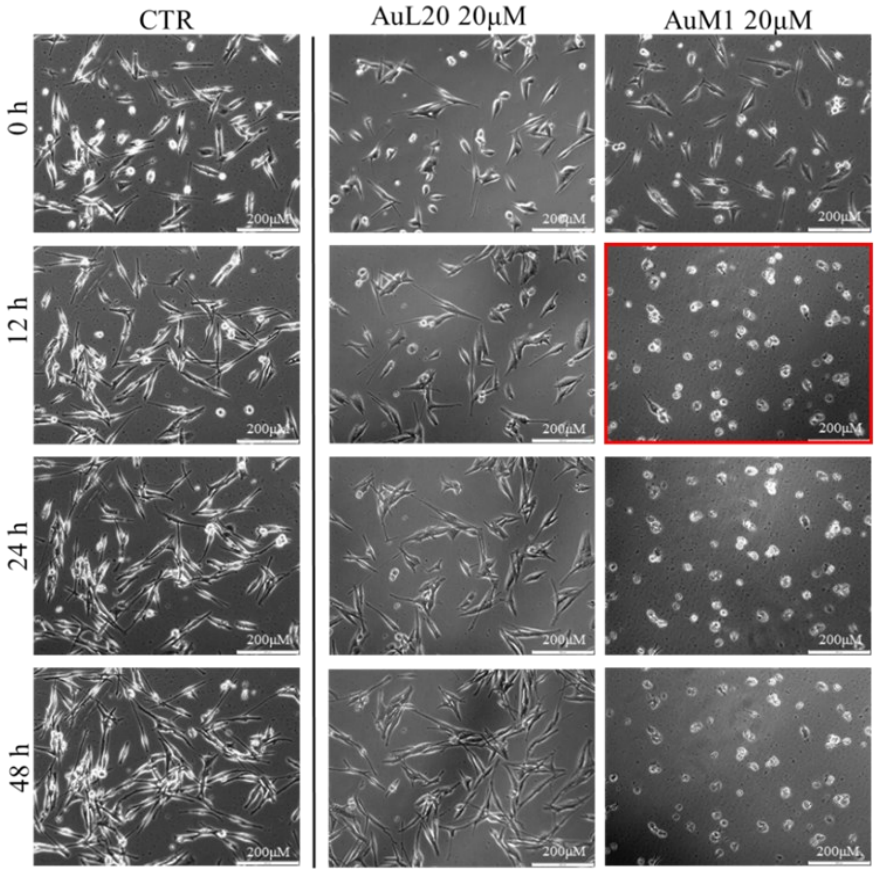

Figure IV.51. *Cell viability of MeWo cells treated with 20 µM of each metallic complex for 48h of cells monitored by Time-lapse Live-Cell Imaging System assay.*

Time-lapse acquisitions confirmed that the AuM1 complex was the fastest and the most active complex in inhibiting cells survival. Indeed, just after 12h, apoptosis occurred, as evidenced by the shape of cells that suddenly changed into a spherical structure (see panel highlighted in red in **Figure IV.51**).

Viability data of functionalized membranes

The membrane experiments turned out to be more complicated than expected. Indeed, preliminary cultures were performed with membranes of 200 µm of thickness and loaded with 1% of AuM1 complexes using the selected MeWo cells adhered to the conventional flask. However, simply inserting the membrane samples within the culture with adherent cells was not successful. Indeed, several membrane samples precipitated on the bottom of each well (see **Figure IV.52**) preventing almost all cells survival but that

was found mainly attributable to the limited gases exchanges (mainly oxygen) and not properly to the presence of complexes incorporated in the membrane fibers. Indeed, also PCL membranes, without complexes, showed high toxicity (data not shown here). Therefore, the results of this first adopted methodology have been considered unreliable data. However, because the functionalized membranes were designed to be used as patches for topical application on solid tumors, MeWo cell line was still considered the best option to be tested. Therefore, a new methodology was adopted by seeding the cells directly on the membrane surface thanks to a silicone ring in order to avoid cells flushing out from the membrane to the bottom of the well plate, as illustrated in **Figure IV.52**. Adopting this methodology, statistically significant data were collected due to proper metabolites and oxygen exchanges as well as prevention of cells losses; therefore, the reduced vitality was considered only due to the membrane toxicity.

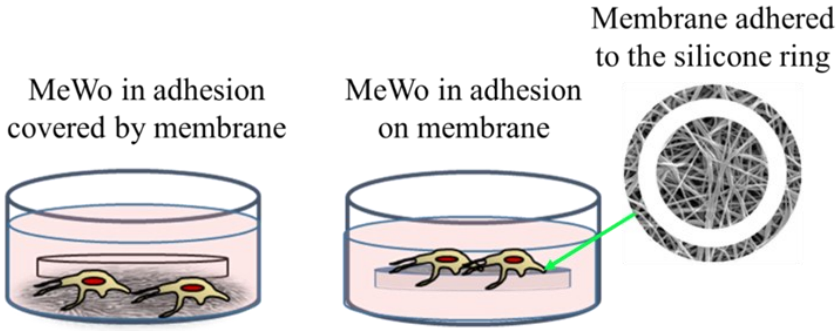

Figure IV.52. *Cells culture and membrane: options tested.*

Complexes-filled PCL membranes at concentrations of 1% and 3% were tested, and the resulting viability data are shown in **Figure IV.53.** All membranes functionalized with the complexes were able to decrease cell viability, both at 24 and 48 h of culture, in comparison to not functionalized membranes (CTR sample). As concern 1% functionalized PCL membranes, cell viability exhibited a reduction of about 50%; whereas the cytotoxic effect was found stronger when PCL membranes were functionalized with 3% of metallic complexes, where the percentage is mainly lower than 50%. Among the two tested complexes, AuM1 was found the most promising and statistically significant compound in reducing cell viability up to 40% when loaded at 3% within PCL membranes, in agreement with the results of the tests performed using the free complexes, which also manifest a dose-dependent cytotoxic behaviour against MeWo cells. All data also suggested that the complexes loaded in the membrane were suddenly released in order to reach the proper cytotoxic concentrations required to promote cells apoptosis. However, further indications on complex release profiles were shown and discussed in the following paragraph.

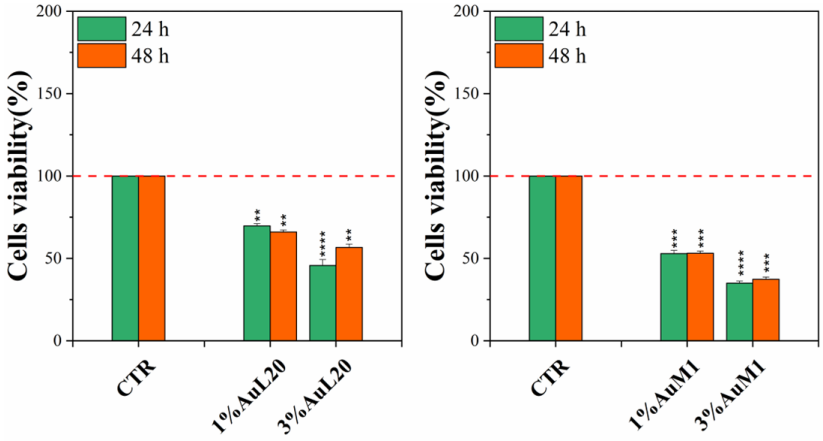

Figure IV.53. *MTT assay on MeWo cells when cultured on 1% and 3% functionalized PCL membranes surface for 24h and 48h. The experiments were analyzed by two-tailed Student's t-test, * $p \leq 0.05$, ** $p < 0.01$, *** $p < 0.001$ and **** $p \leq 0.0001$.*

The same tests performed with the membranes loaded with the complexes have been carried out using unloaded membranes to test the effect of the PCL alone on the viability of the cells. The results are shown in Figure S6 of the section "S.M.". It is well evident that no cytotoxic effect is observed. Actually, after 48 h, the peculiar morphology of the membrane seems even to favor the growth of the tumoral cells, as expected.

Morphological and structural characterization of membranes

Morphological characterization

The membranes tested to evaluate the action on the proliferation of MeWo cells were deeply analyzed from the morphological and structural points of view. FESEM images of all tested membranes are shown in **Figure IV.54**, where continuous fibers without visible defects (broken fibers, debris, etc.) are well evident.

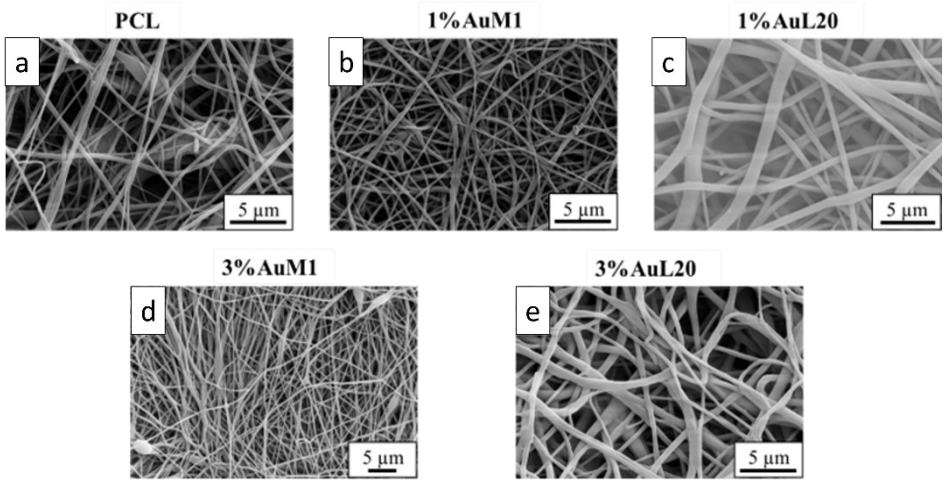

Figure IV.54. *FESEM of the membranes: a) PCL; b) 1%AuM1; c) 1%AuL20; d) 3% AuM1; e) 3%AuL20*

All the membranes show an average fiber diameter below 1 µm, as confirmed by the fiber diameter distribution in **Figure IV.55**. Although quite homogeneous membranes were obtained, **Figure IV.55** highlights a slight dependence of the dimensional distribution of the fibers on the load and nature of the complex, most likely mainly due to the different parameters set for the electrospinning process.

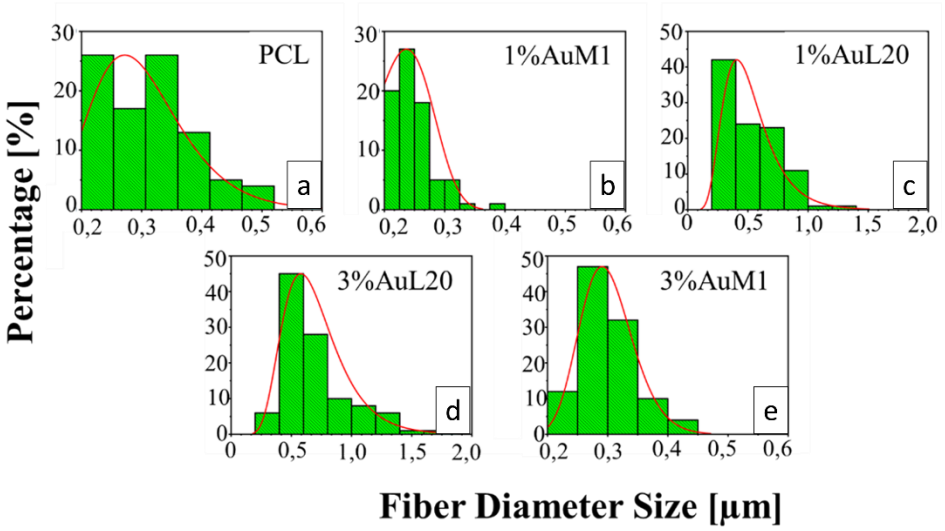

Figure IV.55. *Fiber diameter distribution of: a) PCL; b) 1%AuM1; c) 1%AuL20; d) 3%AuL20; e) 3%AuM1*

The average fibers' diameter falls between 200 and 700 nm, showing monomodal distribution. Moreover, for PCL, 1% AuM1, 3%AuM1 a narrow fiber distribution is evident, with an average fiber diameter below 300 nm. By MATLAB processing of the images, the pore size distribution has been acquired. The results are briefly presented in **Table IV.17**.

Table IV.17. *Pore Size Distribution Parameters*

		PCL	1%Au M1	1%Au L20	3%Au M1	3%Au L20
Pore Diameter	**Mean [µm]**	1.16	0.99	2.59	1.22	2.17
	Standard Deviation [µm]	0.71	0.41	1.30	0.60	1.34

Coherently with literature, higher fiber dimensions induce higher pore sizes (Eichhorn and Sampson, 2005; Ameer, Anil Kumar and Kasoju, 2019).

Given the higher antitumoral efficiency shown by AuM1-membranes, a further morphological analysis was performed to investigate the distribution of the AuM1 complex and its location in the fiber membranes. By EDX analysis, the distribution of Au-complexes was investigated tracking Au and Cl on the membrane surface. The images of EDX analysis with Au and Cl tracked are shown in **Figure IV.56**.

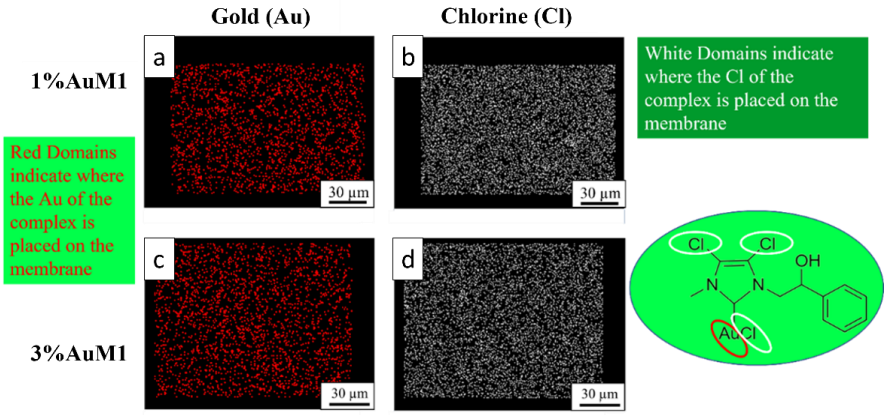

Figure IV.56. *EDX images of 1%AuM1 and 3%AuM1 samples of Gold (a, c) and Chlorine (b, c) respectively. Images a and b refer to samples with 1% of the complex, whereas c and d to samples with 3% of complex.*

Small molecular aggregates of Au-complexes (red zones) are well distributed on the entire surface of the membranes, proving that the electrospinning process is a valid choice to integrate synthesized complexes in patch-like structures ensuring a good distribution along the nanofibers of the mat membrane. Chlorine response is denser than Au since AuM1

structure is based on three atoms of Cl and one of Au. As expected, the tracing of the chlorine leads to the same conclusions about the distribution of the complex in the fibers.

Moreover, height AFM images, shown in Figure 11, evidence that a large amount of the complex aggregates is segregated on the nanofiber surface along the fibers, forming very small aggregates externally attached to the PCL nanofibers.

This phenomenon likely shows that the complexes are loaded above the solubility limit in the polymer. As reported by Natu *et al.* (Natu, de Sousa and Gil, 2010), in these cases the drugs crystallize on the surface of the nanofibers, causing a relevant burst effect. The low solubility of AuM1 in PCL is probably due to the hydrophilicity of the complexes (-OH group in the chemical structure), whereas PCL is hydrophobic, being a polyester.

The small aggregates of complexes on the surface of the wall along the fibers are also well-evidenced by the rugosity of the wall, highlighted through height variations along 3 lines parallel to the axis fibers for each sample (see **Figure IV.57**).

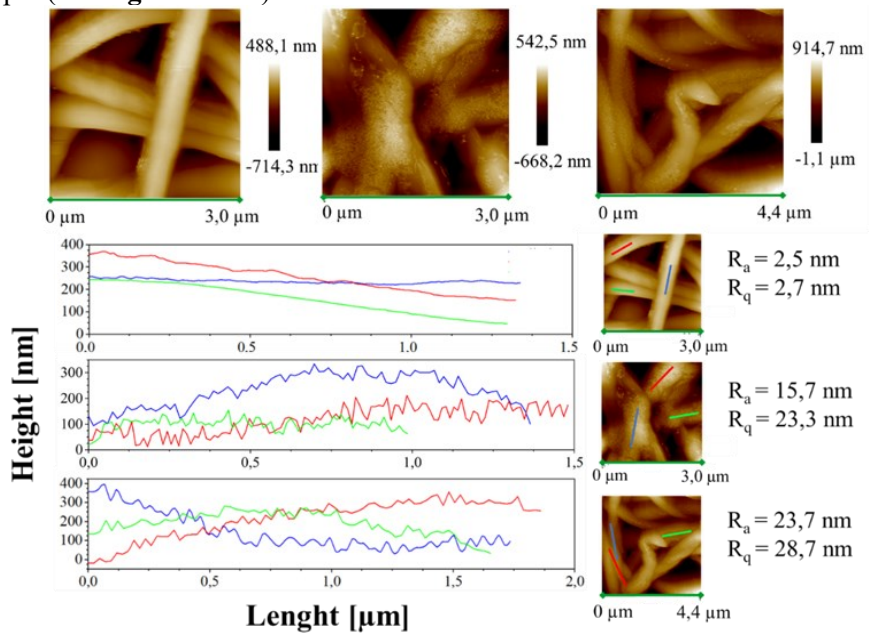

Figure IV.57. *Height AFM images and profiles of the height variations along the lines parallel to the axis fibers for the samples PCL, 1%AuM1 and 3% AuM1.*

Analysing the height profile along the nanofiber surface in PCL sample (see Figure 11) it is evident how the height profile is smooth, with R_a and R_q values quite similar, confirming a very small roughness and the presence of very low peaks and valleys on the surface. In Figure 11, 1%AuM1 and 3%

AuM1 height profiles become knurled, due to the presence of the complex aggregates, which causes an increase in the R_a and R_q. However, by the analysis of the local depth of the roughness, regardless of the concentration of the complex, the aggregates were found to have approximately the same size (30-70 nm).

Structural characterization of the membranes

Figure IV.58 shows the XRD spectra of the unfunctionalized PCL membrane (**Figure IV.58**a) and 1% AuM1 (**Figure IV.58**b) and 3% AuM1 (**Figure IV.58**c) functionalized membranes. All analyzed membranes exhibit 2 intense peaks at 21.5° and 23.8° of 2θ corresponding to the (110) and (200) reflections respectively and the weaker peak at 22.1° of 2θ corresponding to the (111) reflection. (Sownthari and Suthanthiraraj, 2013; Charitidis *et al.*, 2019; Guadagno *et al.*, 2020)

For the deconvolution of RX spectra, reported in Figure 12d, the maximum in the pattern of the amorphous halo was considered at a value of 2θ corresponding to 21°, as suggested in a previous paper.(Jeznach, Kolbuk and Sajkiewicz, 2019) The results of the deconvolution procedure are illustrated in Figure **Figure IV.58**d.

Figure IV.58e shows the crystallite coherence lengths perpendicular to reflection planes 110 (D110), 200 (D200), and 111 (D111) for the PCL, 1% AuM1, and 3% AuM1 electrospun membranes. For the calculation of 110 (D110), 200 (D200), and 111 (D111) the half-height amplitude of the reflections was evaluated after the deconvolution of the RX spectra. The fraction of the crystalline phase (Xc) was calculated, after the deconvolution of the RX spectrum, as the ratio between the area under the crystalline peaks (excluding the area under the amorphous halo) and the area under the entire RX spectrum of the sample. Xc of the analyzed membranes is shown in **Table IV.18**.

The diffractometric data highlight that the presence of the complex AuM1 affects crystallinity degree and crystal dimensions. The crystallinity increases with increasing the complex percentage (see **Table IV.18**). Concerning the size of the crystals, the fibers with the complex manifest a greater size of the crystals, while the percentage of the complex seems to have an almost negligible effect on this parameter (at least in the range of tested AuM1percentage). This result seems to confirm the morphological data. Hence the presence of the complex determines an increase both in the degree of crystallinity and size of the crystals. This difference in the crystallization behaviour is most likely due to the kinetic of the solvent evaporation during the electrospinning process. Solvent evaporation of the PCL solution containing the complex is less rapid with respect to the solution without AuM1 complex; this creates greater mobility of the polymer segments before solidification of the membrane fibers on the collector-

electrode. This confers the polymer chains, during the crystallization phase, not only higher mobility but also a longer time to arrange themself in the crystals and crystalline domains causing crystals of higher size and higher crystallinity degree.

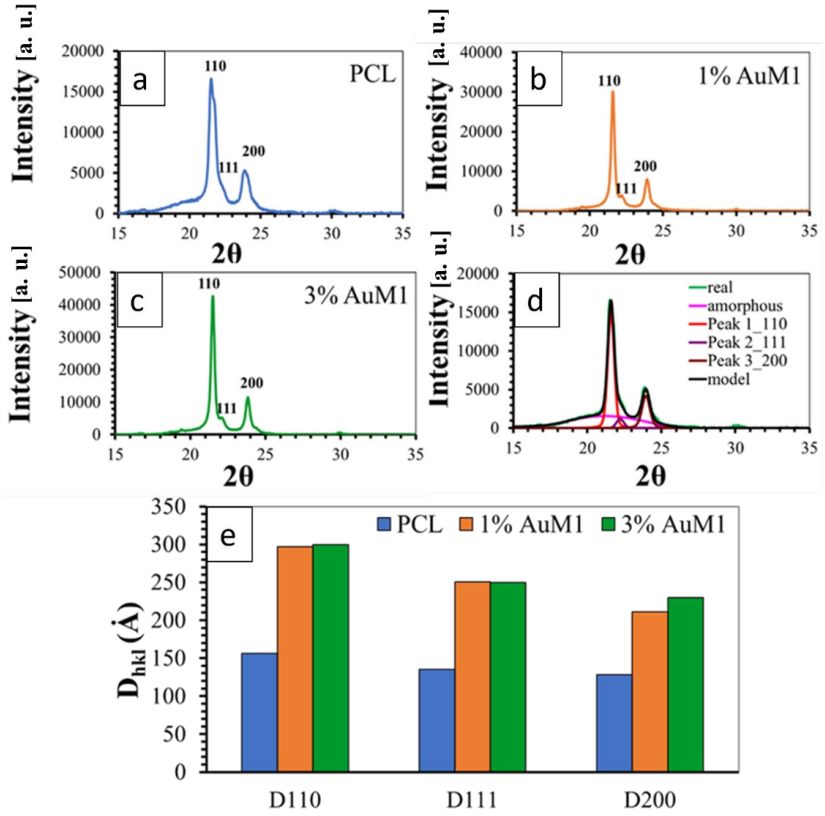

Figure IV.58. *XRD spectra of a) PCL; b) 1%AuM1; c) 3%AuM1; d) Deconvolution Procedure and e) crystallite size.*

Table IV.18. *Degree of Crystallinity*

Crystalline Fraction (Xc)	
PCL	56.2%
1%AuM1	71.4%
3%AuM1	74.0%

This particular structural and morphological arrangement of the fibers/complex strongly affects the release profile of the complex from the membranes, as discussed in the next section.

Encapsulation efficiency and drug release

The analysis of the encapsulation efficiency has been performed by dissolving the membranes in chloroform ($CHCl_3$). In this way, by building a calibration line on the complex absorbance in chloroform, it is possible to evaluate the complex content after the complete dissolution of the membrane. Hence, knowing the complex content dissolved in the polymeric solution before the electrospinning process and evaluating the complex incorporated in the membrane, it is possible to evaluate the encapsulation efficiency of the process. It has been verified also that the PCL absorbs at around 275 nm with a wide peak. For this reason, a PCL calibration line in chloroform has been done, in order to subtract the PCL contribution to the peak of the gold complexes at 255 nm. This procedure has allowed obtaining the absorbance of the dissolved functionalized membranes. Then the encapsulation efficiency has been determined as described in Equation (20).

$$Encapsulation\ Efficiency \equiv \eta = \frac{m_{complex\ in\ the\ membrane}}{m_{theoretical\ complex}} * 100 \qquad (20)$$

In **Table IV.19** are shown the encapsulation efficiencies of the functionalized membranes.

Table IV.19. *Encapsulation Efficiency*

Membrane	η
1%AuL20	95.5%
1%AuM1	98.6%
3%AuL20	86.8%
3%AuM1	79.1%

These results highlight that the encapsulation efficiency is almost total (corresponding to the theoretical value) for the membranes at 1% of loading, whereas ranges between 79% and 87% for the membranes loaded at 3%. The "theoretical value" is the total amount of complex solubilized in the solution before the electrospinning process.

In light of these results, the authors have considered taking into account the encapsulation efficiency also in the drug release curves. For this reason, **Figure IV.59** and **Figure IV.60** have been modified defining the drug released as described in Equation (21):

$$Active\ Substance\ Released\ [\%] = \frac{m(t)}{m_{theoretical\ complex} * \frac{\eta}{100}} * 100 \qquad (21)$$

Where m(t) is the mass of the complex delivered in the medium at the time (t)

In this way, the drug release curves describe in an accurate way the profile of release referring to the real mass of complex encapsulated in the membrane.

Drug delivery behaviour and experimental data modelling

Figure IV.59 shows the release profiles, in the PBS medium, for the 1% AuL20 (a), 1%AuM1 (b), 3% AuL20 (c), 3%AuM1 (d) functionalized membranes. It is well evident, from the profiles of all curves that a large amount (~ 90% of the total released complex) of each active complex is released in the first 3 h. This result is fully in agreement with the peculiar morphological and structural organizations of the fibers constituting the membranes. In fact, since the active complex is consistently located on the nanofiber surface, as proved by AFM analysis, it is quickly released in the PBS medium in the first 3 h. The consistent burst is due to the dissolution of the external aggregates of active complexes, that are directly in contact with the PBS solution. A very small percentage of the complex is released in longer time in an almost plateau region. This slower release is most likely due to the aggregate complexes entrapped among the crystals of the PCL fibers, which start to diffuse in the polymeric matrix toward the outer layer wall of the fibers. However, it is reasonable that in the very first steps, the second stage contribution is neglectable compared to the dissolution of the drug present on the nanofiber surface. However, diffusive phenomena become considerable after the first hours of release. Coherently with XRD spectra, since the crystallinity and the crystalline size increase depending on the complex amount, a small decrease in the maximum amount release is recorded (from 98% to about 89% for AuL20, and from 95% to about 94% for AuM1) because the matrix ordered domains hinder the diffusion of the molecules through nanofibers.

Experimental points in **Figure IV.59** have been fitted by using two different modeling approaches. The first is a modified Weibull model recently proposed in literature (Gorrasi, Longo and Viscusi, 2020). These types of models are generally applied to split the diffusion and the case II transport contribution (Papadopoulou *et al.*, 2006; Gorrasi, Longo and Viscusi, 2020). However, this interpretation may not be appropriate in the presented systems, given the high burst expected because of the complex on the outer walls of the nanofibers. For this reason, in this case, the first part of the model describes the burst effect (A_1, b_1), whereas the second part (A_2, b_2) describes the diffusive effect. The fitting of the experimental data with the theoretical curves obtained from the modified Weibull model is shown in **Figure IV.59** in green color. In **Table IV.20** the parameter values of the release models are reported.

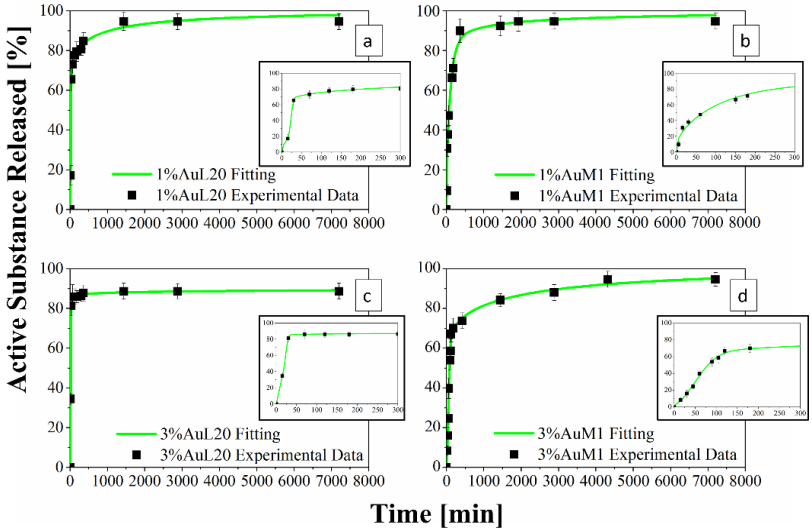

Figure IV.59. *a-d) Drug Release Curve and Modified Weibull Model for 1%AuL20 (a); 1%AuM1 (b); 3%AuL20 (c) and 3%AuM1 (d) functionalized membranes.*

Table IV.20. *Modified Weibull Model Parameters*

	Modified Weibull Parameters			
	1%AuM1	**1%AuL20**	**3%AuL20**	**3%AuM1**
θ [-]	0.533	0.522	0,562	0.544
A_1 [h^{b_1}]	1,901	0.01030	0.01568	1.429
b_1 [-]	1.013	5.186	4.612	2.027
A_2 [h^{b_2}]	1.276	1.793	0.8803	4.058
b_2 [-]	0.284	0.361	0.0429	0.461
R^2	0.9851	0.9951	0.9995	0.9969

To better analyze the contribution of the two release mechanisms, an approach similar to that proposed by Wu et al. (Wu *et al.*, 2020) can be applied, which can be advantageously modified for interpreting the phenomena that occur in the release of the complexes in our case. In particular, Wu et al. have modeled the drug release of their delivery system splitting it into 3 zones, modeling each one appropriately depending on the release mechanism that occurs in that region.

Following this interesting approach, the two different behaviors in the release of the complex have been considered in the present study. In particular, two regions are considered: the initial linear region corresponding

to a very fast kinetic, and the subsequent region corresponding to the slowest kinetics. These two regions are fitted with two different models since the drug release occurs because of different mechanisms. In particular, the first region, in which there is the dissolution of the external complex aggregates, has been fitted by using a first-order model since diffusive models are not suitable for describing the first part of complex dissolution. The second zone of the curves has been described by using a Ritger-Peppas model, which has confirmed for all membranes a diffusive mechanism (n<0.45). The results are reported in **Figure IV.60** and **Table IV.21**.

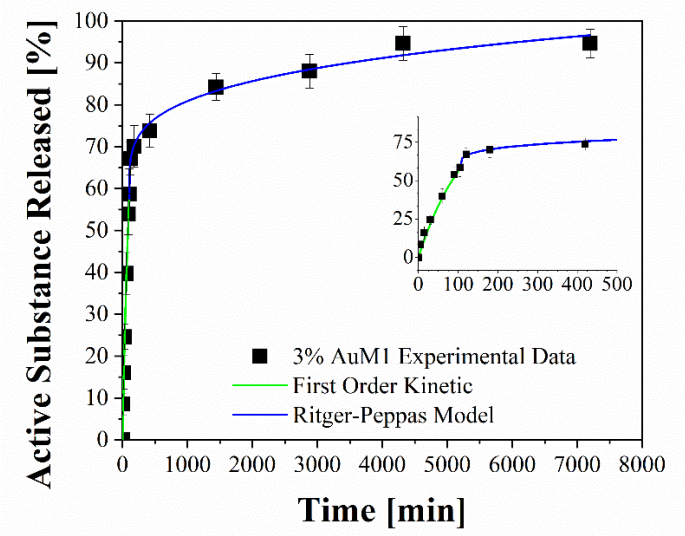

Figure IV.60. *Fitting of experimental data through two-stage release model applied to 3%AuM1.*

Table IV.21. *Fitting parameters of drug release.*

Sample	R^2	First Order Model	Ritger-Peppas Model	
		a [min^{-1}]	k [min^{-n}]	n [-]
1%AuM1	0,9748	$1,84*10^{-2}$	$6.98*10^{-2}$	0.177
3%AuM1	0,9904	$8,18*10^{-3}$	$3,83*10^{-2}$	0,259
1%AuL20	0,9713	$2,32*10^{-2}$	$5,45*10^{-2}$	0,202
3%AuL20	0,9879	$3.90*10^{-2}$	$4,84*10^{-2}$	0,101

IV.4 Considerations: Differences among gold and silver complexes

A scouting phase has been performed to choose between the use of gold complexes and silver complexes. Membranes loaded at 1% and 3% have been produced also for AgL20 and AgM1 (reported in **Figure IV.61**), and the process parameters are reported in **Table IV.22**.

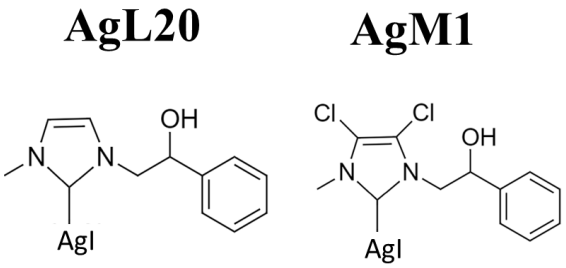

Figure IV.61. *AgL20 and AgM1 chemical structure*

Table IV.22. *Process parameters for membranes loaded with Ag-complexes*

Sample (Acronym)	**Flow Rate [ml/h]**	**Distance Injector-Collector [cm]**	**Active Complex**
1%AgL20	1.7	17	1% of AuL20
3%AgL20	0.8	25	3% of AuL20
1%AgM1	0.8	22.5	1% of AuM1
3%AgM1	0.8	22.5	3% of AuM1

The above-mentioned membranes have been characterized via FESEM morphology, similarly to gold complex ones. The morphology characterizations are reported in **Figure IV.62** and **Table IV.23**.

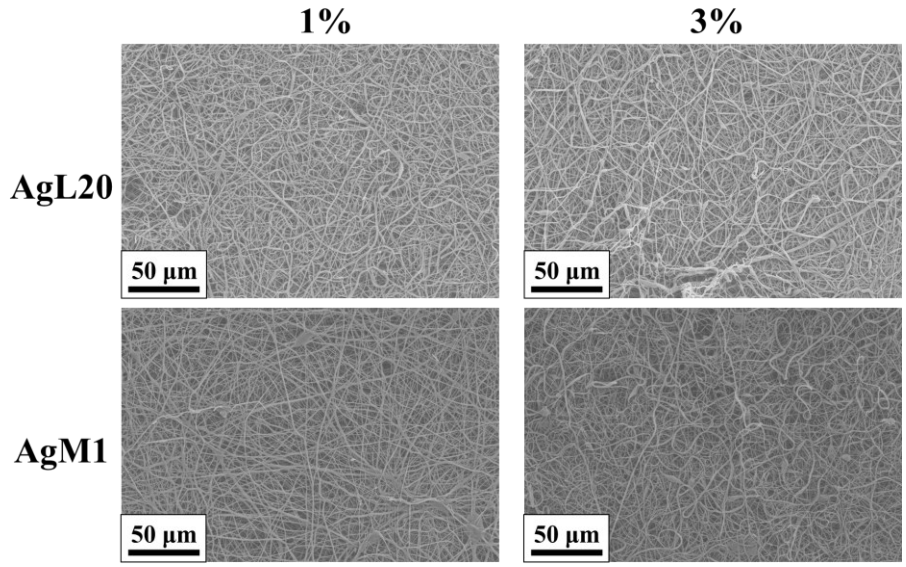

Figure IV.62. *FESEM morphology of 1%AgL20, 3%AgL20, 1%AgM1 and 3%AgM1*

Table IV.23. *Fiber and Pore Diameter distribution*

		1%AgL20	1%AgM1	3%AgL20	3%AgM1
Fiber Diameter	**Mean [µm]**	0.698	0.816	0.696	0.580
	Standard Deviation [µm]	0.352	0.352	0.363	0.358
Pore Diameter	**Mean [µm]**	4.129	2.445	2.98	2.53
	Standard Deviation [µm]	2.323	0.997	1.409	1.17

These systems, which were promising from the morphological point of view, have presented some critical issues. From the first release tests, using the UV-Vis procedure used for the Au-based complexes, the typical peak of the phenyl group was absent (see **Figure IV.63**), which instead was well evident for AuL20 and AuM1 tests. Moreover, during the preliminary biological tests, several problems occurred. Mainly, during cell culture, the presence of dark dots on the Ag-complex loaded membranes occurred diffusively (see **Figure IV.63**). For this reason, given the fact that silver compounds are also known to be photosensitive (Fujita, 2004), it is our idea that the silver complexes tend to photodegrade. In light of these results, and given the lower antitumoral activity of the free silver complexes compared to the gold ones (especially AuM1), we have focused our research mainly on the gold complexes, considering the silver ones less suitable for topical applications.

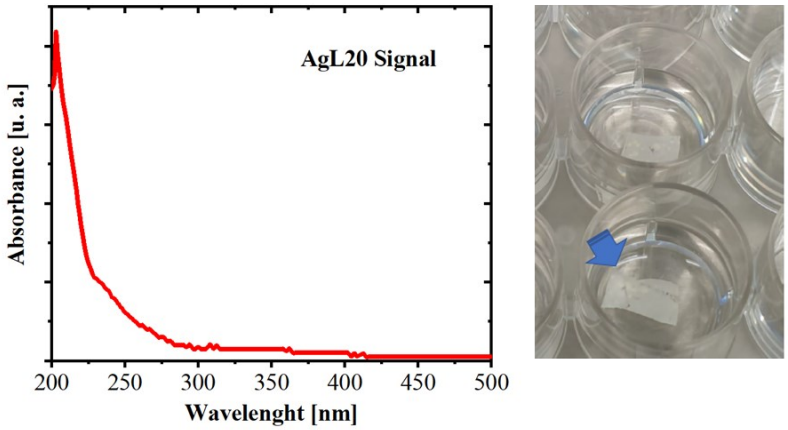

Figure IV.63. *AgL20 UV-Vis spectrum and dark dots appeared on Ag-loaded membranes*

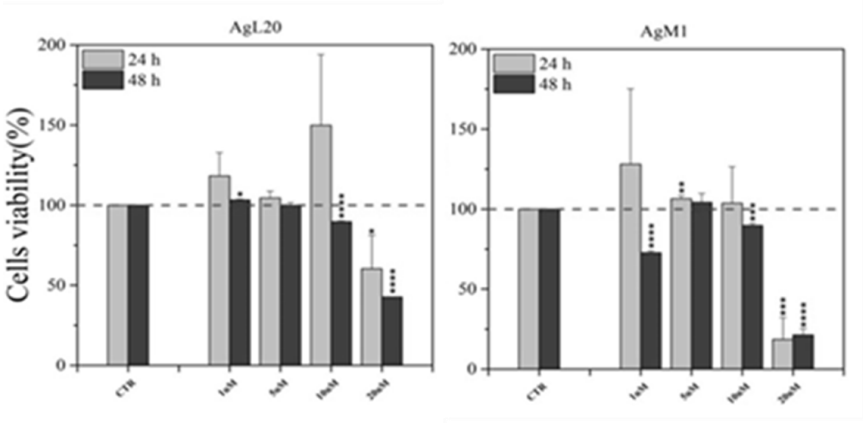

Figure IV.64. *AgL20 and AgM1 antitumoral activity against MeWo cell lines*

Chapter Five

Bottom-up strategy to forecast the drug location and release kinetics

Chapter V
Bottom-up strategy to forecast the drug location and release kinetics

V.1 Introduction

The research for innovative active substances and cutting-edge drug delivery systems are undoubtedly among the most relevant challenges in the biomedical field. However, with the current scientific progress that rapidly overcomes barriers with more effective therapies and more accurate diagnoses, it is crucial to understand the general chemical-physical principles that shape the behavior of the systems to easily forecast how the synthesis of more effective active substances, the development of more performing materials (Lyu and Untereker, 2009) and the progress in more advanced processes can be judiciously exploited and applied based on precedent researches. Generally, it is known that matrix-drug affinity is a relevant parameter that can sensitively affect drug encapsulation and its release.(Wang and Von Recum, 2010; Fu *et al.*, 2011; Vulic and Shoichet, 2014; Ding *et al.*, 2020; Lan *et al.*, 2021) For example, in liposomes, hydrophilic drugs are generally encapsulated in the core, whereas lipophilic drugs are encapsulated in the external phospholipid bilayer membrane. (Wang *et al.*, 2010) However, these types of systems (microcapsules, liposomes, etc.), which are undoubtedly applicable for certain delivery forms(e. g. injection), cannot always besuitable for topical treatments. For example, after surgery, the patient may require combined treatments, from wound dressing to therapeutic delivery. (Deptuła *et al.*, 2019) In this scenario, it is evident that oncological surgery requires devices that can provide the active substance to the patient to efficiently enhance wound healing. Electrospinning is surely one of the processes that meet these requirements since it allows producing highly flexible membranes loaded with active fillers. Furthermore, the obtained nanofibrous morphology guarantees good skin breathing in the zone of interest (Zhao *et al.*, 2020) and simultaneously mimics the features of the extracellular matrix, reducing the healing time for the wound.(Lim, Sardinha and Myers,

2014) For this reason, this technology seems ideal for solid and superficial tumors, such as melanomas, one of the leading causes of death from skin cancer.(Guo *et al.*, 2017) This field of study attracts the scientific community's interest, considering that the therapies against malignant melanoma still lack efficacy due to the heterogeneity (Roesch *et al.*, 2010) and metastatic dissemination (Turner, Ware and Bosenberg, 2018) of this cancer kind (Welch *et al.*, 1991; Płachta *et al.*, 2021). Different types of fillers have been successfully loaded in electrospun membranes (Guadagno *et al.*, 2020; Longo, Gorrasi and Guadagno, 2021), but understanding how to tune the drug release is still unclear.

Among techniques used to control drug release, one of the most promising is coaxial electrospinning since it allows to obtain of efficient bilayer nanofibers of different polymers. (Longo *et al.*, 2022) The coaxial electrospinning generally aims to control the active substance release by adding the shell layer, which limits the burst effect from the membrane and allows a slower release in time. However, it also presents some disadvantages, especially in the control of the process that involves a large number of parameters. The coaxial electrospinning generally aims to control the active substance release through the addition of the shell layer, which limits the burst effect from the membrane and allows a slower release in time. However, it also presents some disadvantages, especially in the control of the process that involves a large number of parameters.

Coaxial electrospinning, which shows great potentialities for obtaining tuneable release curves (Han and Steckl, 2019b) is still not fully exploited because it is not supported by a thorough understanding of how to predict drug release in the uniaxial nanofiber.

The current research chapter studies how to forecast the main properties of the drug delivery device, from the release profile to the morphology, based on the supramolecular interactions between the matrix and the filler. Hence, the study aims to investigate the applicability of these systems in the melanoma field by loading uniaxial electrospun membranes with synthetic and commercial antitumoral agents.

Steffens et al. (Steffens *et al.*, 2020) recently evaluated the inclusion of dacarbazine in electrospun membranes of polyvinyl-alcohol, evaluating the antitumoral activity of the obtained systems. To the authors' knowledge, here electrospun membranes of Polycaprolactone (PCL) loaded with different percentages of dacarbazine, a drug of choice against melanoma (Steffens Reinhardt *et al.*, 2019), have been produced for the first time and tested against

human malignant melanoma derived from lymph node metastatic site (MeWo cell line). Similarly, PCL membranes loaded with synthesis gold complexes (AuM1) have been produced and compared to the ones loaded with dacarbazine. The two compounds present several differences, and the intermolecular interactions have been investigated to determine how they affect the morphology and the release kinetic of the system. In light of relevant results from recent literature (Lage, Aki-Sener and Yalcin, 2006; Liu *et al.*, 2012; Chang *et al.*, 2021) and based on highly promising antitumoral results of AuM1 (Iacopetta *et al.*, 2020), a derivative of the Dacarbazine has been synthesized and complexed with Au (named (NHC^d)AuCl), to evaluate the potentiality of a possibly enhanced antitumoral activity and simultaneously to design membranes with release profiles and morphological features sensitively different to the ones loaded with AuM1. The chemical structure of the active substances used is reported in **Figure V.65**.

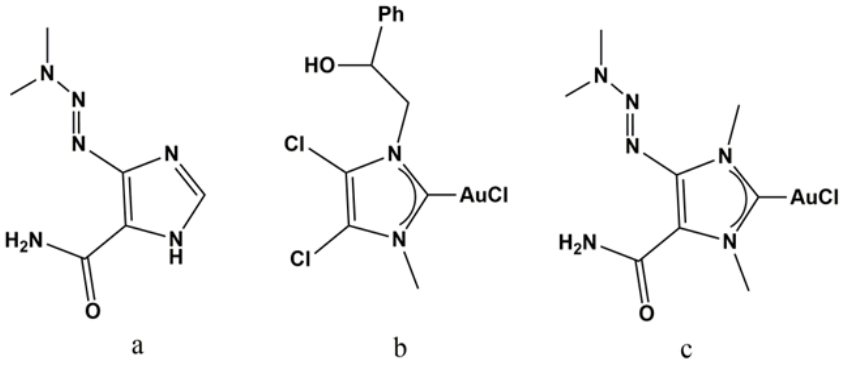

Figure V.65. *a) Dacarbazine; b) AuM1; c) Au-Dacarbazine*

V.2 Experimental Section

Materials

Reagents were purchased from TCI Chemicals and used as received. NMR spectra were recorded, at room temperature,on a Bruker AVANCE 400 spectrometer (400 MHz for ^1H; 100 MHz for ^{13}C). NMR samples were prepared by dissolving about 8 mg of compounds in 0.4 ml of deuterated solvent. The ^1H NMR and ^{13}C NMR chemical shifts are referenced to the residual proton impurities of the deuterated solvents with respect to $SiMe_4$ (δ=0 ppm) as internal standards singlet signals, which are abbreviated as (s). Elemental analyses for C, H, and N were obtained by a Thermo-Finnigan Flash EA 1112 according to standard microanalytical procedures. Chloride

was determined by precipitation of AgCl, using $AgNO_3$ as a reagent. The silver content was determined after dissolution in $Na_2S_2O_3$, by flame atomic absorption spectroscopy (FAAS), and the halogen content was calculated by using the content of silver. MALDI-MS: mass spectra were obtained by a BrukerSolariX XR Fourier transform ion cyclotron resonance mass spectrometer (BrukerDaltonik GmbH, Bremen, Germany) equipped with a 7 T refrigerated actively-shielded superconducting magnet (BrukerBiospin, Wissembourg, France). The samples were ionized in positive ion mode using the MALDI ion source (BrukerDaltonik GmbH, Bremen, Germany). The mass range was set to m/z 200 – 3000. The laser power was 28%, and 22 laser shots were used for each scan.

Perstorp purchased Poly(-caprolactone) (PCL molecular weight of 80,000 Da; CAS number 24980-41-4). (Molecular weight 80,000 Da). Acetone and Dimethylformamide (DMF-CAS 68-12-2) were bought from Carlo Erba (Cornaredo, Italy). Oxoid (Basingstoke, UK). purchased phosphate-buffered saline (PBS pH 7.3).

Synthesis of N, N' dimethyl-4-[(E)-dimethylaminodiazenyl]-5-carboxamide imidazolium iodide

4-[(E)-dimethylaminodiazenyl]-2H-imidazole-5-carboxamide (Dacarbazine 1.00 mmol, 0.1820 g) and potassium carbonate (K_2CO_3, 2.00 mmol, 0.2760 g) were suspended in acetone (25 mL) and stirred at room temperature for 2 h under nitrogen atmosphere. Then, iodomethane was added to the reaction mixture (CH_3I, 10.0 mmol, 1.412 g, 0.60 mL), and the solution was stirred for another 24 h at refluxing temperature. The product was recovered by filtration, and the solvent was removed at reduced pressure and washed with hexane (3x20mL) and diethyl ether (2x20mL), obtaining the N, N' dimethyl-4-[(E)-dimethylaminodiazenyl]-5-carboxamide imidazolium iodide (0.800 mmol, 0.2701 g). Yield: 80%.

Synthesis of N, N' dimethyl-4-[(E)-dimethylaminodiazenyl]-5-carboxamide imidazolyden gold(I) chloride - (NHC^d)AuCl

The imidazolium salt (0.500 mmol, 0.1690 g), chloro(dimethylsulfide) gold(I) ($Au(SMe_2)Cl$, 0.500 mmol, 0.1470 g) was suspended in anhydrous ethanol in a round bottom flask. The reaction mixture was stirred for 3 h at room temperature. Then, potassium carbonate (7.50 mmol, 1.036 g) was added, and the mixture was stirred for another 6 h at room temperature. The gold complex (0.150 mmol, 0.0660 g) was obtained by filtration of the reaction mixture and removing the solvent *in vacuo*. Yield: 30%

The structure of the complex was determined by ^{1}H- and ^{13}C-NMR, MALDI mass spectrometry, and elemental analysis. ^{1}H COSY and NOESY experiments allowed to assign all proton resonances of the ^{1}H NMR

spectrum, whereas resonances of ^{13}C NMR spectrum were attributed using the support of DEPT-135 experiment. All signal attributions are reported in the experimental part. For $(NHC^d)AuCl$ complex, the elemental analysis provides the predictable composition in C, H, N, with a ratio of NHC: Au : Cl of 1 : 1 : 1. Mass spectroscopy analysis gives only a peak at 617,21184 Da corresponding to $[(NHC^d)_2Au]^+$. These data have allowed us to determine the true structure of the complex: $[(NHC^d)_2Au]^+[AuCl_2]^-$.

Electrospinning Procedure

PCL pellets have been put into a 3:1 volume mixture of acetone and DMF at a weight of 11%. In the various solutions, complexes have been added in varying weights: 0%, 1%, and 3% with respect to the polymer amount. To obtain homogeneous solutions, the solutions were maintained under magnetic stirring at 40 °C for 24 hours.

The climate-controlled electrospinning apparatus (EC-CLI by IME Technologies, Spaarpot 147, 5667 KV, Geldrop, The Netherlands) was used to electrospun the polymeric solutions. An illustrative scheme of the electrospinning process is reported in **Figure V.66**.

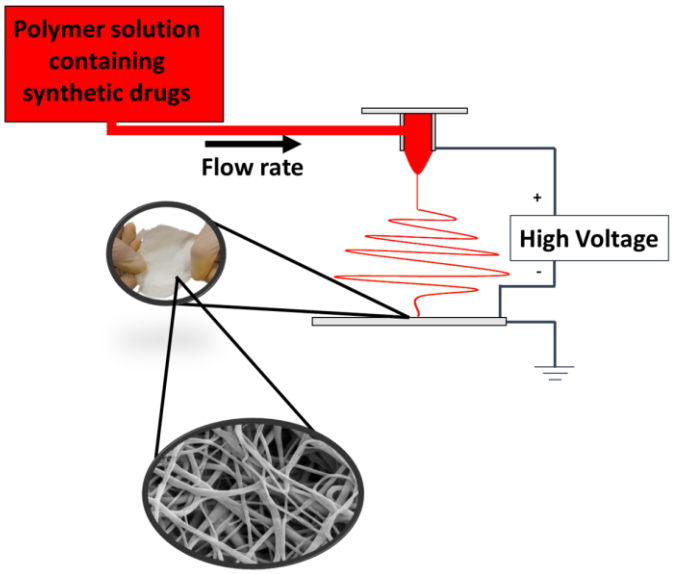

Figure V.66. Electrospinning process

Each solution was placed into a 5 mL syringe and fed via a 0.8 mm needle linked to a power supply. In presence of a strong electric field that enables the polymer to spin, the flow was ejected from the needle. The process parameters have been set to reach a steady spinnability of the solution. For all the membranes, the climate chamber conditions were

established at 25 °C and 35% relative humidity. The additional process parameters are reported in **Table V.24**.

Table V.24. Process Parameters

#	**Flow Rate [ml/h]**	**Distance Injector-Collector [cm]**	**Electric Potential Difference [kV]**	**Active Substance**
PCL	2	28.5	21	-
1%AuM1	1	25	24	1% AuM1
3%AuM1	1	25	25	3% AuM1
1%Dacar	1	25	24	1% Dacarbazine
3%Dacar	1	25	24	3% Dacarbazine
1%(NHC^d)AuCl	1	20	22	1%(NHC^d)AuCl
3%(NHC^d)AuCl	0.5	20	16	3% (NHC^d)AuCl

Sample Preparation and Sterilization Protocol

AuM1, Dacarbazine, and (NHC^d)AuCl (free compounds) were solubilized in dimethyl sulfoxide (DMSO) and diluted in DMEM high glucose (GibcoTM, Waltham, Massachusetts, United States) at a final concentration of 1, 5, 10, 20, 50, 100, 200, 300 and 400 μM, for cell treatments.

For adhesion culture, not functionalized and functionalized PCL membranes were cut to obtain a cycle shape of 15 mm of diameter and, then, deep in 70% ethanol and washed twice in sterile 1X PBS (Corning Cellgro, Manassas, VA, USA). Samples were dried for 24h under a laminar flow cabinet. Silicon rings were cut using a hollow cutter (outer diameter: 14mm; inner diameter: 11mm) and sterilized in 70% ethanol. After ethanol evaporation, silicon rings were stuckon PCL membranes using a non-corrosive silicon rubber and let dry overnight. Samples were deep in 70% ethanol, exposed to UV rays for 5 minutes on both sides, and then used for cell seeding.

Cell Culture

To test the cytotoxicity of free metallic complexes, MeWo (ATCC®, To test the cytotoxicity of free compounds, human melanoma cells (MeWo; ATCC®, HTB-65TM) (P22) were seeded in 96-well plates at a density of 100.000 cells/mL. Cells were cultured in DMEM high glucose (GibcoTM, Waltham, Massachusetts, United States) containing 10% Fetal Bovine Serum (GibcoTM, Waltham, Massachusetts, United States), 100 ng/mL

streptomycin, 1% Penicillin/Streptomycin (Corn-ing, Manassas, VA, United States) and 1% GlutagroTM (Corning, Manassas, VA, United States) at 37 °C in a 5% CO2 atmosphere. After 24h, different concentrations of each compound (1, 5, 10, 20, 50, 100, 200, 300, 400 μM) were added to respective wells and incubated for 24h and 48h.

To test the cytotoxicity of functionalized PCL membranes, human melanoma cells (MeWo; ATCC®, HTB-65TM) (P27) were seeded within silicon rings to prevent cells from flushing from the membrane area at a density of 30.000 cells/cm2. Samples were cultured in DMEM high glucose (GibcoTM, Waltham, Massachusetts, United States) containing 10% Fetal Bovine Serum, 10% Fetal Bovine Serum (GibcoTM, Waltham, Massachusetts, United States), 100 ng/mL streptomycin, 1% Penicillin/Streptomycin (Corn-ing, Manassas, VA, United States) and 1% GlutagroTM (Corning, Manassas, VA, United States) at 37 °C in a 5% CO_2 atmosphere.

Cell Viability Assay

After the treatment, 0.5 mg/ml of 3-(4,5-Dimethylthiazol-2-yl)-2,5-diphenyl-tetrazolium bromide(MTT) was directly added in the culture medium. MTT solution was incubated for 4h at 37°C, protecting the plate from the light. Then, the supernatant was removed, and 100 μl of 100% DMSO was added to solubilize formazan crystals.

The absorbance was measured at 490 nm using a microplate reader (Infinite F200 PRO, Tecan Group Ltd., SW). Cell metabolic activity was calculated as a percentage compared to the control group (considered as 100%), according to the equation 22:

$$\% \text{ Cell viability} = \frac{Abs\,of\,sample - Abs\,blank}{Abs\,of\,control - Abs\,blank} \times 100 \qquad (22)$$

Statistical analysis

Results from multiple experiments (n=3) are presented as mean ± standard deviation (SD). Statistical analysis was performed using ordinary one-way analysis of variance (ANOVA) test, for independent groups. P values less than 0.05 were accepted as significant (Winter, 2019). All statistical analysis was conducted using GraphPad Prism software (6.0 for Windows, LLC, San Diego, CA, USA).

Fourier Transform Infrared Spectroscopy

Fourier Transform Infrared Spectroscopy (FTIR) was carried out using a Bruker Vertex 70 FTIR-spectrophotometer (Bruker Optics Inc., Billerica, MA, USA). The analysis was performed in the range 4000-360 cm^{-1}, with a

resolution of 4 cm^{-1}, and 16 scans were collected. The FTIR on all the samples was performed in absorbance on a thin film of the membranes (≈40 μm).Before each analysis, the membranes were kept under vacuum for 24 hours (at room temperature to not compromise the morphology) to avoid absorbed humidity. The infrared spectra on Dacarbazine, AuM1 and (NHC^d)AuCl were obtained in absorbance using KBr pellets as supports.

Morphology Analysis

The morphology of the materials was examined using atomic force microscopy (AFM). By utilizing the interactions between the tip and the sample surface, AFM is a technique that can recreate a tridimensional image of the surface of the sample. The data are obtained by measuring the cantilever deflection. BrukerNanoScope V multimode AFM (Digital Instruments, Santa Barbara, CA, USA) has been used in ambient atmosphere and ambient atmosphere. . The tip used has a nominal spring constant of 20–100 N/m, resonance frequencies of 200–400 kHz, and a tip radius of 5–10 nm. The utilized tip has a tip radius of 5–10 nm, a nominal spring constant of 20–100 N/m, and resonance frequencies of 200–400 kHz.

The height images have been processed using the software NanoScope Analysis 1.40 (Bruker Corporation, Billerica, MA, USA) and elaborated via OriginPro software (OriginLab Corporation, Northampton, MA, USA). The elaboration of the height profile has been done in accordance with literature. (Guadagno *et al.*, 2022)

For all the samples, the average surface roughness (R_a) and the root mean square roughness parameter (R_q) were evaluated, according to eqs. (23) and (24):

$$R_a = \frac{1}{l_r}\int_0^{l_r} |z(x)| * dx \quad (23)$$

$$R_q = \sqrt{\frac{1}{l_r}\int_0^{l_r} z(x)^2 dx} \quad (24)$$

where l_r is the length of the line, z is the height and x is the position.

Drug Release

Membrane samples were cut in 1 cm diameter and stirred in PBS in an orbital shaker at 300 rpm. Drug release kinetics were monitored by using a Spectrometer UV-2401 PC (Shimadzu, Kyoto, Japan). The tests were performed using rectangular plates with an exposed area of about 3 cm^2 and 1 cm of the light path.

For AuM1, the phenyl group was tracked in the release medium to monitor drug release, as previously reported in literature. (Guadagno *et al.*, 2022) By tracking the absorbance of the target group (phenyl for AuM1, R-

N=N-R for Dacarbazine, and (NHC^{d})AuCl) of known quantities of the various active substances, the calibration curves are well described by the Lambert-Beer Equation (25).

$$A = \varepsilon * c * l \quad (25)$$

where A is the absorbance, ε is the absorptivity of the substance, c is the concentration of the solution and l is the light path length. Table 2 reports the ε values for the complexes.

The peak monitored for AuM1 complex is detected around the expected value (252 nm). For AuM1 spectrum, π→π* transitions are caused by phenyl around 254 nm and around 200 nm. The band at λ=328 nm has been attributed to the transition n→π* transition that could be from R-N=N-R (that has been tracked for Dacarbazine and (NHC^{d})AuCl). As already reported in literature, the amidic groups bonded, such as imidazole, can shift from 210 nm to over 225 nm. (Saraiva, 2020) In particular, it is already reported in literature that the second peak of Dacarbazine in UV-Vis region is at 236 nm. (Chis *et al.*, 2016) However, it is worth noticing that the lower conjugation in (NHC^{d})AuCl leads to a hypsochromic shift (to 228 nm) of the peak. The spectra are reported in **Figure V.67**.

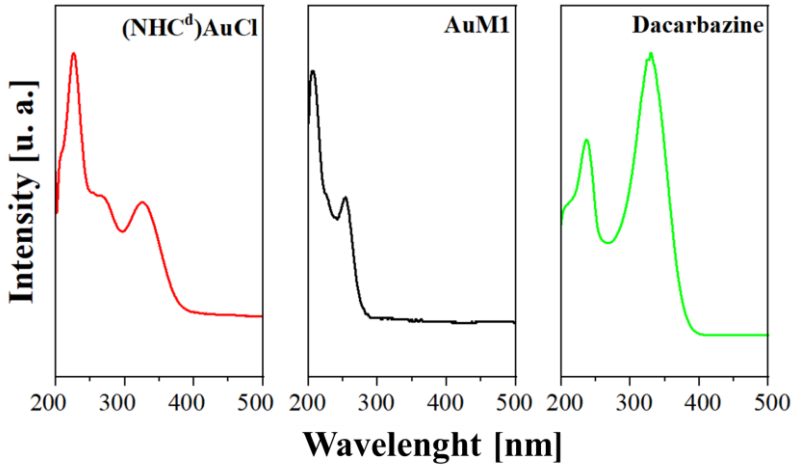

Figure V.67. UV-Vis Spectra of Dacarbazine, AuM1 and (NHC^{d})AuCl

The absorptivities of the active substances are reported in **Table V.25**.

Table V.25. Absorptivity of the active substances in PBS solution

#	ε [mL*mg^{-1}*cm^{-1}]
AuM1 [Peak 252 nm]	9.8847
Dacarbazine [Peak 328 nm]	92.059
(NHC^{d})AuCl [Peak 328 nm]	12.549

Observing the spectra, π→π* transitions around 254 nm and around 200 nm caused by phenyl are evident for both complexes dissolved in the solution. Since AuM1 shows the presence of two chlorines on the backbone, it is reasonable that Cl atoms attract electronic density given its high electronegativity, decreasing and shifting the intensity of the π→π* transition of the electrons involved in the double bond of the two carbons. For (NHC^{d})AuCl, a shoulder around 266 nm is evident. This transition is probably due to π→π* double bond transition but is shifted to the AuM1 peak because of the chemical surrounding. In literature can be found in very different ranges of the UV-vis spectrum, from 184 nm for ethylene to over 400 nm for molecules such as β-carotene (Pavia *et al.*, 2015) For release profile fitting, a statistical approach was followed by using a modified Weibull model (26) recently proposed in literature (Gorrasi, Longo and Viscusi, 2020):

$$\frac{M_t}{M_\infty} = \theta * [1 - \exp\left(-\frac{1}{A_1} * t^{b_1}\right)] + (1-\theta) * [1 - \exp\left(-\frac{1}{A_2} * t^{b_2}\right)] \quad (26)$$

where M is the substance amount released at a certain time, M_∞ is the total substance amount in the sample (evaluated by weighting the sample and knowing the complex percentage in the membrane), A_1, A_2, b_1, b_2 and θ are kinetic constant parameters, t is the time. The first principles Fick model, reported in Equation 27, has been applied to fit the diffusive release curve, according to Siepmann et al. (Verhoeven *et al.*, 2009; Siepmann and Siepmann, 2012), considering the system as a matrix drug delivery system.

$$\frac{M_t}{M_\infty} = 1 - \frac{8}{\pi^2} * \sum_{n=0}^{\infty} \frac{\exp\left(-D * (2n+1)^2 * \pi^2 * \frac{t}{L^2}\right)}{(2n+1)^2} \quad (27)$$

where L is the thickness of the membrane and the only fitting parameter is D, the diffusivity of the system.

The encapsulation efficiency of the electrospinning process for the various membranes has been evaluated by dissolving the sample in chloroform. In this way, a calibration line of the various active substances in chloroform has been built up. The encapsulation efficiency has been defined as follows in Equation 28.

$$Encapsulation\ Efficiency \equiv \eta = \frac{m_{active\ substance\ in\ the\ membrane}}{m_{theoretical}} * 100 \quad (28)$$

V.3 Results and Discussion

Chemistry

AuM1was synthesized according to the procedure already reportedin the literature.(Iacopetta *et al.*, 2020)
The synthesis scheme of the proligand (A) and (NHCd)AuCl complex (B) is shown in **Figure V.68**.
Synthesis of proligand: N, N' dimethyl-4-[(E)-dimethylaminodiazenyl]-5-carboxamide imidazolium iodide was obtained by reaction of 4-[(E)-dimethylaminodiazenyl]-2H-imidazole-5-carboxamide (Dacarbazine) with iodomethane (CH_3I). The product was characterized by ^{1}H and ^{13}C NMR and obtained with a good yield (80%). Synthesis of gold complex(NHC^{d})AuCl:N, N' dimethyl-4-[(E)-dimethylaminodiazenyl]-5-carboxamide imidazolyden gold(I) chloridewas synthesized by reaction of the proligand with gold(I)-chloro-(dimethylsulfide) [(Me_2S)AuCl] in inert nitrogen atmosphere. The corresponding (NHC^{d})AuCl complex was obtained in 30% yield (see scheme 1B) (Saturnino *et al.*, 2016; Iacopetta *et al.*, 2017; Mariconda *et al.*, 2020, 2022; Costabile *et al.*, 2021; Ceramella *et al.*, 2022; Sirignano *et al.*, 2022). The new complex was characterized by^{1}H and ^{13}C NMR, mass spectroscopy and elemental analysis. ^{1}H and ^{13}C NMR spectra show the expected signals (the attributions are reported in the Supplementary Materials) and the sharp resonance for carbene was at 178.43 ppm. The elemental analysis (reported in the Supplementary Materials) gives a ratio among ligand, gold and chloride of 1:1:1 and mass spectrometry analysis allows to establish the structure of the gold complex. Indeed, MALDI-MS spectrum show the peak leading, associated to the compound at 617,21184 m/z, corresponding to $[(NHC)_2Au]^{+}$. Thus, the complex is constituted of $[(NHC^{d})_2Au]^{+}$cation and of $[AuCl_2]^{-}$ anion as it was been shown for an analogous silver complex by the solid-state structure determined by X-ray diffraction (Mariconda *et al.*, 2014). It is worth note that, from literature, a dynamic equilibrium in solution is known between mono and biscarbenic metallic species.

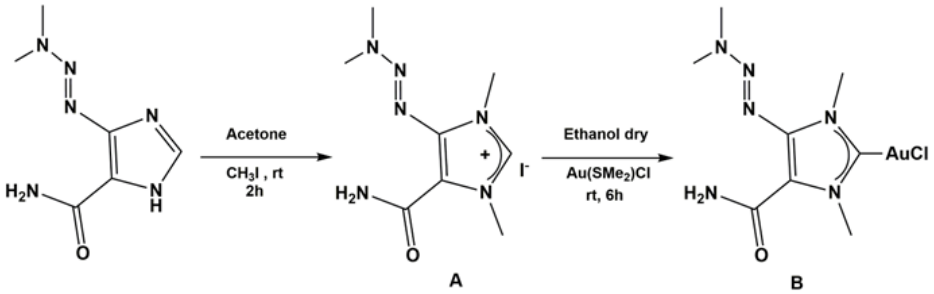

Figure V.68. Synthesis of proligand (A) and (NHC^{d})AuCl complex (B).

FTIR Analysis

FTIR spectra of PCL, 3%AuM1, 3%Dacar, and 3%(NHC^d)AuCl were detected to determine the presence of interactions between the active substance and the hosting polymeric matrix. The typical peaks of the PCL remain unchanged in the FTIR spectra, probably because of the small amount of filler loading in the nanofibers. **Figure V.69** shows the spectrum of the PCL membrane.

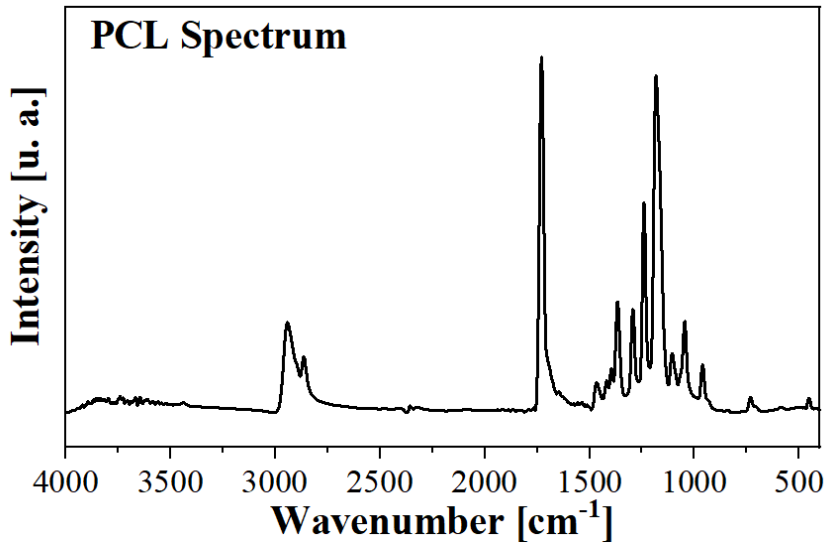

Figure V.69. FTIR Spectrumof the PCL membrane.

However, by focusing on the 3000-3500 cm^{-1}wavenumber range (**Figure V.70**), it is possible to track down one of the typical peaks of the dacarbazine due to the N-H stretching of the amide group of the dacarbazine. Interestingly, the same peak is evident also in the 3%Dacarbazine membrane, shifting from 3383 cm^{-1} to 3372 cm^{-1}. The NH_2 group of the dacarbazine gives hydrogen bonding with the carbonyl group of the PCL and, for this reason, the N-H bondings are affected(Drobota *et al.*, 2020) by the intermolecular interactions with the matrix. A bathochromic shift to lower wavenumber (so higher wavelength and, so, lower energy) is observed when dacarbazine is included in PCL.

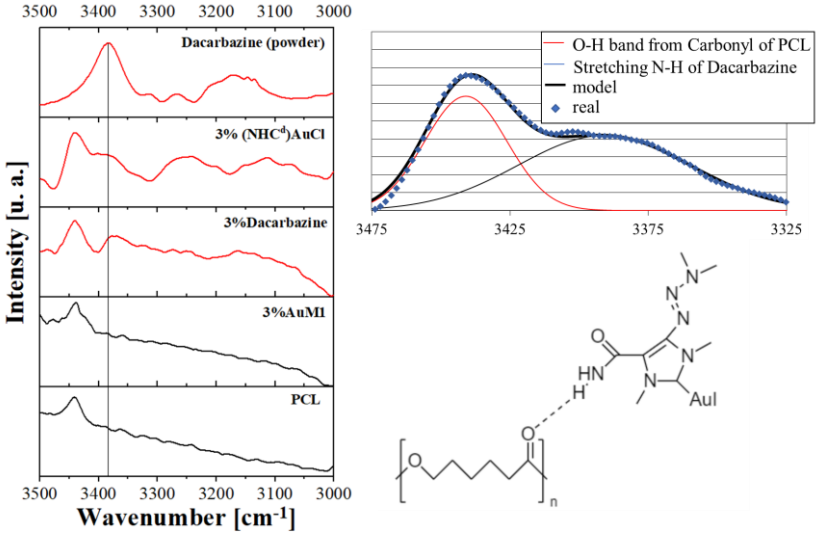

Figure V.70. FTIR between 3000-3500 $cm^{-1}$of Dacarbazine powder and the membranes unloaded (PCL) and loaded with AuM1 (3%AuM1), Dacarbazine (3%Dacar) and (NHC^d)AuCl (3%(NHC^d)AuCl).

The significant affinity between the PCL matrix and the dacarbazine (and (NHCd)AuCl) rather than AuM1, which has been proved via FTIR analysis, strongly influences the placement of the active substance along the nanofibers during the electrospinning process, as widely explored in the AFM analysis section.

AFM Analysis

AFM analysis has been performed to define the nanofiber size in the electrospun membranes and to study the surface characteristics of the nanofibrous membranes. From precedent research of the group [21], the peculiar morphology of electrospun membranes can be investigated via AFM to determine where the filler is loaded during the process. As reported in **Figure V.71**, even if for all the produced membranes the morphology is nanofibrous, several peculiarities are evident for the different matrix-drug systems. For PCL membranes (in the first row of **Figure V.71**), PCL is electrospun without the presence of fillers, and from the AFM morphology, it is possible to notice that the PCL electrospun membranes are very smooth. This information is confirmed by the roughness parameters (R_a and R_q) and phase acquisitions.Similar results, both in height and phase images,have also been obtained for the membranes loaded with Dacarbazine (1% and 3%), with roughness parameters that are very similar to the ones of PCL. In the case of membranes loaded with 1% and 3% AuM1, the feature of the superficial morphology is sensitively different. AuM1 complex, which has a

low affinity with the PCL matrix, tends to be segregated in a large amount on the surface of the nanofibers. Natu et al. (Natu, de Sousa and Gil, 2010) reported that when the filler is loaded in a fibrous delivery system above the solubility threshold, it tends to be segregated on the fiber surface. However, given that the solubility depends strictly on the affinity between the matrix and the filler, it is possible to forecast where the active substance tends to be distributed,just considering the interactions between the matrix and the filler. In this case, the intermolecular interactions (hydrogen bonding type) between PCL and Dacarbazine, confirmed via FTIR, allow the inclusion of the Dacarbazine homogeneously in the nanofiber. The absence of strong intermolecular interactions between AuM1 and PCL causes the placement of AuM1 away from the PCL core and, therefore, its segregation on the nanofiber surface. (NHC^{d})AuCl gives interactions with PCL likewise Dacarbazine-PCL membranes, being so included in all PCL material of the fibers. Hence, no segregation effect of the active substance is observed on the fiber surface, as evidenced by the last row of **Figure V.71**.

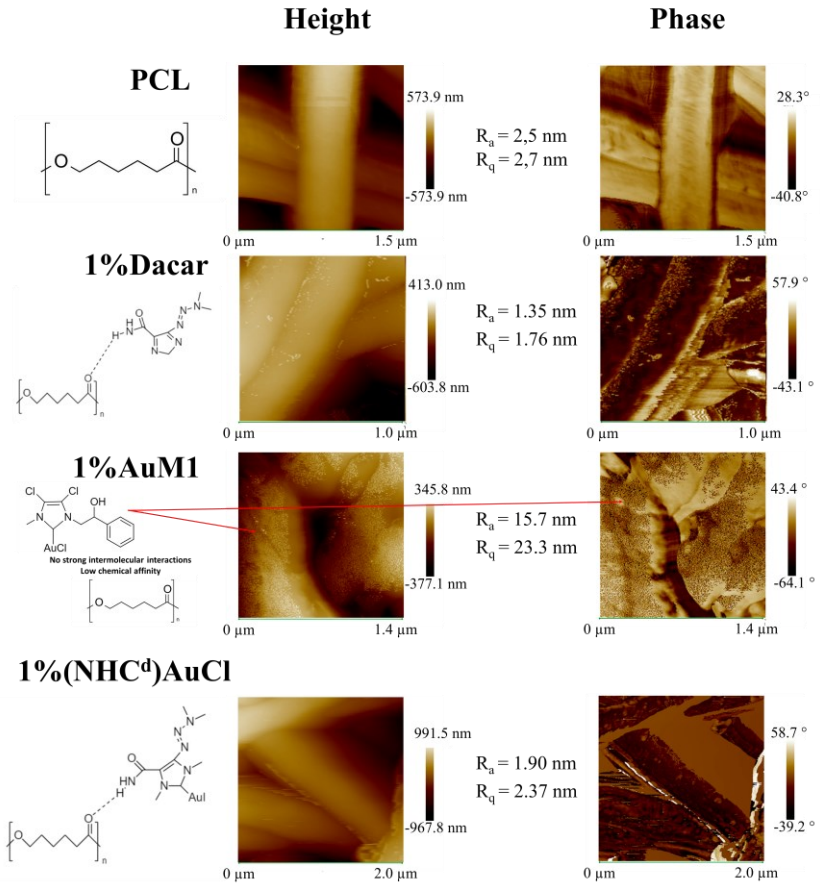

Figure V.71. AFM images of the unfilled and filled membranes

In **Table V.26**, the roughness parameters evaluated for the unloaded membrane and the membranes loaded with AuM1, Dacarbazine, and (NHCd)AuCl are reported. By comparing the results, it is evident that the roughness sensitively increases as lower is the affinity between the filler and matrix. In fact, by comparing the results obtained for the membranes loaded with Dacarbazine and the unloaded membranes, the roughness parameters are very similar, confirming the inclusion of the active substance in the polymeric matrix.

Table V.26. Roughness Parameters evaluated for the various membranes

#	**R_a [nm]**	**R_q [nm]**
PCL	2.5	2.7
1%AuM1	15.7	23.3
3%AuM1	23.7	28.7
1%Dacar	1.35	1.76
3%Dacar	1.37	1.69
1%(NHC^d)AuCl	1.90	2.37
3%(NHC^d)AuCl	4.67	6.21

Active Substance Release

The encapsulation efficiency of the active substance in the different membranes has been evaluated, and the results are reported in **Table V.30**. The results highlight that the encapsulation efficiency is almost total (corresponding to the theoretical value) for the membranes at 1% of loading, whereas it decreases to 75% for the membranes loaded at 3% of the active substance. The "theoretical value" is the total amount of complex solubilized in the solution before the electrospinning process.

Table V.27. Encapsulation Efficiency of the systems

Membrane	**η**
1%AuM1	98.6%
1%Dacar	98.0%
1%(NHC^d)AuCl	98.3%
3%AuM1	79.1%
3%Dacar	76.0%
3%(NHC^d)AuCl	74.8%

The release curves were evaluated for the membranes loaded with the various active substances via UV-Vis spectroscopy. In order to evaluate the drug release of the drug encapsulated in the membranes, the active substance released has been defined as reported in Equation 29.

$$Active\ Substance\ Released\ [\%] = \frac{m(t)}{m_{theoretical\ complex} * \frac{\eta}{100}} * 100 \quad (29)$$

The release curves display several differences both in terms of the mechanism of release and in terms of kinetic. As expected, 1%AuM1 and 3%AuM1 have a relevant burst effect, given the presence of the complex on the nanofiber surface. As soon as the membranes come into contact withthe PBS solution, the crystallite aggregates on the nanofibers start to dissolve in the solution. Only when the complex on the surface has dissolved, doesthe diffusive contribution, due to the complex inclusion in the nanofiber, start to manifest. However, this contribution is limited since most of the active substance was segregated on the nanofiber surface because of the little interaction with the matrix. By contrast, 1%Dacar, 3%Dacar, 1%(NHC^d)AuCland 3%(NHC^d)AuCl, in which the active substance is included inside the nanofiber structure, have significantly slower release curves, as reported in **Figure V.72**.
The different release mechanisms are confirmed by the first principles modeling analysis. Firstly, a Fickian diffusive release has been hypothesized for all the systems, obtaining the diffusivity term by modeling the curves in the first region of the curves (around 1 h) according to the approximation in Equation 30.

$$\frac{M_t}{M_\infty} < 0.6;\ \frac{M_t}{M_\infty} = 4 * \left(D * \frac{t}{\pi * L^2}\right)^{\frac{3}{2}} \quad (30)$$

Then, the fitting diffusivity parameter has been applied to all the systems using the generalized Fick model for these types of systems, (Siepmann and Siepmann, 2012) reported below in Equation 31.

$$\frac{M_t}{M_\infty} = 1 - \frac{8}{\pi^2} * \sum_{n=0}^{\infty} \frac{\exp\left(-D * (2n+1)^2 * \pi^2 * \frac{t}{L^2}\right)}{(2n+1)^2} \quad (31)$$

However, as it is evident in **Figure V.72**, the Fickian model does not describe accurately 1%AuM1 and 3%AuM1 releases. In fact, the diffusive parameter (D), evaluated in the first region of the sample, is affected by the burst effect, which is sensitively lower/absent for 1%Dacar, 3%Dacar, 1%(NHC^d)AuCland 3%(NHC^d)AuCl. In fact, the diffusivity for all these last systems is around 10^{-8} mm^2/s, whereas is 100 times higher (around 10^{-6} mm^2/s) for AuM1-membranes. This is because the Fick model does not describe appropriately these types of systems. Semi-empirical models derived from the Weibull model, here reported in Equation 32, recently applied in literature (Gorrasi, Longo and Viscusi, 2020; Guadagno *et al.*, 2022) are more efficient to describe when two mechanisms of release occur.

$$\frac{M_t}{M_\infty} = \theta * [1 - \exp\left(-\frac{1}{A_1} * t^{b_1}\right)] + (1-\theta) * [1 - \exp\left(-\frac{1}{A_2} * t^{b_2}\right)] \quad (32)$$

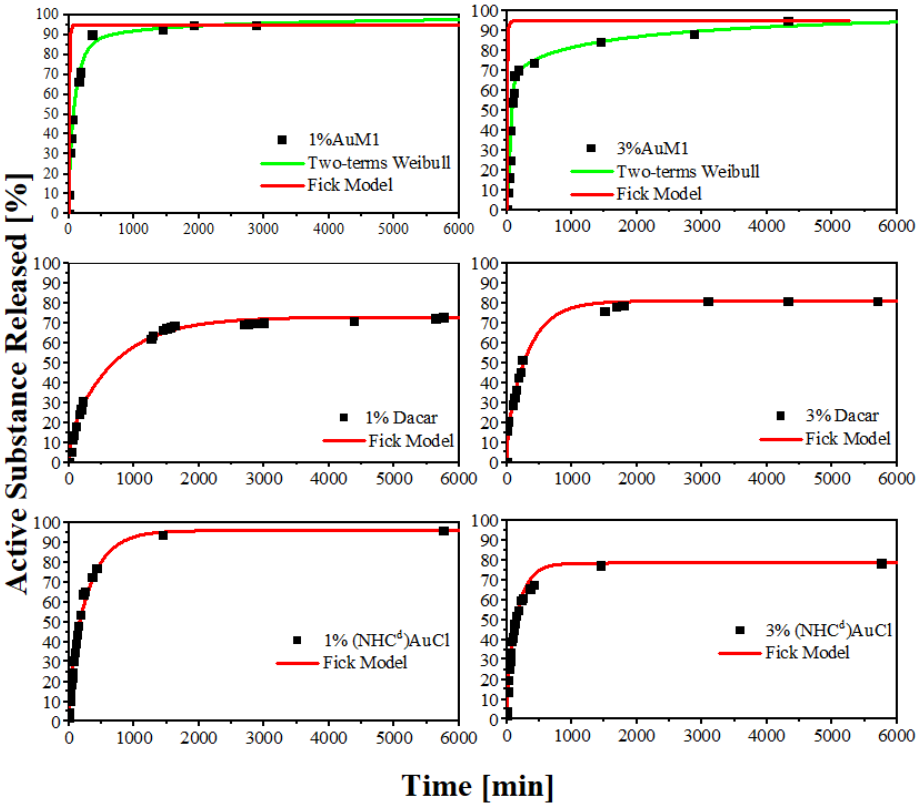

Figure V.72. Release curve of the electrospun membranes

It is worth noticing that the asymptotic value for the membranes loaded with Dacarbazine, which have a higher affinity to the matrix, is generally lower than the one obtained for AuM1-loaded matrices. It is probably due to the higher matrix-filler interaction, that leads to holding a higher quantity in the polymer matrix.(Dogan, Dabkowski and von Recum, 2022)

By comparing the very first zone of the curve the difference is even more evident. In the first region for 3%(NHC^d)AuCl and 3%AuM1, is evident how changing the ligand of the complex is possible to obtain completely different release profiles. The results are reported in **Figure V.73**.

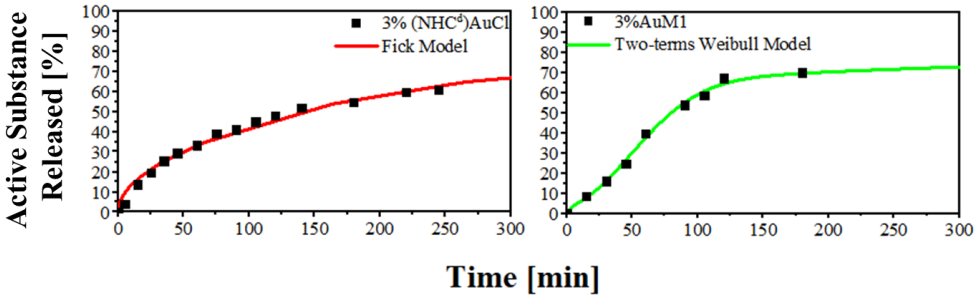

Figure V.73. Release kinetic in the first region of the curves

In **Table V.28** are reported the Weibull Parameters evaluated for AuM1 loaded membranes. In
Table V.29 below the fickian diffusive parameters for the membranes are reported.

Table V.28. Two-terms Weibull parameters for electrospun systems

Weibull Parameters	**1%AuM1**	**3%AuM1**
θ	0.533	0.544
A_1 [h^{b1}]	1.901	1.429
b_1 [-]	1.013	2.027
A_2 [h^{b2}]	1.276	4.058
b_2 [-]	0.284	0.461
R^2	0.9851	0.9969

Table V.29. Diffusive Parameters for diffusive electrospun systems

Electrospun systems	**D [mm^2/s]**	**R^2**
1%Dacar	2,34 E-08	0,9921
3%Dacar	4,95 E-08	0,9757
1%(NHC^d)AuCl	5,44 E-08	0,9795
3%(NHC^d)AuCl	1,00 E-08	0,9807

Cytotoxicity of free compounds and PCL functionalized membranes

Compared to the commercial Dacarbazine, the synthetic complexes AuM1 and Au-Dacarbazine showed better performance against MeWo. The concentrations of 5 µM and 50 µM were identified as the Minimum Inhibitory Concentrations (MIC) for AuM1 and Au-Dacarbazine, respectively (**Figure V.74a-c**).

Also, by testing PCL functionalized membranes, the best antitumoral activity was observed for the synthetic systems. In particular, the synthetic complexes had again a significantly higher activity than the commercial Dacarbazine, showing a cell viability of less than 50% at 24h and 48h, as reported in **Figure V.74**. MeWo cell line has been chosen because of its well-known chemo-resistance, but the current research stresses the possibility to approach this challenge in two ways: firstly, the possibility to synthesize completely new metal-complex chemotherapeutics (e. g. AuM1) with high effectiveness against the specific cell line; secondly, the possibility to integrate the proven activity of the metal developing cutting-edge metal complexes, starting from the proved knowledge of the ligand.

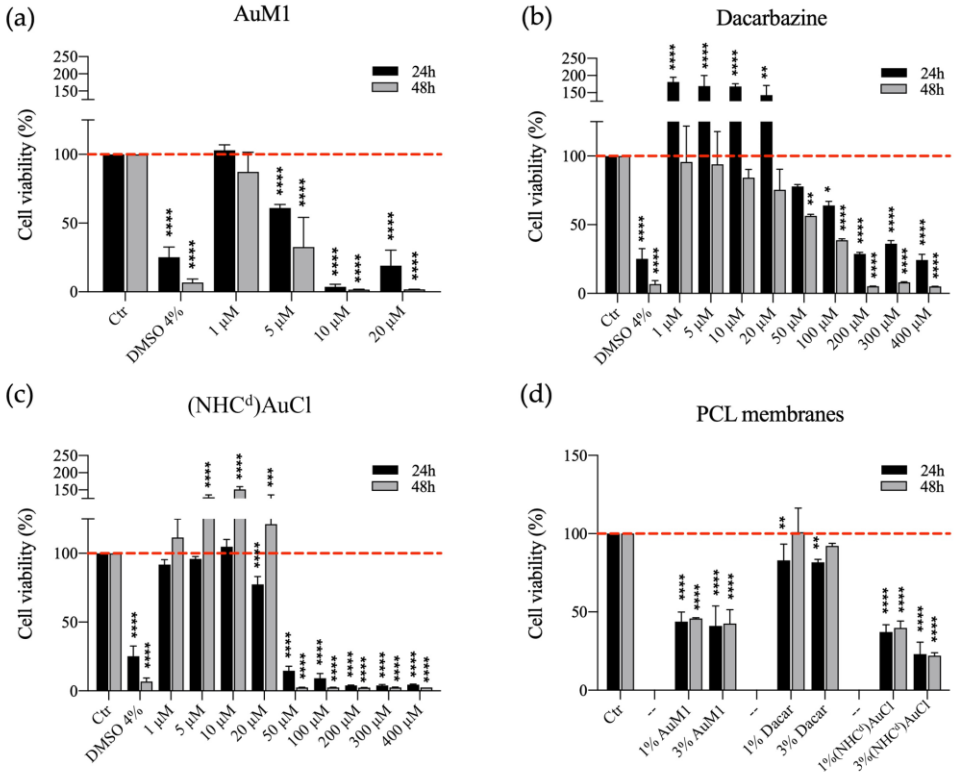

Figure V.74. MTT assay on MeWo cells treated with free compounds or seeded on PCL functionalized membranes. 1, 5, 10, 20, 50, 100, 200, 300 and 400 µM of AuM1 (a), Dacarbazine (b) and Au-Dacarbazine (c) were tested to evaluate the cytotoxic effect of free compounds on MeWo cells; MeWo viability was also studied seeding cells on PCL membranes (c), functionalized with 1% and 3% of each compound. The experiments were

analyzed by ordinary one-way ANOVA test. * $p \leq 0.05$, **$p < 0.01$, ***$p < 0.001$ and ****$p \leq 0.0001$ (n=3).

V.4 Coaxial systems

The precedent paragraph has highlighted the possibility to tune the release profile by varying the affinity between active substance and matrix. However, it may not be possible to change the matrix-filler system. In the current paragraph, it is analyzed the possibility to modify the release profile of an antitumoral electrospun membrane by varying the process configuration. As discussed in the Introduction section, coaxial electrospinning results to be an efficient method to produce bilayer nanofibers, tailoring so the wettability, the mechanical properties and the drug release of the nanofibrous systems. In this case, coaxial electrospun membranes made of polyvinyl alcohol (PVA) and PCL are produced and the process conditions are presented, investigating the thermal stability and the typical main thermal transition by Differential Scanning Calorimetry (DSC) and Thermogravimetric Analysis (TGA) of the complex systems. The aim of this study is to evaluate the possibility to tune the drug delivery not only by changing the polymeric matrix but, also, by using coaxial system. In particular, in the current study the configuration 1%AuM1, reported in Chapter IV, has been produced coaxially, by covering the PCL with a PVA coaxial layer. In this way it is proved that active chemotherapic membranes loaded with an active filler are strongly affected by the process configuration, noticing strong differences in wettability, cristalliniy, thermal transitions, drug release and morphology. In **Table V.30**, the process parameters for the production of the coaxial membranes are reported.

Table V.30. *Process Parameters Coaxial Systems*

#		Concentration	Solvent	Flow Rate [ml/h]	Injector-Collector Distance [cm]	Applied Voltage [kV]	Loading
PVA	PVA	16.5	H_2O-EtOH (1:1)	0.5	15	16	-
PCL	PCL	6	HFIP	1	22.5	13	-
Coax	Core:PCL	5	HFIP	2	20	19.9	-
	Shell:PVA	6	HFIP	2			-
1%AuM1-Coax	Core:PCL	5	HFIP	1	17.5	25	1%AuM1
	Shell:PVA	6	HFIP	1			-

The thermogravimetric analysis is reported in **Figure V.75**. As expected, since PVA degrades at lower temperatures than PCL, the starting degradation temperature of the coaxial system is similar to the one of PVA. (Peng and Kong, 2007) As reported in **Figure V.75**, Coax and 1%AuM1-Coax have similar thermogravimetric spectra. However, the loss in weight of 5% is around 270 °C for coaxial systems, proving that these types of systems are thermally stable considering their applicability in the biomedical field.

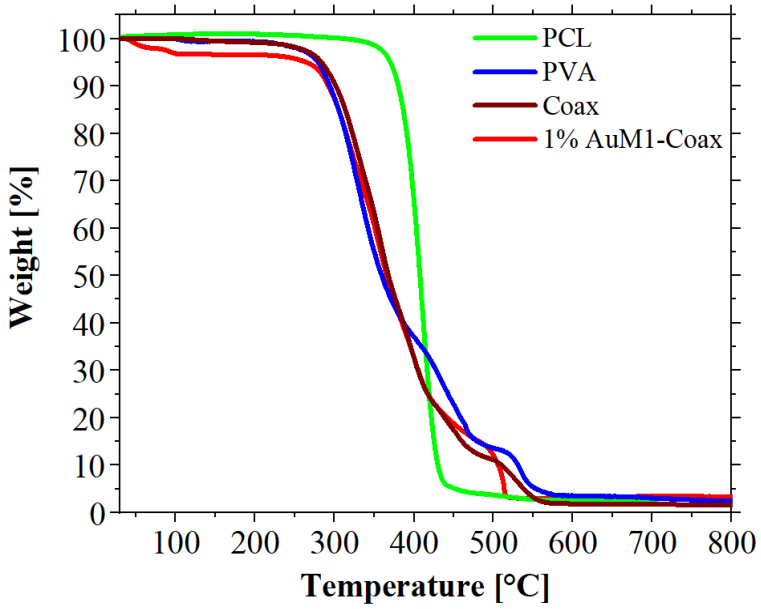

Figure V.75. *TGA of Coaxial uniaxial electrospun systems*

By putting the coaxial systems in water for 24 h, the weight after dissolution has been evaluated to have information regarding the PVA and PCL percentages. In particular, in the coaxial systems, PCL is 43.8% and PVA is 56.2%. By the DSC analysis, it is possible to observe the presence of PCL and PVA melting peaks in the thermograms, and the crystallinity of the two polymers has been evaluated according to Longo et al. (Longo *et al.*, 2022).

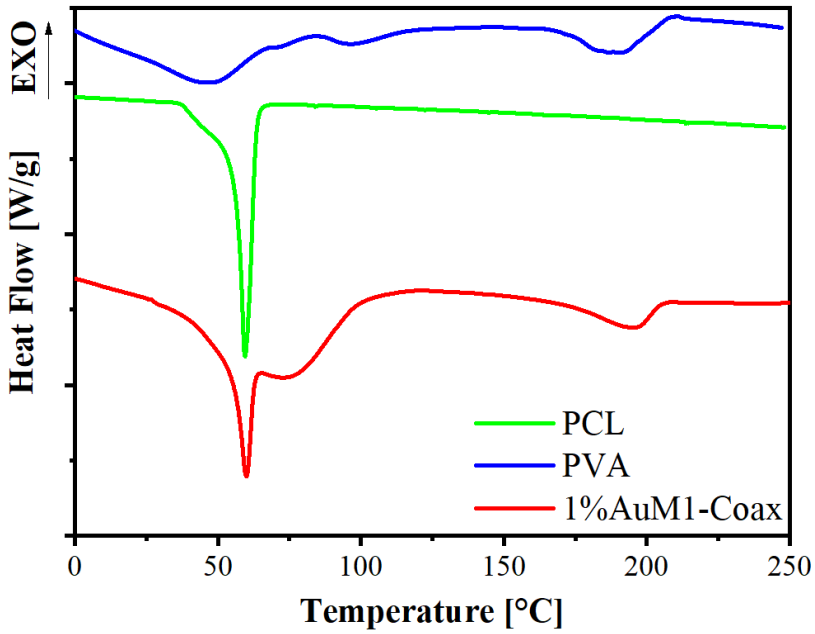

Figure V.76. *DSC of Coaxial uniaxial electrospun systems*

In agreement with previous results (see Chapter III), the coaxial process does not affect sensitively the melting transitions of the system. However, the crystallinity of the two polymers slightly increases with the coaxial configuration, probably because of the higher stresses that occur during the electrospinning. Moreover, the inclusion of AuM1 causes a further increase of the crystallinity content (probably acting as a nucleating agent), in accordance with the results of Chapter IV. The results are reported in **Table V.31**.

Table V.31. *Crystallinity of the systems*

Sample	Crystallinity [%]
PCL	50,70
PVA	22,68
Coax	PCL: 56,97
	PVA:26,25
1%AuM1-Coax	PCL: 62.15
	PVA: 33.79

The coexistence of PCL, PVA and the inclusion of AuM1 in the matrix has been confirmed via FTIR analysis. As it is possible to see in **Figure V.77**, the typical peaks of the PCL (C-O-C stretching, Carbonyl group) and of the PVA (-OH band, C-C) remain well-evident in the case of coaxial system.

Moreover, in the inset it is possible to see the C-Cl bonding (absent in the FTIR curve reported of the unloaded coaxial membrane), which is due to the AuM1 active substance, in which there is the presence of two C-Cl bonds.

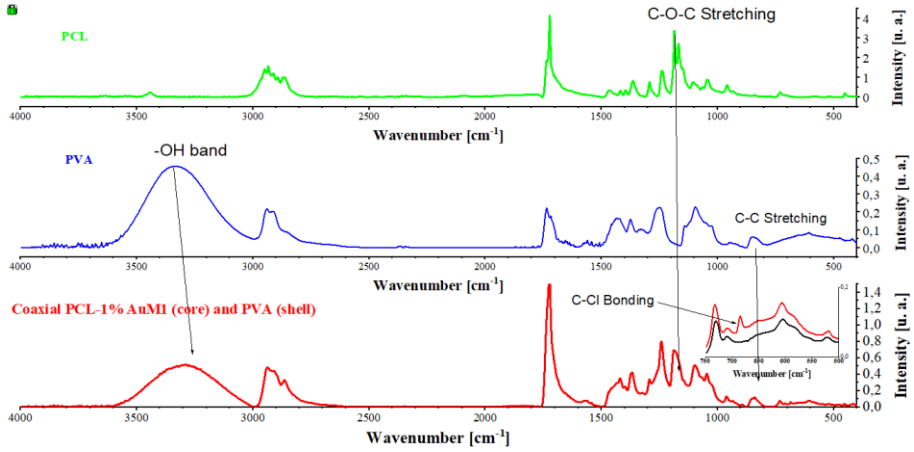

Figure V.77*. FTIR of the membranes*

By the AFM analysis, the coaxial system morphology has been investigated in depth. As it is possible to observe in **Figure V.78**, the morphology of the membrane is sensitively different from the 1%AuM1 membrane in Chapter IV. It is probably due to the coaxial process, in which the PVA is in the outer layer of the fiber. In fact, even if AuM1 is included in PCL now, it is not evident in this case on the outer part of the nanofiber (whereas in PCL alone fiber it was in the outer layer as seen in Chapter IV). This result is even more evident looking at Phase images, in which it is evident the difference with PCL membranes. Moreover, it is possible to notice the presence of lamellar structures (Guadagno *et al.*, 2006), that were not evident in previous AFM (see Chapter IV). It is probably due to the fact that the crystallinity increases because of the PVA and because of the higher crystallinity obtained via coaxial electrospinning.

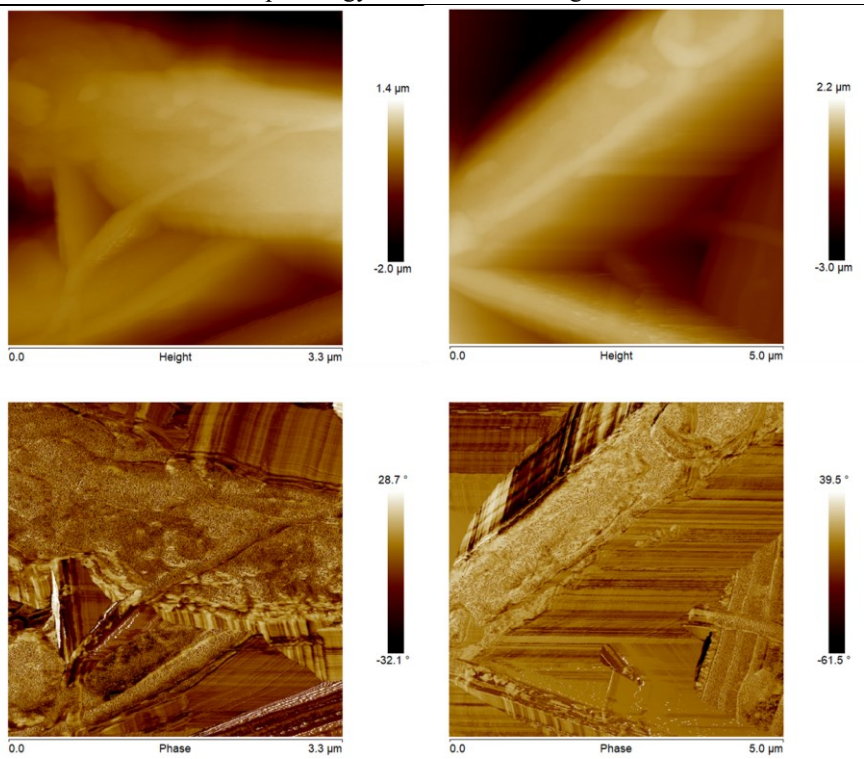

***Figure V.78**. AFM of the coaxial membrane loaded with 1%AuM1-Coax*

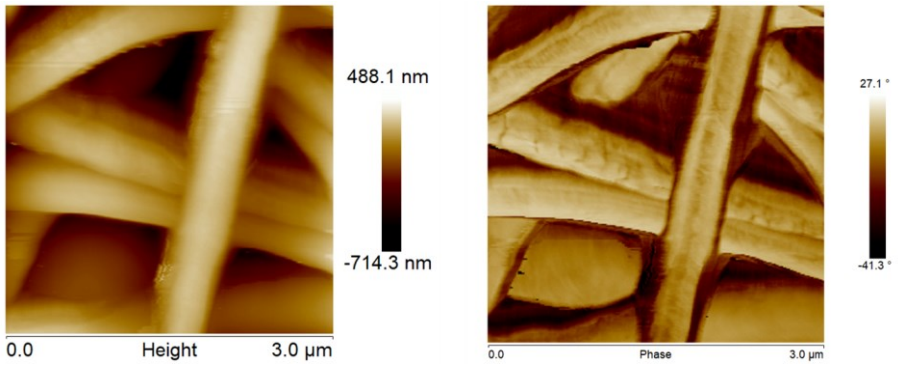

***Figure V.79**. AFM of PCL membrane: Height (left) and Phase (right)*

This phenomenon strongly affects the release kinetics, because the erosion of the outer layer affects the delivery of AuM1 in the surrounding environment. As reported in **Figure V.80**, the release kinetic in case of 1%AuM1-Coax is evidently multistep. In fact, in the first step, an erosion of the PVA occurs whereas in the second step there is a diffusion of AuM1 from the PCL to the

surrounding environment. This type of phenomenon can be successfully described by the Gallagher-Corrigan model, which describes the drug release in case of the erosion of the matrix and simultaneous diffusion. (Gallagher and Corrigan, 2000; Bugatti *et al.*, 2018) The model is reported in eq. 32.

$$X(t) = A + X_1\left(1 - e^{-C_1 t}\right) + X_2\left(\frac{e^{-C_2(t_{max}-t)}}{\left(1 + e^{-C_2(t_{max}-t)}\right)}\right) \quad (32)$$

where A is the burst, X_1 and X_2 are the fraction contribution of each step, C_1 and C_2 are the kinetic factors and t_{max} is the time after which there is a complete dissolution of the drug.

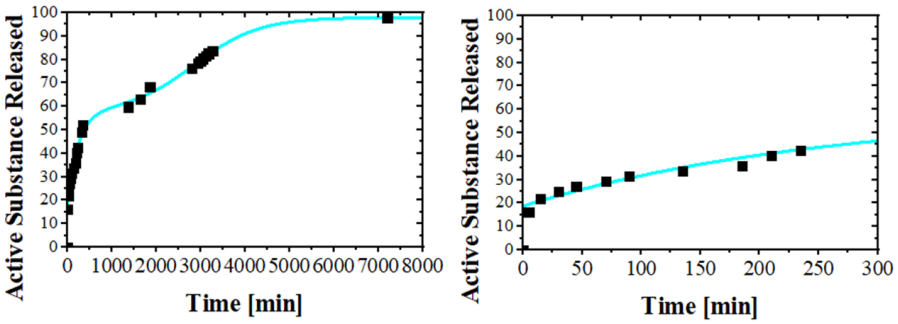

Figure V.80. *Release kinetics of PCL-1%AuM1/PVA Coaxial System*

The parameters of the models are reported below in Table 31.

Table V.32. *Parameters of Gallagher-Corrigan Model*

A []	0,179
X_1	0,394
C_1	2,38E-01
X_2	0,407
C_2	8,19E-02
t_{max}	47,56
R^2	0,9953

By comparing the results obtained for the coaxial system with the results obtained in Chapter IV for the 1%AuM1 membrane, in which the design enhances the burst effect, the difference is very evident (see **Figure V.81**).

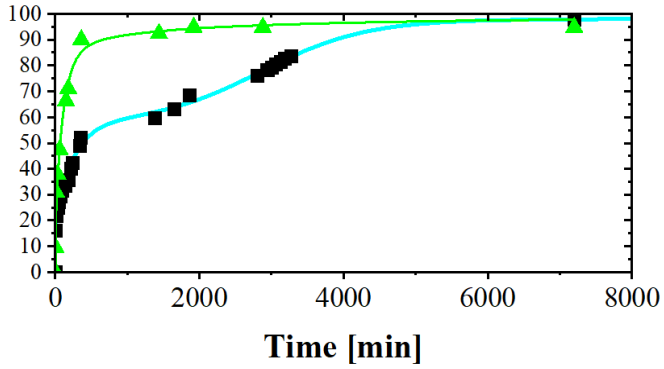

Figure V.81. *Drug Release of 1% AuM1 in uniaxial PCL and in coaxial PCL-PVA*

In accordance with the results obtained by release curves in **Figure V.80**, it has been possible to detect from molecular to macroscopic level what happens after each step of release. During the first step (see **Figure V.84**), PCL-PVA coaxial structure is present. Thanks to the solubility of PVA in water, the PVA erosion occurs, which is well evident both spectroscopically (see **Figure V.82**) and morphologically (see **Figure V.83**). In fact, after 16 hours of release, by looking at the Amplitude and Phase AFM images, it is possible to notice several differences compared to the membrane at time 0, recognizing much smoother fibers and the disappearance of the dots on the surface, due to the erosion of PVA. In FTIR spectrum, the PVA peaks have disappeared, but it is still possible to recognize the C-Cl bond peak due to AuM1 still included in the PCL structure. After 5 days of release, it is possible to observe that the PCL remains undamaged, the PVA is absent and AuM1, still visible in the previous step, is now absent since the drug is almost completely released in the surrounding environment.

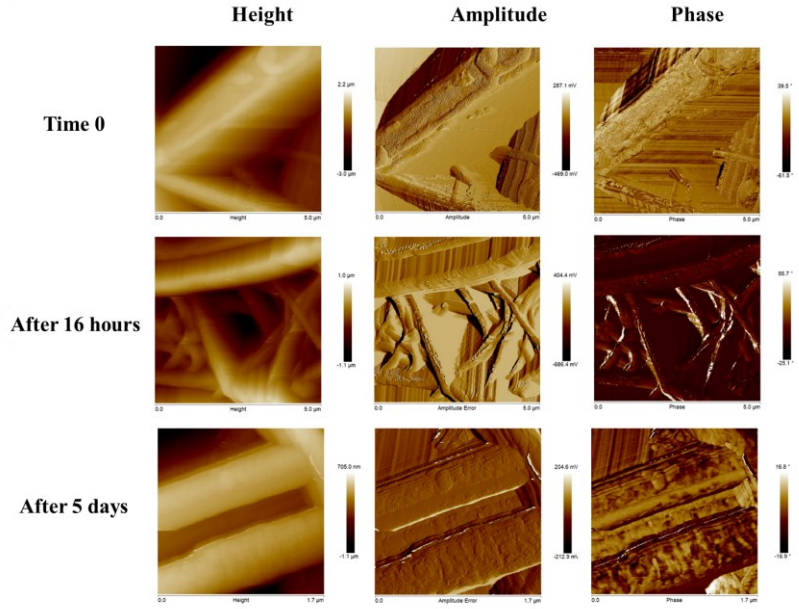

Figure V.82. *AFM of 1%AuM1-Coax after various time of release*

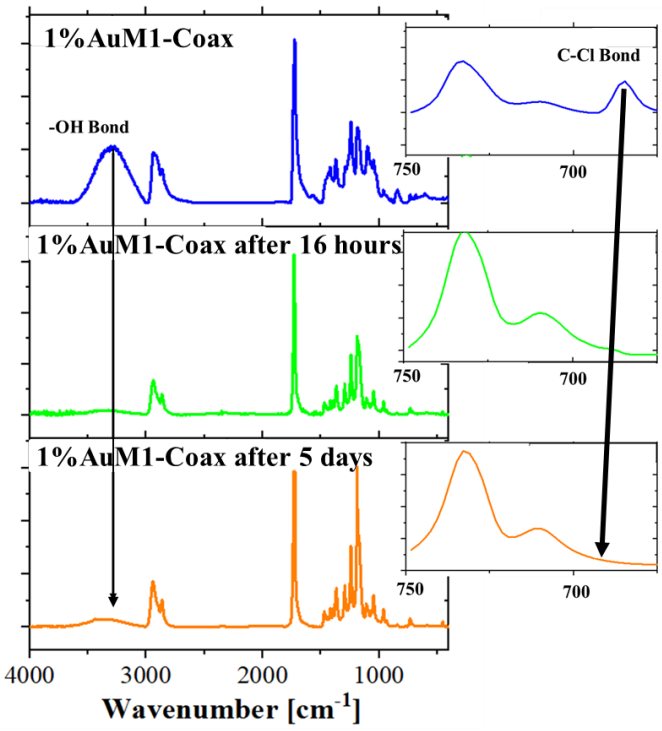

Figure V.83. *FTIR of 1%AuM1-Coax after various times of release*

From this analysis, FTIR, morphology, drug release and modeling are in perfect agreement with each other. In **Figure V.84**, an overview of the drug release of the system is given, from the spectroscopic, morphological and kinetic point of view.

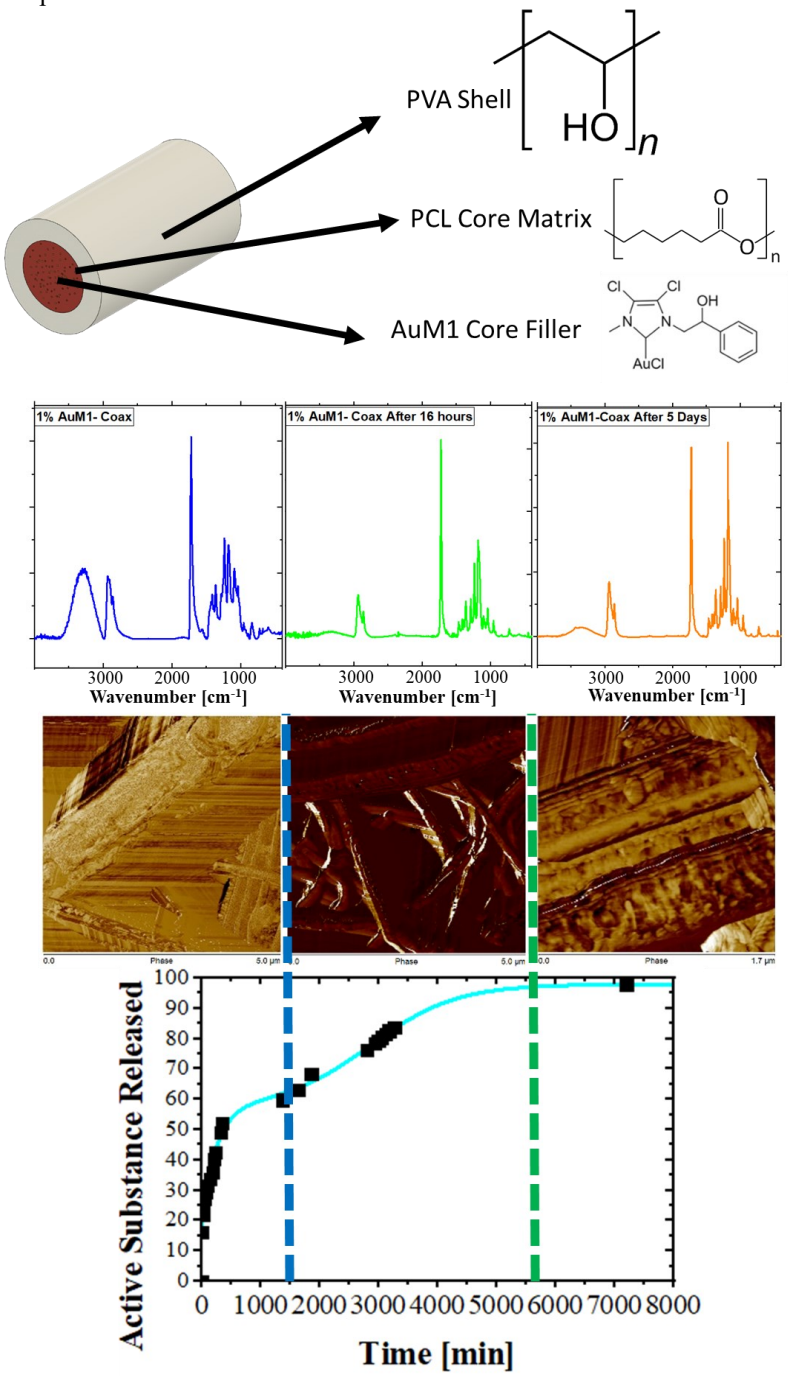

Figure V.84. *Overview of the morphology, spectroscopy and drug release of 1%AuM1-Coax after various time of release*

In conclusion, in the current chapter, the possibility of widely tuning the drug release of chemotherapy agents from electrospun membranes has been explored. The proposed strategies start from increasing the matrix-filler affinity to the use of different process configurations. The understanding of the electrospinning process, and the possibility to tune the drug release in the produced system, can be schematized as a flux diagram, reported in **Figure V.85**, to efficiently choose the process configuration and the matrix-filler system based on the desired characteristics.

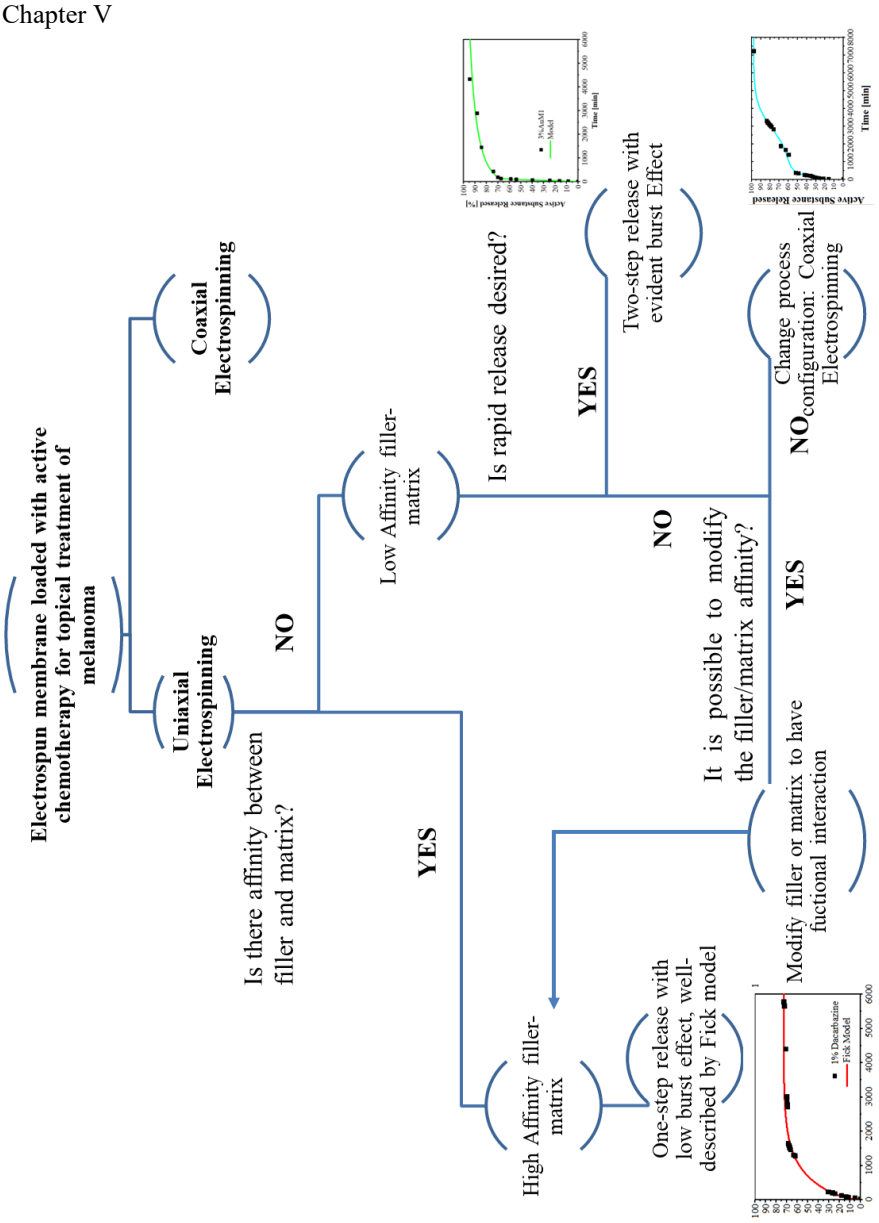

Figure V.85. *Flux diagram for the choice of the electrospun system based on the drug delivery characteristics.*

Final Conclusions

Conclusions

In conclusion, the current Ph. D. Thesis has highlighted the possibility to produce electrospun membranes, usable for biomedical applications, in particular for the topical treatment of melanoma.
To reach this goal, natural and synthetic biopolymers have been used, evidencing how the different process configurations, uniaxial and coaxial electrospinning affect the thermal, structural, and mechanical properties of the polymers.
Two types of fillers have been loaded in the electrospun systems: nanoparticles and active molecules.
Magnetic nanoparticles have been successfully embedded in nanofibrous systems, proving that the efficient dispersion of the nanofiller does not sensitively affect the morphology of the membrane. On the other hand, it has been evidenced that the nanoparticles affect the crystallinity of the membrane, varying so the mechanical properties from nanometric to the macroscopic level. Interestingly, cytotoxic tests have proved that these types of systems are effective against different types of tumoral cell lines, proving that this technology can be of great interest for topical treatments.
The second part of the activity has evidenced the possibility to design the release profile of the drug delivery system for highly active chemotherapeutic agents by considering the filler-matrix affinity and the process configuration.
For uniaxial electrospun membranes, two drugs with low affinity with the matrix have been chosen and loaded in different percentages in non—erodible electrospun membranes. In this case, two highly-promising synthetic gold complexes have been loaded in PCL electrospun membranes. By FESEM images, homogeneous morphology of the nanofibers has been observed, but interestingly AFM morphology has evidenced that the complex is placed on the surface of the nanofibers, leading to a highly-prominent burst effect and, in a second step, to a diffusive mechanism of release, as evidenced by the release kinetics and by the modelling.
In case of higher affinity between the drug and the matrix, a slower release is observed, that occurs toward a diffusive mechanism. In this case, Dacarbazine (drug of choice for melanoma treatment) and gold complex based on the Dacarbazine structure have been loaded in PCL electrospun membranes. FTIR analyses have evidenced an interaction between the Dacarbazine group and the PCL, and in fact, the AFM morphology does not show an increase in the fiber roughness, proving that the drug is successfully included in the fiber core thanks to the interaction with the PCL. This result is confirmed by the release kinetic, which is slower with no evident burst, and by the modelling, which has evidenced a Fickian profile. For all the

obtained systems, the antitumoral tests performed have evidenced the high cytotoxic activity against melanoma cell lines of the loaded nanofibrous systems.

However, another effective method to tune the release profile of a drug is modify the process configuration. Coaxial electrospinning has been proven to be an efficient approach to slow down the release kinetic in systems with low affinity between the drug and the matrix. In this case, coaxial fibers formed by a non-erodible core (PCL), loaded with an effective gold complex (with low affinity with PCL) and erodible shell (PVA) have been produced. AFM analysis has evidenced that, as expected, the drug is not present on the fiber surface, and in fact, the burst effect is not evident. In this case, a much slower, multistep release is observed, because of the erosion of the PVA (that occurs during the first step of release), whereas in the second step of release a diffusion between PCL and the environment is observed. By considering these factors, it is possible to efficiently design an antitumoral topical system. for having the desired release kinetic by considering the matrix-filler affinity and the process configuration.

References

Adeli-Sardou, M. *et al.* (2019) 'Controlled release of lawsone from polycaprolactone/gelatin electrospun nano fibers for skin tissue regeneration', *International Journal of Biological Macromolecules*, 124, pp. 478–491. doi: 10.1016/j.ijbiomac.2018.11.237.

Agarwal, A. *et al.* (2009) 'Nanoparticles as Novel Carrier for Brain Delivery: A Review', *Current Pharmaceutical Design*, 15(8). doi: 10.2174/138161209787582057.

Albarqi, H. A. *et al.* (2020) 'Systemically delivered magnetic hyperthermia for prostate cancer treatment', *Pharmaceutics*, 12(11), pp. 1–14. doi: 10.3390/pharmaceutics12111020.

Amarjargal, A. *et al.* (2013) 'Controlled assembly of superparamagnetic iron oxide nanoparticles on electrospun PU nanofibrous membrane: A novel heat-generating substrate for magnetic hyperthermia application', *European Polymer Journal*, 49(12). doi: 10.1016/j.eurpolymj.2013.08.026.

Ameer, J. M., Anil Kumar, P. R. and Kasoju, N. (2019) 'Strategies to tune electrospun scaffold porosity for effective cell response in tissue engineering', *Journal of Functional Biomaterials*. MDPI AG. doi: 10.3390/jfb10030030.

American Cancer Society (2020) *Current Grants by Cancer Type*.

Augustine, R., Kalarikkal, N. and Thomas, S. (2016) 'Effect of zinc oxide nanoparticles on the in vitro degradation of electrospun polycaprolactone membranes in simulated body fluid', *International Journal of Polymeric Materials and Polymeric Biomaterials*, 65(1). doi: 10.1080/00914037.2015.1055628.

Ayala, V. *et al.* (2013) 'Effect of surface charge on the colloidal stability and in vitro uptake of carboxymethyl dextran-coated iron oxide nanoparticles', *Journal of Nanoparticle Research*, 15(8). doi: 10.1007/s11051-013-1874-0.

Azman, M. F. and Azman, A. W. (2017) 'The Effect of Electrical Stimulation in Improving Muscle Tone (Clinical)', *IOP Conference Series: Materials Science and Engineering*, 260(1), p. 012020. doi: 10.1088/1757-899X/260/1/012020.

Bae, K. H., Chung, H. J. and Park, T. G. (2011) 'Nanomaterials for cancer therapy and imaging', *Molecules and Cells*, 31(4), pp. 295–302. doi: 10.1007/s10059-011-0051-5.

Baji, A. *et al.* (2007) 'Morphological and X-ray diffraction studies of crystalline hydroxyapatite-reinforced polycaprolactone', *Journal of Biomedical Materials Research - Part B Applied Biomaterials*, 81(2), pp. 343–350. doi: 10.1002/jbm.b.30671.

Behzadi, S. *et al.* (2017) 'Cellular uptake of nanoparticles: Journey inside the cell', *Chemical Society Reviews*, 46(14). doi: 10.1039/c6cs00636a.

Bernardi, R. J. *et al.* (2008) 'Immunonanoshells for targeted photothermal ablation in medulloblastoma and glioma: An in vitro evaluation using human cell lines', *Journal of Neuro-Oncology*, 86(2). doi: 10.1007/s11060-007-9467-3.
Bittiger, H., Marchessault, R. H. and Niegisch, W. D. (1970) 'No Crystal structure of poly-[epsilon]-caprolactoneTitle', *Acta Crystallographica Section B*, 26, pp. 1923–1927.
Boland, E. D. *et al.* (2005) 'Electrospinning polydioxanone for biomedical applications', *Acta Biomaterialia*, 1(1), pp. 115–123. doi: 10.1016/j.actbio.2004.09.003.
Braakhuis, H. M. *et al.* (2016) 'Identification of the appropriate dose metric for pulmonary inflammation of silver nanoparticles in an inhalation toxicity study', *Nanotoxicology*, 10(1), pp. 63–73. doi: 10.3109/17435390.2015.1012184.
Brasseur, F. *et al.* (1980) 'Actinomycin D adsorbed on polymethylcyanoacrylate nanoparticles: Increased efficiency against an experimental tumor', *European Journal of Cancer and Clinical Oncology*, 16(11), pp. 1441–1445. doi: 10.1016/0014-2964(80)90053-5.
Bugatti, V. *et al.* (2018) 'Antimicrobial Membranes of Bio-Based PA 11 and HNTs Filled with Lysozyme Obtained by an Electrospinning Process', *Nanomaterials*, 8(3). doi: 10.3390/NANO8030139.
Buzea, C., Pacheco, I. and Robbie, K. (2007) 'Nanomaterials and nanoparticles: sources and toxicity', *Biointerphases*, 2(4), pp. MR17–MR71. doi: 10.1116/1.2815690.
Cacciotti, I. *et al.* (2014) 'Effect of silver nanoparticles and cellulose nanocrystals on electrospun poly(lactic) acid mats: Morphology, thermal properties and mechanical behavior', *Carbohydrate Polymers*, 103(1). doi: 10.1016/j.carbpol.2013.11.052.
Campardelli, R. *et al.* (2013) 'Encapsulation of titanium dioxide nanoparticles in PLA microspheres using supercritical emulsion extraction to produce bactericidal nanocomposites', *Journal of Nanoparticle Research*, 15(10), pp. 1–11. doi: 10.1007/s11051-013-1987-5.
Campardelli, R. *et al.* (2014) 'Au-PLA nanocomposites for photothermally controlled drug delivery', *Journal of Materials Chemistry B*, 2(4), pp. 409–417. doi: 10.1039/c3tb21099e.
Campelo, S. *et al.* (2017) 'An evaluation of irreversible electroporation thresholds in human prostate cancer and potential correlations to physiological measurements', *APL Bioengineering*, 1(1). doi: 10.1063/1.5005828.
Cannon, R. *et al.* (2013) 'Safety and early efficacy of irreversible electroporation for hepatic tumors in proximity to vital structures', *Journal of Surgical Oncology*, 107(5). doi: 10.1002/jso.23280.
Carpin, L. B. *et al.* (2011) 'Immunoconjugated gold nanoshell-mediated photothermal ablation of trastuzumab-resistant breast cancer cells', *Breast*

Cancer Research and Treatment, 125(1). doi: 10.1007/s10549-010-0811-5.
Carrillo-Cazares, A. *et al.* (2017) 'Study of the Optical Properties of Functionalized Gold Nanoparticles in Different Tissues and Their Correlation with the Temperature Increase', *Journal of Nanomaterials*, 2017. doi: 10.1155/2017/3628970.
Catauro, M. and Pacifico, S. (2017) 'Synthesis of bioactive chlorogenic acid-silica hybrid materials via the sol-gel route and evaluation of their biocompatibility', *Materials*, 10(7). doi: 10.3390/ma10070840.
Cellai, F. *et al.* (2017) 'Magnetic hyperthermia and oxidative damage to dna of human hepatocarcinoma cells', *International Journal of Molecular Sciences*, 18(5). doi: 10.3390/ijms18050939.
Ceramella, J. *et al.* (2020) 'From coins to cancer therapy: Gold, silver and copper complexes targeting human topoisomerases', *Bioorganic and Medicinal Chemistry Letters*, 30(3), p. 126905. doi: 10.1016/j.bmcl.2019.126905.
Ceramella, J. *et al.* (2022) 'Novel Au Carbene Complexes as Promising Multi-Target Agents in Breast Cancer Treatment', *Pharmaceuticals*, 15(5), p. 507. doi: 10.3390/PH15050507/S1.
Chan, S. Y. *et al.* (2017) 'Electrospun Pectin-Polyhydroxybutyrate Nanofibers for Retinal Tissue Engineering', *ACS Omega*, 2(12), pp. 8959–8968. doi: 10.1021/ACSOMEGA.7B01604.
Chang, D. *et al.* (2018) 'Biologically targeted magnetic hyperthermia: Potential and limitations', *Frontiers in Pharmacology*, 9(AUG), p. 831. doi: 10.3389/fphar.2018.00831.
Chang, S. H. *et al.* (2021) 'Imiquimod Accelerated Antitumor Response by Targeting Lysosome Adaptation in Skin Cancer Cells', *Journal of Investigative Dermatology*, 141(9), pp. 2219-2228.e8. doi: 10.1016/J.JID.2021.01.034.
Charitidis, C. A. *et al.* (2019) 'Synthesis, nanomechanical characterization and biocompatibility of a chitosan-graft-poly(e- caprolactone) copolymer for soft tissue regeneration', *Materials*, 12(1). doi: 10.3390/MA12010150.
Chastellain, M., Petri, A. and Hofmann, H. (2004) 'Particle size investigations of a multistep synthesis of PVA coated superparamagnetic nanoparticles', *Journal of Colloid and Interface Science*, 278(2). doi: 10.1016/j.jcis.2004.06.025.
Chen, S. and Kimura, K. (1999) 'Synthesis and Characterization of Carboxylate-Modified Gold Nanoparticle Powders Dispersible in Water', *Langmuir*, 15(4). doi: 10.1021/la9812828.
Chen, Y. W. *et al.* (2016) 'Functionalized graphene nanocomposites for enhancing photothermal therapy in tumor treatment', *Advanced Drug Delivery Reviews*, 105, pp. 190–204. doi: 10.1016/j.addr.2016.05.022.
Cheng, M. *et al.* (2014) 'Gold nanorod-embedded electrospun fibrous membrane as a photothermal therapy platform', *ACS Applied Materials and Interfaces*, 6(3). doi: 10.1021/am405839b.

Cherukuri, P., Glazer, E. S. and Curley, S. A. (2010) 'Targeted hyperthermia using metal nanoparticles', *Advanced Drug Delivery Reviews*, 62(3), pp. 339–345. doi: 10.1016/j.addr.2009.11.006.
Chis, M. *et al.* (2016) 'UV-VIS PH DEPENDENCE OF DACARBAZINE: EXPERIMENTAL AND TD-DFT INVESTIGATIONS', *Studia Ubb Physica*, 61, pp. 9–19.
Chithrani, B. D., Ghazani, A. A. and Chan, W. C. W. (2006) 'Determining the size and shape dependence of gold nanoparticle uptake into mammalian cells', *Nano Letters*, 6(4). doi: 10.1021/nl052396o.
Chung, H. J. *et al.* (2018) 'Transferrin as a thermosensitizer in radiofrequency hyperthermia for cancer treatment', *Scientific Reports 2018 8:1*, 8(1), pp. 1–11. doi: 10.1038/s41598-018-31232-9.
Church, T. J. and Haines, S. T. (2016) 'Treatment Approach to Patients With Severe Insulin Resistance', *Clinical Diabetes*, 34(2), pp. 97–104. doi: 10.2337/DIACLIN.34.2.97.
Ciaglia, E. *et al.* (2019) 'A bioavailability study on microbeads and nanoliposomes fabricated by dense carbon dioxide technologies using human-primary monocytes and flow cytometry assay', *International Journal of Pharmaceutics*, 570, p. 118686. doi: 10.1016/j.ijpharm.2019.118686.
Ciardulli, M. C. *et al.* (2021) '3d biomimetic scaffold for growth factor controlled delivery: An in-vitro study of tenogenic events on wharton's jelly mesenchymal stem cells', *Pharmaceutics*, 13(9), p. 1448. doi: 10.3390/PHARMACEUTICS13091448/S1.
Coimbra, P. *et al.* (2017) 'Coaxial electrospun PCL/Gelatin-MA fibers as scaffolds for vascular tissue engineering', *Colloids and Surfaces B: Biointerfaces*, 159, pp. 7–15. doi: 10.1016/j.colsurfb.2017.07.065.
Connor, E. E. *et al.* (2005) 'Gold nanoparticles are taken up by human cells but do not cause acute cytotoxicity', *Small*, 1(3). doi: 10.1002/smll.200400093.
Correia, D. M. *et al.* (2013) 'Thermal and hydrolytic degradation of electrospun fish gelatin membranes', *Polymer Testing*, 32(5), pp. 995–1000. doi: 10.1016/j.polymertesting.2013.05.004.
Costabile, C. *et al.* (2021) 'A green approach for A 3-coupling reactions: an experimental and theoretical study on NHC silver and gold catalysts †', *New J. Chem*, 45, p. 18509. doi: 10.1039/d1nj03444h.
'COUNCIL RECOMMENDATION of 2 December 2003 on cancer screening' (2003).
Couvreur, P. *et al.* (1977) 'Nanocapsules: A new type of lysosomotropic carrier', *FEBS Letters*, 84(2), pp. 323–326. doi: 10.1016/0014-5793(77)80717-5.
Couvreur, P. *et al.* (1982) 'Toxicity of polyalkylcyanoacrylate nanoparticles II: Doxorubicin-loaded nanoparticles', *Journal of Pharmaceutical Sciences*, 71(7), pp. 790–792. doi: 10.1002/jps.2600710717.
Cricchio, V. *et al.* (2017) 'Novel Superparamagnetic Microdevices Based on

Magnetized PLGA/PLA Microparticles Obtained by Supercritical Fluid Emulsion and Coating by Carboxybetaine-Functionalized Chitosan Allowing the Tuneable Release of Therapeutics', *Journal of Pharmaceutical Sciences*, 106(8), pp. 2097–2105. doi: 10.1016/j.xphs.2017.05.005.

Dan, M. *et al.* (2015) 'Alternating Magnetic Field-Induced Hyperthermia Increases Iron Oxide Nanoparticle Cell Association/Uptake and Flux in Blood-Brain Barrier Models', *Pharmaceutical Research*, 32(5). doi: 10.1007/s11095-014-1561-6.

Denardo, S. J. *et al.* (2007) 'Thermal Dosimetry Predictive of Efficacy of 111 In-ChL6 Nanoparticle AMF-Induced Thermoablative Therapy for Human Breast Cancer in Mice', *J Nucl Med*, 48, pp. 437–444.

Deptuła, M. *et al.* (2019) 'Wound healing complications in oncological patients: perspectives for cellular therapy', *Advances in Dermatology and Allergology/Postępy Dermatologii i Alergologii*, 36(2), p. 139. doi: 10.5114/ADA.2018.72585.

Desoize, B. (2004) 'Metals and metal compounds in cancer treatment - PubMed', *Anticancer Research*, 24, pp. 1529–1544.

Ding, S. *et al.* (2020) 'Overcoming blood–brain barrier transport: Advances in nanoparticle-based drug delivery strategies', *Materials Today*, 37, pp. 112–125. doi: 10.1016/J.MATTOD.2020.02.001.

Directorate-General for Research and Innovation (2020) *Conquering cancer: Mission Possible*.

Dogan, A. B., Dabkowski, K. E. and von Recum, H. A. (2022) 'Leveraging Affinity Interactions to Prolong Drug Delivery of Protein Therapeutics', *Pharmaceutics 2022, Vol. 14, Page 1088*, 14(5), p. 1088. doi: 10.3390/PHARMACEUTICS14051088.

Drobota, M. *et al.* (2020) 'Preparation and Characterization of Electrospun Collagen Based Composites for Biomedical Applications', *Materials*, 13(18), p. 3961. doi: 10.3390/ma13183961.

Dummer, R. *et al.* (2015) 'Cutaneous melanoma: ESMO Clinical Practice Guidelines for diagnosis, treatment and follow-up', *Annals of oncology : official journal of the European Society for Medical Oncology*, 26 Suppl 5, pp. v126–v132. doi: 10.1093/ANNONC/MDV297.

Dung, D. T. K. *et al.* (2009) 'Preparation and characterization of magnetic nanoparticles with chitosan coating', *Journal of Physics: Conference Series*, 187. doi: 10.1088/1742-6596/187/1/012036.

Dutz, S. and Hergt, R. (2013) 'Magnetic nanoparticle heating and heat transfer on a microscale: Basic principles, realities and physical limitations of hyperthermia for tumour therapy', *International Journal of Hyperthermia*, 29(8). doi: 10.3109/02656736.2013.822993.

Edhemovic, I. *et al.* (2011) 'Electrochemotherapy: A new technological approach in treatment of metastases in the liver', *Technology in Cancer Research and Treatment*, 10(5). doi: 10.7785/tcrt.2012.500224.

Eichhorn, S. J. and Sampson, W. W. (2005) 'Statistical geometry of pores

and statistics of porous nanofibrous assemblies', *Journal of the Royal Society Interface*. Royal Society, pp. 309–318. doi: 10.1098/rsif.2005.0039.
Elkhoury, K. *et al.* (2019) 'Soft-Nanoparticle Functionalized Natural Hydrogels for Tissue Engineering Applications', *Advanced healthcare materials*, 8(18), p. e1900506. doi: 10.1002/ADHM.201900506.
Epstein, J. B. *et al.* (2012) 'Oral complications of cancer and cancer therapy', *CA: A Cancer Journal for Clinicians*, 62(6), pp. 400–422. doi: 10.3322/CAAC.21157.
Esmaeili, N. and Friebe, M. (2019) 'Electrochemotherapy: A Review of Current Status, Alternative IGP Approaches, and Future Perspectives', *Journal of Healthcare Engineering*, 2019. doi: 10.1155/2019/2784516.
Etemadi, H. and Plieger, P. G. (2020) 'Magnetic Fluid Hyperthermia Based on Magnetic Nanoparticles: Physical Characteristics, Historical Perspective, Clinical Trials, Technological Challenges, and Recent Advances', *Advanced Therapeutics*, 3(11), p. 2000061. doi: 10.1002/adtp.202000061.
Eurostat (2017) *Causes of death - deaths by country of residence and occurrence*.
Faramarzi, N. *et al.* (2018) 'Patient-Specific Bioinks for 3D Bioprinting of Tissue Engineering Scaffolds', *Advanced healthcare materials*, 7(11). doi: 10.1002/ADHM.201701347.
Farzin, A. *et al.* (2020) 'Magnetic Nanoparticles in Cancer Therapy and Diagnosis', *Advanced Healthcare Materials*, 9(9). doi: 10.1002/adhm.201901058.
Feng, L. and Kamal, M. R. (2004) 'Distributions of crystal size from DSC melting traces for polyethylenes', *Canadian Journal of Chemical Engineering*, 82(6), pp. 1239–1251. doi: 10.1002/cjce.5450820611.
Feng, X. *et al.* (2019) 'Electrospun polymer micro/nanofibers as pharmaceutical repositories for healthcare', *Journal of Controlled Release*, 302, pp. 19–41. doi: 10.1016/J.JCONREL.2019.03.020.
Fratoddi, I. (2018) 'Hydrophobic and hydrophilic au and ag nanoparticles. Breakthroughs and perspectives', *Nanomaterials*. MDPI AG, p. 11. doi: 10.3390/nano8010011.
Fröhlich, E. (2012) 'The role of surface charge in cellular uptake and cytotoxicity of medical nanoparticles', *International Journal of Nanomedicine*, 7, pp. 5577–5591. doi: 10.2147/IJN.S36111.
Fu, A. S. *et al.* (2011) 'Experimental Studies and Modeling of Drug Release from a Tunable Affinity-Based Drug Delivery Platform', *Annals of Biomedical Engineering*, 39, pp. 2466–2475. doi: 10.1007/s10439-011-0336-z.
Fujita, S. (2004) 'Silver Halide Crystals. Photo-Sensitivity', *Organic Chemistry of Photography*, pp. 75–92. doi: 10.1007/978-3-662-09130-2_4.
Fung, S. K. *et al.* (2017) 'Cyclometalated Gold(III) Complexes Containing N-Heterocyclic Carbene Ligands Engage Multiple Anti-Cancer Molecular Targets', *Angewandte Chemie (International ed. in English)*, 56(14), pp.

3892–3896. doi: 10.1002/ANIE.201612583.
Funk, R. K., Stockham, A. L. and Laack, N. N. I. (2016) 'Basics of Radiation Therapy', in *Clinical Cardio-oncology*. Elsevier Inc., pp. 39–60. doi: 10.1016/B978-0-323-44227-5.00003-X.
Gallagher, K. M. and Corrigan, O. I. (2000) 'Mechanistic aspects of the release of levamisole hydrochloride from biodegradable polymers', *Journal of Controlled Release*, 69(2), pp. 261–272. doi: 10.1016/S0168-3659(00)00305-9.
Garcia, P. A. *et al.* (2016) 'Microfluidic screening of electric fields for electroporation', *Scientific Reports*, 6(1), pp. 1–11. doi: 10.1038/srep21238.
Gautam, S., Dinda, A. K. and Mishra, N. C. (2013) 'Fabrication and characterization of PCL/gelatin composite nanofibrous scaffold for tissue engineering applications by electrospinning method', *Materials Science and Engineering C*, 33(3), pp. 1228–1235. doi: 10.1016/j.msec.2012.12.015.
Gehl, J. *et al.* (1999) 'In vivo electroporation of skeletal muscle: Threshold, efficacy and relation to electric field distribution', *Biochimica et Biophysica Acta - General Subjects*, 1428(2–3). doi: 10.1016/S0304-4165(99)00094-X.
Genchi, G. G. *et al.* (2017) 'Smart materials meet multifunctional biomedical devices: Current and prospective implications for nanomedicine', *Frontiers in Bioengineering and Biotechnology*, 5, p. 80. doi: 10.3389/fbioe.2017.00080.
Gibot, L. *et al.* (2013) 'Antitumor drug delivery in multicellular spheroids by electropermeabilization', *Journal of Controlled Release*, 167(2). doi: 10.1016/j.jconrel.2013.01.021.
Gilbert, R. A., Jaroszeski, M. J. and Heller, R. (1997) 'Novel electrode designs for electrochemotherapy', *Biochimica et Biophysica Acta - General Subjects*, 1334(1). doi: 10.1016/S0304-4165(96)00119-5.
Goki, E. (2006) 'Effects of Solution Rheology on Electrospinning of Polystyrene', *Worchester Polythecnic Institute*, Msc Thesis.
Gorrasi, G., Longo, R. and Viscusi, G. (2020) 'Fabrication and Characterization of Electrospun Membranes Based on "Poly(ε-caprolactone)", "Poly(3-hydroxybutyrate)" and Their Blend for Tunable Drug Delivery of Curcumin', *Polymers*, 12(10), p. 2239. doi: 10.3390/polym12102239.
Gothelf, A., Mir, L. M. and Gehl, J. (2003) 'Electrochemotherapy: Results of cancer treatment using enhanced delivery of bleomycin by electroporation', *Cancer Treatment Reviews*, 29(5). doi: 10.1016/S0305-7372(03)00073-2.
Gottlieb, N. L. (1982) 'Comparative pharmacokinetics of parenteral and oral gold compounds', *Journal of Rheumatology*, 8, pp. 99–109.
Guadagno, L. *et al.* (2006) 'Morphology and Elasticity of Oriented Syndiotactic Polypropylene from Solvent Cast Films'. doi: 10.1021/cg0601103.
Guadagno, L. *et al.* (2019) 'materials UV Irradiated Graphene-Based Nanocomposites: Change in the Mechanical Properties by Local HarmoniX

Atomic Force Microscopy Detection'. doi: 10.3390/ma12060962.
Guadagno, L. *et al.* (2020) 'Development and characterization of antitumoral electrospun polycaprolactone/functionalized Fe3O4 hybrid membranes', *Materials Today Chemistry*, 17, p. 100309. doi: 10.1016/j.mtchem.2020.100309.
Guadagno, L. *et al.* (2022) 'Electrospun Membranes Designed for Burst Release of New Gold-Complexes Inducing Apoptosis of Melanoma Cells', *International Journal of Molecular Sciences 2022, Vol. 23, Page 7147*, 23(13), p. 7147. doi: 10.3390/IJMS23137147.
Guo, T. *et al.* (2018) 'The recent advances of magnetic nanoparticles in medicine', *Journal of Nanomaterials*, 2018. doi: 10.1155/2018/7805147.
Guo, W. *et al.* (2017) 'Down-regulated miR-23a Contributes to the Metastasis of Cutaneous Melanoma by Promoting Autophagy', *Theranostics*, 7(8). doi: 10.7150/thno.18835.
Ha, P. T. *et al.* (2019) 'Doxorubicin release by magnetic inductive heating and in vivo hyperthermia-chemotherapy combined cancer treatment of multifunctional magnetic nanoparticles', *New Journal of Chemistry*, 43(14). doi: 10.1039/C9NJ00111E.
Han, D. and Steckl, A. J. (2019a) 'Coaxial Electrospinning Formation of Complex Polymer Fibers and their Applications', *ChemPlusChem*, 84(10), pp. 1453–1497. doi: 10.1002/CPLU.201900281.
Han, D. and Steckl, A. J. (2019b) 'Coaxial Electrospinning Formation of Complex Polymer Fibers and their Applications', *ChemPlusChem*, 84(10), pp. 1453–1497. doi: 10.1002/CPLU.201900281.
Harlepp, S. *et al.* (2019) 'N-Heterocyclic Carbene-Platinum Complexes Featuring an Anthracenyl Moiety: Anti-Cancer Activity and DNA Interaction', *International Journal of Molecular Sciences*, 20(17). doi: 10.3390/IJMS20174198.
Havlíček, K. *et al.* (2020) 'Influence of electrospinning methods on characteristics of polyvinyl butyral and polyurethane nanofibres essential for biological applications', *Materials and Design*, 194, p. 108898. doi: 10.1016/j.matdes.2020.108898.
Held, G. A. *et al.* (2001) 'Competing interactions in dispersions of superparamagnetic nanoparticles', *Physical Review B - Condensed Matter and Materials Physics*, 64(1), pp. 124081–124084. doi: 10.1103/physrevb.64.012408.
Heller, R. *et al.* (1998) 'Treatment of cutaneous and subcutaneous tumors with electrochemotherapy using intralesional bleomycin', *Cancer*, 83(1). doi: 10.1002/(SICI)1097-0142(19980701)83:1<148::AID-CNCR20>3.0.CO;2-W.
Heller, R., Gilbert, R. and Jaroszeski, M. J. (1999) 'Clinical applications of electrochemotherapy', *Advanced Drug Delivery Reviews*, 35(1), pp. 119–129. doi: 10.1016/S0169-409X(98)00067-2.
Hilger, I. (2013) 'In vivo applications of magnetic nanoparticle

hyperthermia', *International Journal of Hyperthermia*, 29(8). doi: 10.3109/02656736.2013.832815.
Hindi, K. M. *et al.* (2009) 'The Medicinal Applications of Imidazolium Carbene−Metal Complexes', *Chemical Reviews*, 109(8), pp. 3859–3884. doi: 10.1021/CR800500U.
Hlaing, M. *et al.* (2016) 'Absorption and scattering cross-section extinction values of silver nanoparticles', *Optical Materials*, 58. doi: 10.1016/j.optmat.2016.06.013.
Ho, M. H. *et al.* (2014) 'The morphology and degradation behavior of electrospun poly(3- hydroxybutyrate)/Magnetite and poly(3-hydroxybutyrate-co-3-hydroxyvalerate)/ Magnetite composites', *Journal of Applied Polymer Science*, 131(22). doi: 10.1002/app.41070.
Hoi-Kuan Lao, † *et al.* (2006) 'Modification of Poly(3-hydroxybutyrate-co-3-hydroxyvalerate) Film by Chemical Graft Copolymerization', *Biomacromolecules*, 8(2), pp. 416–423. doi: 10.1021/BM0609700.
Honary, S. and Zahir, F. (2013) 'Effect of zeta potential on the properties of nano-drug delivery systems - A review (Part 1)', *Tropical Journal of Pharmaceutical Research*, 12(2), pp. 255–264. doi: 10.4314/tjpr.v12i2.19.
Hong, N. H. (2019) 'Introduction to Nanomaterials: Basic Properties, Synthesis, and Characterization', *Nano-sized Multifunctional Materials: Synthesis, Properties and Applications*, pp. 1–19. doi: 10.1016/B978-0-12-813934-9.00001-3.
Hu, H. *et al.* (2013) 'Synergic effect of magnetic nanoparticles on the electrospun aligned superparamagnetic nanofibers as a potential tissue engineering scaffold', *RSC Advances*, 3(3). doi: 10.1039/c2ra22726f.
Huang, S. *et al.* (2014) 'Gold nanoparticles electroporation enhanced polyplex delivery to mammalian cells', *Electrophoresis*, 35(12–13). doi: 10.1002/elps.201300617.
Huang, X. *et al.* (2011) 'The shape effect of mesoporous silica nanoparticles on biodistribution, clearance, and biocompatibility in vivo', *ACS Nano*, 5(7), pp. 5390–5399. doi: 10.1021/nn200365a.
Huang, X. and El-Sayed, M. A. (2010) 'Gold nanoparticles: Optical properties and implementations in cancer diagnosis and photothermal therapy', *Journal of Advanced Research*, 1(1). doi: 10.1016/j.jare.2010.02.002.
Iacopetta, D. *et al.* (2017) 'Novel Gold and Silver Carbene Complexes Exert Antitumor Effects Triggering the Reactive Oxygen Species Dependent Intrinsic Apoptotic Pathway', *ChemMedChem*, 12(24), pp. 2054–2065. doi: 10.1002/CMDC.201700634.
Iacopetta, D. *et al.* (2020) 'Is the way to fight cancer paved with gold? Metal-based carbene complexes with multiple and fascinating biological features', *Pharmaceuticals*, 13(5). doi: 10.3390/ph13050091.
Iacopetta, D. *et al.* (no date) *Old Drug Scaffold, New Activity:T halidomide-Correlated Compounds Exert Different Effects on Breast Cancer Cell*

Growth and Progression.
Ignatova, M. G. *et al.* (2010) 'Electrospun nanofibrous mats containing quaternized chitosan and polylactide with in vitro antitumor activity against hela cells', *Biomacromolecules*, 11(6), pp. 1633–1645. doi: 10.1021/bm100285n.
Institute for Health Metrics and Evaluation (2018) *Global Burden of Disease*.
Irani, M., Mir Mohamad Sadeghi, G. and Haririan, I. (2017) 'Electrospun biocompatible poly (ε-caprolactonediol)-based polyurethane core/shell nanofibrous scaffold for controlled release of temozolomide', *https://doi.org/10.1080/00914037.2017.1331350*, 67(6), pp. 361–366. doi: 10.1080/00914037.2017.1331350.
Istituto Superiore di Sanità (2020) *Characteristics of SARS-CoV-2 patients dying in Italy Report based on available data on September 7 th , 2020*.
Ivkov, R. *et al.* (2006) 'Development of tumor targeting magnetic nanoparticles for cancer therapy', in *2006 NSTI Nanotechnology Conference and Trade Show - NSTI Nanotech 2006 Technical Proceedings*, pp. 21–24.
Jain, P. K. *et al.* (2006) 'Calculated absorption and scattering properties of gold nanoparticles of different size, shape, and composition: Applications in biological imaging and biomedicine', *Journal of Physical Chemistry B*, 110(14). doi: 10.1021/jp057170o.
Jalaja, K. *et al.* (2016) 'Potential of electrospun core–shell structured gelatin–chitosan nanofibers for biomedical applications', *Carbohydrate Polymers*, 136, pp. 1098–1107. doi: 10.1016/J.CARBPOL.2015.10.014.
Jeznach, O., Kolbuk, D. and Sajkiewicz, P. (2019) 'Aminolysis of Various Aliphatic Polyesters in a Form of Nanofibers and Films', *Polymers 2019, Vol. 11, Page 1669*, 11(10), p. 1669. doi: 10.3390/POLYM11101669.
Jiang, W. *et al.* (2008) 'Nanoparticle-mediated cellular response is size-dependent', *Nature Nanotechnology*, 3(3), pp. 145–150. doi: 10.1038/nnano.2008.30.
Jin, Y. *et al.* (2010) 'Fabrication of necklace-like structures via electrospinning', *Langmuir*, 26(2). doi: 10.1021/la902313t.
Jo, D. H. *et al.* (2015) 'Size, surface charge, and shape determine therapeutic effects of nanoparticles on brain and retinal diseases', *Nanomedicine: Nanotechnology, Biology, and Medicine*. Elsevier Inc., pp. 1603–1611. doi: 10.1016/j.nano.2015.04.015.
De Jong, W. H. *et al.* (2008) 'Particle size-dependent organ distribution of gold nanoparticles after intravenous administration', *Biomaterials*, 29(12), pp. 1912–1919. doi: 10.1016/j.biomaterials.2007.12.037.
Joniec, A., Sek, S. and Krysinski, P. (2016) 'Magnetoliposomes as Potential Carriers of Doxorubicin to Tumours', *Chemistry - A European Journal*, 22(49), pp. 17715–17724. doi: 10.1002/chem.201602809.
Jordan, A. *et al.* (2006) 'The effect of thermotherapy using magnetic nanoparticles on rat malignant glioma', *Journal of Neuro-Oncology*, 78(1).

doi: 10.1007/s11060-005-9059-z.
Ju, Y. *et al.* (2017) 'Monodisperse Au-Fe2C Janus Nanoparticles: An Attractive Multifunctional Material for Triple-Modal Imaging-Guided Tumor Photothermal Therapy', *ACS Nano*, 11(9), pp. 9239–9248. doi: 10.1021/acsnano.7b04461.
Jurašin, D. D. *et al.* (2016) 'Surface coating affects behavior of metallic nanoparticles in a biological environment', *Beilstein Journal of Nanotechnology*, 7(1), pp. 246–262. doi: 10.3762/bjnano.7.23.
Kaidar-Person, O., Bar-Sela, G. and Person, B. (2011) 'The two major epidemics of the twenty-first century: obesity and cancer', *Obesity surgery*, 21(11), pp. 1792–1797. doi: 10.1007/S11695-011-0490-2.
Kamath, S. D., Kircher, S. M. and Benson, A. B. (2019) 'Comparison of Cancer Burden and Nonprofit Organization Funding Reveals Disparities in Funding Across Cancer Types', *Journal of the National Comprehensive Cancer Network : JNCCN*, 17(7), pp. 849–854. doi: 10.6004/JNCCN.2018.7280.
Kim, H. *et al.* (2014) 'Mechanically-reinforced electrospun composite silk fibroin nanofibers containing hydroxyapatite nanoparticles', *Materials Science and Engineering C*, 40. doi: 10.1016/j.msec.2014.04.012.
Kim, K. and Lee, W. G. (2017) 'Electroporation for nanomedicine: a review', *Journal of Materials Chemistry B*, 5(15). doi: 10.1039/c7tb00038c.
Kobayashi, H., Watanabe, R. and Choyke, P. L. (2014) 'Improving conventional enhanced permeability and retention (EPR) effects; What is the appropriate target?', *Theranostics*, 4(1). doi: 10.7150/thno.7193.
Kobayashi, K. *et al.* (2014) 'Surface engineering of nanoparticles for therapeutic applications', *Polymer Journal*, 46, pp. 460–468. doi: 10.1038/pj.2014.40.
Kotnik, T. *et al.* (2012) 'Cell membrane electroporation - Part 1: The phenomenon', *IEEE Electrical Insulation Magazine*, 28(5). doi: 10.1109/MEI.2012.6268438.
Kowalik, P. *et al.* (2020) 'Yttrium-Doped Iron Oxide Nanoparticles for Magnetic Hyperthermia Applications', *Journal of Physical Chemistry C*, 124(12), pp. 6871–6883. doi: 10.1021/acs.jpcc.9b11043.
Krishnan, K. M. (2010) 'Biomedical nanomagnetics: A spin through possibilities in imaging, diagnostics, and therapy', *IEEE Transactions on Magnetics*, 46(7). doi: 10.1109/TMAG.2010.2046907.
Lage, H., Aki-Sener, E. and Yalcin, I. (2006) 'High antineoplastic activity of new heterocyclic compounds in cancer cells with resistance against classical DNA topoisomerase II-targeting drugs', *International journal of cancer*, 119(1), pp. 213–220. doi: 10.1002/IJC.21792.
Lamparelli, E. P. *et al.* (2021) 'Chondrogenic Commitment of Human Bone Marrow Mesenchymal Stem Cells in a Perfused Collagen Hydrogel Functionalized with hTGF-β1-Releasing PLGA Microcarrier', *Pharmaceutics 2021, Vol. 13, Page 399*, 13(3), p. 399. doi:

10.3390/PHARMACEUTICS13030399.
Lan, X. *et al.* (2021) 'Multidrug-loaded electrospun micro/nanofibrous membranes: Fabrication strategies, release behaviors and applications in regenerative medicine', *Journal of Controlled Release*, 330, pp. 1264–1287. doi: 10.1016/J.JCONREL.2020.11.036.
Laurent, S. *et al.* (2011) 'Magnetic fluid hyperthermia: Focus on superparamagnetic iron oxide nanoparticles', *Advances in Colloid and Interface Science*, 166(1–2). doi: 10.1016/j.cis.2011.04.003.
Lee, H. W. *et al.* (2009) 'Electrospinning fabrication and characterization of Poly(vinyl alcohol)/montmorillonite nanofiber mats', *Journal of Applied Polymer Science*, 113(3). doi: 10.1002/app.30165.
Lee, L. *et al.* (2020) 'COVID-19 prevalence and mortality in patients with cancer and the effect of primary tumour subtype and patient demographics: a prospective cohort study', *The Lancet. Oncology*, 21(10), pp. 1309–1316. doi: 10.1016/S1470-2045(20)30442-3.
Lee, S. H. *et al.* (2008) 'Amine-functionalized gold nanoparticles as non-cytotoxic and efficient intracellular siRNA delivery carriers', *International Journal of Pharmaceutics*, 364(1). doi: 10.1016/j.ijpharm.2008.07.027.
Lee, S. M., Park, H. and Yoo, K. H. (2010) 'Synergistic cancer therapeutic effects of locally delivered drug and heat using multifunctional nanoparticles', *Advanced Materials*, 22(36). doi: 10.1002/adma.201001040.
Lee, Y. H. *et al.* (2005) 'Electrospun dual-porosity structure and biodegradation morphology of Montmorillonite reinforced PLLA nanocomposite scaffolds', *Biomaterials*, 26(16). doi: 10.1016/j.biomaterials.2004.08.018.
Li, G. *et al.* (2013) '5-Fluorouracil-loaded poly-L-lactide fibrous membrane for the prevention of intestinal stent restenosis', *Journal of Materials Science*, 48, pp. 6186–6193. doi: 10.1007/s10853-013-7415-5.
Li, L. *et al.* (2013) 'Effect of synthesis conditions on the properties of citric-acid coated iron oxide nanoparticles', *Microelectronic Engineering*, 110. doi: 10.1016/j.mee.2013.02.045.
Li, Q. *et al.* (2017) 'Correlation between particle size/domain structure and magnetic properties of highly crystalline Fe3O4 nanoparticles', *Scientific Reports*, 7(1). doi: 10.1038/s41598-017-09897-5.
Li, Y. F. *et al.* (2017) 'Light responsive hybrid nanofibres for on-demand therapeutic drug and cell delivery', *Journal of Tissue Engineering and Regenerative Medicine*, 11(8). doi: 10.1002/term.2169.
Lim, E.-H., Sardinha, J. P. and Myers, S. (2014) 'Nanotechnology Biomimetic Cartilage Regenerative Scaffolds', *Archives of Plastic Surgery*, 41(3), p. 231. doi: 10.5999/APS.2014.41.3.231.
Lin, T. C., Lin, F. H. and Lin, J. C. (2012) 'In vitro feasibility study of the use of a magnetic electrospun chitosan nanofiber composite for hyperthermia treatment of tumor cells', *Acta Biomaterialia*, 8(7). doi: 10.1016/j.actbio.2012.03.045.

Liu, L. *et al.* (2012) 'A novel 7-bromoindirubin with potent anticancer activity suppresses survival of human melanoma cells associated with inhibition of STAT3 and Akt signaling) A novel 7-bromoindirubin with potent anticancer activity suppresses survival of human melanoma cell', *Cancer Biology & Therapy*, 13, pp. 1255–1261. doi: 10.4161/cbt.21781.

Liu, W. and Gust, R. (2012) 'Metal N-heterocyclic carbene complexes as potential antitumor metallodrugs', *Chemical Society Reviews*, 42(2), pp. 755–773. doi: 10.1039/C2CS35314H.

Lojk, J. *et al.* (2015) 'Cell type-specific response to high intracellular loading of polyacrylic acid-coated magnetic nanoparticles', *International Journal of Nanomedicine*, 10. doi: 10.2147/IJN.S76134.

Longo, R. *et al.* (2022) 'Thermal and mechanical characterization of complex electrospun systems based on polycaprolactone and gelatin', *Journal of Thermal Analysis and Calorimetry*, 147, pp. 5391–5399. doi: 10.1007/s10973-022-11225-7.

Longo, R., Gorrasi, G. and Guadagno, L. (2021) 'Electromagnetically Stimuli-Responsive Nanoparticles-Based Systems for Biomedical Applications: Recent Advances and Future Perspectives', *Nanomaterials*, 11(4), p. 848. doi: 10.3390/nano11040848.

Longo, R., Guadagno, L. and Lamberti, P. (2020) 'Electromagnetic Characterization of Polycaprolactone electrospun nanofibers filled with Fe3O4 Nanoparticles', in *2020 4th International Symposium on Multidisciplinary Studies and Innovative Technologies (ISMSIT)*, pp. 1–5. doi: 10.1109/ISMSIT50672.2020.9254745.

De Luna-Bertos, E. *et al.* (2013) 'Therapeutic doses of nonsteroidal anti-inflammatory drugs inhibit osteosarcoma MG-63 osteoblast-like cells maturation, viability, and biomineralization potential', *TheScientificWorldJournal*, 2013. doi: 10.1155/2013/809891.

Lunnoo, T., Assawakhajornsak, J. and Puangmali, T. (2019) 'In Silico Study of Gold Nanoparticle Uptake into a Mammalian Cell: Interplay of Size, Shape, Surface Charge, and Aggregation', *Journal of Physical Chemistry C*, 123(6), pp. 3801–3810. doi: 10.1021/acs.jpcc.8b07616.

Lv, Z. *et al.* (2021) 'Noble Metal Nanomaterials for NIR-Triggered Photothermal Therapy in Cancer', *Advanced Healthcare Materials*, 10(6), p. 2001806. doi: 10.1002/adhm.202001806.

Lyu, S. P. and Untereker, D. (2009) 'Degradability of Polymers for Implantable Biomedical Devices', *International Journal of Molecular Sciences 2009, Vol. 10, Pages 4033-4065*, 10(9), pp. 4033–4065. doi: 10.3390/IJMS10094033.

Mackiewicz, M. *et al.* (2019) 'Degradable, thermo-, pH- and redox-sensitive hydrogel microcapsules for burst and sustained release of drugs', *International Journal of Pharmaceutics*, 569, p. 118589. doi: 10.1016/j.ijpharm.2019.118589.

Magherini, F. *et al.* (2018) 'Antiproliferative effects of two gold(I)-N-

heterocyclic carbene complexes in A2780 human ovarian cancer cells: a comparative proteomic study', *Oncotarget*, 9(46), p. 28042. doi: 10.18632/ONCOTARGET.25556.
Mahmoudi, K. *et al.* (2018) 'Magnetic hyperthermia therapy for the treatment of glioblastoma: a review of the therapy's history, efficacy and application in humans', *International Journal of Hyperthermia*, 34, pp. 1316–1328. doi: 10.1080/02656736.2018.1430867.
Mahmoudi, M. *et al.* (2011) 'Superparamagnetic iron oxide nanoparticles (SPIONs): Development, surface modification and applications in chemotherapy', *Advanced Drug Delivery Reviews*, 63(1–2). doi: 10.1016/j.addr.2010.05.006.
Mai, B. T. *et al.* (2019) 'Thermoresponsive Iron Oxide Nanocubes for an Effective Clinical Translation of Magnetic Hyperthermia and Heat-Mediated Chemotherapy', *ACS Applied Materials and Interfaces*. doi: 10.1021/acsami.8b16226.
Maier-Hauff, K. *et al.* (2011) 'Efficacy and safety of intratumoral thermotherapy using magnetic iron-oxide nanoparticles combined with external beam radiotherapy on patients with recurrent glioblastoma multiforme', *J. Neurooncol.*, 103, pp. 317–324. doi: 10.1007/s11060-010-0389-0.
Mariconda, A. *et al.* (2014) 'Synthesis, characterization and catalytic behaviour of a palladium complex bearing a hydroxyfunctionalized N-heterocyclic carbene ligand', *New J. Chem*, 38, p. 762. doi: 10.1039/c3nj01281f.
Mariconda, A. *et al.* (2020) 'New NHC- silver and gold complexes active in A3-coupling (aldehyde-alkyne-amine) reaction', *Molecular Catalysis*, 480, p. 110570. doi: 10.1016/J.MCAT.2019.110570.
Mariconda, A. *et al.* (2022) 'N-Heterocyclic Carbene (NHC) Silver Complexes as Versatile Chemotherapeutic Agents Targeting Human Topoisomerases and Actin', *ChemMedChem*, 17(18), p. e202200345. doi: 10.1002/CMDC.202200345.
Martínez, M. F. and Quiñones, L. A. (2018) 'Relationship Between Pharmacokinetics and Pharmacogenomics and Its Impact on Drug Choice and Dose Regimens', in *ADME Processes in Pharmaceutical Sciences*. Springer International Publishing, pp. 169–202. doi: 10.1007/978-3-319-99593-9_8.
McKeon-Fischer, K. D. and Freeman, J. W. (2011) 'Characterization of electrospun poly(L-lactide) and gold nanoparticle composite scaffolds for skeletal muscle tissue engineering', *Journal of Tissue Engineering and Regenerative Medicine*, 5(7). doi: 10.1002/term.348.
McNamara, K. and Tofail, S. A. M. (2017) 'Nanoparticles in biomedical applications', *Advances in Physics: X*, 2(1). doi: 10.1080/23746149.2016.1254570.
Medintz, I. L. *et al.* (2005) 'Quantum dot bioconjugates for imaging,

labelling and sensing', *Nature Materials*, 4(6). doi: 10.1038/nmat1390.
Melamed, J. R., Edelstein, R. S. and Day, E. S. (2015) 'Elucidating the fundamental mechanisms of cell death triggered by photothermal therapy', *ACS Nano*, 9(1). doi: 10.1021/acsnano.5b00021.
Miller, L., Leor, J. and Rubinsky, B. (2005) 'Cancer cells ablation with irreversible electroporation', *Technology in Cancer Research and Treatment*, 4(6). doi: 10.1177/153303460500400615.
Mir, L. M. *et al.* (1991) 'L'ELECTROCHIMIOTHERAPIE, UN NOUVEAU TRAITEMENT ANTITUMORAL: PREMIER ESSAI CLINIQUE', *Comptes Rendus de l'Academie des Sciences - Serie III*, 313(13), pp. 613–618.
Mir, L. M., Tounekti, O. and Orlowski, S. (1996) 'Bleomycin: Revival of an old drug', *General Pharmacology*, 27(5). doi: 10.1016/0306-3623(95)02101-9.
Mochane, M. J. *et al.* (2019) 'Morphology and Properties of Electrospun PCL and Its Composites for Medical Applications: A Mini Review', *Applied Sciences 2019, Vol. 9, Page 2205*, 9(11), p. 2205. doi: 10.3390/APP9112205.
Moise, S. *et al.* (2018) 'The potential of magnetic hyperthermia for triggering the differentiation of cancer cells', *Nanoscale*, 10(44), pp. 20519–20525. doi: 10.1039/c8nr05946b.
Moore, A. *et al.* (2000) 'Tumoral Distribution of Iron Oxide Nanoparticles in a Rodent Model', *Radiology*, 214(2). doi: https://doi.org/10.1148/radiology.214.2.r00fe19568.
Mora, M., Gimeno, M. C. and Visbal, R. (2019) 'Recent advances in gold–NHC complexes with biological properties', *Chemical Society Reviews*, 48(2), pp. 447–462. doi: 10.1039/C8CS00570B.
Moses, M. A., Brem, H. and Langer, R. (2003) 'Advancing the field of drug delivery: Taking aim at cancer', *Cancer Cell*, 4(5), pp. 337–341. doi: 10.1016/S1535-6108(03)00276-9.
Muenzner, J. K. *et al.* (2016) 'Ferrocenyl-Coupled N-Heterocyclic Carbene Complexes of Gold(I): A Successful Approach to Multinuclear Anticancer Drugs', *Chemistry (Weinheim an der Bergstrasse, Germany)*, 22(52), pp. 18953–18962. doi: 10.1002/CHEM.201604246.
Munj, H. R., Lannutti, J. J. and Tomasko, D. L. (2017) 'Understanding drug release from PCL/gelatin electrospun blends', *Journal of Biomaterials Applications*, 31(6), pp. 933–949. doi: 10.1177/0885328216673555.
Naddeo, C. *et al.* (2017) 'Nano-Charged Polypropylene Application: Realistic Perspectives for Enhancing Durability', *Materials*, 10, p. 943. doi: 10.3390/ma10080943.
Narayanan, G. (2015) 'Irreversible Electroporation', *Seminars in Interventional Radiology*, 32(4). doi: 10.1055/s-0035-1564706.
National Cancer Institute (2018) *Cancer Statistics Review, 1975-2014*.
Natu, M. V., de Sousa, H. C. and Gil, M. H. (2010) 'Effects of drug

solubility, state and loading on controlled release in bicomponent electrospun fibers', *International Journal of Pharmaceutics*, 397(1–2), pp. 50–58. doi: 10.1016/J.IJPHARM.2010.06.045.
Naves, L. B. *et al.* (2017) 'Nanotechnology for the treatment of melanoma skin cancer', *Progress in Biomaterials*, 6(1–2), p. 13. doi: 10.1007/S40204-017-0064-Z.
Niiyama, E. *et al.* (2019) 'Hyperthermia Nanofiber Platform Synergized by Sustained Release of Paclitaxel to Improve Antitumor Efficiency', *Advanced Healthcare Materials*, 8(13). doi: 10.1002/adhm.201900102.
Oberdörster, G. *et al.* (2005) 'Principles for characterizing the potential human health effects from exposure to nanomaterials: Elements of a screening strategy', *Particle and Fibre Toxicology*. BioMed Central, pp. 1–35. doi: 10.1186/1743-8977-2-8.
Ognjanović, M. *et al.* (2019) '99mTc-, 90Y-, and 177Lu-Labeled Iron Oxide Nanoflowers Designed for Potential Use in Dual Magnetic Hyperthermia/Radionuclide Cancer Therapy and Diagnosis', *ACS Applied Materials and Interfaces*, 11(44), pp. 41109–41117. doi: 10.1021/acsami.9b16428.
Orvig, C. and Abrams, M. J. (1999) 'Medicinal Inorganic Chemistry: Introduction', *Chemical Reviews*, 99(9), pp. 2202–2203. doi: 10.1021/CR980419W.
Osaka, T. *et al.* (2009) 'Effect of surface charge of magnetite nanoparticles on their internalization into breast cancer and umbilical vein endothelial cells', *Colloids and Surfaces B: Biointerfaces*, 71(2). doi: 10.1016/j.colsurfb.2009.03.004.
Osaki, F. *et al.* (2004) 'A quantum dot conjugated sugar ball and its cellular uptake. On the size effects of endocytosis in the subviral region', *Journal of the American Chemical Society*, 126(21). doi: 10.1021/ja048792a.
Otsuka, H. *et al.* (2001) 'Quantitative and reversible lectin-induced association of gold nanoparticles modified with α-lactosyl-ω-mercapto-poly(ethylene glycol)', *Journal of the American Chemical Society*, 123(34). doi: 10.1021/ja010437m.
Pakhomov, A. G. *et al.* (2019) 'Excitation and electroporation by MHz bursts of nanosecond stimuli', *Biochemical and Biophysical Research Communications*, 518(4), pp. 759–764. doi: 10.1016/J.BBRC.2019.08.133.
Pala, K. *et al.* (2013) 'Tumor-specifc hyperthermia with aptamer-tagged superparamagnetic nanoparticles', *International Journal of Nanomedicine*, 9(1). doi: 10.2147/IJN.S52539.
Palazzo, I. *et al.* (2021) 'Supercritical emulsion extraction fabricated PLA/PLGA micro/nano carriers for growth factor delivery: Release profiles and cytotoxicity', *International Journal of Pharmaceutics*, 592, p. 120108. doi: 10.1016/J.IJPHARM.2020.120108.
Papadopoulou, V. *et al.* (2006) 'On the use of the Weibull function for the discernment of drug release mechanisms', *International journal of*

pharmaceutics, 309(1–2), pp. 44–50. doi: 10.1016/J.IJPHARM.2005.10.044.
Park, J. H. *et al.* (2019) 'Gold nanocage-incorporated poly(ε-caprolactone) (PCL) fibers for chemophotothermal synergistic cancer therapy', *Pharmaceutics*, 11(2), p. 60. doi: 10.3390/pharmaceutics11020060.
Patel, Sarfaraz U. *et al.* (2012) 'Permeability of electrospun superhydrophobic nanofiber mats', *Journal of Nanotechnology*. doi: 10.1155/2012/483976.
Paunescu, V. *et al.* (2014) 'Enucleation: a possible mechanism of cancer cell death', *Journal of cellular and molecular medicine*, 18(6), pp. 962–965. doi: 10.1111/JCMM.12271.
Pavia, D. L. *et al.* (2015) *Introduction to Spectroscopy*.
Peng, Z. and Kong, L. X. (2007) 'A thermal degradation mechanism of polyvinyl alcohol/silica nanocomposites', *Polymer Degradation and Stability*, 92(6), pp. 1061–1071. doi: 10.1016/J.POLYMDEGRADSTAB.2007.02.012.
Persenaire, O. *et al.* (2001) 'Mechanisms and kinetics of thermal degradation of poly(ε-caprolactone)', *Biomacromolecules*, 2(1), pp. 288–294. doi: 10.1021/bm0056310.
Petryayeva, E. and Krull, U. J. (2011) 'Localized surface plasmon resonance: Nanostructures, bioassays and biosensing-A review', *Analytica Chimica Acta*, 706(1). doi: 10.1016/j.aca.2011.08.020.
Petryk, A. A. *et al.* (2009) 'Iron oxide nanoparticle hyperthermia and chemotherapy cancer treatment', *Proceedings of SPIE - The International Society for Optical Engineering*, 7181, p. 71810N. doi: 10.1117/12.810024.
Pitkethly, M. J. (2004) 'Nanomaterials – the driving force', *Materials Today*, 7(12), pp. 20–29. doi: 10.1016/S1369-7021(04)00627-3.
Płachta, I. *et al.* (2021) 'Current diagnosis and treatment options for cutaneous adnexal neoplasms with apocrine and eccrine differentiation', *International Journal of Molecular Sciences*, 22(10). doi: 10.3390/ijms22105077.
Pradhan, S., Ghosh, D. and Chen, S. (2009) 'Janus nanostructures based on Au-TiO2 heterodimers and their photocatalytic activity in the oxidation of methanol', *ACS Applied Materials and Interfaces*, 1(9), pp. 2060–2065. doi: 10.1021/am900425v.
Quirt, I. *et al.* (2007) 'Temozolomide for the treatment of metastatic melanoma', *Current Oncology*, 14(1), p. 27. doi: 10.3747/CO.2007.98.
Rabanel, J.-M. *et al.* (2019) 'Nanoparticle heterogeneity: an emerging structural parameter influencing particle fate in biological media?', *Nanoscale REVIEW Cite this: Nanoscale*, 11, p. 383. doi: 10.1039/c8nr04916e.
Radoń, A. *et al.* (2018) 'Electrical Conduction Mechanism and Dielectric Properties of Spherical Shaped Fe_3O_4 Nanoparticles Synthesized by Co-Precipitation Method', *Materials (Basel, Switzerland)*, 11(5). doi: 10.3390/MA11050735.

Ramakrishna, S. *et al.* (2005) *An introduction to electrospinning and nanofibers*, *An Introduction to Electrospinning and Nanofibers*. doi: 10.1142/5894.
Rashid, T. U., Gorga, R. E. and Krause, W. E. (2021) 'Mechanical Properties of Electrospun Fibers—A Critical Review', *Advanced Engineering Materials*, 23(9), p. 2100153. doi: 10.1002/ADEM.202100153.
Rastinehad, A. R. *et al.* (2019) 'Gold nanoshell-localized photothermal ablation of prostate tumors in a clinical pilot device study', *Proc Natl Acad Sci USA*, 116, pp. 18590–18596. doi: 10.1073/pnas.1906929116.
Riley, R. S. and Day, E. S. (2017) 'Gold nanoparticle-mediated photothermal therapy: applications and opportunities for multimodal cancer treatment', *Wiley Interdisciplinary Reviews: Nanomedicine and Nanobiotechnology*, 9(4). doi: 10.1002/wnan.1449.
Roesch, A. *et al.* (2010) 'A Temporarily Distinct Subpopulation of Slow-Cycling Melanoma Cells Is Required for Continuous Tumor Growth', *Cell*, 141(4), pp. 583–594. doi: 10.1016/J.CELL.2010.04.020.
Romand, J. and Vodar, B. (1951) 'Spectres d'absorption du benzene a l'etat vapeur et a l'etat condense dans l'ultraviolet lointain', *Compt. Rend.*, 233, pp. 930–932.
Rosensweig, R. E. (2002) 'Heating magnetic fluid with alternating magnetic field', *Journal of Magnetism and Magnetic Materials*, 252(1-3 SPEC. ISS.), pp. 370–374. doi: 10.1016/S0304-8853(02)00706-0.
Ryan, R. F., Krementz, E. T. and Litwin, M. S. (1988) 'A role for topical 5-fluorouracil therapy in melanoma', *Journal of Surgical Oncology*, 38, pp. 250–256.
S Y Lee (1996) 'Bacterial polyhydroxyalkanoates ', *Biotechnology and Bioengineering*, 49, pp. 1–14.
Safaie, N. and Ferrier, R. C. (2020) 'Janus nanoparticle synthesis: Overview, recent developments, and applications', *Journal of Applied Physics*, 127(17), p. 220901. doi: 10.1063/5.0003329.
Salman, U. M. A. and Ubed, U. R. M. (2018) *Synthesis of Fe3O4 nanoparticles for the treatment of oral cancer*.
Sapio, L. *et al.* (2020) 'Chlorogenic acid activates ERK1/2 and inhibits proliferation of osteosarcoma cells', *Journal of Cellular Physiology*, 235(4), pp. 3741–3752. doi: 10.1002/jcp.29269.
Saraiva, M. A. (2020) 'Interpretation of α-synuclein UV absorption spectra in the peptide bond and the aromatic regions', *Journal of Photochemistry and Photobiology B: Biology*, 212, p. 112022. doi: 10.1016/J.JPHOTOBIOL.2020.112022.
Sarno, M. *et al.* (2017) 'High activity and selectivity immobilized lipase on Fe3O4 nanoparticles for banana flavour synthesis', *Process Biochemistry*, 56. doi: 10.1016/j.procbio.2017.02.004.
Sarno, M. and Iuliano, M. (2019) 'Highly active and stable Fe3O4/Au nanoparticles supporting lipase catalyst for biodiesel production from waste

tomato', *Applied Surface Science*, 474, pp. 135–146. doi: 10.1016/J.APSUSC.2018.04.060.
Saturnino, C. *et al.* (2016) 'N-heterocyclic carbene complexes of silver and gold as novel tools against breast cancer progression', *Future medicinal chemistry*, 8(18), pp. 2213–2229. doi: 10.4155/FMC-2016-0160.
Saturnino, C. *et al.* (2018) 'Inhibition of Human Topoisomerase II by N,N,N-Trimethylethanammonium Iodide Alkylcarbazole Derivatives', *ChemMedChem*, 13(24), pp. 2635–2643. doi: 10.1002/cmdc.201800546.
Scala, P. *et al.* (2022) 'Myogenic commitment of human stem cells by myoblasts Co-culture: a static vs. a dynamic approach', *Artificial Cells, Nanomedicine, and Biotechnology*, 50(1), pp. 49–58. doi: 10.1080/21691401.2022.2039684/SUPPL_FILE/IANB_A_2039684_SM8140.DOCX.
Scheffel, U. *et al.* (1972) 'Albumin microspheres for study of the reticuloendothelial system.', *Journal of Nuclear Medicine*, 13(7), pp. 498–503.
Schmaljohann, D. (2006) 'Thermo- and pH-responsive polymers in drug delivery', *Advanced Drug Delivery Reviews*, 58(15). doi: 10.1016/j.addr.2006.09.020.
Schueler, B. A. (1998) 'The AAPM/RSNA Physics Tutorial for Residents: Clinical Applications of Basic X-ray Physics Principles', *Radiographics*, 18(3), pp. 731–744. doi: 10.1148/radiographics.18.3.9599394.
Sersa, G. (2006) 'The state-of-the-art of electrochemotherapy before the ESOPE study; advantages and clinical uses', *European Journal of Cancer, Supplement*, 4(11), pp. 52–59. doi: 10.1016/j.ejcsup.2006.08.007.
Shapero, K. *et al.* (2011) 'Time and space resolved uptake study of silica nanoparticles by human cells', *Molecular BioSystems*, 7(2). doi: 10.1039/c0mb00109k.
Shin, S. W., Song, I. H. and Um, S. H. (2015) 'Role of Physicochemical Properties in Nanoparticle Toxicity', *Nanomaterials*, 5, pp. 1351–1365. doi: 10.3390/nano5031351.
Siepmann, J. and Siepmann, F. (2012) 'Modeling of diffusion controlled drug delivery', *Journal of Controlled Release*, 161(2), pp. 351–362. doi: 10.1016/J.JCONREL.2011.10.006.
Silveira, D. C. *et al.* (2019) 'Electromagnetic characterization of recyclable polymer nanofibers based on PSU/carbonyl iron', *Journal of Renewable Materials*, 7(3), pp. 279–287. doi: 10.32604/jrm.2019.01834.
Sinicropi, M. S. *et al.* (2018) 'N-thioalkylcarbazoles derivatives as new anti-proliferative agents: synthesis, characterisation and molecular mechanism evaluation', *Journal of enzyme inhibition and medicinal chemistry*, 33(1), pp. 434–444. doi: 10.1080/14756366.2017.1419216.
Sirignano, M. *et al.* (2022) 'Catalytic and biological activity of silver and gold complexes stabilized by nhc with hydroxy derivatives on nitrogen atoms', *Catalysts*, 12(1), p. 18. doi: 10.3390/CATAL12010018/S1.

Skrabalak, S. E. *et al.* (2007) 'Gold nanocages for biomedical applications', *Advanced Materials*, 19(20). doi: 10.1002/adma.200701972.
Smith, A. M., Mancini, M. C. and Nie, S. (2009) 'Bioimaging: Second window for in vivo imaging', *Nature Nanotechnology*, 4(11). doi: 10.1038/nnano.2009.326.
Son, Y., Kim, W. and Yoo, H. (2014) 'Therapeutic applications of electrospun nanofibers for drug delivery systems', *Archives of pharmacal research*, 37(1), pp. 69–78. doi: 10.1007/S12272-013-0284-2.
Sownthari, K. and Suthanthiraraj, S. A. (2013) 'Synthesis and characterization of an electrolyte system based on a biodegradable polymer', *Express Polymer Letters*, 7(6), pp. 495–504. doi: 10.3144/EXPRESSPOLYMLETT.2013.46.
Steffens, L. *et al.* (2020) 'Electrospun PVA-Dacarbazine nanofibers as a novel nano brain-implant for treatment of glioblastoma: in silico and in vitro characterization', *European Journal of Pharmaceutical Sciences*, 143, p. 105183. doi: 10.1016/J.EJPS.2019.105183.
Steffens Reinhardt, L. *et al.* (2019) 'Freeze-thaw electrospun PVA-dacarbazine nanoparticles: preparation, characterization and anticancer evaluation', *https://doi.org/10.1080/00914037.2019.1605606*, 69(12), pp. 749–760. doi: 10.1080/00914037.2019.1605606.
Stupp, R. *et al.* (2005) 'Radiotherapy plus Concomitant and Adjuvant Temozolomide for Glioblastoma', *New England Journal of Medicine*, 352(10), pp. 987–996. doi: 10.1056/nejmoa043330.
Sukhanova, A. *et al.* (2018) 'Dependence of Nanoparticle Toxicity on Their Physical and Chemical Properties', *Nanoscale Research Letters*, 13. doi: 10.1186/s11671-018-2457-x.
Sun, L., Liu, D. and Wang, Z. (2008) 'Functional gold nanoparticle - Peptide complexes as cell-targeting agents', *Langmuir*, 24(18). doi: 10.1021/la8015063.
Szlezak, M. *et al.* (2017) 'Monoolein cubic phase gels and cubosomes doped with magnetic nanoparticles-hybrid materials for controlled drug release', *ACS Applied Materials and Interfaces*, 9(3), pp. 2796–2805. doi: 10.1021/acsami.6b12889.
Takae, S. *et al.* (2005) 'Ligand density effect on biorecognition by PEGylated gold nanoparticles: Regulated interaction of RCA120 lectin with lactose installed to the distal end of tethered PEG strands gold surface', *Biomacromolecules*, 6(2). doi: 10.1021/bm049427e.
Tan, S. H. *et al.* (2005) 'Systematic parameter study for ultra-fine fiber fabrication via electrospinning process', *Polymer*, 46(16), pp. 6128–6134. doi: 10.1016/J.POLYMER.2005.05.068.
Tang, H. *et al.* (2018) 'Recent Development of pH-Responsive Polymers for Cancer Nanomedicine', *Molecules*, 24(1), p. 4. doi: 10.3390/molecules24010004.
Teo, R. D., Termini, J. and Gray, H. B. (2016) 'Lanthanides: Applications in

Cancer Diagnosis and Therapy', *Journal of Medicinal Chemistry*, 59(13), pp. 6012–6024. doi: 10.1021/acs.jmedchem.5b01975.
Tieleman, D. P. (2004) 'The molecular basis of electroporation', *BMC Biochemistry*, 5, pp. 1–12. doi: 10.1186/1471-2091-5-10.
Tkachenko, A. G. *et al.* (2003) 'Multifunctional gold nanoparticle-peptide complexes for nuclear targeting', *Journal of the American Chemical Society*, 125(16). doi: 10.1021/ja0296935.
Tomitaka, A. *et al.* (2011) 'Magnetic characterization of surface-coated magnetic nanoparticles for biomedical application', *Journal of Magnetism and Magnetic Materials*, 323(10). doi: 10.1016/j.jmmm.2010.11.054.
Tran, L. T. C., Lesieur, S. and Faivre, V. (2014) 'Janus nanoparticles: Materials, preparation and recent advances in drug delivery', *Expert Opinion on Drug Delivery*, 11(7), pp. 1061–1074. doi: 10.1517/17425247.2014.915806.
Tran, N. and Webster, T. J. (2010) 'Magnetic nanoparticles: Biomedical applications and challenges', *Journal of Materials Chemistry*, 20(40). doi: 10.1039/c0jm00994f.
Trevor, A. J., Katzung, B. G. and kruidering-Hall, M. (2013) 'Chapter 2. Pharmacodynamics ', in *Pharmacology Examination & Board Review*. McGraw Hill Educati…, pp. 16–25.
Tsai, S. R. and Hamblin, M. R. (2017) 'Biological effects and medical applications of infrared radiation', *Journal of Photochemistry and Photobiology B: Biology*, 170, pp. 197–207. doi: 10.1016/j.jphotobiol.2017.04.014.
Turner, N., Ware, O. and Bosenberg, M. (2018) 'Genetics of metastasis: melanoma and other cancers', *Clinical & Experimental Metastasis 2018 35:5*, 35(5), pp. 379–391. doi: 10.1007/S10585-018-9893-Y.
U. S. Food and Drug Administration (1992) *Route of Administration* .
Verhoeven, E. *et al.* (2009) 'Modeling drug release from hot-melt extruded mini-matrices with constant and non-constant diffusivities', *European Journal of Pharmaceutics and Biopharmaceutics*, 73(2), pp. 292–301. doi: 10.1016/J.EJPB.2009.06.010.
Vinardell, M. and Mitjans, M. (2015) 'Antitumor Activities of Metal Oxide Nanoparticles', *Nanomaterials*, 5(2), pp. 1004–1021. doi: 10.3390/nano5021004.
De Vivo, B. *et al.* (2013) 'Numerical investigation on the influence factors of the electrical properties of carbon nanotubes-filled composites', *Journal of Applied Physics*, 113(24), p. 244301. doi: 10.1063/1.4811523.
Vulic, K. and Shoichet, M. S. (2014) 'Affinity-Based Drug Delivery Systems for Tissue Repair and Regeneration'. doi: 10.1021/bm501084u.
Wang, G. *et al.* (2013) 'Facile preparation of poly(e-caprolactone)/ Fe 3 O 4 @graphene oxide superparamagnetic nanocomposites', *Polym. Bull*, 70, pp. 2359–2371. doi: 10.1007/s00289-013-0957-5.
Wang, L. *et al.* (2018) 'Combination therapy comprising irreversible

electroporation and hydroxycamptothecin loaded electrospun membranes to treat rabbit VX2 subcutaneous cancer', *Biomedical Microdevices*, 20(4). doi: 10.1007/s10544-018-0336-y.
Wang, N. X. and Von Recum, H. A. (2010) 'Affinity-Based Drug Delivery', *Macromolecular Bioscience*, 11, pp. 321–332. doi: 10.1002/mabi.201000206.
Wang, S. *et al.* (2010) 'Targeted nanoparticles enhanced flow electroporation of antisense oligonucleotides in leukemia cells', *Biosensors and Bioelectronics*, 26(2). doi: 10.1016/j.bios.2010.06.025.
Wang, Y. *et al.* (2007) 'Fabrication of Au/PVP nanofiber composites by electrospinning', *Journal of Applied Polymer Science*, 105(6). doi: 10.1002/app.25003.
Wang, Y. C. *et al.* (2018) 'Synthetic methodologies to gold nanoshells: An overview', *Molecules*, 23(11). doi: 10.3390/molecules23112851.
Wang, Z. *et al.* (2014) 'Medical applications of microwave imaging', *Scientific World Journal*, 2014. doi: 10.1155/2014/147016.
Wei, Y. *et al.* (2011) 'Magnetic biodegradable Fe3O4/CS/PVA nanofibrous membranes for bone regeneration', *Biomedical Materials*, 6(5). doi: 10.1088/1748-6041/6/5/055008.
Welch, D. R. *et al.* (1991) 'Characterization of a highly invasive and spontaneously metastatic human malignant melanoma cell line', *International Journal of Cancer*, 47(2), pp. 227–237. doi: 10.1002/IJC.2910470211.
Widder, K. J. *et al.* (1983) 'Selective targeting of magnetic albumin microspheres containing low-dose doxorubicin: Total remission in Yoshida sarcoma-bearing rats', *European Journal of Cancer and Clinical Oncology*, 19(1). doi: 10.1016/0277-5379(83)90408-X.
Willets, K. A. and Van Duyne, R. P. (2007) 'Localized surface plasmon resonance spectroscopy and sensing', *Annual Review of Physical Chemistry*, 58. doi: 10.1146/annurev.physchem.58.032806.104607.
Winter, J. C. F. de (2019) 'Using the Student's t-test with extremely small sample sizes', *Practical Assessment, Research, and Evaluation*, 18(1), p. 10. doi: https://doi.org/10.7275/e4r6-dj05.
Wu, J. *et al.* (2020) 'Mechanism of a long-term controlled drug release system based on simple blended electrospun fibers', *Journal of Controlled Release*, 320, pp. 337–346. doi: 10.1016/J.JCONREL.2020.01.020.
Xiao, K. *et al.* (2011) 'The effect of surface charge on in vivo biodistribution of PEG-oligocholic acid based micellar nanoparticles', *Biomaterials*, 32(13), pp. 3435–3446. doi: 10.1016/j.biomaterials.2011.01.021.
Xu, W. *et al.* (2014) 'Mechanical flexible PI/MWCNTs nanocomposites with high dielectric permittivity by electrospinning', *European Polymer Journal*, 59, pp. 129–135. doi: 10.1016/j.eurpolymj.2014.07.028.
Yadollahpour, A. and Rezaee, Z. (2014) 'Electroporation as a new cancer treatment technique: A review on the mechanisms of action', *Biomedical*

and Pharmacology Journal, 7(1), pp. 53–62. doi: 10.13005/bpj/452.
Yagawa, Y. *et al.* (2017) 'Cancer immunity and therapy using hyperthermia with immunotherapy, radiotherapy, chemotherapy, and surgery', *Journal of Cancer Metastasis and Treatment*, 3(10). doi: 10.20517/2394-4722.2017.35.
Yanase, M. *et al.* (1998) 'Intracellular hyperthermia for cancer using magnetite cationic liposomes: An in vivo study', *Japanese Journal of Cancer Research*, 89(4). doi: 10.1111/j.1349-7006.1998.tb00586.x.
Yao, R. *et al.* (2016a) 'Electrospun PCL/Gelatin composite fibrous scaffolds: mechanical properties and cellular responses', *Journal of Biomaterials Science, Polymer Edition*, 27(9), pp. 824–838. doi: 10.1080/09205063.2016.1160560.
Yao, R. *et al.* (2016b) 'Electrospun PCL/Gelatin composite fibrous scaffolds: Mechanical properties and cellular responses', *Journal of Biomaterials Science, Polymer Edition*, 27(9), pp. 824–838. doi: 10.1080/09205063.2016.1160560.
Yew, Y. P. *et al.* (2020) 'Green biosynthesis of superparamagnetic magnetite Fe3O4 nanoparticles and biomedical applications in targeted anticancer drug delivery system: A review', *Arabian Journal of Chemistry*, 13(1), pp. 2287–2308. doi: 10.1016/J.ARABJC.2018.04.013.
Yoo, D. *et al.* (2011) 'Theranostic magnetic nanoparticles', *Accounts of Chemical Research*, 44(10), pp. 863–874. doi: 10.1021/ar200085c.
You, J. *et al.* (2012) 'Photothermal-chemotherapy with doxorubicin-loaded hollow gold nanospheres: A platform for near-infrared light-trigged drug release', *Journal of Controlled Release*, 158(2). doi: 10.1016/j.jconrel.2011.10.028.
Yue, Z.-G. *et al.* (2011) 'Surface Charge Affects Cellular Uptake and Intracellular Trafficking of Chitosan-Based Nanoparticles', *Biomacromolecules*, 12, pp. 2440–6. doi: 10.1021/bm101482r.
Zahid, A. A. S. M. *et al.* (2019) 'Effect of amino, hydroxyl, and carboxyl terminal groups of alkyl chains of self-assembled monolayers on the adsorption pattern of gold nanoparticles', *Surface and Interface Analysis*, 51(11). doi: 10.1002/sia.6697.
Zelzer, M. *et al.* (2013) 'Enzyme responsive materials: Design strategies and future developments', *Biomaterials Science*, 1(1), pp. 11–39. doi: 10.1039/c2bm00041e.
Zhan, S. *et al.* (2019) 'Preparation and in vitro release kinetics of nitrendipine-loaded PLLA–PEG–PLLA microparticles by supercritical solution impregnation process', *RSC Advances*, 9(28), pp. 16167–16175. doi: 10.1039/C9RA01068H.
Zhang, C. L. and Yu, S. H. (2014) 'Nanoparticles meet electrospinning: Recent advances and future prospects', *Chemical Society Reviews*, 43(13). doi: 10.1039/c3cs60426h.
Zhang, H. *et al.* (2017) 'Magnetic nanoparticle-loaded electrospun polymeric nanofibers for tissue engineering', *Materials Science and Engineering C*, 73.

doi: 10.1016/j.msec.2016.12.116.
Zhang, H. *et al.* (2019) 'Photothermal-assisted surface-mediated gene delivery for enhancing transfection efficiency', *Biomaterials Science*, 7(12). doi: 10.1039/c9bm01284b.
Zhang, L. *et al.* (2018) 'Dual drug delivery and sequential release by amphiphilic Janus nanoparticles for liver cancer theranostics', *Biomaterials*, 181, pp. 113–125. doi: 10.1016/j.biomaterials.2018.07.060.
Zhang, L., He, R. and Gu, H. C. (2006) 'Oleic acid coating on the monodisperse magnetite nanoparticles', *Applied Surface Science*, 253(5). doi: 10.1016/j.apsusc.2006.05.023.
Zhang, X. D. *et al.* (2011) 'Size-dependent in vivo toxicity of PEG-coated gold nanoparticles.', *International journal of nanomedicine*, 6. doi: 10.2147/ijn.s21657.
Zhang, Y. *et al.* (2005) 'Electrospinning of gelatin fibers and gelatin/PCL composite fibrous scaffolds', *Journal of Biomedical Materials Research - Part B Applied Biomaterials*, 72(1), pp. 156–165. doi: 10.1002/jbm.b.30128.
Zhang, Z. *et al.* (2015) 'Electrospun PLA/MWCNTs composite nanofibers for combined chemo- and photothermal therapy', *Acta Biomaterialia*, 26. doi: 10.1016/j.actbio.2015.08.003.
Zhao, J. *et al.* (2017) 'Influence of nanoparticle shapes on cellular uptake of paclitaxel loaded nanoparticles in 2D and 3D cancer models', *Polymer Chemistry*, 8(21), pp. 3317–3326. doi: 10.1039/c7py00385d.
Zhao, Y. T. *et al.* (2020) 'Self-powered portable melt electrospinning for in situ wound dressing', *Journal of Nanobiotechnology*, 18(1), pp. 1–10. doi: 10.1186/S12951-020-00671-W/TABLES/1.
Zheng, Y. *et al.* (2020) 'Photothermally Activated Electrospun Nanofiber Mats for High-Efficiency Surface-Mediated Gene Transfection', *ACS Applied Materials and Interfaces*, 12(7). doi: 10.1021/acsami.9b20221.
Zhong, L. *et al.* (2021) 'Small molecules in targeted cancer therapy: advances, challenges, and future perspectives', *Signal Transduction and Targeted Therapy*, 6, p. 201. doi: 10.1038/s41392-021-00572-w.
Zhong, Y. *et al.* (2015) 'Electrospun magnetic nanofibre mats - A new bondable biomaterial using remotely activated magnetic heating', *Journal of Magnetism and Magnetic Materials*, 380. doi: 10.1016/j.jmmm.2014.09.069.
Zhong, Z. J. (2009) 'Introduction', *Optical Properties and Spectroscopy of Nanomaterials*, pp. 1–9. doi: 10.1142/9789812836663_0001.
Zu, Y. *et al.* (2014) 'Gold nanoparticles enhanced electroporation for mammalian cell transfection', *Journal of Biomedical Nanotechnology*, 10(6), pp. 982–992. doi: 10.1166/jbn.2014.1797.